Distilling Information from Noisy Data: Examples from Microscopy

by

Erik Forbes Y. Hom

DISSERTATION

Submitted in partial satisfaction of the requirements for the degree of

DOCTOR OF PHILOSOPHY

in

BIOPHYSICS

in the

GRADUATE DIVISION

of the

UNIVERSITY OF CALIFORNIA, SAN FRANCISCO

Approved by Committee in Charge:

Chair	Date
	Date
	Date

Deposited in the Library, University of California, San Francisco

Date	University Librarian

Degree Conferred:

Distilling Information from Noisy Data: Examples from Microscopy

Erik Forbes Y. Hom

To my family:

Mom, Dad, and Xenia;

and Christine,

my beautiful bride.

Acknowledgments

Science is a community affair and without the technical assistance, scientific insights, and steady encouragement of numerous people, the research described herein would not have been realized.

Sudipta Maiti, J. Balaji, and Parijat Sengupta in the Laboratory for Biophotonics at the Tata Institute for Fundamental Research (TIFR) in Mumbai, India, provided wonderful advice and counsel on the nuts-and-bolts of fluorescence correlation spectroscopy during a summer sabbatical visit in 2000 (funded by a NIH-Fogarty International grant). Their comraderie, warm welcome, and sharp minds, helped make my visit productive and forever memorable. Sudpita, who was largely responsible for reviving FCS in Watt Webb's group, helped lay a foundation for me to truely appreciate the experimental nuances of FCS. I also thank Dr. N. Periasamy (aka "Peri") in the Department of Chemical Sciences at TIFR for serving as my wonderful host, and for cooking my first meal in India – dhosai with coconut chutney!

David Thompson, formerly a post-doc in George Feher's lab at Stanford and now on the faculty of the Chemistry Department at Lawrence University, was both kind, committed, and gracious beyond expectation in helping me set-up the Ti:sapphire laser system described in Part I. Only a good friend would drive up from Palo Alto, work into the wee-hours of the morning teaching me the ropes, hike up (the very steep) Medical Center Way to fetch his car and drive back home – and do this all more than once to help me out of a bind.

Sebastian Haase, the computer guru in the Sedat lab, was the one who convinced me that Numerical Python was "awesome" and helped me extensively with programming

nitty-gritties related to the AIDA program described in Part II. AIDA wouldn't have been written as quickly as it was nor be functional without his help.

Franck Marchis, a research astronomer at UC Berkeley was my collaborator on the AIDA project. His experience with MISTRAL and expertise in astronomical data processing from an experimentalist's perspective were vital to the project. Not only did I learn about astronomy and some cool cutting-edge findings, I experienced the joy of working with a Frenchman. I thoroughly enjoyed his blunt musings about other "Frenchies" – and the soap opera that is science.

I thank Elliot Elson of Washington University in St. Louis for providing a copy of Ron Icenogle's doctoral thesis, which was a great help to me in working out the FCS theory in Chapter 2. Kendall Read of KMLabs, Ltd. (Boulder, CO) was always a saint in answering my many technical specifications questions about their Ti:Sapph laser kit. I thank Lily Jan and the confocal/two-photon microscopy users group at the UCSF Parnassus campus for an extended loan of their 60X water immersion objective and power meter for my experimental FFM work. I thank Lily also for always believing in me as a scientist and for her quiet but sure support ever since I rotated in her lab. Jixiang Zhu of Correlator.com (Bridgewater, NJ) was very helpful in providing me with bug fixes and requested extensions to his correlator card acquisition/analysis software in an almost on-demand time frame (now that's customer support!). John Weeks at WaveMetrics, Inc. (Lake Oswego, OR) was gracious to accomodate my request for a more flexible global analysis package that would be useful for the analysis of TCFFM experimental data. I'm happy to report that that package is now available in versions of 5.02 and higher (see what you get for asking!).

I thank Tziki Kam (Weizmann Institute, Rehovat, Israel), Eugene Ingerman (UC Davis and Lawrence Livermore National Labs), Mats Gustafsson, and Peter Kner for discussions related to the work of Part II. Eugene Ingerman and Stephen Lane (Center for Biophotonics, UC Davis; Lawrence Livermore National Labs) are to be thanked for making Dennis Goodman's excellent conjugate gradient code available to me. Deserving particular mention are Timothy Lee, an undergraduate at UC Berkeley who spent several summers working with me, and Siddharth Shah, a visiting graduate student from the University of Michigan. Both worked with me on AIDA related extensions (which are currently under development and unfortunately are not presented here): Sid on extending AIDA to electron microscopy data and Tim on extending AIDA for structured illumination microscopy. Tim was also a vital help early on in building AIDA's multi-frame capabilities. Working as a team with them has been a great deal of fun and I expect both will do well in their future endeavors.

Alan Verkman gave me the independence and resources to chase the crazy idea of measuring equilibium constants of proteins within their native cellular environment when I arrived at UCSF. Although this ambitious goal couldn't be reached during my time in his lab, the experience taught me a lot about the hard realities of the scientific enterprise and challenged me to keep pushing to surmount apparently daunting hurdles. While we often didn't see eye-to-eye, I learned a great deal from Alan about how to run a lab and write successful grants.

John Sedat was very kind, gracious, and patient to let me take up residence in his lab while I was contemplating switching labs, and finally for letting me join his lab.

John continually thinks about science and the people in his lab, caring deeply about their well-being. He set a good example for me as a scientist who focuses on the important and classical over the trendy and popular, who thinks outside of the box and is willing to challenge orthodoxy, and who learns broadly. Having worked with John, a bona fide O.B.M. ("one banana monkey"), I see why many of his students and post-docs have gone on to do so well in science.

To my other thesis committee members, David Agard and Ron Vale, I owe much - if not my Ph.D. Without their constant support, guidance, and advocacy, I may very well have gotten off the scientific research track. While I probably could have sought their guidance more often, both were really good mentors and for some flattering reason to me took a genuine interest in my scientific career and development. I thank David for taking a special interest in the work described in this thesis and for keeping me honest. His scientific questioning may not have led to me generating better or the desired results, but they always resulted in better, objective science. And I thank Ron for giving me level-headed advice at all levels; I appreciate his wisdom and hope as a mentor one day, I'll be able to dole out advice like his.

Julie Ransom, program administrator and "mother hen" for the Biophysics program, was always interested in us students as people first and scientists second. She deserves as much credit as my thesis committee in seeing me through to the end. Thank you Julie, for all your support and counsel, and for taking care of all the thankless little things over the years like dealing with registration logistics. Dennis Deen and Dick Shafer were great listeners during difficult times in graduate school. I thank Dennis in particular for his generosity in

time and interest; he went far beyond the call of duty as a graduate advisor, taking me out to lunch periodically to talk and making sure I was able to do well.

I thank Peter Haggie, Javier Farinas, and Sujatha Jayaraman for their comraderie while we overlapped in the Verkman Lab. Felix Aburto, Emerick Gallego, Sebastian Haase, Mike Lowenstein, Lin Shao, and Satoru Uzawa all welcomed me into the Sedat Lab and made me feel at home when I first joined. Since then, crazy conversations, fun lunches discussing the Examiner "Scoop!", and "la-la-la-la-la" song-singing have been had with Suchie Bhattacharyya, Heather McCune, Sid Shah, Yuri Strukov, and others in the Agard/Gustafsson/Sedat consortium and Genentech Hall N-414/416 neighborhood, making the day-to-day entertaining and creating a lab environment filled with comic relief and good spirits. Sid Shah in particular must be thanked for the many free shoulder massages that alleviated the pains of working for hours hunched over a computer.

Hector Aldaz, Mark Dayel, Andrew Tan, and Kurt Thorn have become good friends and colleagues and were a great source of encouragement during rough times. It is also with them that I've discussed and dreamt about scientific matters both grand and small throughout my time in graduate school. I expect this will continue well into the future.

My family, though often questioning my decision and plans to become a "poor" academic, have always respected, loved, and been supportive of me doing what I felt I should be doing even if it didn't make much lifestyle sense to them. My lovely wife, Christine, wasn't around for the early years during which my love for science developed. Nevertheless, she's quickly taken up my passion and vision as her own even though the "science world" is terribly foreign to her. Such is love! I thank them all for keeping me grounded in the things

that matter most in life.

Finally, this work was supported in part by NIH grants EB00415 (formerly DK43840) to Alan Verkman and GM25101-26 to John Sedat. I thank the American Heart Association (Western States Affiliates) for supporting me with a pre-doctoral fellowship and the Mustard Seed Foundation for a Harvey Fellowship.

Contribution Synopsis

Chapter 2 is a reprint of material that was originally published in the *Biophysical Journal*. The paper includes Alan Verkman as a co-author. Erik Hom developed the theory, carried out the calculations, and wrote the paper with the research support of Alan Verkman.

Chapter 3 describes unpublished work involving the assembly of a two-photon, two-color fluorescence fluctuation microscope, and pilot experiments using the microscope. Erik Hom helped design, built and tested the apparatus, performed the experiments, and worked out the proposed data analysis schemes. Alan Verkman provided the space and financial support that made this project possible.

Chapter 4 is a reprint of material that will be published in the *Journal of Physical Chemistry, B*. The paper includes James Dix and Alan Verkman as co-authors. James Dix performed the molecular/brownian dynamics simulations, conducted most of the analysis, and helped write the paper. Erik Hom developed the photon arrival time analysis framework, helped with data analysis (IGOR Pro and Mathematica), outlined the paper, and helped write portions of the paper. Alan Verkman supported the research and provided editorial direction.

Chapter 5 describes Erik Hom's unpublished ideas on how the theory and application of fluorescence fluctuation microscopy can be further developed.

Chapters 6 through 9 contain material that will be submitted for publication in the *Journal of the Optical Society of America, A*. The paper includes Franck Marchis, Timothy Lee, Sebastian Haase, David Agard, and John Sedat as co-authors. Erik Hom developed and wrote the AIDA program and paper. Franck Marchis provided feedback on the AIDA

algorithm, helped with data analysis, provided counsel on the practicalities of astronomical imaging, helped generate key figures, and wrote portions of the astronomical imaging sections. Timothy Lee helped refurbish and develop early versions of the multiframe analysis AIDA code. Sebastian Haase built the Priithon framework upon which AIDA is based and provided vital programming expertise and counsel. David Agard and John Sedat supported and directed this work.

Appendix A is a reprint of a paper that was published in the *Biophysical Journal*. The paper includes Mark Dayel and Alan Verkman as co-authors. This work grew out of Erik Hom's pre-doctoral fellowship proposals directed at understanding protein-misfolding and chaperone activity within the endoplasmic reticulum. Mark Dayel (a technician in the Verkman lab at the time) performed the experiments and prepared the Figures. Erik Hom helped interpret the data, worked out the analytical diffusion analysis in the Appendix, and wrote most of the paper. Alan Verkman directed and supervised the research.

Abstract

Distilling Information from Noisy Data: Examples from Microscopy

by

Erik Forbes Y. Hom

Doctor of Philosophy in Biophysics

University of California, San Francisco

Professor John W. Sedat, Chair

Noise is intrinsic to every experiment. While often viewed as a nuisance, work on the theory of fluctuations has shown that noise may actually contain useful information. This two-part thesis explores the duality of noise as information and disinformation, specifically in applications of fluorescence microscopy.

In Part I, I describe theoretical, experimental, and computational developments in two-color fluorescence fluctuation microscopy (TCFFM). In TCFFM, intensity fluctuations of fluorescently-labeled molecules within a small optical volume are analyzed to glean information about the dynamics of system components. Focusing on bimolecular reactive systems of the form ($A+B \rightleftharpoons C$), I present a general TCFFM theory and discuss how the analysis of fluctuation correlations can be used to measure absolute particle numbers and kinetic rates of binding. I also discuss the influence of Förester resonance energy transfer, reaction rates and reactant concentrations, diffusion, and component visibility on correlation analyses. After describing a two-photon microscope system that I assembled for TCFFM measurements, I

present experimental proof-of-principle results in a discussion of how TCFFM can be used to measure the equilibrium constant of two fluorescently-labeled interacting molecules. Complimenting these experimental TCFFM studies, I describe a molecular dynamics/Monte Carlo-based simulation tool and demonstrate how it can be used to study more complex systems and experimental conditions that cannot be accounted for with the current theory.

In Part II, I describe work on the Adaptive Image Deconvolution Algorithm (AIDA). AIDA is a computational tool for processing and de-noising astronomical and microscopy images. It is based on the proprietary MISTRAL method developed by Mugnier and coworkers (J. Opt. Soc. Am. A. 21, 1841 (2004)), which has been shown to yield object reconstructions with excellent edge preservation, noise suppression, and photometric precision. Using a Bayesian maximum *a posteriori* framework, I present the theoretical basis for the AIDA approach. I describe how AIDA was implemented and discuss improvements over the original MISTRAL program, including a scheme to automatically balance maximum-likelihood estimation and object regularization and the ability to deconvolve multiple image frame and three-dimensional data. I present validation results using synthetic data spanning a broad range of signal-to-noise ratios and image types, and demonstrate that AIDA is effective for experimental data from adaptive optics-equipped telescope systems and wide-field microscopy.

Professor John W. Sedat
Dissertation Committee Chair

Contents

List of Figures

List of Tables

Chapter 1

Preface

"We must understand variation" –*W. Edwards Deming*

"Noise" is intrinsic to every measurement and must be properly dealt with in order to distill information from experimental data. In principal, an experimental system is defined by a vast number of fundamental "primitive" degrees of freedom (e.g., particle positions and momenta).[137] In practice however, all these degrees of freedom are impossible to track for at least two reasons. First, no mode of measurement is comprehensive: measurements are fundamentally limited in scope and report only a few observables at given time. Second, measured quantities rarely correspond to specific primitive degrees of freedom but instead reflect aggregates or clusters of these (e.g., the measured pressure of a gas arises from the forces exerted by a collection of colliding gas molecules).[237] This practical reduction in the number of descriptive variables may be due to inherent limitations in the nature of the measurement and/or an experimental design that provides only a contracted macroscopic description of the system.[1] Ironically, a contracted description is necessary for experimental

[1]Measurement errors due either to faulty instrumentation or human error can be considered to result

measurements to make sense, even though such a description is statistically imprecise and inaccurate due to incompleteness.[207]

Statistical imprecision and inaccuracy are the basis for two facets of noise in data. Statistical imprecision implies that no two systems, while characterized by the same contracted description, will be exactly the same. Differences or variations in a measured observable constitute one facet of noise: *noise as random fluctuations*. Factors not completely accounted for by a contracted description may affect the measurement of an observed quantity of interest in an unexpected manner. The second facet of noise: *noise as unwanted peripheral contributions*, result from factors external to the contracted system description. In the recent literature, these two facets are often called *intrinsic noise* and *extrinsic noise*, respectively.[2, 190]

This two-part thesis explores each of these facets of noise in applications of fluorescence microscopy. In Part I, I consider intrinsic fluctuations and show that they can be a rich source of system information. In Part II, I deal with noise as *dis*information that obscures a signal of interest and describe an inversion method to effectively filter out such noise from data in the context of image processing. In both cases, a careful inventory and evaluation of factors affecting the measured quantity is critical. While the principles I discuss here are relevant to any methodological approach, the focus of my work has been on fluorescence microscopic methods because they are most relevant to biology.[155, 271] The degree of specificity, selectivity, and sensitivity that is possible with fluorescence methods is simply unmatched by other biophysical methods[74, 85, 145]

from a \emph{practically}-forced contracted description of the system; these errors could be accounted for if the degrees of freedom describing what "went wrong" with the instrument or person were known.

Part I of this thesis describes my developments in the technique of two-color fluorescence fluctuation microscopy (TCFFM) and methods for exploiting noise as a source of information. The conceptual strategy for TCFFM was proposed by Magde and co-workers in 1972 as fluorescence correlation spectroscopy (FCS).[159] At the time it was developed, the full potential of FCS was not be realized because of technological limitations. However, recent advances in photon detector technology, microscope optics, and data acquisition hardware have led to a renewed interest in FCS as a realistic tool to measure not only diffusion and equilibrium constants, but also binding kinetics of interacting molecules.[64]

In an FCS experiment, the fluorescence emitted from fluorophores in a sample at steady-state is monitored within a small, optically defined open volume element as a function of time. By "correlating" or analyzing the fluctuations of the fluorescence signal, it is possible to derive a spectrum of characteristic relaxation times describing temporally-limited processes inherent to the system, including diffusion, chemical reaction, and photophysical transformations. TCFFM extends the FCS method to the analysis of two fluorescence signals of different colors.

In Chapter 2, I present a general theoretical framework for TCFFM, focused mainly on the analysis of fluctuation correlation functions and bimolecular reactive systems. I discuss the consequences of chemical reaction kinetics, Förster resonance energy transfer, and cross-talk detection artifacts, and I assess the practical limitations of using TCFFM to study biochemical reactions. In Chapter 3, I describe a microscope system assembled to perform TCFFM experiments and present proof-of-principle results showing how TCFFM can be used to measure the equilibrium constant of two fluorescently-labeled interacting

molecules. In Chapter 4, I describe a combined molecular dynamics/Monte Carlo-based TCFFM simulation tool that is intended to compliment experimental TCFFM studies. I show how such simulations can be useful for studying complex systems and experimental conditions for which no theory exists. In Chapter 5, I highlight some ideas that merit further development; these include new analysis methods, implementation improvements, and systems apt for experimental study with TCFFM.

Part II of this thesis describes the Adaptive Image Deconvolution Algorithm (AIDA), a computational tool for processing noisy image data. Here, noise is treated more classically as a signal-obscuring contribution from extraneous sources. The image of an object observed through an optical microscope is fundamentally limited by the information transfer capacity or "transfer function" of the microscope. For example, object features below the resolution limit of the microscope may not be retained in the observed image. This image is further contaminated by noise from measurement detectors and the statistical photo-detection process. The goal of deconvolution image processing is to recover the "truest" representation of the object from a noisy image or set of images. The combination of information loss and the presence of noise makes this inversion problem notoriously difficult, requiring sophisticated theoretical and computational strategies to be solved.

AIDA is based on the MISTRAL method originally developed for astronomical image processing.[177] MISTRAL has garnered attention from the astronomy community for its ability to generate object reconstructions with excellent noise suppression, fine-feature preservation, and photometric accuracy. Like MISTRAL, AIDA allows the transfer function of the imaging system, which may not be fully known, to adapt during the object recon-

struction process. This aspect is central to the success of AIDA in cases where the estimate of the transfer function is inaccurate. AIDA was built as an extension of the MISTRAL method, specifically to process microscope imaging data.

In Chapter 6, I present the basic AIDA approach within a Bayesian, maximum *a posteriori* framework. In Chapter 7, I describe how AIDA was developed and extended from the MISTRAL method. Features that distinguish AIDA from MISTRAL include: (1) an automatic scheme to suppress noise while preserving sharp features in the reconstruction of the imaged object, (2) the ability to process multiple image frame data simultaneously assuming a common object or common microscope transfer function, and (3) the ability to process three-dimensional image data stacks. In Chapter 8, I demonstrate the effectiveness of AIDA in processing synthetic and experimental image datasets, including multiple image frame datasets and three-dimensional image data stacks. In Chapter 9, I provide a survey of possible algorithmic improvements and applications of the AIDA method.

Appendix A is a reprint of a paper describing work that I began in the context of my pre-doctoral fellowship proposal. The goal of this proposal was to quantify the associations between unfolded proteins and the chaperone machinery within the endoplasmic reticulum (ER). This paper served to establish the use of diffusion coefficients from fluorescence recovery after photobleaching (FRAP) to indicate the bound-state of proteins in the ER. It soon became apparent to me, however, that FRAP and diffusion measurements alone were too insensitive to detect changes in protein binding. This started me on a pilgrimage of thought, from the modern though highly perturbative method of FRAP, to the moderately perturbative method of continuous microphotolysis,[193] and ultimately to non-perturbative

fluctuation-based methods, of which fluorescence correlation spectroscopy is an archetype and motivation for the first part of this thesis.

Part I

Developments in Two-Color Fluorescence Fluctuation Microscopy

Chapter 2

Theoretical Foundations

A version of this chapter was published by Erik F. Y. Hom and Alan S. Verkman as: "Analysis of Coupled Bimolecular Reaction Kinetics and Diffusion by Two-Color Fluorescence Correlation Spectroscopy: Enhanced Resolution of Kinetics by Resonance Energy Transfer," *Biophysical Journal* **83**(1):533-546 (2002).

2.1 Abstract

In two-color fluorescence correlation spectroscopy (TCFCS), the fluorescence intensities of two fluorescently-labeled species are cross-correlated over time and can be used to identify static and dynamic interactions. Generally, fluorophore labels are chosen that do not undergo Förster resonance energy transfer (FRET). Here, a general TCFCS theory is presented that accounts for the possibility of FRET between reactants in the reversible bimolecular reaction, $A + B \underset{k_b}{\overset{k_a}{\rightleftharpoons}} C$, where k_f and k_b are forward and reverse rate constants, respectively (dissociation constant $K_d = k_b/k_f$). Using this theory, I systematically investigated the influence on the correlation function of FRET, reaction rates, reactant concentrations, diffusion, and component visibility. For reactants of comparable size and an energy transfer efficiency of ∼90%, experimentally measurable *cross*-correlation functions should be sensitive to reaction kinetics for $K_d > 10^{-8}$ M and $k_f \gtrsim 10^7$ $M^{-1}s^{-1}$. Measured *auto*-correlation functions corresponding to donor and acceptor labels are generally less sensitive to reaction kinetics, although for the acceptor, this sensitivity increases as the visibility of the donor increases relative to the acceptor. In the absence of FRET or a significant hydrodynamic difference between reactant species, there is little effect of reaction kinetics on the shape of auto- and cross-correlation functions. My results suggest that a subset of biologically relevant association-dissociation kinetics can be measured by TCFCS and that FRET can be advantageous in enhancing these effects.

2.2 Introduction

In fluorescence correlation spectroscopy (FCS), the spontaneous fluorescence fluctuations arising from a small probe volume within a fluorescent sample are temporally correlated to obtain information about the molecular processes that cause these fluctuations.[65,159,160,251] The shape of the correlation function is dependent upon the dynamics of the fluorescent particles in the probe volume, whereas the amplitude of the autocorrelation function at zero time is inversely proportional to the average number of particles.[65,161,251,253] Hydrodynamic properties, particle concentration, fluorescence photophysics, conformational kinetics, aggregation state, and binding thermodynamics have been measured using FCS.[21,33,99,102,147,149,187,214,231,252,264,268] The kinetics of slow intermolecular reactions[138,173,208,226,235] and to a lesser extent, the kinetics of fast reversible intermolecular reactions,[20,65,99,116,147] have also been measured using FCS.

The rate constants of very fast reactions can be deduced directly from the time-dependent decay of the correlation function. For slow reactions, rate constants are typically estimated indirectly by measuring reactant:product ratios as a function of time following a sudden change in reactant concentration (or a reaction initiation event) under pseudo-first order conditions. This latter approach is unlikely to be useful, however, when the time scale for kinetic relaxation is comparable to that needed to make numerous FCS measurements of reasonable quality (each typically >30 s). Moreover, a macroscopic concentration perturbation is required which goes counter to the conceptual motivations of FCS as a non-perturbative method.

For FCS to be useful in measuring reaction kinetics, a sufficient number of reaction

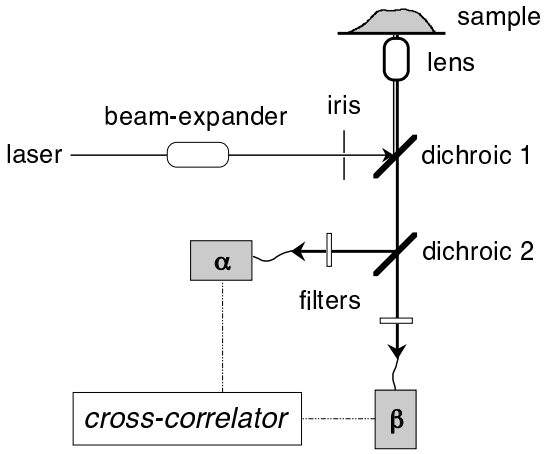

Figure 2.1: **TCFCM measurement scheme**. Schematic of a double-detector FCS apparatus in which emitted fluorescence is spectrally separated by a dichroic mirror and focused onto fiber-optic light guides coupled to detectors α and β.

turnover events must be observed before reaction components diffuse out of the probe volume. What constitutes a "sufficient number" is not clear. If the time scales for reaction and diffusion are very different, approximations have been made that either incorporate the influence of kinetics at early times when they are fast, or neglect the effects of kinetics on the correlation curve-shape when they are slow.[266] The precise conditions under which these approximations are appropriate are likewise not clear. Consequently, there is little in the literature to document the usefulness of FCS for studying reactions with moderate time kinetics.

In this paper, I assess the utility of FCS for studying bimolecular reactions. Based on the work of Schwille and co-workers,[103, 138, 234] a general FCS theory is presented that applies to the experimental situation in which two detectors are used to monitor the fluorescence fluctuations arising from two fluorescently labeled, interacting species (Figure 2.1).

The influence of key parameters on experimentally detected auto- and cross-correlation

curves are examined, including the reaction rate and reactant concentrations, and the diffusion and visibility of reaction components. Importantly, the two-color FCS (TCFCS) theory presented here includes the possibility of resonance energy transfer in the bound complex, which is shown to be of considerable value in enhancing the effects of reaction kinetics on experimentally measurable correlation functions. I will use the term two-color fluorescence fluctuation microscopy (TCFFM) instead in this thesis to emphasize the fact that FCS is only one example of a broader set of methods focussed on the analysis of fluctuations and that fluorescence microscope and imaging optics are the tools used to monitor fluctuations.

2.3 Theory

2.3.1 The double-detector correlation function

Consider an open system of particles containing m differently labeled fluorescent species. The goal is to extract information about the diffusion and reaction dynamics of these particles by temporally correlating the fluorescence fluctuations observed within a small probe volume, V. The experimentally accessible correlation function of the fluorescence fluctuations measured using *two* detector channels, x and y, can be defined as:

$$G_{xy}(\tau) \triangleq \frac{\langle \delta F^x(t) \cdot \delta F^y(t+\tau) \rangle}{\langle F^x \rangle \cdot \langle F^y \rangle} \tag{2.1}$$

where τ is the correlation time (the angular brackets denote an average over a time $T \gg \tau$), $F^x(t)$ is the total fluorescence signal registered in channel x at a time t, and the fluorescence fluctuation about the mean is $\delta F^x(t) = \langle F^x \rangle - F^x(t)$. $G_{xy}(\tau)$ is the *double-detector correlation function.* If an uncorrelated background signal, $b^x(t)$, is present, the total fluorescence

signal can be written as $F^x(t) = f^x(t) + b^x(t)$, where $f^x(t)$ is the fluorescence signal arising from all m fluorescent species at time t ($f^x(t) = \sum_i^m f_i^x(t)$) and $b^x(t)$ accounts for any uncorrelated background signal. It follows that:

$$G_{xy}(\tau) = \underbrace{\left(1 + \frac{\overline{b^x}}{\overline{f^x}}\right)^{-1}\left(1 + \frac{\overline{b^y}}{\overline{f^y}}\right)^{-1}}_{\aleph_x \cdot \aleph_y} \cdot \underbrace{\left[\left\langle \left(\sum_i^m \delta f_i^x(t)\right) \cdot \left(\sum_j^m \delta f_j^y(t+\tau)\right)\right\rangle / \left(\overline{f^x} \cdot \overline{f^y}\right)\right]}_{g_{xy}(\tau)} \tag{2.2}$$

where $g_{xy}(\tau)$ is the fluctuation correlation function for the m-particle system of interest, and $\aleph_y$ and $\aleph_y$ are correction factors ($\leq$1) for the uncorrelated background. In practice, an offset term is sometimes added to Eq. 2.2 to account for any accidental correlation background due to sample contamination or systematic error;[231,269] I will assume that this offset is negligible.

The time-dependent fluorescence fluctuation for the i^{th}species monitored by detector channel x can be expressed as:

$$\delta f_i^x(t) = \eta_i^x(\lambda_i) \int W(\mathbf{r}) \cdot \delta C_i(\mathbf{r}, t)\, d\mathbf{r}; \qquad \eta_i^x(\lambda_i) \triangleq W_0 \cdot \varepsilon_i(\lambda_i) \cdot Q_i \cdot g_x \tag{2.3}$$

where $\delta C_i(\mathbf{r}, t)$ is the time-dependent fluctuation in the molar concentration of species i at spatial position $\mathbf{r}$, and $W(\mathbf{r})$ is a dimensionless function characterizing the illumination profile of the effective volume element normalized by W_0, the excitation amplitude of the illumination beam at the center of focus ($W(0)$=1).[170] λ_i is the wavelength of the illumination beam used to excite species i, ε_i and Q_i are the intensity-dependent absorptivity and fluorescence quantum yield, and g_x is the collection efficiency of detector channel x. $\eta_i^x(\lambda_i)$ is the *x-detector visibility* (or "molecular brightness") defined as the number of pho-

tons detected in channel x per second per molecule of i.[32,180] The λ_i-dependence of η_i^x will hereafter be implicit.

$G_{xy}(\tau)$ can then be expressed in terms of diffusion/reaction kinetic parameters using Eq. (2.3) and by solving for δC_i according to the set of coupled reaction-diffusion equations at equilibrium: $\partial\delta\mathbf{C}(\mathbf{r},\tau)/\partial\tau = \left(\mathbf{D}\cdot\nabla^2 + \mathbf{R}\right)\cdot\delta\mathbf{C}(\mathbf{r},\tau)$, where $\delta\mathbf{C}$ is the vector of concentration fluctuations for the m species, $\mathbf{D}$ is the vector of diffusion constants (assuming no hydrodynamic coupling between components), and $\mathbf{R}$ is the linearized matrix of rate constants and equilibrium concentrations ($\overline{C_i}$) that describe the reaction mechanism.[14,65,251] By spatial Fourier transform:

$$\frac{\partial\delta\widetilde{\mathbf{C}}(\mathbf{q},\tau)}{\partial\tau} = \mathbf{M}\cdot\delta\widetilde{\mathbf{C}}(\mathbf{q},\tau) \tag{2.4}$$

where $\mathbf{M} \triangleq \left(\mathbf{R} - \mathbf{D}\cdot\mathbf{q}^2\cdot\mathbf{I}\right)$ and $\mathbf{I}$ is the identity matrix, which can be solved by standard matrix methods[65] (see Section 2.7). Using solutions to Eq. 2.4, $G_{xy}(\tau)$ can be written as an integral over Fourier spatial frequencies ($\mathbf{q}$) and ultimately expressed as:

$$G_{xy}(\tau) = \aleph_x\aleph_y\cdot\sum_i^m\sum_j^m d_{ij}^{xy}\cdot h_{ij}(\tau) \tag{2.5}$$

where d_{ij}^{xy} is the detectability weight and $h_{ij}(\tau)$ is the component correlation function for species i and j. d_{ij}^{xy} can be expressed as:

$$d_{ij}^{xy} \triangleq \left(\frac{1}{\overline{N}_{tot}}\right)\left[\frac{r_i^x r_j^y\sqrt{\chi_i\chi_j}}{\left(\sum_i^m r_i^x\chi_i\right)\left(\sum_j^m r_j^y\chi_j\right)}\right] \tag{2.6}$$

where $\overline{N}_{tot}$ is the average total number of particles in the observation volume, χ_i is the mole fraction of the i^{th} species, and r_i^x is the x-detector visibility of species i *normalized* by the x-visibility of the brightest singly-labeled species in the sample. The component correlation

function, $h_{ij}(\tau)$, is defined as:

$$h_{ij}(\tau) = h_{ji}(\tau) \triangleq \int Z_{ij}(\mathbf{q},\tau) \cdot \Omega(\mathbf{q})\, d\mathbf{q} \tag{2.7}$$

where the function $Z_{ij}(\mathbf{q},\tau)$ characterizes how spontaneous particle number fluctuations are spatio-temporally dissipated (see Section 2.7) and $\Omega(\mathbf{q})$ is a geometric weighting factor that is dependent upon characteristics of the observation volume having units of reciprocal volume. For an n-photon excited 3-D Gaussian-ellipsoidal (3DG) volume, $V = (\pi/n)^{3/2} w_r^2 w_z$ and $\Omega(\mathbf{q}) = \left(w_r^2 w_z/(4n\pi)^{3/2}\right) \exp\left(-w_r^2(q_x^2+q_y^2)/4n\right) \exp\left(-w_z^2 q_z^2/4n\right)$, where w_r and w_z are the radial and axial radii of the volume element, respectively. In general, Eq. 2.7 cannot be integrated analytically and component correlation functions, $h_{ij}(\tau)$, must be determined by numerical integration.

It is assumed that the particles under study are chemically ideal. Practically, this means that if the particles interact, they do so without any memory effects at a time $\tau = 0_+$ where $\tau_{TS} \ll 0_+ \ll \tau_{reac}$, τ_{TS} being the average lifetime of the reaction transition state which separates *experimentally distinguishable* chemical species, and τ_{reac}, the average lifetime of the particles before they react.[29] With this assumption, $h_{ij}(0_+) = \delta_{ij}$,[65] and only the *component auto*-correlation functions contribute to the initial *detector* correlation amplitude, $G_{xy}(0_+)$. As needed below, it is convenient to write the detector correlation function as a product of this amplitude and a shape function, $H_{xy}(\tau)$:

$$G_{xy}(\tau) = G_{xy}(0_+) \cdot H_{xy}(\tau) \tag{2.8}$$

where $H_{xy}(0_+) = 1$ and $H_{xy}(\infty) = 0$.

2.3.2 Application to reversible bimolecular reactions

The above formalism is applicable to an arbitrary m-particle system. My analysis will focus exclusively on reversible bimolecular reactions of the form, $A + B \underset{k_b}{\overset{k_a}{\rightleftharpoons}} C$, where k_f and k_b are the forward and backward rate constants, respectively, and $K_d = k_b/k_f$ is the equilibrium dissociation constant. I assume that reactant species A and B are labeled with fluorophores that are distinct in their emission spectra upon exciting at wavelengths λ_A and λ_B, and monitored by detector channels α and β respectively (Figure 2.1). Using Eqs. 2.5 and 2.6, the double-detector correlation functions, $G_{xy}(\tau)$, can be expressed as a linear combination of component correlation functions, $h_{ij}(\tau)$. Assuming there is zero "bleed-through" fluorescence registered in detector channels ($r_A^\beta = r_B^\alpha = 0$) (see Section 2.8), the two detector *auto*-correlation functions are:

$$G_{\alpha\alpha} = \frac{\aleph_\alpha^2}{\overline{N}_A}\left(\frac{\theta_A}{\left(\theta_A^2 + r_C^\alpha\theta_C^2\right)}\right)^2\left[\theta_A^2 h_{AA}(\tau) + \left(r_C^\alpha\right)^2\theta_C^2 h_{CC}(\tau) - 2r_C^\alpha\theta_A\theta_C h_{AC}(\tau)\right] \quad (2.9)$$

$$G_{\beta\beta} = \frac{\aleph_\beta^2}{\overline{N}_B}\left(\frac{\theta_B}{\left(\theta_B^2 + r_C^\beta\theta_C^2\right)}\right)^2\left[\theta_B^2 h_{BB}(\tau) + \left(r_C^\beta\right)^2\theta_C^2 h_{CC}(\tau) - 2r_C^\beta\theta_B\theta_C h_{BC}(\tau)\right]$$

and the double-detector *cross*-correlation function is:

$$G_{\alpha\beta} = \frac{\aleph_\alpha\aleph_\beta}{\overline{N}_C}\left(\frac{\theta_C^2}{\left(\theta_A^2 + r_C^\alpha\theta_C^2\right)\left(\theta_A^2 + r_C^\alpha\theta_C^2\right)}\right) \times\left[r_C^\alpha r_C^\beta\theta_C^2 h_{CC}(\tau) + \theta_A\theta_B h_{AB}(\tau) - r_C^\beta\theta_B\theta_C h_{BC}(\tau) - r_C^\alpha\theta_A\theta_C h_{CC}(\tau)\right] \quad (2.10)$$

where $\theta_A \triangleq \sqrt{\chi_A/\chi_C}$, $\theta_B \triangleq \sqrt{\chi_B/\chi_C}$, and $\theta_C = -1$. The correlation functions in Eqs. 2.9 and 2.10 may be expressed explicitly in terms of the dissociation constant, K_d, and the total reactant concentrations, $\overline{C}_A^{tot}$ and $\overline{C}_B^{tot}$, using the following relations:

$$\theta_A^2 = \frac{\overline{C}_A^{tot}}{\overline{C}_C} - 1 \qquad \text{and} \qquad \theta_B^2 = \frac{\overline{C}_B^{tot}}{\overline{C}_C} - 1$$

$$\text{with} \qquad \overline{C}_C = \tfrac{1}{2}\left[\left(\overline{C}_A^{tot} + \overline{C}_B^{tot} + K_d\right) - \sqrt{\left(\overline{C}_A^{tot} + \overline{C}_B^{tot} + K_d\right)^2 - 4\overline{C}_A^{tot}\overline{C}_B^{tot}}\right]$$

$$= \tfrac{1}{2}\left[\overline{C}_A^{tot} + \overline{C}_B^{tot} + K_d\left(1 - \tfrac{1}{\Gamma}\right)\right] \tag{2.11}$$

2.3.3 Förster resonance energy transfer (FRET)

If species A and B are labeled with donor and acceptor fluorophores, respectively, which undergo FRET with mean efficiency E upon forming complex C, then the relative α- and β-visibilities for C can written as:

$$r_C^\alpha = (1 - E) \qquad \text{and} \qquad r_C^\beta = \left(1 + \left[\eta_A^\alpha/\eta_B^\beta\right] E\right) \tag{2.12}$$

For simplicity, I have assumed an ideal case in which there is no detector bleed-through (see Section 2.8).

2.3.4 The correlation function amplitude: $G_{xy}(0_+)$

As given by Eq. 2.8, the detector correlation function can be expressed as a product of the amplitude at $\tau = 0_+$ and a unimodal shape factor. With perfect fluorophore discrimination ($r_A^\beta = r_B^\alpha = 0$), the correlation function amplitudes can be written as:

$$\begin{aligned}
G_{\alpha\alpha}(0_+) &= \frac{\aleph_\alpha^2}{\overline{N}_A}\left(\frac{\theta_A}{\left(\theta_A^2 + r_C^\alpha\right)}\right)^2\left[\theta_A^2 + (r_C^\alpha)^2\right] \\
G_{\beta\beta}(0_+) &= \frac{\aleph_\beta^2}{\overline{N}_B}\left(\frac{\theta_B}{\left(\theta_B^2 + r_C^\beta\theta_C^2\right)}\right)^2\left[\theta_B^2 + \left(r_C^\beta\right)^2\right] \\
G_{\alpha\beta}(0_+) &= \frac{\aleph_\alpha\aleph_\beta}{\overline{N}_C}\left(\frac{\left[r_C^\alpha r_C^\beta\right]}{\left(\theta_A^2 + r_C^\alpha\right)\left(\theta_A^2 + r_C^\alpha\right)}\right)
\end{aligned} \tag{2.13}$$

Here it is assumed that the fluorescence energy transfer event is much faster than the time scale for intermolecular association and the time $\tau = 0_+ (\tau_{FRET} \ll 0_+ \ll \tau_{reac})$. Using Eq. 2.13, the average number of reactant and complex molecules in the observation volume, $\overline{N}_A$, $\overline{N}_B$and $\overline{N}_C$, can be solved for simultaneously and explicitly. Although these expressions are quite lengthy for the case at hand (see Section 2.9), they simplify if no spectral changes occur upon complex formation (*i.e.*, $r_C^\alpha = r_C^\beta = 1$):[103, 138, 234]

$$\overline{N}_C = \aleph_\alpha \aleph_\beta \cdot \frac{G_{\alpha\beta}(0_+)}{G_{\alpha\alpha}(0_+) \cdot G_{\beta\beta}(0_+)}, \quad \overline{N}_A = \frac{\aleph_\alpha^2}{G_{\alpha\alpha}(0_+)} - \overline{N}_C, \quad \overline{N}_A = \frac{\aleph_\beta^2}{G_{\beta\beta}(0_+)} - \overline{N}_C \tag{2.14}$$

2.3.5 Diffusion and reaction time scales

To assess whether reaction kinetics influence the shape of double-detector correlation functions in an experimentally detectable manner, it is helpful to define characteristic diffusion and reaction times, $\tau_{diff} \triangleq w_r^2 / 4 n_p \langle D \rangle$ and $\tau_{reac} \triangleq \left(k_f \left[\overline{C}_A + \overline{C}_B \right] + k_b \right)^{-1}$. Here, $\langle D \rangle$ is the ensemble-averaged diffusion coefficient of the particles in the volume, V,[212] and n_p is the number of photons used to excite a Gaussian-cylindrical or -ellipsoidal probe volume of radial waist, w_r (for a 2-photon excited Gaussian-Lorentzian volume,[170] n_p=1.5). The difference in diffusion and reaction timescales can then be expressed using the dimensionless metric, ζ:

$$\zeta \triangleq \frac{\tau_{diff}}{\tau_{reac}} = \left(\frac{w_r k_b}{4 n_p \langle D \rangle} \right) \cdot \frac{k_b}{\Gamma} \tag{2.15}$$

where $\Gamma \triangleq \left(\theta_A^{-2} + \theta_B^{-2} + \theta_C^{-2} \right)^{-1}$. ζ characterizes the number of reaction turnover events observed per dwell time for the ensemble of particles within the probe volume; within this time, about half of the particles diffusively exchange with those outside the volume.[170] The parameter Γ characterizes the position of reaction equilibrium. Using Eq. **??**, Γ may

be expressed explicitly in terms of the dissociation constant, K_d, and the total reactant concentrations, $\overline{C}_A^{tot}$ and $\overline{C}_B^{tot}$:

$$\Gamma = \frac{K_d}{\sqrt{\left(\overline{C}_A^{tot} + \overline{C}_B^{tot} + K_d\right)^2 - 4\overline{C}_A^{tot}\overline{C}_B^{tot}}} \tag{2.16}$$

When $K_d < \left(\overline{C}_A^{tot} = \overline{C}_B^{tot}\right)$ (complex formation is favored), $\Gamma \to 0$; when $K_d = \left(\overline{C}_A^{tot} = \overline{C}_B^{tot}\right)$, $\Gamma = \sqrt{1/5}$; when $K_d > \left(\overline{C}_A^{tot} = \overline{C}_B^{tot}\right)$ (reactants are favored), $\Gamma \to 1$.

2.4 Methods

Detector correlation functions, $G_{xy}(\tau)$, were simulated using Mathematica 4.1 (Wolfram Research Inc., Champaign, IL) on a 1.2 GHz Athlon processor, 256 MB Gateway computer (Linux OS). Eigenvalues and eigenvectors of the matrix M_{sym} were solved and $Z_{ij}(\mathbf{q}, \tau)$ expressions constructed symbolically as described in Section 2.7. An function corresponding to either a one- or two-photon-excited Gaussian-ellipsoid volume was used. When required, correlation functions were integrated by numerical cubature to six-digits of precision using an adaptive Genz-Malik algorithm. Integrations were performed in reciprocal **q**-space over a range corresponding to $x_{min} \leq |x| \leq \infty$ with $x_{min} = w_r/10$ in a single dimension; identical results were obtained to within six-digit precision with a discretization of $x_{min} = w_r/1000$. The correlation function integration protocol was verified by comparison with correlation function curves generated using analytical expressions for the case in which $D_A = D_B = D_C$ and those derived by Elson and Magde (1974)[65] in the limit of $D_A = D_C \ll D_B$.

To assess whether detector correlation shape functions for a system with coupled

reaction-diffusion, $H_{xy}^{reac-diff}(\tau)$, are experimentally distinguishable from those expected from a comparable system without reaction, $H_{xy}^{diff}(\tau)$, the variance between sets of curves were compared using the F-statistic:[18] $F_{xy} \triangleq \left\langle \chi^2_{\upsilon_{diff}} / \chi^2_{\upsilon} \right\rangle_{N_{exp}}$, where the brackets denote an average over N_{exp} correlation curves. χ^2_{υ} and $\chi^2_{\upsilon_{diff}}$ are the reduced chi-squares that characterize the difference between the data, $H_{xy}(\tau_i)$, and the best-fit reaction-diffusion model or diffusion-only model, respectively:

$$\begin{aligned} \chi^2_{\upsilon} &\triangleq \frac{1}{\upsilon} \sum_{i}^{N_d} \left(\frac{H_{xy}^{reac-diff}(\tau_i) - H_{xy}^{diff}(\tau_i)}{\sigma_{xy}(\tau_i)} \right)^2 \\ \chi^2_{\upsilon_{diff}} &\triangleq \frac{1}{\upsilon_{diff}} \sum_{i}^{N_d} \left(\frac{H_{xy}^{diff}(\tau_i) - H_{xy}(\tau_i)}{\sigma_{xy}(\tau_i)} \right)^2 \end{aligned} \tag{2.17}$$

where υ and υ_{diff} are the number of degrees of freedom for the fit (number of data points minus number of fitting parameters), $\sigma(\tau_i)$ is the standard deviation for the $H_{xy}(\tau_i)$ data, and N_d is the total number of time points used. Expressing $H_{xy}(\tau_i)$ as $\overline{H}_{xy}(\tau_i) + \{\phi_i\}$, with $\overline{H}_{xy}(\tau_i)$ corresponding to a reaction-diffusion parent function and $\{\phi_i\}$, a random number sampled from a Gaussian distribution of mean zero and variance $\sigma^2(\tau_i)$:

$$F_{xy} = \left\langle \left(\frac{\upsilon}{\upsilon_{diff}} \right) \left(\frac{\sum_i^{N_d} \left(\left[H_{xy}^{diff}(\tau_i) - \overline{H}_{xy}(\tau_i) \right] + \{\phi_i\} \right)^2 / \sigma^2(\tau_i)}{\sum_i^{N_d} \left(\left[H_{xy}^{reac-diff}(\tau_i) - \overline{H}_{xy}(\tau_i) \right] + \{\phi_i\} \right)^2 / \sigma^2(\tau_i)} \right) \right\rangle_{N_{exp}} \tag{2.18}$$

F-statistics were computed using $N_{exp} = 50$, assuming the difference between best-fit values, $H_{xy}^{reac-diff}(\tau_i)$, and the parent function used to generate the simulated data, $\overline{H}_{xy}(\tau_i)$, is negligible relative to $\{\phi_i\}$. $\sigma^2(\tau_i)$ values were estimated using an analytical formula derived by Koppel (1974),[141] validated by Meseth *et al.* (1999),[172] and Wohland *et al.* (2001),[269] and modified for the case in which data is acquired via two detectors and normalized by $G_{xy}(0_+)$:

$$\sigma^2(\tau_i) = \left(\frac{\Delta t}{T}\right) \cdot \left(\begin{array}{c} \frac{\left[1+H_{xy}^2(\Delta t)\right]\left[1+H_{xy}^2(t_i)\right]}{\left[1-H_{xy}^2(\Delta t)\right]} + 2H_{xy}^2\left(\frac{t_i}{\Delta t}\right) \\ + \frac{2\left[1+H_{xy}^2(t_i)\right]}{G_{xy}(0_+)\sqrt{\langle n_x\rangle\langle n_y\rangle}} + \frac{\left[1+G_{xy}(0_+)H_{xy}(t_i)\right]}{G_{xy}^2(0_+)\langle n_x\rangle\langle n_y\rangle} \end{array} \right) \tag{2.19}$$

Δt is the detector channel sampling width; in practice, fluorescence intensities are monitored over a series of time bins of varying duration and correlated as photon counts per bin.[80,251,269] $\langle n_x\rangle$ is the average number of photon counts registered indetector channel x in a given Δt: $\langle n_x\rangle = \left(\sum_i \eta_i^x \overline{N}_i + b^x\right)\Delta t$. An expression equivalent to Eq. 2.12 of Meseth et al. (1999)[172] is obtained by multiplying Eq. 2.19 by $G_{xy}(0_+)$ and substituting: $(\Delta t/T) = 1/M$, $\Delta t = \Delta\tau$, $\tau_i/\Delta t = m$, $H_{xy} = g$, $G_{xy}(0_+) = 1/N$, and $\sqrt{\langle n_x\rangle\langle n_y\rangle} = \langle n\rangle$. An expression similar to Eq. 47 of Kask *et al.* (1997)[130] may be obtained by substituting: $T = U$, $\Delta t = T$, and R=parenthetical terms; Kask *et al.*'s terms in $1/m$ have been omitted here assuming $m \gg 1$, where m is the average number of particles in the probe volume that contribute to the mean fluorescence intensity in each channel.

A value of $\Delta t = \tau/10$ and 25 τ_i-divisions per $\log\tau$ were used in the calculation of F_{xy} (Eq. 2.18), which approximates the quasi-logarithmic binning structure of available hardware correlator cards[171,269] (e.g., from ALV-Laser Vertriebsgesellschaft m.b.H., Langen, Germany). Eq. 2.19 typically overestimates the true variance of the data, particularly at long τ values, but is qualitatively correct;[172,212,269] Eq. 2.19 becomes more accurate as the number of particles in the probe volume contributing to the mean fluorescence increases.[130,141,205] F_{xy} were calculated using a τ-range of $\min[\tau_{reac},\tau_{reac}]\cdot 10^{-2}$ to $\max[\tau_{reac},\tau_{reac}]\cdot 10^{2}$, amounting to N_d~100-200 data points. $\tau = 0_+$ was set equivalent to $\min[\tau_{reac},\tau_{reac}]\cdot 10^{-3}$. A minimum τ-range of 4 orders of magnitude (when $\tau_{reac} \sim \tau_{reac}$) is a conservative estimate of what is used experimentally to fit correlation data. Given the

number of degrees of freedom (υ and υ_{diff}) and a value for F_{xy}, a reaction-diffusion model can be considered a better descriptor of the simulated correlation data than a diffusion-only model to within a confidence level dictated by the F-distribution.[18] For calculations with $N_d \sim \upsilon \sim \upsilon_{diff} \sim 100 - 200$, an F_{xy} value of 1.3 implies that a reaction-diffusion model can be considered a better descriptor of the data with a p-value of 0.09-0.002. The validity of my F_{xy} calculation approach was confirmed by reproducing F-statistic values of Meseth *et al.* (1999)[172] for conditions in which the auto-correlation function curves between a one-component diffusing system and a two-component diffusing system could be distinguished with a p-value of 0.01.

2.5 Results

2.5.1 Basic features of $G_{xy}(\tau)$

The experimentally measured detector correlation functions are linear combinations of component correlation functions, $h_{ij}(\tau)$, weighted by detectablity factors, d_{ij}^{xy}, for each fluorescent species in the sample (Eq. 2.5). These detectability factors are a function of both the mole fraction, χ_i, and the relative visibility properties, r_i^x, for each species (Eq. 2.6). By using spectrally distinct reactant labels and monitoring fluorescence using two detectors, additional information is available to determine the kinetics of the reaction, $A + B \underset{k_b}{\overset{k_a}{\rightleftharpoons}} C$. In Figure 2.2, the detector correlation functions for such a reaction (in the absence of energy transfer, E=0), are shown schematically as a sum of component correlation functions. The total reactant concentrations and dissociation constant for the reaction were set to $\overline{C}_A^{tot} = \overline{C}_B^{tot} = K_d = 10^{-8}$ M with both reactants equally visible to their

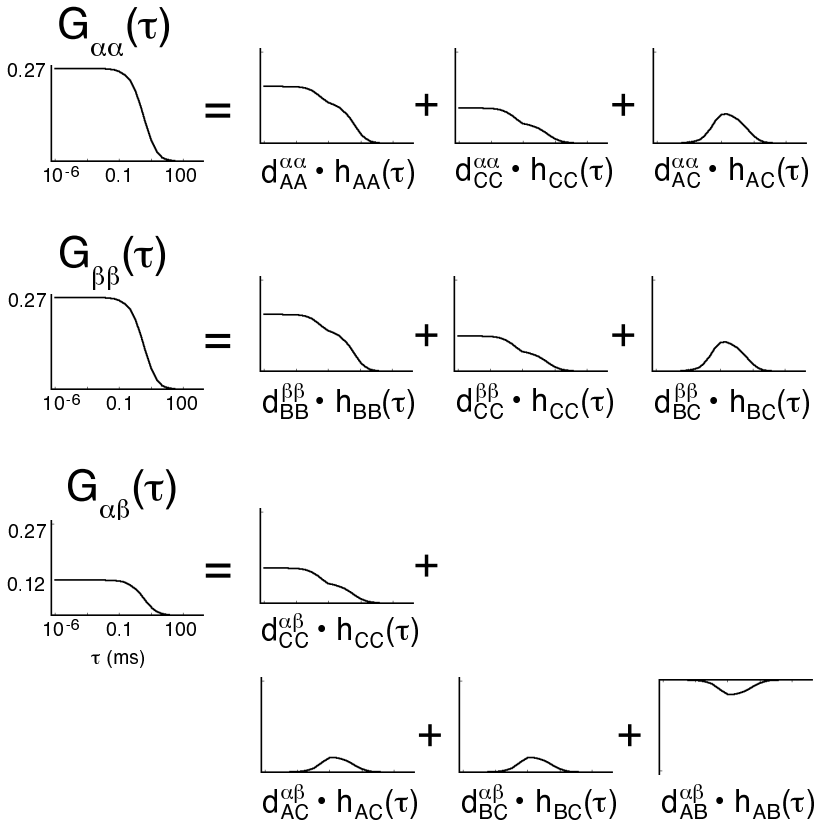

Figure 2.2: **Detector correlation functions are a linear combination of component contributions**. Double-detector auto- and cross-correlation functions ($G_{\alpha\alpha}(\tau)$, $G_{\beta\beta}(\tau)$, and $G_{\alpha\beta}(\tau)$) for the reversible bimolecular reaction, $A + B \leftrightharpoons C$, shown as a sum of component correlation functions, $h_{ij}(\tau)$, weighted by detectability factors, (Eq. 2.6). Detector channels α and β monitor the fluorescence from species A and B, respectively. Parameters (assuming 2-photon excited 3D-Gaussian-ellipsoidal volume): $w_r = 0.48$ μm, $\kappa = 2.8$, $\overline{C}_A^{tot} = \overline{C}_B^{tot} = K_d = 10^{-8}$ M, $D_A = D_B = D_C = 8.5 \times 10^{-7}$ cm^2/s, $\eta_A^\alpha = \eta_B^\beta = 15$ kHz, and $\zeta = 100$.

intended detector ($\eta_A^\alpha = \eta_B^\beta$). The number of reaction turnover events per diffusive dwell time, ζ (Eq. 7.5), was set to 100 with equal diffusion coefficients for A, B, and C. Each of the component *auto*-correlation functions, $d_{ij}^{xy} \cdot h_{ij}(\tau)$, decays monotonically with two shoulders, the first occurring at $\tau = \tau_{reac}$ and the second at $\tau_{diff} = \zeta \cdot \tau_{reac}$. For this case in which $\overline{C}_A^{tot} = \overline{C}_B^{tot} = K_d$, $\chi_C = 0.62 \cdot (\chi_A = \chi_B)$, so that component auto-correlation contributions of C are smaller than those of A or B: $d_{CC}^{xy} \cdot h_{CC}(0_+) < \left(d_{AA}^{xy} \cdot h_{AA}(0_+) \sim d_{BB}^{xy} \cdot h_{BB}(0_+)\right)$.

In contrast, the component cross-correlation functions start from zero, increase over a characteristic time $\tau \sim \tau_{reac}$, and decrease due to diffusional de-correlation at a later time $\tau \sim \tau_{diff}$. By mass action, a small, spontaneous increase in the concentration of A or B would lead to a comparable increase in the formation of complex C at a later time ; thus, reactants are positively cross-correlated with C ($h_{AC}(\tau) > 0$ and $h_{BC}(\tau) > 0$). Similarly, a small, spontaneous increase in the concentration of one reactants would lead to a *decrease* in the concentration of the other reactant so that reactants are negatively cross-correlated ($h_{AB}(\tau) < 0$). For the case shown, $d_{AC}^{\alpha\beta} \cdot h_{AC}(\tau) = d_{BC}^{\alpha\beta} \cdot h_{BC}(\tau) = -d_{AB}^{\alpha\beta} \cdot h_{AB}(\tau)$.

In the absence of hydrodynamic differences and energy transfer between particles, the component auto-correlation and cross-correlation contributions sum to yield detector correlation functions, $G_{xy}(\tau)$, with a single, smooth shoulder. As given by Eq. 2.8, it is useful to express $G_{xy}(\tau)$as the product of a shape function, $H_{xy}(\tau)$, and an amplitude factor, $G_{xy}(0_+)$. Below, I examine the influence of FRET, reaction kinetics, and differential visibilities of the reactants on $H_{xy}(\tau)$ and $G_{xy}(0_+)$, with the goal of determining conditions under which reaction would influence $G_{xy}(\tau)$ to permit experimental determination of kinetic parameters.

2.5.2 Determining bimolecular reaction kinetics by analysis of $H_{xy}(\tau)$

In principle, kinetic parameters can be deduced from an analysis of the measured correlation decay. By toggling between different observable reaction states - states that may be characterized by different intrinsic hydrodynamic and fluorescence properties - kinetic inter-conversion indirectly modifies the shape of the detector correlation function. I consider first the "worst-case" scenario in which $D_A = D_B = D_C$ so that reaction components can only be resolved based on differences in their fluorescence characteristics. In this case, analytical forms for $H_{xy}(\tau)$ exist in which the effects of reaction and diffusion can be decoupled[65,251] (see Section 2.7). For a 3DG volume:

$$\begin{aligned} H_{xy}(\tau) &= \left(1+\frac{\tau}{\tau_{diff}}\right)^{-1}\left(1+\frac{\tau}{\kappa^2\tau_{diff}}\right)^{-1/2} \\ &\quad \times \frac{\sum_i^m \sum_j^m d_{ij}^{xy}\left[\delta_{ij}+\frac{\Gamma}{\theta_i\theta_j}\left(e^{-\tau/\tau_{reac}}-1\right)\right]}{\sum_i^m \sum_j^m d_{ij}^{xy}} \end{aligned} \tag{2.20}$$

where κ (termed the structure factor) is the axial:radial ratio of the observation volume, w_z/w_r.[149] The first bracketed term in Eq. 2.20 accounts for correlations arising from diffusion alone while the second bracketed term accounts for correlations due to reaction.

Energy transfer enhances the influence of reaction kinetics on $H_{xy}(\tau)$. Example detector auto- and cross-correlation shape functions, $H_{xy}(\tau)$ (Eq. 2.20), are shown in Figure 2.3 for different E in the presence of reaction. A typical 2-photon 3DG volume[103] of radial waist w_r=0.48 μm and κ=2.8 was used, with an average of one reaction event observed per diffusive dwell time (*i.e.*, $\zeta = 1$: $\tau_{reac} = \tau_{diff}$), $\eta_A^\alpha = \eta_B^\beta$ =15 kHz, and $K_d = 10^{-6}$ M, $\overline{C}_A^{tot} = \overline{C}_B^{tot} = 10^{-8}$ M. For the detector auto-correlation functions, as E increases the presence of reaction kinetics causes the curves to shift to smaller τ. For the case shown,

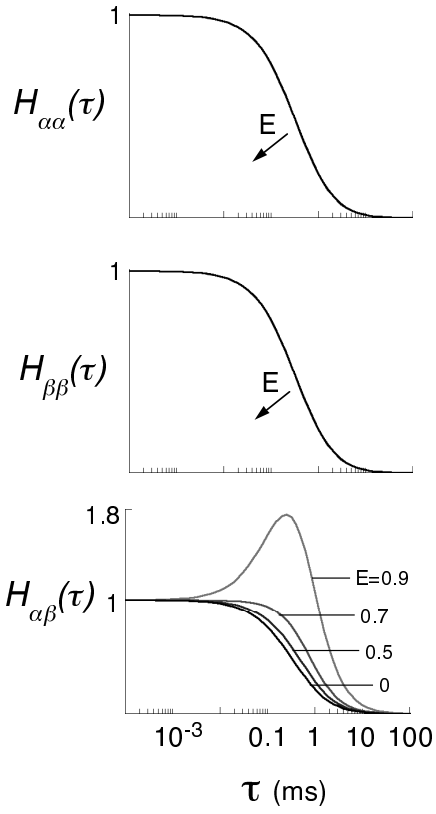

Figure 2.3: **Energy transfer enhances the influence of chemical reaction on the shape of the detector correlation functions**. Detector correlation shape functions, $H_{xy}(\tau)$ (see Eq. 2.8), plotted as a function of E. Arrows point in the direction of increasing energy transfer between donor reactant A and acceptor reactant B, with E=0, 0.5, 0.7, and 0.9. An average of one reaction turnover for every diffusive passage through the probe volume ($\zeta = 1$) was assumed. Parameters: $w_r = 0.48$ μm, $\kappa = 2.8$, $\overline{C}_A^{tot} = \overline{C}_B^{tot} = 10^{-8}$ M, $K_d = 10^{-6}$ M, $D_A = D_B = D_C = 8.5 \times 10^{-7}$ cm^2/s, and $\eta_A^\alpha = \eta_B^\beta = 15$.

however, the reaction kinetic effects are very small. As E increases, reaction significantly changes the shape of the detector cross-correlation function: contributions from the component cross-correlation functions, $d_{AC}^{\alpha\beta} \cdot h_{AC}(\tau)$ and $d_{BC}^{\alpha\beta} \cdot h_{BC}(\tau)$, increase dramatically (not shown), causing the shoulder in $H_{\alpha\beta}(\tau)$ to shift upwards (to values greater than 1). With $D_A = D_B = D_C$, the maximum in $H_{\alpha\beta}(\tau)$ (see Eq. 2.20) occurs at:

$$\tau_{max} \approx \tau_{reac} \left(\left| W_{-1} \left[e^{\left(-A\left(1+\tau_{diff}/\tau_{reac}\right)\right)} \right] \right| - 1 \right) - \tau_{diff}$$

where $A \triangleq 1 - \left(\sum_i^m d_{ii} / \sum_i^m \sum_j^m d_{ij}^{xy} \Gamma / \theta_i \theta_j \right)$ is the non-principal, real branch Lambert W-function[263] that can be approximated by: $W_{-1}[x] \approx L_1 - L_2 + L_1/L_2$ with $L_1 \triangleq \ln[-x]$ and $L_2 \triangleq \ln[-L_1]$.

The FRET-enhanced effects of reaction kinetics on $H_{xy}(\tau)$ can be augmented by an increase in ζ. ζ characterizes the number of reaction turnover events observed per diffusive dwell time for the particles in the probe volume, V (Eq. 7.5). Figure 2.4A shows the effects of ζ, in conjunction with E, on the detector cross-correlation shape function. Using similar parameters as in Figure 2.3, a ten-fold increase in ζ ($\tau_{reac} < \tau_{diff}$) remarkably enhances the effects of kinetics on the cross-correlation function curve shape in synergy with E. A ten-fold decrease in ζ significantly diminishes these E-induced enhancements. Similar trends were observed for the detector auto-correlation functions, although the effects are less obvious (not shown). Importantly, if $D_A = D_B = D_C$ and E=0, the presence of reaction *cannot* be detected no matter how many reaction events are observed per dwell time.

The FRET-enhanced effects of reaction kinetics on $H_{xy}(\tau)$ can be augmented when the donor reactant is more visible relative to the acceptor reac-

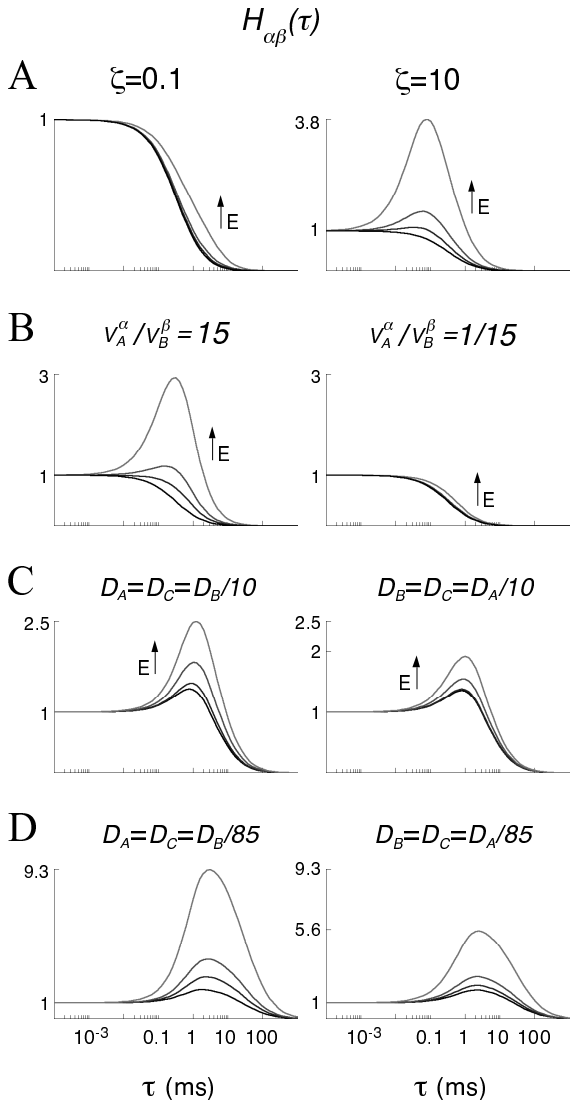

Figure 2.4: **Effects of FRET on TCFFM cross-correlation functions**. In the presence of FRET, the shape of the detector cross-correlation is sensitive to the average number of reaction turnover events observed per diffusive dwell time, the ratio of reactant visibilities, and a difference in the diffusion coefficients of reactants. (A) Effect of ζ, the number of reaction turnover events observed per diffusive dwell time (Eq. 7.5), on $H_{\alpha\beta}(\tau)$: (*left*) $\zeta = 0.1$; (*right*) $\zeta = 10$. (B) Effect of differential reactant visibility: (*left*) $\eta_A^\alpha = 15$ kHz and $\eta_B^\beta = 1$ kHz; (*right*) $\eta_A^\alpha = 1$ kHz and $\eta_B^\beta = 15$ kHz. (C) Effect of differential reactant diffusion: (*left*) $D_A = D_C = 8.5 \times 10^{-8}$ cm^2/s and $D_B = 8.5 \times 10^{-7}$ cm^2/s and (*right*) $D_B = D_C = 8.5 \times 10^{-8}$ cm^2/s and $D_A = 8.5 \times 10^{-7}$ cm^2/s. (D) Same as (C) with (*left*) $D_A = D_C = 1 \times 10^{-8}$ cm^2/s and $D_B = 8.5 \times 10^{-7}$ cm^2/s, and (*right*) $D_B = D_C = 1 \times 10^{-8}$ cm^2/s and $D_A = 8.5 \times 10^{-7}$ cm^2/s. Arrows point in the direction of increasing E=0, 0.5, 0.7, and 0.9. Parameters are as in Figure 2.3 unless otherwise indicated.

tant. In the left panel of Figure 2.4B, the cross-correlation shape function is plotted as a function of E assuming that the visibility of acceptor reactant, B, is 15 times lower than for donor reactant, A (η_A^α=15 kHz and η_B^β=1 kHz). In this case, direct excitation of acceptor B is relatively poor (e.g., by 1-photon excitation) but energy transfer from donor A can lead to sensitized emission from acceptor B. With such a visibility difference, the sensitivity of $H_{\alpha\beta}(\tau)$ to reaction kinetics is enhanced by nearly 50% for the case shown (E=0.9). In the right panel of Figure 2.4B, the opposite case is presented in which donor A is 15 times dimmer than the acceptor B (η_A^α=1 kHz and η_B^β=15 kHz). Energy-transfer enhancements are significantly reduced. In general, a simple difference in the visibility of reactants (without energy transfer or a difference in reactant hydrodynamics) does *not* lead to an enhancement of reaction effects on the shape of the correlation functions.

The FRET-enhanced effects of reaction kinetics on $H_{xy}(\tau)$ can be enhanced if a hydrodynamic change accompanies reaction. In Figure 2.4C, the cross-correlation shape function is shown as a function of E for a system in which one reactant (and the complex) diffuses 10 times slower than the other reactant. For a hydrodynamic difference of this magnitude, reaction kinetics can have a significant effect on $H_{\alpha\beta}(\tau)$ even without energy transfer (cf. Figure 2.3, bottom). The synergy between energy transfer and a hydrodynamic difference is greatest when the donor A is the slower diffusing reactant (Figure 2.4C, left and right). For an even larger difference between reactant diffusion coefficients, the influence of kinetics on $H_{\alpha\beta}(0_+)$ is further enhanced by energy transfer (Figure 2.4D).

Sensitivity of $G_{xy}(\tau)$ to reaction kinetics. The shape functions in Figs. 3 and 4 are exact theoretical predictions without added experimental errors. Because of the statisti-

cal nature of TCFCM, points along the correlation curve will have intrinsic errors (approximated by Eq. 2.19) that limit the ability to resolve reaction kinetics. To assess whether the effects of reaction kinetics on the measured correlation functions are experimentally detectable, F-statistics, F_{xy}, were computed (see Section 2.4). The F_{xy} statistics quantify the appropriateness of a reaction-diffusion model vs. a diffusion-only model in describing the simulated correlation function data (Eq. 2.18). In Figure 2.5, F_{xy}-contour plots are shown for the worse-case scenario $D_A = D_B = D_C$ as a function of K_d, ζ, and E, assuming a 2-photon 3DG volume of $w_r 0.48$ and $\kappa = 2.8$, $\overline{C}_A^{tot} = \overline{C}_B^{tot} = 10^{-8}$ M, $D = 8.5 \times 10^{-7}\text{cm}^2/\text{s}$ and a total data acquisition time of 60 s. Contour plots do not change significantly if a 1-photon 3DG volume of $w_r = 0.33$ and $\kappa = 5$ (e.g., see Langowski and Tewes (2000)[149]) is used (not shown). Results for equivalently visible reactants ($\eta_A^\alpha = \eta_B^\beta = 15$ kHz) are shown in panel A and for a less visible acceptor reactant B ($\eta_A^\alpha = 15$ kHz and $\eta_B^\beta = 1$ kHz) in panel B; a background fluorescence of $\overline{b^\alpha} = \overline{b^\beta} = 0.45$ kHz was assumed (Eq. 2.2).

The gray shading denotes regions in which $F_{xy} \geq 1.3$, as demarcated by the solid contour. Using ≥ 100 correlation function time points to compute F_{xy}, values ≥ 1.3 imply that reaction can be detected with a statistically significant p-value of <0.09 (see Section 2.4). The variance for each time point along the detector correlation function, and thus the value of F_{xy}, is dependent upon the total data acquisition time, T (Eqs. 2.18 and 2.19). As acquisition time increases, detection sensitivity improves in a manner proportional to $\sqrt{T}$, as indicated by the dashed contour (T=240 s) and the long-dashed contour (T=960 s) (Figure 2.5A, center, bottom).

As energy transfer efficiency increases, a larger subset of $K_d : \zeta$ reaction conditions

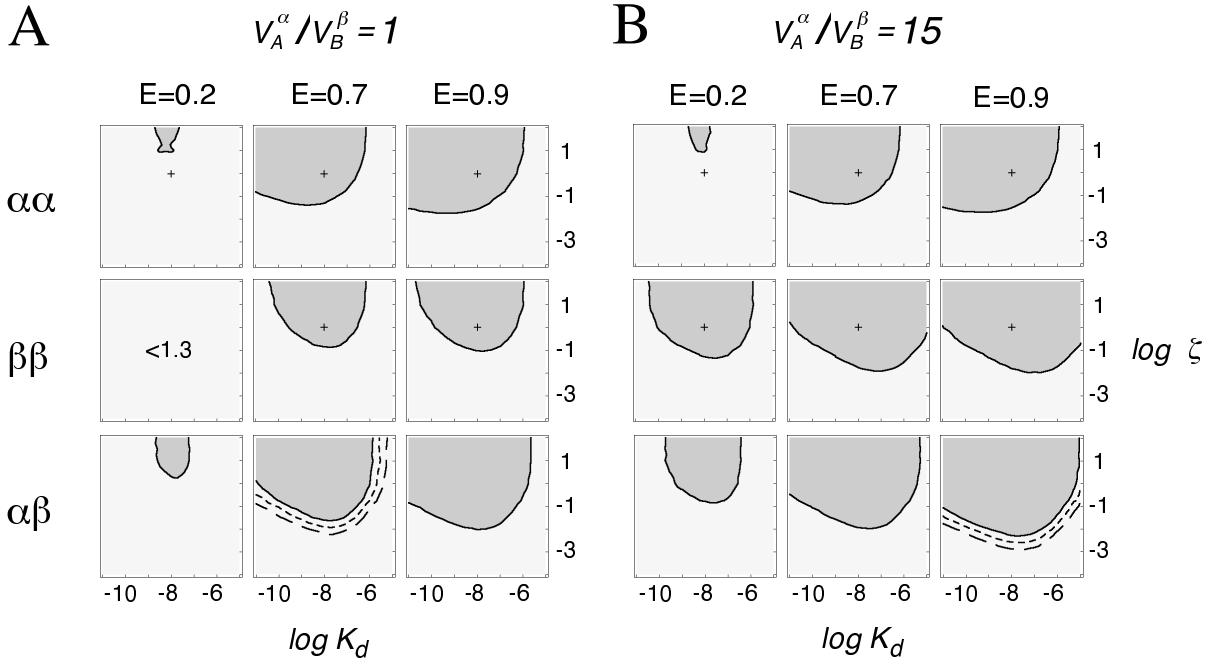

Figure 2.5: **Limits of detector correlation function sensitivity to reaction**. Contour plots of F_{xy} as a function of E. F_{xy} characterizes the feasibility of discriminating between the detector correlation functions (Eqs. 2.9 and 2.10) expected for a diffusion-only system (A, B, C) vs. a reaction-diffusion system ($A + B \leftrightharpoons C$) (Eq. 2.18). Solid contour lines demarcate regions (in gray) in which the presence of reaction can be detected with a confidence level of p<0.09 using a data acquisition time of 60 sec (see 2.4). Detection sensitivity is improved in a manner proportional to the square root of the data acquisition time (Eq. 2.19) as shown indicated by the dashed contour (240 sec) and long-dashed contour (960 sec). Parameters: $\overline{C}_A^{tot} = \overline{C}_B^{tot} = 10^{-8}$ M, $w_r = 0.48$ μm, $r_A^\alpha = r_B^\beta = 0$, $\kappa = 2.8$, $\overline{b^\alpha} = \overline{b^\beta} = 0.45$ kHz (Eq. 2.2), and (A) $\eta_A^\alpha = \eta_B^\beta = 15$ kHz; or (B) $\eta_A^\alpha = 15$ kHz, $\eta_B^\beta = 1$ kHz. The cross-hair marks the condition in which $\overline{C}_A^{tot} = \overline{C}_B^{tot} = K_d$, with one reaction turnover event observed on average per diffusive dwell time ($\log \zeta = 0$). Contours shift to the right as $\overline{C}_A^{tot} = \overline{C}_B^{tot}$ increases (see text).

becomes accessible to TCFCM curve-shape analysis. As E increases, fewer reaction turnover events per diffusive dwell time are needed to observe the effects of reaction kinetics (contour boundaries shift to lower log ζ values). Consistent with the results of Figure 2.3 showing that the shape of the cross-correlation function is most sensitive to E, when reactants are comparable in visibility a larger subset of E-enhanced reactions are accessible by $G_{\alpha\beta}(\tau)$ analysis than by $G_{\alpha\alpha}(\tau)$ or $G_{\beta\beta}(\tau)$ auto-correlation analysis (Figure 2.5A). When $\eta_A^\alpha > \eta_B^\beta$, the subset of reactions amenable to $G_{\beta\beta}(\tau)$ and $G_{\alpha\beta}(\tau)$ analysis increases (contours shift down to lower ζ values, by about an order of magnitude) (Figure 2.5B). Contour boundaries are approximately parabolic in ζ and with minima centered around $\overline{C}_A^{tot} = \overline{C}_B^{tot} = 10^{-8}$ M for the case shown. If the total concentration of reactants ($\overline{C}_A^{tot} = \overline{C}_B^{tot}$) is increased, contour boundaries shift to the right toward higher K_d by a comparable amount without a significant change in shape (not shown).

2.5.3 Determining particle concentrations by $G_{xy}(0_+)$ analysis

The magnitude of the double-detector correlation function amplitude, $G_{xy}(0_+)$, is a function of both the average number and relative visibility of particles in the probe volume, V (Eq. 2.13). In Figure 2.6, the detector auto- and cross-correlation amplitudes in the absence of energy transfer are plotted as a function of K_d with $\overline{C}_A^{tot} = \overline{C}_B^{tot} = 10^{-8}$ M. Both detector auto-correlation function amplitudes, $G_{\alpha\alpha}(0_+)$ and $G_{\beta\beta}(0_+)$, are independent of K_d as expected according to Eq. 2.14, since $1/G_{\alpha\alpha}(0_+) \propto \left(\overline{N}_A + \overline{N}_C\right) \propto \overline{C}_A^{tot}$ and $1/G_{\beta\beta}(0_+) \propto \left(\overline{N}_B + \overline{N}_C\right) \propto \overline{C}_B^{tot}$. In contrast, the cross-correlation function amplitude vs. K_d relation is sigmoidal. Unlike the auto-correlation function amplitudes, the cross-correlation amplitude is *directly* proportional to the number of C molecules (Eq. 2.14).

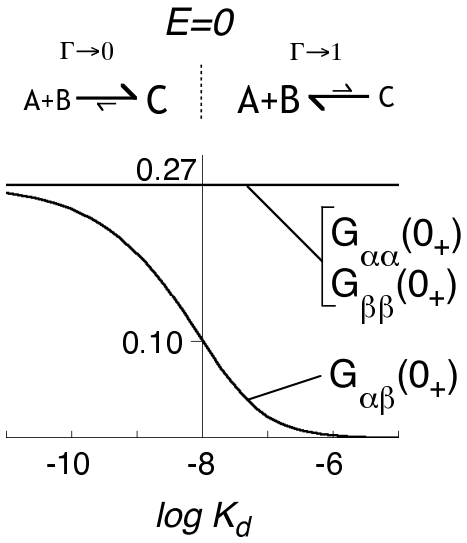

Figure 2.6: **Detector correlation function amplitudes as a function of the dissociation constant for the reaction,** $A + B \leftrightharpoons C$**.** $G_{xy}(0_+)$ amplitudes computed assuming zero energy transfer (Eq. 7.5). Parameters: $\overline{C}_A^{tot} = \overline{C}_B^{tot} = K_d = 10^{-8}$ M, $w_r = 0.48$ μm, $\kappa = 2.8$, $\eta_A^\alpha = \eta_B^\beta = 15$ kHz, and zero background fluorescence.

$G_{\alpha\beta}(0_+)$ amplitudes decrease as K_d increases above $\overline{C}_A^{tot} = \overline{C}_B^{tot}$ ($\Gamma \to 1$ and reaction equilibrium favors reactants, Eq. 2.16). As K_d decreases below $\overline{C}_A^{tot} = \overline{C}_B^{tot}$ (equilibrium favors the formation of C), the cross-correlation amplitude approaches an asymptotic value corresponding to $\overline{C}_C \to \overline{C}_A^{tot} = \overline{C}_B^{tot}$.

Energy transfer results in lower cross-correlation amplitudes, $\mathbf{G}_{\alpha\beta}(\mathbf{0}_+)$. As energy transfer efficiency increases, both α- and β-detector auto-correlation amplitude curves increase in a complicated fashion as governed by Eq. 2.13 (Figure 2.7A). The cross-correlation function amplitude, $G_{\alpha\beta}(0_+)$, is proportional to $r_C^\alpha r_C^\beta$. Using Eq. 2.12 and assuming equivalently visible reactants, $r_C^\alpha r_C^\beta = (1 - E)(1 + E)$, which is a parabolic function in energy transfer efficiency with a maximum at E=0. Thus, as E increases, $G_{\alpha\beta}(0_+)$ amplitudes decrease for all values of K_d (Figure 2.7B). The right panel of Figure 2.7B shows

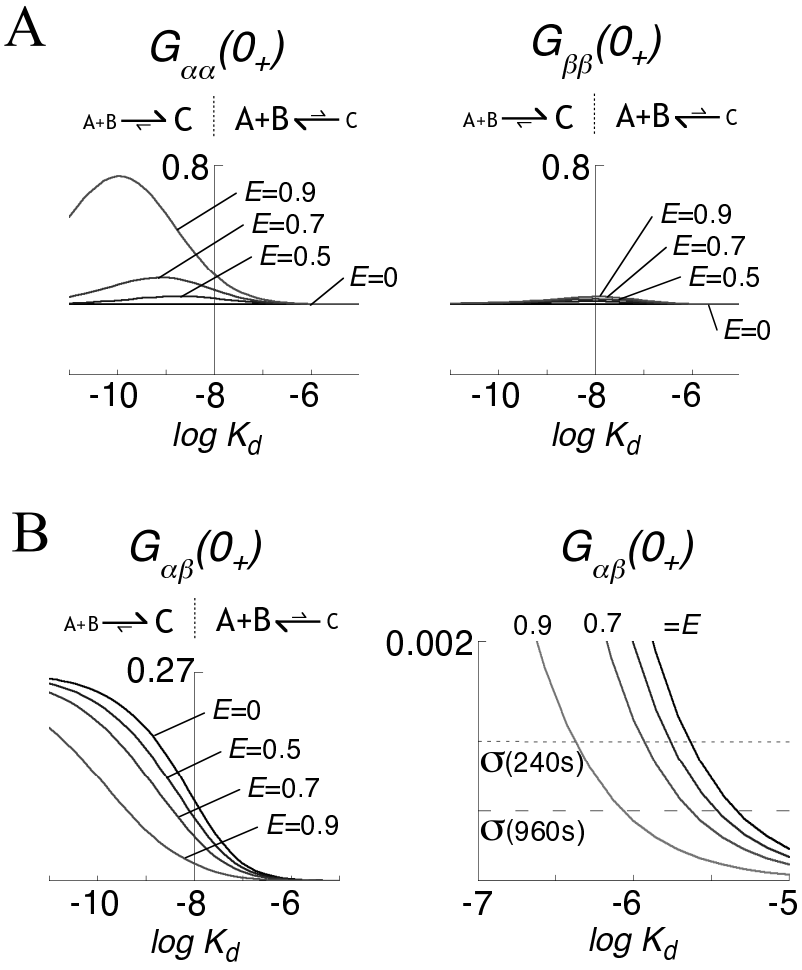

Figure 2.7: **Detector correlation function amplitudes are sensitive to energy transfer**. (*A*) Detector auto-correlation and (*B*) cross-correlation amplitudes vs. log K_d as a function of E (Eq. 2.13). (*B*, *right*) Expanded view in the region where cross-correlation amplitudes are comparable to the experimental amplitude errors assuming data acquisition times of 240 sec or 960 sec (*dashed lines*). Parameters: as in Figure 2.6.

an expanded view in the region where cross-correlation amplitudes drop below the statistical noise/detection limits indicated by the dashed (T=240 s) and long-dashed (T=960 s) lines. For the case shown ($\overline{C}_A^{tot} = \overline{C}_B^{tot} = 10^{-8}$ M), with T=240 s and E=0.9 or T=960 s and E=0.7, the maximum K_d that yields a cross-correlation amplitude greater than the estimated statistical error is $K_d^{max} \approx 10^{-6}$ M. For $\overline{C}_A^{tot} = \overline{C}_B^{tot} = 10^{-7}$ M under similar conditions, $K_d^{max} \approx 10^{-5}$ M (not shown). In general, the maximum K_d that leads to a measurable cross-correlation amplitude above statistical noise is given by $K_d^{max} \approx \left(\overline{C}_A^{tot} = \overline{C}_B^{tot}\right) \cdot 10^2$.

2.6 Discussion

2.6.1 Energy transfer in TCFCM

The motivations for this study were two-fold: (1) to assess the utility of TCFCM for studying reversible bimolecular reactions without the need for reaction initiation or chemical perturbation and (2) to determine the influence of resonance energy transfer on TCFCM auto- and cross-correlation functions. The results presented in Figure 2.7 suggest that determination of particle concentrations via $G_{xy}(0_+)$ amplitude analysis is complicated by FRET (Eq. 2.14 and 2.9). Moreover, the presence of FRET produces decreased detector cross-correlation amplitudes. If E<0.3, the effects of FRET on $G_{xy}(0_+)$ can generally be ignored and particle concentrations can be determined using Eq. 2.14 to within an error of $\leq$10%. As mean energy transfer efficiencies increase above E=0.3, the error increases exponentially.

Although FRET complicates $G_{xy}(0_+)$ analysis and is best avoided if only particle concentrations (or ratios) are of interest, FRET is advantageous for measurements of bi-

molecular reaction kinetics. If reaction components are of comparable size, reaction kinetics cannot be detected without FRET. My results suggest that under certain conditions, TCFCM in conjunction with FRET can be used to monitor reaction kinetics. The interplay between energy transfer and reaction kinetics in altering the shape of the correlation function as proposed here has been demonstrated recently in a different context by Widengren *et al.* (2001).[267] In contrast to my results (which assess the possibility of measuring reaction kinetics *given* a known amount of energy transfer), Widengren *et al.* exploited the effects of a well-characterized fluorophore cis-trans isomerization reaction on the shape of the auto-correlation function *as a means* to measure FRET efficiencies of double-labeled DNA duplexes of varying lengths.

2.6.2 Analysis of bimolecular reaction kinetics by TCFCM

To successfully measure reaction kinetics by curve-shape analysis, a sufficient number of "reaction fluctuations" per observation interval, ζ, must be observed. The dimensionless parameter ζ is a function of the characteristic diffusion time of the reacting particles in the probe volume, τ_{diff} the position of equilibrium variable, Γ, and the reverse rate constant, k_b (Eq. 7.5). For unimolecular reactions, $\Gamma = 1 + k_f/k_b$, and ζ is a function of the forward and reverse rate constants but not reactant concentrations. For bimolecular reactions, however, Γ and thus ζ are functions of k_f and k_b, as well as the equilibrium constant for the reaction *relative* to the total concentration of the reactants (see Eq. 2.16). When $\overline{C}_A^{tot} = \overline{C}_B^{tot}$, the relative concentration fluctuations for both the reactants *and* complex are greatest,[14] leading to maximal detector cross-correlation function amplitudes.

From the $G_{xy}(\tau)$ reaction sensitivity landscapes in Figure 2.5, the reaction conditions

that permit measurable differences in the detector correlation functions can be determined. For a 2-photon 3DG volume of w_r=0.48 μm and κ=2.8, with $D_A = D_B = D_C = 8.5 \times 10^{-7}$ cm^2/s (D for green fluorescent protein in water[49]), $\tau_{diff} \sim 3.7 \times 10^{-4}$ s; this value is similar for a 1-photon 3DG with w_r=0.33 μm and κ=5. Using Eq. 7.5, $\zeta = \tau_{diff} k_f K_d / \Gamma$, and expressing Γ as a function of $\overline{C}_A^{tot}$, $\overline{C}_B^{tot}$, and K_d (Eq. 2.16), the conditions under which reactions are accessible by $G_{\alpha\beta}(\tau)$ analysis can be estimated from the contours of Figure 2.5. These reaction conditions are shown in Figure 2.8 assuming E=0.9, T=960 s, and $\eta_A^\alpha / \eta_B^\beta = 15$, for different values of $\overline{C}_A^{tot} = \overline{C}_B^{tot}$. For reactions with a $K_d \sim 10^{-9}$ M, reaction kinetics are typically inaccessible unless $k_f \gtrsim 10^9$ M^{-1}s^{-1}. Reactions with $k_f \gtrsim 10^8$ M^{-1}s^{-1} are accessible if the K_d is within the window of $\sim 10^{-8}$ to $\sim 10^{-6}$ M, for all the total reactant concentrations shown (dark gray). As $\overline{C}_A^{tot} = \overline{C}_B^{tot}$ increases, lower affinity reactions with slower forward rates can be studied: if $\overline{C}_A^{tot} = \overline{C}_B^{tot} = 10^{-7}$ M, reactions with a $K_d \leq 10^{-5}$ M and $k_f \gtrsim 10^7$ M^{-1}s^{-1} are accessible; if $\overline{C}_A^{tot} = \overline{C}_B^{tot} = 10^{-6}$ M, reactions with a $K_d \leq 10^{-4}$ M and $k_f \gtrsim 10^6$ M^{-1}s^{-1} should be accessible. To optimize the influence of kinetics on the detector cross-correlation function, the reactive system is best poised when $K_d \cdot 10^{-2} \leq \left(\overline{C}_A^{tot} = \overline{C}_B^{tot}\right) \leq K_d \cdot 10^2$, where the upper limit ensures that $G_{xy}(0_+)$ amplitudes are measurable above statistical noise.

The resolution of reaction kinetics by $G_{xy}(\tau)$ analysis can also be improved if other reactant property differences exist and/or these properties change upon reaction. As demonstrated in Figs. 2.4C and D, if the diffusion coefficient for one reactant is significantly larger than the other, the influence of kinetics on $G_{\alpha\beta}(0_+)$ can be observed without the presence of energy transfer, although energy transfer magnifies these effects. A significant quantum

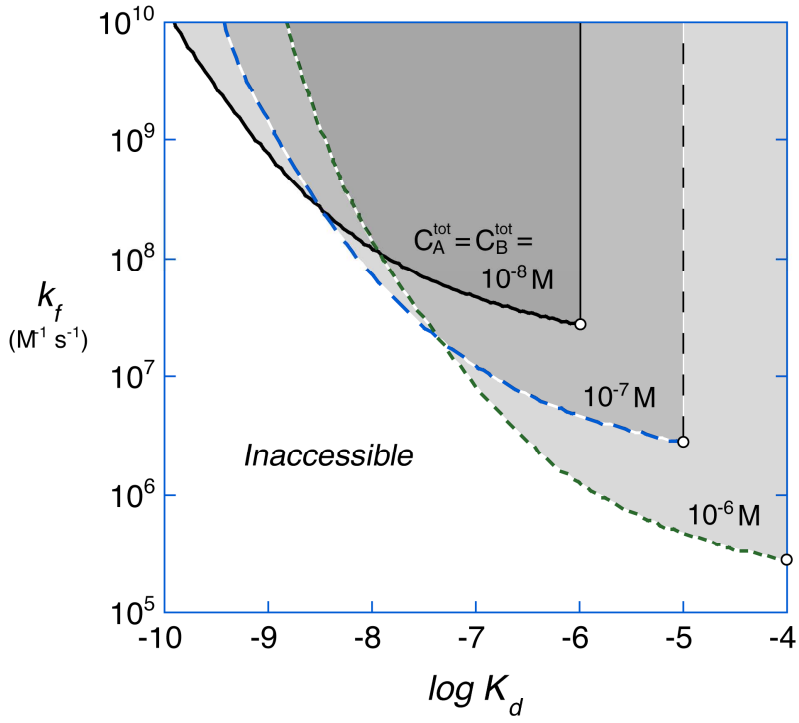

Figure 2.8: **Subset of bimolecular reaction kinetics accessible to detector cross-correlation function analysis**. Subset of reaction parameters (k_f, K_d, and $\overline{C}_A^{tot} = \overline{C}_B^{tot}$) that lead to measurable differences in $G_{\alpha\beta}(\tau)$ ($F_{\alpha\beta} \geq 1.3$) indicated in different tones of gray. Determined from Figure 2.5 using $\zeta \sim \tau_{diff} k_f K_d / \Gamma$ (Eqs. 7.5 and 2.16) with $\tau_{diff} \approx 3.7 \times 10^{-4}$ s, for E=0.9, T=960 s, and $\eta_A^\alpha / \eta_B^\beta = 15$. Open circles mark the condition, $K_d = \left(\overline{C}_A^{tot} = \overline{C}_B^{tot}\right) \cdot 10^2$, an estimate of the maximum K_d with detectable $G_{\alpha\beta}(0_+)$ amplitudes above statistical noise. Shown for $\overline{C}_A^{tot} = \overline{C}_B^{tot} = 10^{-8}$ M (*solid line*), 10^{-7} M (*dashed*), and 10^{-6} M (*short dashed*).

yield change of one reactant upon binding could also result in a pronounced effect of reaction on $G_{xy}(\tau)$. This has been demonstrated in studies of ethidium bromide binding to DNA[65,116,160] and of 1-anilino-8-naphthalene sulfonic acid binding to partially folded proteins.[20,147] Quantum yield enhancement upon binding in combination with FRET would likely extend the set of reactions accessible to TCFCM analysis.

2.6.3 Biochemical relevance

The association rate for two molecules can be expressed as $k_f \triangleq p_{bind} \cdot k_{coll}$, where k_{coll} is the diffusional encounter rate and p_{bind} is the probability of successful binding upon colliding. From simple collision theory, $k_{coll} \sim 7 \times 10^9$ $\mathrm{M^{-1}s^{-1}}$ in water for comparably sized reactants; if one reactant is larger than the other, k_{coll} may be higher due to the larger target area of the former and higher mobility of the latter.[70] For protein-protein complexes, p_{bind} is typically $\sim 10^{-5}$ and basal protein-protein docking rates *in vitro* are $\sim 10^5$ $\mathrm{M^{-1}s^{-1}}$,[125] although long-range electrostatic factors can accelerate these rates by up to 10^3.[124,183,225] Thus, association rates constants, k_f, for protein complexes typically are in the range $10^4 - 10^5$ $\mathrm{M^{-1}s^{-1}}$ with the majority being $\sim 10^6$ $\mathrm{M^{-1}s^{-1}}$.[70,77,125,183] Dissociation rates are much more varied, typically in the range $10^{-7} - 10^4$ $\mathrm{s^{-1}}$,[70,125] so that K_ds are in the range $10^{-13} - 10^2$ M. Protein-ligand (e.g., antibody-hapten) and small nucleic acid duplex interactions generally have faster association and dissociation rates ($10^7 - 10^9$ $\mathrm{M^{-1}s^{-1}}$ and $10^1 - 10^4$ $\mathrm{s^{-1}}$, respectively), with K_ds typically spanning the range $10^{-8} - 10^{-3}$ M.[28,70,191]

The results of the analysis here suggest that the kinetic rate constants for a subset of these protein-protein and protein-ligand reactions can be deduced by curve-shape analysis of the detector cross-correlation function, provided energy transfer efficiency within the

reaction complex is sufficiently high ($E \geq 0.7$), a sufficient experimental data acquisition time, the total concentration of reactants is sufficiently high ($\geq 10^{-8}$ M), and the reaction equilibrium is properly poised. When reactants are comparably sized, reactions must typically be near the diffusion-limit ($k_f \geq 10^7$ $M^{-1}s^{-1}$) to be observable. Examples of macromolecular interactions characterized by very fast association rates, include: barnase and barstar ($10^8 - 10^{10}$ $M^{-1}s^{-1}$),[225] insulin dimerization (10^8 $M^{-1}s^{-1}$),[142] cytochrome c with cytochrome c peroxidase or cytochrome b5 ($10^7 - 10^9$ $M^{-1}s^{-1}$),[183] various tRNA and tRNA synthetases (10^8 $M^{-1}s^{-1}$),[70] and unfolded bovine pancreatic trypsin inhibitor and the *E. coli* chaperone, SecB ($10^9 - 10^{10}$ $M^{-1}s^{-1}$).[69] When one reactant is considerable larger than the other reactant, the subset of kinetic parameters that lead to detectable changes in the cross-correlation function is extended. Some biological examples where reactants have very different diffusion coefficients include the binding of cytosolic proteins to membrane proteins, lipidic domains, or scaffold proteins,[68,113] and of soluble factors to relatively immobile cytoskeletal or vesicular structures.

In summary, it should be possible to study a subset of biologically relevant bimolecular reactions by analysis of TCFCM correlation functions without the need for chemical perturbation. While $G_{xy}(0_+)$ analysis of reactant concentrations is substantially complicated by the presence of energy transfer, FRET is advantageous for kinetic studies, and essential if there is little hydrodynamic difference between interacting components. If particle concentrations are the primary quantities of interest, the effects of FRET may be neglected for $E \leq 0.3$ without incurring significant error ($\leq$10%).

2.7 Appendix 2A: Solution for the spatio-temporal dissipation function, $Z_{ij}(\mathbf{q},\tau)$

For the bimolecular reaction, $A+B \underset{k_b}{\overset{k_a}{\rightleftharpoons}} C$, the linearized reaction-diffusion matrix Eq. 2.4 is:

$$\mathbf{M} = \begin{bmatrix} -k_f\overline{C}_B - D_A\mathbf{q}^2 & -k_f\overline{C}_A & k_b \\ -k_f\overline{C}_B & -k_f\overline{C}_A - D_B\mathbf{q}^2 & k_b \\ k_f\overline{C}_B & k_f\overline{C}_A & -k_b - D_C\mathbf{q}^2 \end{bmatrix} \tag{2.21}$$

By detailed balance ($R_{ij}C_j = R_{ji}C_i$), $\mathbf{M}$ can be made symmetric by the similarity transformation $\mathbf{M}_{sym} \triangleq \mathbf{X}^{-1}\mathbf{M}\mathbf{X}$, where $\mathbf{X}$ is the diagonal matrix with $X_{ij} \triangleq \delta_{ij}\sqrt{\overline{C}_i}$.[65,115,260] Using the following reduced variables: $\rho = k_b/D_C$, $\theta_A = \sqrt{\overline{C}_A/\overline{C}_C}$, $\theta_B = \sqrt{\overline{C}_B/\overline{C}_C}$, $\theta_C = -1$, $\hat{D}_A \triangleq D_A/D_C$, and $\hat{D}_B \triangleq D_B/D_C$, the matrix $\mathbf{M}_{sym}$ becomes:

$$\mathbf{M}_{sym} = \rho D_C \begin{bmatrix} -\theta_A^{-2} - \hat{D}_A\mathbf{q}^2/\rho & -(\theta_A\theta_B)^{-1} & \theta_A^{-1} \\ -(\theta_A\theta_B)^{-1} & -\theta_B^{-2} - \hat{D}_B\mathbf{q}^2/\rho & \theta_B^{-1} \\ \theta_A^{-1} & \theta_B^{-1} & -\theta_C^{-2} - \mathbf{q}^2/\rho \end{bmatrix} \tag{2.22}$$

Solutions to Eq. 2.4 for $\delta\widetilde{\mathbf{C}}(\mathbf{q},\tau)$ are obtained by solving for the eigenvalues and eigenfunctions of $\mathbf{M}_{sym}$. The spatio-temporal dissipation function $Z_{ij}(\mathbf{q},\tau)$ in Eq. 2.7 can then be written as: $Z_{ij}(\mathbf{q},\tau) = \sum_s Y_j^{(s)} \cdot \exp\left[\lambda^{(s)}\tau\right] \cdot \left(Y_j^{(s)}\right)^{-1}$, where $Y_j^{(s)}$ and $\left(Y_j^{(s)}\right)^{-1}$ are the s^{th} eigenvector and inverse eigenvector, respectively, corresponding to the eigenvalue, $\lambda^{(s)}$.[65,115] Use of a symmetric matrix leads to six unique $Z_{ij}(= Z_{ji})$ expressions rather than eight if the matrix M were used directly (for which $Z_{ij} \neq Z_{ji}$).

For the bimolecular reaction, $A + B \underset{k_b}{\overset{k_a}{\rightleftharpoons}} C$, with $\hat{D}_A = \hat{D}_B = 1$, the diffusive and

reactive components of $Z_{ij}(\mathbf{q},\tau)$ decouple:

$$Z_{ij}(\mathbf{q},\tau) = \left(\delta_{ij} + \frac{\Gamma\left(e^{-\tau/\tau_{reac}} - 1\right)}{\theta_i\theta_j}\right) \cdot \exp\left[-\frac{w_r\mathbf{q}^2\tau}{4n_p\tau_{diff}}\right] \tag{2.23}$$

where Γ is defined in association with Eq. 2.16. With $\hat{D}_A = 1$ and $\hat{D}_B \gg 1$, the $Z_{ij}(\mathbf{q},\tau)$ functions are:

$$\begin{aligned}
Z_{AA}(\mathbf{q},\tau) &= \left(1+\theta_A^{-2}\right)^{-1}\left[E_{diff} + \theta_A^{-2}E_{reac}\left(C - \left(1+\mathbf{q}^2T - Q\right)S\right)\right] \\
Z_{BB}(\mathbf{q},\tau) &= E_{reac}\left(C - \left(1+\mathbf{q}^2T - Q\right)S\right) \\
Z_{CC}(\mathbf{q},\tau) &= \left(1+\theta_A^{-2}\right)^{-1}\left[\theta_A^{-2}E_{diff} + E_{reac}\left(C - \left(1+\mathbf{q}^2T - Q\right)S\right)\right] \\
Z_{AB}(\mathbf{q},\tau) &= -\left(\theta_B/\theta_A\right)E_{reac}QS \\
Z_{BC}(\mathbf{q},\tau) &= \theta_B E_{reac}QS \\
Z_{AC}(\mathbf{q},\tau) &= \left(\theta_A+\theta_A^{-1}\right)^{-1}\left[E_{diff} - E_{reac}\left(C - \left(1+\mathbf{q}^2T - Q\right)S\right)\right]
\end{aligned} \tag{2.24}$$

where

$$\begin{aligned}
E_{diff} &\triangleq \exp\left[-\left(\frac{w_r^2\mathbf{q}^2}{4n_p}\right)\frac{\tau}{\tau_C}\right] \\
E_{reac} &\triangleq \exp\left[-\left(\frac{1+\mathbf{q}^2P}{2}\right)\frac{\tau}{\tau_{reac}}\right] \\
C &\triangleq \cosh\left[\frac{U\left(\mathbf{q}^2\right)\tau}{2\tau_{reac}}\right] \\
S &\triangleq \sinh\left[\frac{U\left(\mathbf{q}^2\right)\tau}{2\tau_{reac}}\right]/U\left(\mathbf{q}^2\right) \\
U\left(\mathbf{q}^2\right) &\triangleq \sqrt{\left(1+\mathbf{q}^2L\right)^2 - 2\mathbf{q}^2LQ} \\
Q &\triangleq 2\Gamma/\theta_B^2 \\
L &\triangleq D_C\left(1-\hat{D}_B\right)\tau_{reac} \\
P &\triangleq D_C\left(1+\hat{D}_B\right)\tau_{reac} \\
\tau_C &\triangleq w_r^2/4n_pD_C
\end{aligned} \tag{2.25}$$

For $D_A \neq D_B \neq D_C$, the eigenvalues and eigenvectors for $\mathbf{M}_{sym}$ (Eq. 2.22) must be solved using a modified cubic root equation assuming real roots.[263] Since $\mathbf{M}_{sym}$ is a symmetric 3×3 matrix, the associated eigenvalues must be real and distinct. The resulting $Z_{ij}(\mathbf{q}, \tau)$ functions are provided below; note that these are mostly dependent upon one reactant species explicitly (the "pivot" species, in this case, B), with implicit dependence on the other reactant species (A):

$$
\begin{aligned}
Z_{AA}(\mathbf{q},\tau) &= \sum_j^3 \frac{(-1)^j e^{\lambda_j \tau} \Lambda_{kl} \left(\Gamma^2 - \left(\Gamma + (D_C\mathbf{q}^2 + \lambda_j)\tau_{reac}\right)\left(\Gamma + \theta_B^2 \left(D_B\mathbf{q}^2 + \lambda_j\right)\tau_{reac}\right)\right)}{\left(\theta_B^2 \Lambda_{12}\Lambda_{13}\Lambda_{23}\tau_{reac}^2\right)} \\
Z_{BB}(\mathbf{q},\tau) &= \sum_j^3 \frac{(-1)^j e^{\lambda_j \tau} \Lambda_{kl} \left(D_C\mathbf{q}^2 + \lambda_j\right)\left(\Gamma\Delta_{BC}\mathbf{q}^2 + \theta_B^2 \left(D_B\mathbf{q}^2 + \lambda_k\right)\left(D_B\mathbf{q}^2 + \lambda_l\right)\tau_{reac}\right)}{\theta_B \Delta_{BC}\Lambda_{12}\Lambda_{13}\Lambda_{23}\tau_{reac}\mathbf{q}^2} \\
Z_{CC}(\mathbf{q},\tau) &= \sum_j^3 \frac{(-1)^j e^{\lambda_j \tau} \Lambda_{kl} \left(D_C\mathbf{q}^2 + \lambda_j\right)\left(\Gamma\Delta_{BC}\mathbf{q}^2 - \left(D_B\mathbf{q}^2 + \lambda_k\right)\left(D_B\mathbf{q}^2 + \lambda_l\right)\tau_{reac}\right)}{\Delta_{BC}\Lambda_{12}\Lambda_{13}\Lambda_{23}\tau_{reac}\mathbf{q}^2} \\
Z_{AB}(\mathbf{q},\tau) &= \sum_j^3 \frac{(-1)^j e^{\lambda_j \tau} \Lambda_{kl} \Gamma \left(D_C\mathbf{q}^2 + \lambda_j\right)}{\theta_A\theta_B \Lambda_{12}\Lambda_{13}\Lambda_{23}\tau_{reac}} \\
Z_{BC}(\mathbf{q},\tau) &= \sum_j^3 \frac{(-1)^{j-1} e^{\lambda_j \tau} \Lambda_{kl} \left(D_B\mathbf{q}^2 + \lambda_j\right)\left(\Gamma\Delta_{BC}\mathbf{q}^2 - \theta_B^2 \left(D_B\mathbf{q}^2 + \lambda_k\right)\left(D_B\mathbf{q}^2 + \lambda_l\right)\tau_{reac}\right)}{\theta_B \Delta_{BC}\Lambda_{12}\Lambda_{13}\Lambda_{23}\tau_{reac}\mathbf{q}^2} \\
Z_{AC}(\mathbf{q},\tau) &= \sum_j^3 \frac{(-1)^{j-1} e^{\lambda_j \tau} \Lambda_{kl} \Gamma \left(D_B\mathbf{q}^2 + \lambda_j\right)}{\theta_A \Lambda_{12}\Lambda_{13}\Lambda_{23}\tau_{reac}}
\end{aligned}
\tag{2.26}
$$

where k and l (in Λ_{kl}) are indices excluding j from the ordered set $\{1, 2, 3\}$ (*i.e.,* for: $j = 1$, $(k, l) \rightarrow (2, 3)$; $j = 2$, $(k, l) \rightarrow (1, 3)$; $j = 3$, $(k, l) \rightarrow (1, 2)$) and:

$$
\begin{aligned}
\lambda_j(\mathbf{q}) &\triangleq \frac{1}{3}\left(2V(\mathbf{q})\cos\left(\frac{\Theta(\mathbf{q})+(j-1)2\pi}{3}\right)-\left[D_\Sigma\mathbf{q}^2+\frac{1}{\tau_{reac}}\right]\right)\\
\Lambda_{jk}(\mathbf{q}) &\triangleq \frac{2V(\mathbf{q})}{3}\left(\cos\left(\frac{\Theta(\mathbf{q})+(j-1)2\pi}{3}\right)-\cos\left(\frac{\Theta(\mathbf{q})+(k-1)2\pi}{3}\right)\right)\\
V(\mathbf{q}) &\triangleq \sqrt{\left[\Delta_{AB}^2+\Delta_{CA}\Delta_{CB}\right]\mathbf{q}^4+\left[3\Gamma\left(\frac{D_A}{\theta_A^2}-\frac{D_B}{\theta_B^2}-1\right)-D_\Sigma\right]\mathbf{q}^2+\frac{1}{\tau_{reac}^2}}\\
\Theta(\mathbf{q}) &\triangleq \arccos\left(\frac{1}{4V(\mathbf{q})}\left\{\left[\left(D_\Sigma-3D_A\right)\left(D_\Sigma-3D_B\right)\left(D_\Sigma-3\right)\right]\mathbf{q}^6\right.\right.\\
&\qquad+\left[\frac{3\Gamma}{\tau_{reac}}\left(3\Sigma_{BC}\theta_A^{-2}\left(D_\Sigma-3\right)+\Sigma_{AC}\theta_B^{-2}\left(D_\Sigma-3\right)\right.\right.\right.\\
&\qquad\qquad\left.\left.\left.+\,3\Gamma\left(\Sigma_{AC}\Sigma_{BC}-\Delta_{AB}^2-4\right)+\left(9-D_\Sigma^2-\Delta_{AB}^2-\Delta_{CA}\Delta_{CB}\right)\right)\right]\mathbf{q}^4\right.\\
&\qquad\left.\left.+\left[\frac{3\Gamma}{\tau_{reac}^2}\left(3\left(\Sigma_{AB}+\Sigma_{AC}\theta_B^{-2}+\Sigma_{BC}\theta_A^{-2}\right)-2D_\Sigma\right)\right]\mathbf{q}^2+\frac{2}{\tau_{reac}^3}\right\}\right)\\
\Delta_{XY} &\triangleq \left(D_X-D_Y\right)\\
\Sigma_{XY} &\triangleq \left(D_X+D_Y\right)\\
D_\Sigma &\triangleq \left(D_A+D_B+D_C\right)
\end{aligned}
\tag{2.27}
$$

Note that for the sake of printed compactness, the equations associated with the general solution (Eqs. 2.26-2.27) are expressed in terms of *dimensioned* diffusion coefficients (D_X) instead of the dimensionless ones ($\hat{D}_X$).

2.8 Appendix 2B: Double-detector correlation function expressions, $G_{xy}(\tau)$

The double-detector correlation functions of Eq. 2.5 can be written explicitly and generally as:

$$
\begin{aligned}
G_{\alpha\alpha}(\tau) &= \left(\frac{\aleph_\alpha^2}{\overline{N}_A}\right)\left(\frac{\theta_A^2}{\left(\theta_A^2+r_B^\alpha\theta_B^2+r_C^\alpha\theta_C^2\right)^2}\right) \\
&\quad\times\left[\begin{array}{l}\theta_A^2 h_{AA}(\tau)+\left(r_B^\alpha\right)^2\theta_B^2 h_{BB}(\tau)+\left(r_C^\alpha\right)^2\theta_C^2 h_{CC}(\tau) \\ \quad +2\left(r_B^\alpha\theta_A\theta_B h_{AB}(\tau)-r_C^\alpha\theta_A\theta_C h_{AC}(\tau)-r_B^\alpha r_C^\alpha\theta_B\theta_C h_{BC}(\tau)\right)\end{array}\right] \\
G_{\beta\beta}(\tau) &= \left(\frac{\aleph_\beta^2}{\overline{N}_B}\right)\left(\frac{\theta_B^2}{\left(r_A^\beta\theta_A^2+\theta_B^2+r_C^\beta\theta_C^2\right)^2}\right) \\
&\quad\times\left[\begin{array}{l}\left(r_A^\beta\right)^2\theta_A^2 h_{AA}(\tau)+\theta_B^2 h_{BB}(\tau)+\left(r_C^\beta\right)^2\theta_C^2 h_{CC}(\tau) \\ \quad +2\left(r_A^\beta\theta_A\theta_B h_{AB}(\tau)-r_A^\beta r_C^\beta\theta_A\theta_C h_{AC}(\tau)-r_C^\beta\theta_B\theta_C h_{BC}(\tau)\right)\end{array}\right] \\
G_{\alpha\beta}(\tau) &= \left(\frac{\aleph_\alpha\aleph_\beta}{\overline{N}_C}\right)\left(\frac{\theta_C^2}{\left(\theta_A^2+r_B^\alpha\theta_B^2+r_C^\alpha\theta_C^2\right)\left(r_A^\beta\theta_A^2+\theta_B^2+r_C^\beta\theta_C^2\right)}\right) \\
&\quad\times\left[\begin{array}{l}r_A^\beta\theta_A^2 h_{AA}(\tau)+r_B^\alpha\theta_B^2 h_{BB}(\tau)+r_C^\alpha r_C^\beta\theta_A^2 h_{CC}(\tau) \\ \quad +\left(1+r_B^\alpha r_A^\beta\right)\theta_A\theta_B h_{AB}(\tau)-\left(r_C^\beta+r_C^\alpha r_A^\beta\right)\theta_A\theta_C h_{AC}(\tau) \\ \qquad\qquad -\left(r_B^\alpha r_C^\beta+r_C^\alpha\right)\theta_B\theta_C h_{BC}(\tau)\end{array}\right]
\end{aligned}
\tag{2.28}
$$

where $r_B^\alpha = \eta_B^\alpha/\eta_A^\alpha$ and $r_A^\beta = \eta_A^\beta/\eta_B^\beta$ are conjugate variables that describe the amount of non-ideal bleed-through fluorescence registered in a non-preferred detector channel. When $r_A^\beta = r_B^\alpha = 0$, the expressions of Eq. 2.28 simplify to those of Eqs. 2.9 and 2.10.

The relative α- and β-visibilities for the complex C, formed by the association of donor A and acceptor B, can be written in terms of intended and bleed-through contributions as

follows:

$$\begin{array}{rcccccl} & & & & \text{intended} & & \text{bleed-through} \\ r_C^\alpha & = & \eta_C^\alpha/\eta_A^\alpha & = & (1-E) & + & \left\{\left(r_B^\alpha \eta_B^\beta/\eta_A^\alpha\right)\left(1+\left[\Phi_B \eta_A^\alpha/\eta_B^\beta\right]E\right)\right\} \\ r_C^\beta & = & \eta_C^\beta/\eta_B^\beta & = & \left(1+\left[\Phi_B \eta_A^\alpha/\eta_B^\beta\right]E\right) & + & \left\{\left(r_A^\beta \eta_A^\alpha/\eta_B^\beta\right)(1-E)\right\} \end{array} \tag{2.29}$$

where Φ_B is the product of the quantum yield for acceptor species B (Q_B) and the ratio of the β to α channel detection efficiencies (g_β/g_α). When $\Phi_B = 1$ and $r_A^\beta = r_B^\alpha = 0$, Eq. 2.29 simplifies to Eq. 2.12.

2.9 Appendix 2C: Expressions for $\overline{N}_i$ in the absence of bleed-through fluorescence

Expressions for $\overline{N}_A$, $\overline{N}_B$, and $\overline{N}_C$ as a function of $G_{\alpha\alpha}(0_+)$, $G_{\beta\beta}(0_+)$ and $G_{\alpha\beta}(0_+)$ for the case in which there is no bleed-through fluorescence:

$$
\begin{aligned}
\overline{N}_A &= (r_C^\alpha)^2 \left(r_C^\beta \aleph_\alpha G_{\alpha\alpha}(0_+) G_{\beta\beta}(0_+) - \left(r_C^\beta - 1 \right) \aleph_\alpha G_{\alpha\beta}^2(0_+) - \aleph_\beta G_{\alpha\alpha}(0_+) G_{\alpha\beta}(0_+) \right) \\
&\quad \times \frac{\left(r_C^\beta \aleph_\alpha G_{\beta\beta}(0_+) + (r_C^\alpha - 1) \aleph_\beta G_{\alpha\beta}(0_+) \right)}{\left((r_C^\alpha - 1) \left(r_C^\beta - 1 \right) G_{\alpha\beta}^2(0_+) - r_C^\alpha r_C^\beta G_{\alpha\alpha}(0_+) G_{\beta\beta}(0_+) \right)^2} \\
\overline{N}_B &= \left(r_C^\beta \right)^2 \left(r_C^\alpha \aleph_\beta G_{\alpha\alpha}(0_+) G_{\beta\beta}(0_+) - (r_C^\alpha - 1) \aleph_\beta G_{\alpha\beta}^2(0_+) - \aleph_\alpha G_{\beta\beta}(0_+) G_{\alpha\beta}(0_+) \right) \\
&\quad \times \frac{\left(r_C^\alpha \aleph_\beta G_{\alpha\alpha}(0_+) + \left(r_C^\beta - 1 \right) \aleph_\alpha G_{\alpha\beta}(0_+) \right)}{\left((r_C^\alpha - 1) \left(r_C^\beta - 1 \right) G_{\alpha\beta}^2(0_+) - r_C^\alpha r_C^\beta G_{\alpha\alpha}(0_+) G_{\beta\beta}(0_+) \right)^2} \\
\overline{N}_C &= G_{\alpha\beta}(0_+) \left(r_C^\alpha \aleph_\beta G_{\alpha\alpha}(0_+) - \left(r_C^\beta - 1 \right) \aleph_\alpha G_{\alpha\beta}(0_+) \right) \\
&\quad \times \frac{\left(r_C^\beta \aleph_\alpha G_{\beta\beta}(0_+) + (r_C^\alpha - 1) \aleph_\beta G_{\alpha\beta}(0_+) \right)}{\left((r_C^\alpha - 1) \left(r_C^\beta - 1 \right) G_{\alpha\beta}^2(0_+) - r_C^\alpha r_C^\beta G_{\alpha\alpha}(0_+) G_{\beta\beta}(0_+) \right)^2}
\end{aligned}
\tag{2.30}
$$

Chapter 3

Instrumentation and Pilot Experiments

Quantitative Two-Color Fluorescence Correlation Spectroscopy Determinations of Absolute Particle Concentrations: Towards a Proof-of-Principle Demonstration On a Model Interacting DNA Duplex System

3.1 Introduction

Fluorescence fluctuation microscopy (FFM) is a technique by which absolute particle numbers can be quantified in a chemically non-pertubative manner. Recently, I helped develop a general theory for evaluating bimolecular interactions using a two-color fluorescence correlation microscopy variant of FFM (TCFCM) (*Biophys. J.* 83:533-546) . Here, I describe my efforts towards establishing an approach for measuring the concentrations of fluorescently labeled components that undergo the reversible bimolecular association, $A + B \underset{k_b}{\overset{k_a}{\rightleftharpoons}} C$. The specific goal of this approach would be to determine the equilibrium constant for these components *from a single two-color fluorescence fluctuation microscopy (TCFFM) measurement.* An important aspect of this approach is to explicitly account for background fluorescence, fluorophore-detector bleed-through/cross-talk, and Föorster resonance energy transfer (FRET) between interacting components. Such detection non-idealities, while often present in TCFFM experiments, are rarely accounted for in practice. A home-built two-photon excitation TCFFM apparatus was constructed to perform very sensitive TCFFM measurements. Using this apparatus, I have made pilot measurements of a variety of Green Fluorescent and Red Fluorescent proteins, and a pair of non-self-complementary DNA strands, d(ATCTACGAGTG):d(CACTCGTAGAT), each strand labeled with either Rhodamine Green or Texas Red. The instrumentation and work described in this chapter lay the groundwork for determining K_ds directly from auto- and cross-correlation function amplitudes, without resorting to titration/strand-displacement experiments as is current practiced.

3.2 Materials and Methods

3.2.1 TCFFM Instrumentation

TCFFM measurements were made using a home-built apparatus shown schematically in Figure 3.1. A kit-assembled, water-cooled Ti:Sapph laser (Kapteyn-Murnane Laboratories, LLC, Boulder, CO) was pumped by a 5W 532 nm Nd:YAG laser (Verdi; Coherent Inc., Santa Clara, CA), tuned and mode-locked at 830 nm ($\lesssim$50 fs pulses at 91 MHz; average power >300 mW, beam diameter $\sim$ 1 mm). Residual 532 nm forward scattered laser light was block using a RG780 Schott Glass filter (Schott Corp., Yonkers, NY). After Galilean beam expansion (10X) (lenses from New Focus Inc., Santa Clara, CA), <20% of this IR laser beam was reflected by a beam-splitting mirror (BS1-790-20-1025-45P; CVI Laser Corp., Albuquerque, NM) and attenuated by an appropriate absorption neutral density (ND) filter to achieve <100 mW of average power. This expanded beam was steered into a Nikon TE300 inverted epi-fluorescence microscope (Nikon Inc., Melville, NY) and reflected by an infrared dichroic mirror (TLM1-800-45; CVI Laser Corp.) to sufficiently fill the back aperture of a mounted Nikon infinity-corrected 60X 1.2 NA water immersion objective. Collected sample fluorescence was focused through a second dichroic mirror with green/red selective filters (see Sec. 3.2.2) and onto two 125 μm core diameter (0.37 NA) multi-mode fiber light-guides (CF01493-09; Thor Labs Inc., Newton NJ) mounted on precision x-y-z translation stages (New Focus Inc., Santa Clara, CA). Fluorescence emission was detected by two avalanche photodiodes (APD), each with a dark currents < 50 cps (SPCM-AQR-15-FC; Perkin Elmer Optoelectronics, Quebec, Canada). Auto- and cross-correlation functions of the APD TTL pulsed signals were computed online using a mutiple-tau digital correlator

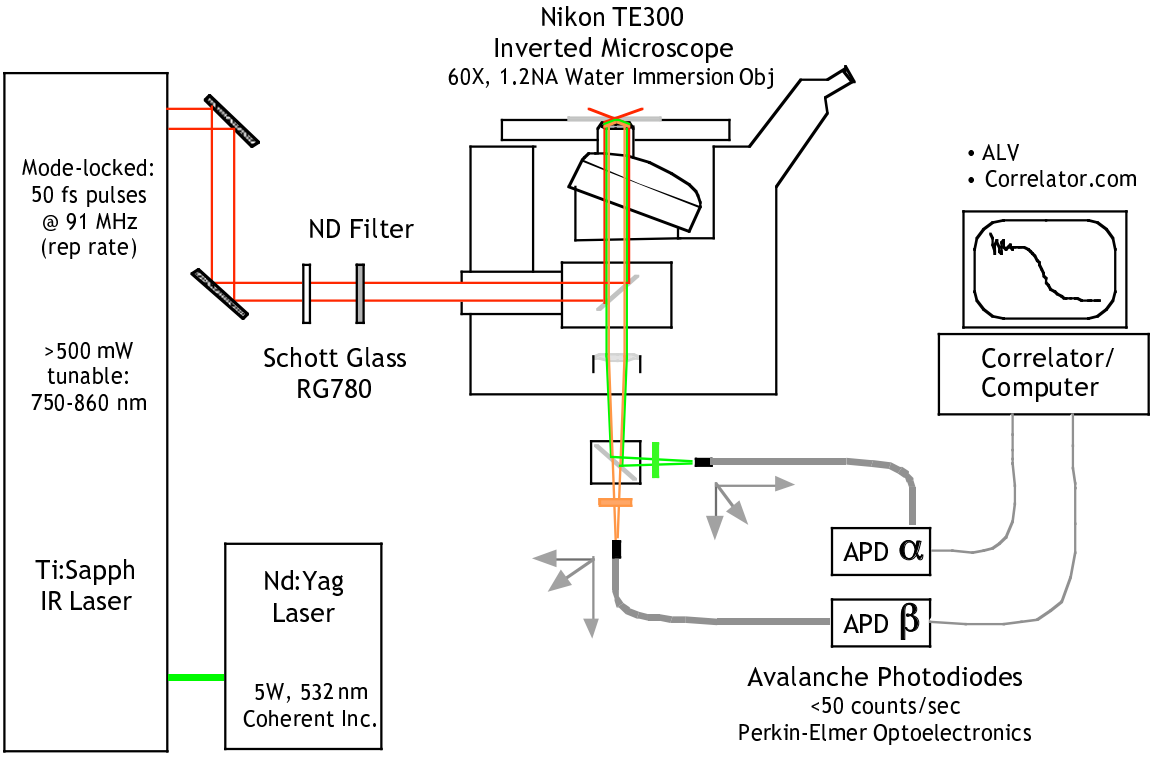

Figure 3.1: **Schematic of the home-built TCFFM apparatus.**

card (Flex01LQ-08; Correlator.com, Bridgewater, NJ) with 8 ns time resolution and multi-time scale (quasi-logarithmic) parallel correlation. Sample positioning was accomplished using a micromotor-driven mechanical stage (Prior Scientific, Rockland MA). 200 μL sample volumes were placed in an 8-well chambered #1.5 coverglass system (Lab-Tek II; Nalge Nunc International, Rochester, NY), held in place by a custom-made stage-adapter plate.

A femtosecond pulsed Ti:Sapph laser was used as an illumination source for two reasons: (1) to ensure a spatially well-defined focal volume via two-photon fluorescence excitation,[53] and (2) to excite fluorophore pairs that normally cannot be excited efficiently using a single laser line in the visible spectrum.[270] Fluorophore pairs could also be excited using a dual laser line excitation scheme;[211,234] however, this can lead to unavoidable chromatic differences in observation volume for each fluorophore and significantly complicate data analysis

The Ti:Sapph laser schematic is shown in Figure 3.2 Photos of the laser sub-assembly and overall cavity are shown in Figs. 3.3 and 3.4, respectively. The Ti:Sapph laser cavity is $\sim$1.5 m, bounded by two outer mirrors: a high reflecting (HR) mirror of 99.99% reflectance and an output coupler (OC) mirror transmits $\sim$1-10% of the cavity laser light. At the core of the laser cavity is a sub-assembly containing a lens that focuses a "pump" excitation laser beam onto a the Ti:Sapph crystal and a set of dichroic mirrors that direct infrared laser fluorescence collected from the crystal towards the outer cavity mirrors. Fluorescence directed from the sub-assembly to the HR mirror is first positively dispersed by a prism, wavelength selected by a computer controlled slit, and then negatively dispersed by a second prism (both prisms are aligned at Brewsters angle relative to the incident beam to minimize

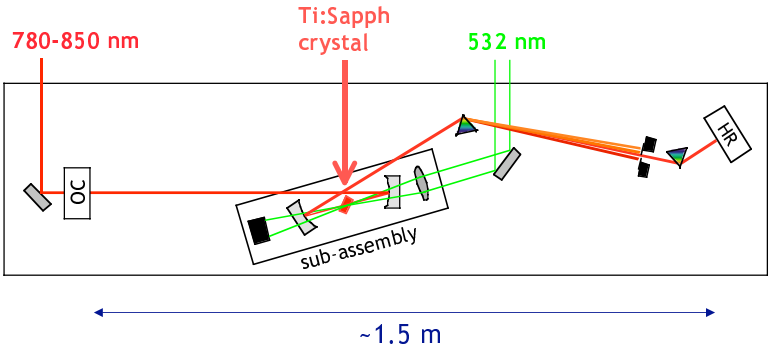

Figure 3.2: **Schematic of the Ti:Sapph laser cavity**. A 5W 532 nm Nd:Yag laser is focused onto a titanium:sapphire crystal, exciting infrared (IR) fluorescence that is collected by highly reflective IR dichroic mirrors, reflected by cavity end mirrors, and focused back onto the crystal to get stimulated emission and lasing. A slit and a pair of prisms is used tune laser wavelength. The set of cavity mirrors used (high reflecting (HR; 99.99% reflecting) and output coupler (OC; 90-99% reflecting) is effective over wavelengths of 780-850 nm. An average laser power of 300 mW is routinely achieved at 820-830 nm. The cavity length is ∼1.5 m, resulting in a repetition rate of 91 MHz between femtosecond pulses upon mode-locking (see text for details).

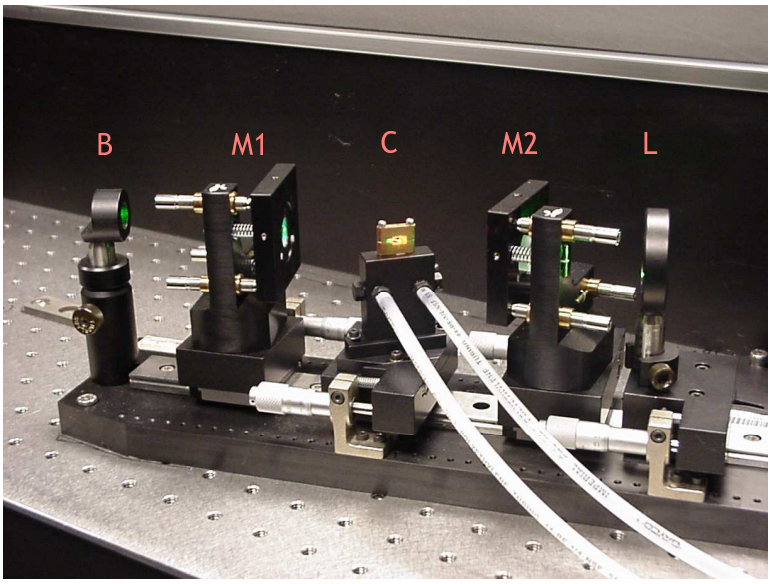

Figure 3.3: **Photo of Ti:Sapph laser sub-assembly**. 532 nm excitation light is focused through a lens (L) and dichroic mirror (M2) onto a water-cooled titanium-doped sapphire crystal (C), through a second dichroic mirror (M1) and beam dumped (B). Infrared fluorescence from the crystal is collected via the two dichroic mirrors and directed to two cavity mirrors (not shown; see Figs. 3.2 and 3.4).

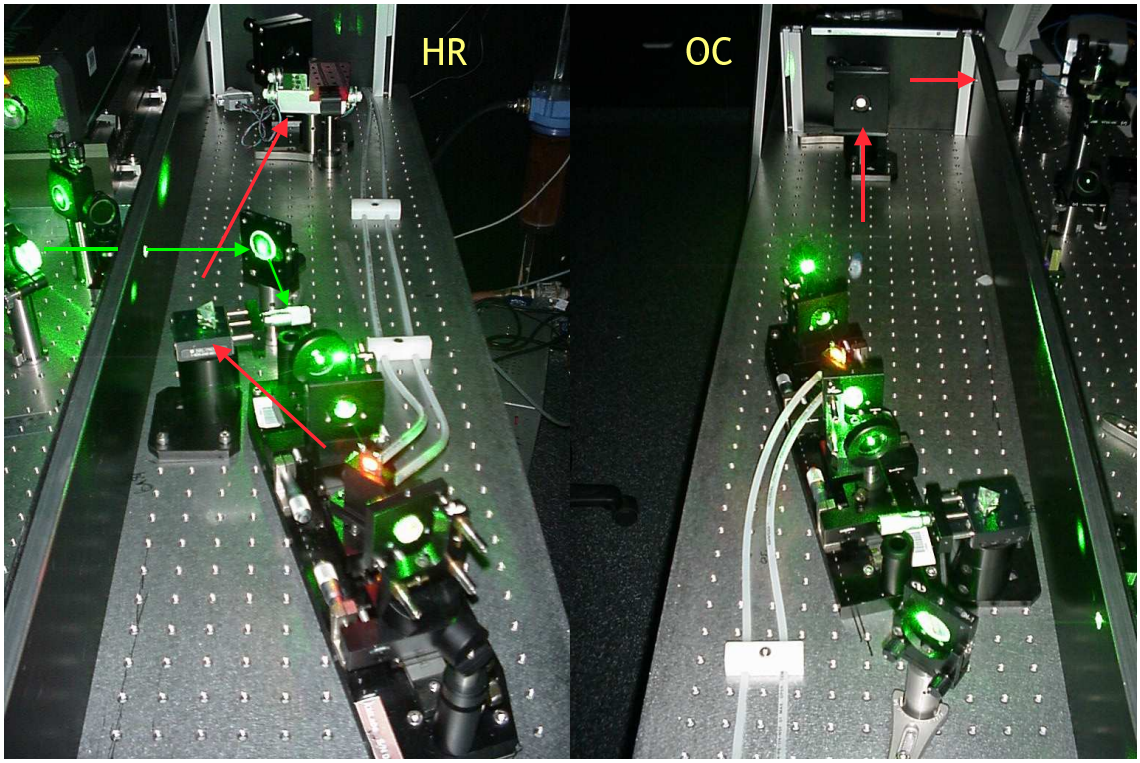

Figure 3.4: **Photo of Ti:Sapph laser cavity**. *Left*, view showing the high reflectance mirror (HR); *right*, view showing the output coupler mirror (OC). Green arrows show path of the 532 nm excitation pump beam. Red arrows show the path of the infrared fluorescence/laser light. (See Figure 3.1)

reflections). Lasing readily results upon proper alignment. Lasing was tuned to 820-830 nm via prism and slit adjustments, with 300 mW of average power routinely achieved. 830nm was selected as a balance between three objectives: (1) maximizing the simultaneous fluorescence of Rhodamine Green, Texas-Red, Green Fluorescent Protein (GFP), and Red Fluorescent Protein (RFP) (see Sec. 3.2.2); (2) autofluorescence and phototoxicity in live cells is relatively low at this wavelength[182] and (3) this wavelength is within the window of what is achievable with the laser cavity optics set available to me (730-850nm). 920 nm may be the optimal compromise between fluorescence excitation of multiple fluorophores and biological sample transparency.

The Ti:Sapph laser was operated in "mode-locked" configuration,[236] established by propagating an intensity perturbation. In practice, I caused this perturbation by jittering the prism closest to the HR mirror. The Ti:Sapph crystal is a non-linear optical medium in which a "Kerr lens" can form in response to such a perturbation. This optical Kerr lens causes the laser beam to self-focus in a manner that phase-aligns the cavity modes of the laser, resulting in spatio-temporal coherence of photons. This coherence is amplified by every pass through the Ti:Sapph crystal until femtosecond pulses with ultra-high photon densities ($\sim 10^{28}$ photons/pulse) result. The temporal pulse width is ultimately limited by the intrinsic dispersion of optical elements in the laser path. Shown in Figure 3.5 are emission spectra of the laser tuned to ∼820 nm and operated in continuous-wave (CW) mode (before intensity perturbation) and in mode-locked (ML) configuration, measured using a fiber-optic coupled spectrophotometer from Ocean Optics Inc. (Dunedin, FL). Using Heisenberg's Uncertainty Principle, $\Delta E \Delta t \sim \hbar$, a 50 fs pulse width for the ML laser was

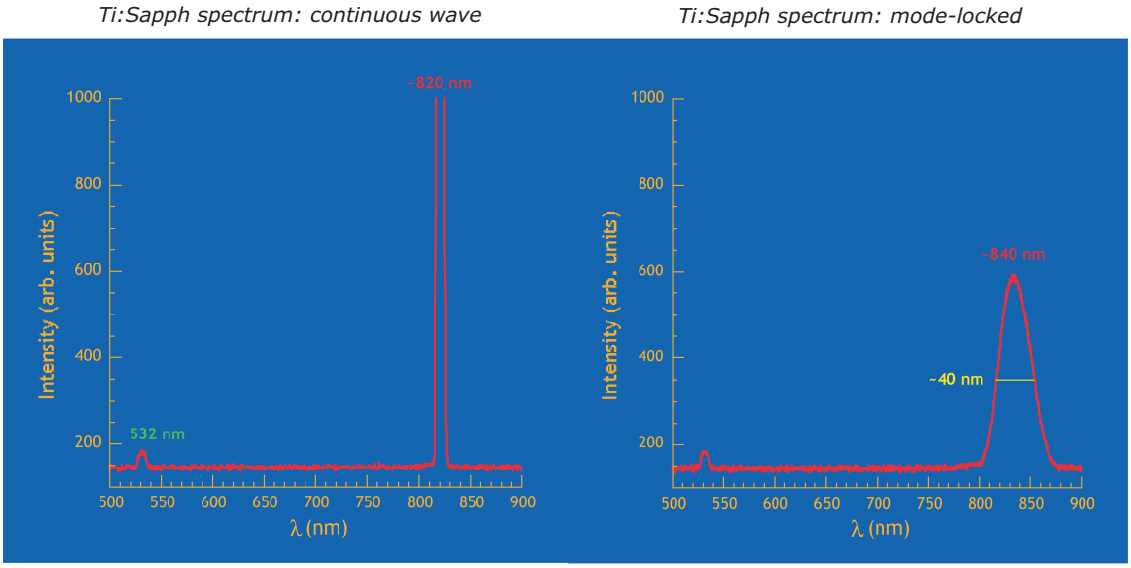

Figure 3.5: **Ti:Sapph laser spectrum**. *Top*, spectrum for laser operated in CW mode. *Bottom*, spectrum for laser in mode-locked configuration.

deduced based on the full-width-half-max of the spectral output. This pulse width refers to the laser *prior* to entering the microscope objective and other dispersive optical elements associated with the microscope. Although not measured directly at the sample,[181] the pulse width after the microscope objective lens is likely ∼100 fs; this values seems independent of the pulse width before the objective (personal communication, Magnus Bengtsson, Spectra Physics Inc., Santa Clara, CA)

3.2.2 Fluorophores and Filters

Rhodamine Green (excitation maximum: 504 nm; emission maximum: 532 nm) and Texas-Red (excitation maximum: 588 nm; emission maximum: 601 nm) were chosen as TCFFM dye pairs based on the optimization of three criteria: (1) the similarity of spectral properties with GFP and RFP, respectively; (2) high quantum yields with limited photo-

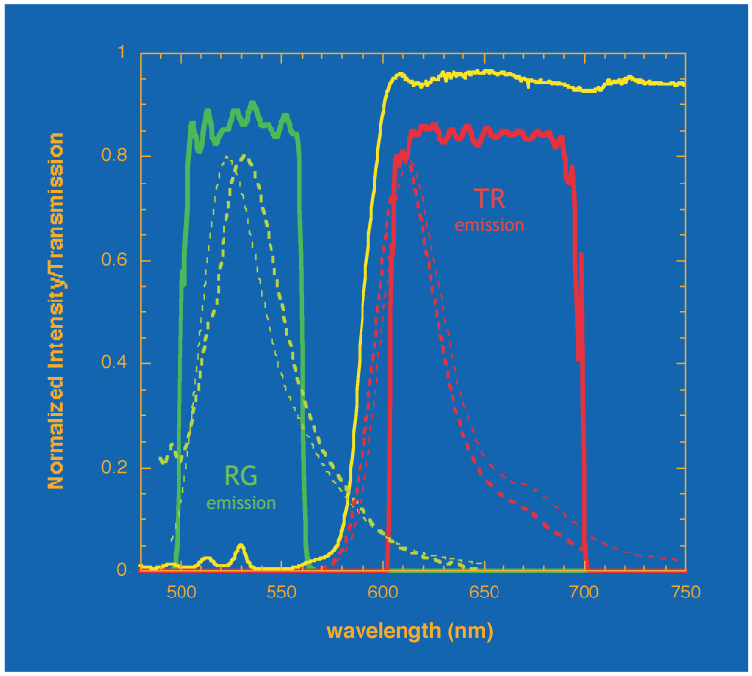

Figure 3.6: **TCFFM secondary filter transmission properties**. Dichroic spectrum is shown in yellow, green channel filter in green, and red channel filter in red. Spectra of Rhodamine Green (RG, green, bold dashed), Texas Red (TR, red, bold dashed), and Rhodamine Green- and Texas Red-labeled oligonucleotides (green thin dashed and red thin dashed, respectively) are overlaid for comparison. Samples were prepared in PBS.

physical dynamics and resistance to photobleaching;[103] and (3) a good separation of emission spectra to minimize cross-fluorescence signal detection.

The secondary dichroic with green/red filters in Figure 3.1, were custom designed in conjunction with Chroma Technologies, Inc. (Brattleboro, VT) to maximize collection and separation of fluorescence from Rhodamine Green and Texas Red (dichroic: 590dxcr; green filter: HQ530-60m; red filter: HQ653-95m). The transmission properties of these optics are shown in Figure 3.6, with the emission spectra of the dyes and dye-labeled oligos overlapped

(see Sec. 3.2.3).

3.2.3 Sample Preparation

Rhodamine 6G (R6G; R-634), Rhodamine Green (RG; R-6107), and Texas Red (TR; T-353) dyes were purchase from Molecular Probes/Invitrogen (Carlsbad, CA). Dual HPLC-PAGE purified fluorophore labeled oligonucleotides (5'-RG-X-d(ACTCATAGATC), 5'-TR-X-d(GATCTATGAGT), and 5'-d(ACTCATAGATC)-X-RG-3', where "X" is an aminohexynoyl spacer) were purchased from Integrated DNA Technologies (Coralville, IA). Oligo samples were prepared as 100 μm stock solutions with NANOpure water (Barnstead International, Dubuque, IA) or Phosphate Buffered Saline (PBS) using low-retention siliconized pipet tips and observed in 8-well LabTek II Chambered Coverslips (see Sec. 3.2.1). Oligo stock solutions were serially diluted by a factor of 3 down to 5 nM (ninth serial dilution).

Green Fluorescent Protein (S65T mutant) was expressed in Escherichia coli BL21(DE3) and purified by nickel chromatography. Red Fluorescent Proteins (dsRed, tdimer2, mRFP) and Green Fluorescent Protein-FKBP and -FRB chimeras (YFP-FKBP, CFP-FRB) were a gift from Kurt Thorn (Bauer Center for Genomics Research, Harvard University, MA). All protein solutions were prepared using PBS.

3.3 Results and Discussion

3.3.1 Focal Volume and Fluorophore Characterization

The TCFFM apparatus was calibrated and characterized using Rhodamine 6G (R6G); Figure 3.7 shows the auto- and cross-correlation function curves for the set-up. Non-linear

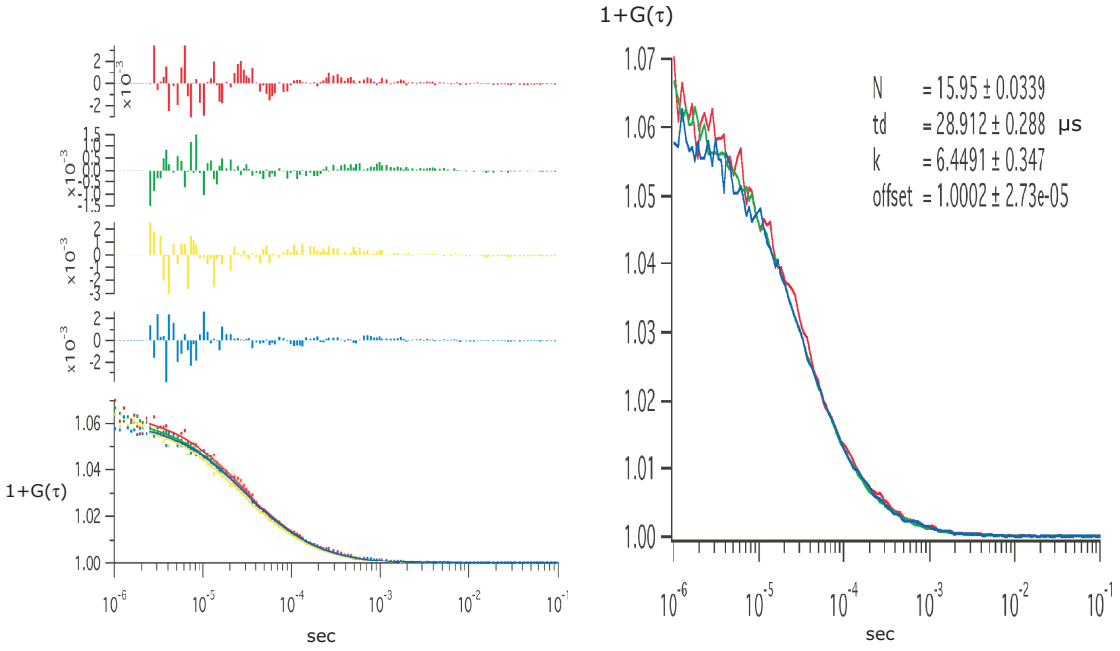

Figure 3.7: **TCFFM calibration using Rhodamine 6G**. *Left,* auto-correlation (red and green) and cross-correlation (yellow and blue) curves and residual plots (top) for a dilute solution of R6G. *Right,* expanded view of the correlation data. Data is an average of three 60 s acquisitions. Non-linear least squares fitting to a diffusion-only model yields an average number of particles per focal volume of 15.95 ± 0.03, a characteristic diffusion time through the focal volume of 28.9 ± 0.3 μs, and a volume characterized by a $\kappa = 6.4 \pm 0.3$ aspect ratio. See text for further details.

least squares fits of the data were performed using IGOR Pro (Wavemetrics Inc., Lake Oswego. OR), assuming a 3-dimensional Gaussian ellipsoidal focal volume and the following diffusion-only model for the correlation functions:

$$G_{xy}(\tau) = \frac{1}{\overline{N}} \left(1 + \tau/\tau_D\right)^{-1} \left(1 + \tau/\kappa^2\tau_D\right)^{-1/2} \tag{3.1}$$

where $\overline{N}$ is the average number of particles in the focal volume, τ_D is the characteristic diffusion time through the focal volume, and κ is the aspect ratio of the ellipsoid volume. The focal volume is given as $V = \left(\frac{\pi}{2}\right)^{3/2} \kappa w_r^3$, where w_r is the characteristic radial (xy-) waist of the ellipsoid. Using the reported diffusion coefficient for R6G of 280 $\mu m^2/s$[212] and the relation of the radial waist to the diffusion coefficient for 2-photon illumination of $w_r = \sqrt{8D\tau_d}$,[170] I computed the effective focal volume to be 0.21 fL.

Figure 3.6 shows sample spectra for Texas Red and Rhodamine Green labeled DNA oligos measured in PBS. Spectra for the fluorescent proteins studied are shown in Figure 3.8 and Table 3.1 summarizes the brightness and bleed-through fluorescence properties for these proteins. Rhodamine Green has a significant fluorescence bleeding of 13.5% into the red filter channel. In contrast, Texas Red is well isolated, with less than 1% bleed-through in the green channel. The S65T mutant of GFP has about half the red fluorescence bleed-through as Rhodamine Green and is nearly 2 times brighter. The red fluorescent protein, dsRed, has comparable properties to S65T, though in the red channel. However, dsRed is known to be non-covalently tetrameric,[27] which is consistent with tdimer2 (a dimer of 2 monomers) and mRFP (monomeric red fluorescent protein) having visibilities that are 1/2 and 1/4 of dsRed, respectively. Homo-FRET processes among monomeric RFP units are known to occur, with the possibility of dsRed monomers existing in a green fluorescence

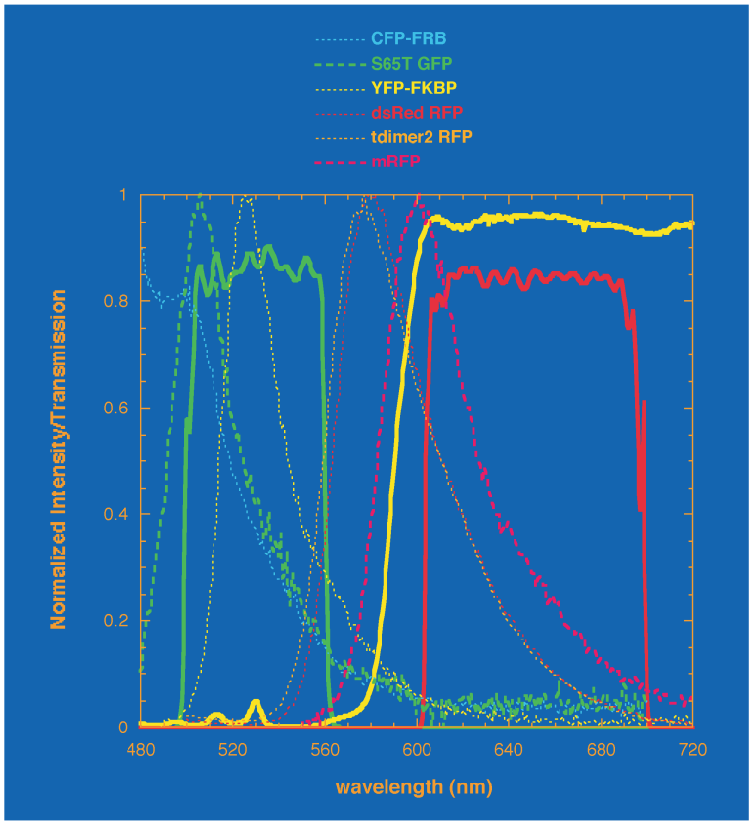

Figure 3.8: **Spectra for fluorescent proteins overlaid with the TCFFM secondary filter transmission properties**. Cf. Figure 3.6. CFP-FRB is a Cyan Fluorescent Protein:FKBP-rapamycin-binding-protein chimera. S65T GFP is the main mutation in the Enhanced Green Fluorescent Protein which is commercially available. YFP-FKBP is a Yellow Fluorescent Protein:FK506-binding-protein chimera. dsRed was one of the first isolated Red Fluorescent Proteins and exists and a homo-tetramer. tdimer2 is a mutated version of dsRed which forms convalent dimers of dsRed monomers. mRFP is a monomeric version of dsRed.

Fluorophore	η (kHz/molecule)	Green bleed-through	Red bleed-through
Rhodamine 6G (R6G)	8.9 (3.2)	–	36%
Rhodamine Green (RG)	1.9	–	13.5%
Texas Red (TR)	3.2	0.56%	–
S65T GFP	3.6	–	5.3%
dsRed RFP	2.5	6.7%	–
tdimer2 RFP	1.1	10.4%	–
mRFP	0.5	2.1%	–
CFP-FRB	0.54	–	9.4%
YFP-FKBP	0.23	–	10.4%

Table 3.1: **Visibility (specific brightness) and bleed-through fluorescence for fluorophores and fluorescent proteins studied with two-photon excitation at 830 nM (average power ∼40 mW)**. Visibility of Rhodamine 6G in the green channel is shown with the value in the red channel in parentheses. See Figure 3.8 for fluorescent protein descriptions

state upon excitation;[79,162,248] this may explain the differences in green channel bleed-through between dsRed, tdimer2, and mRFP. Under two-photon excitation with $\gtrsim$50 mW average power, I have observed unusual anti-correlated cycling of red *and* green fluorescence emission from dsRed samples (data not shown), indicating a complex photocycle. Given this, mRFP is the recommended red fluorescent protein form to use for cellular/protein labeling. Unfortunately, its photic output is relatively low, and tuning of the current RG/TR secondary filter set and/or excitation wavelength will likely be needed for optimal TCFFM experiments using mRFP. Cyan fluorescent protein (CFP) and yellow fluorescent protein (YFP) also have low visibility values, and have about 10% bleed-through fluorescence in the red.

Shown in Figure 3.9 are auto-correlation results for some of the fluorescent proteins in Table 3.1. S65T-GFP and dsRed were quite robust using the current instrument set-up. As mentioned above, however, dsRed is tetrameric and this fact motivated measurements

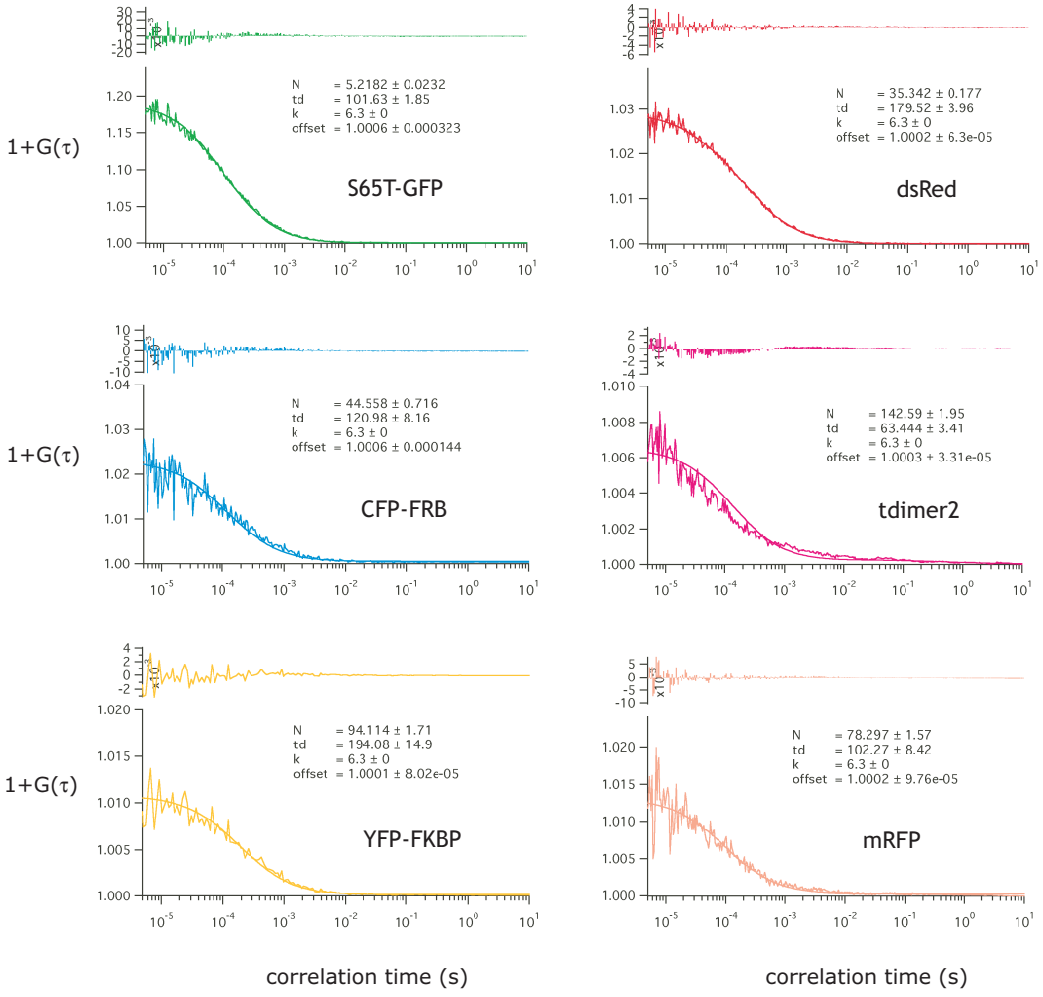

Figure 3.9: **TCFFM auto-correlation curves for fluorescent proteins in Table 3.1**. Auto-correlation data (averages of three 60 s acquisitions) were non-linear least-squares fitted using Eq. 3.1, with N (particle number), τ_D (characteristic time), and a correlation offset as variables. κ (focal volume aspect ratio) was constrained to be 6.3 based on focal volume measurments with R6G (cf. Figure 3.7). Residuals of the fit are shown above the correlation functions curves. S65T-GFP, CFP-FRB, and YFP-FKBP data were measured in the green channel; dsRed, tdimer2, and mRFP data were measured in the red channel.

on tdimer2 and mRFP. tdimer2 yielded correlation data that was consistently difficult to fit using a diffusion-only FFM model, suggesting that monomer-monomer photophysics may be interfering with these measurements. In contrast, mRFP correlation data was fit well with Eq. 3.1, although its low visibility compromised correlation function signal-to-noise. Likewise, the YFP-FKBP and CFP-FRB data were fit well by a diffusion-only model, though the data was noisier due to a low visibility.

To establish the feasibility of TCFFM, I sought to study a model 2-component interacting system with well defined interaction thermodynamics. I settled on using non-complementary DNA oligonucleotides whose association thermodynamics can be reliably predicted and controlled by buffer conditions, notably ionic strength. Below, I present some preliminary qualitative TCFFM data for the association of two non-self-complementary undodecamers, d(ACTCATAGATC) and d(GATCTATGAGT). This sequence pair was designed to minimize self-complementarity, balance purine:pyrimidine base composition, and exhibit a K_d on the order of tens of nM at room temperature in PBS (see below). As explored in Chapter 2, a K_d in the nM range would be appropriate for initial TCFFM studies of association-dissociation thermodynamics.

3.3.2 d(ACTCATAGATC):d(GATCTATGAGT) Association

Using the nucleic acid hybridization prediction program HyTher,[195] I estimated the K_d for the pair d(ACTCATAGATC):d(GATCTATGAGT) in PBS ($[Na^+]$ = 0.16 M, $[Mg^{2+}]$ = 0 M) to be $\sim$ 13 nM at room temperature (23 °C). In Figure 3.10, a schematic of the 3 fluorescently-labeled non-self-complementary strands used in this section are shown. Strands 1:2 and 2:3 are complementary, with strands 2:3 expected to exhibit significant

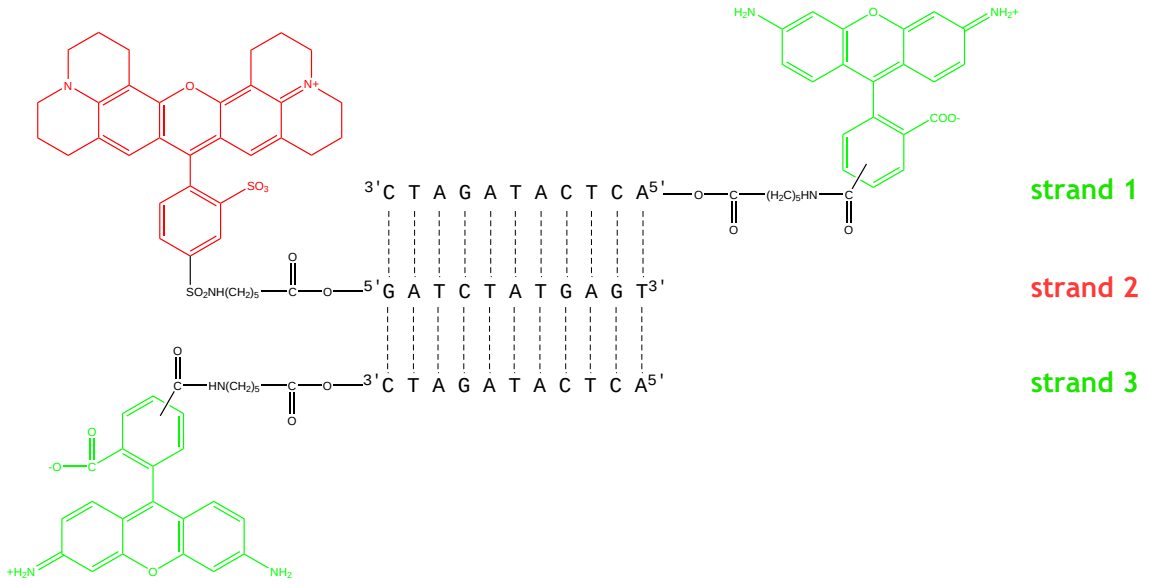

Figure 3.10: **Schematic of the fluorescently labeled DNA oligonucleotide strands studied**.

FRET due to fluorophore proximity. TCFFM correlation results for these strands is show in Figure 3.11. At zero ionic strength, strand 1 and 2 are predicted to not associate, due to charge repulsion of the DNA phosphate backbones of complementary strands. The cross-correlation of green and red channels, $G_{xy}(\tau)$, is expected to be zero and is essentially the case in the experiment (*left*, Figure 3.11). There is a slight non-zero cross-correlation signal that is attributable to ∼14% bleed-through fluorescence of RG into the red channel (cf. Table 3.1). In PBS, strands 1 and 2 are expected to associate, and in Figure 3.11 (*middle*), a significant cross-correlation amplitude can be seen. Strands 2 and 3 also are expected to associate in PBS, although fluorophore labels are expected to undergo FRET. The cross-correlation between these strands is essentially zero (*right*, Figure 3.11), highlighting the compromising effects of FRET on cross-correlation amplitudes that were theorized in Chapter 2, Section 2.5.3. Moreover, the auto-correlation functions are correspondingly higher,

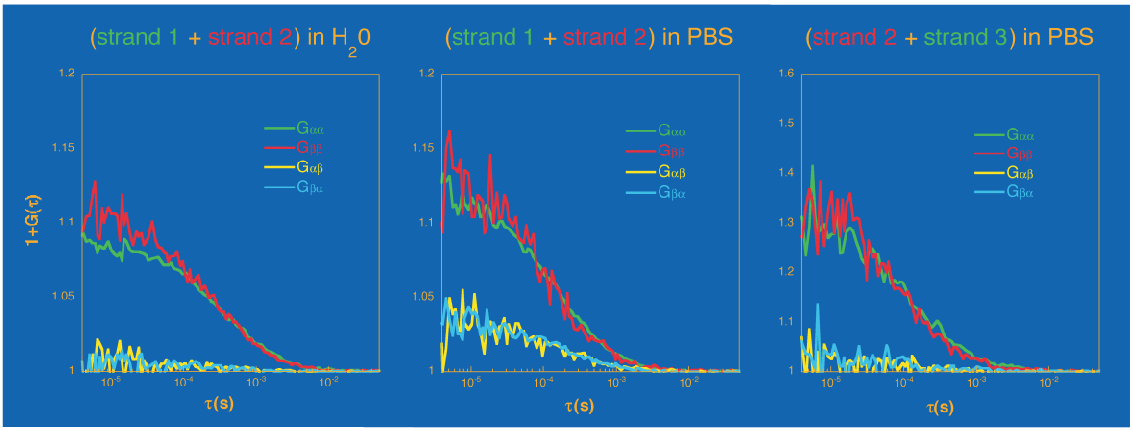

Figure 3.11: **TCFFM results for the fluorescently-labeled d(ACTCATAGATC) : d(GATCTATGAGT) oligos**. See Figure 3.10 for strand definitions. Green and red curves are auto-correlation results from the green channel (RG label) and red channel (TR label), respectively. Cross-correlation curves (green channel × red channel and red channel × green channel) are shown in yellow and cyan; these cross-correlation curves are identical within statistical noise. The final concentration of strands nominally used was 100 nM.

which is also expected in the presence of FRET (cf. Figure 2.7). It should be noted that the total concentration (complexed and free) of strands 1 and 2 was ca. 100 nM, an order of magnitude higher than the predicted K_d for the complex; this shifts the equilibrium towards the formation of a duplex (cf. Section 2.5.3 and Figure 2.7B). In the presence of FRET, cross-correlation amplitudes would be lower, making it appear as if fewer complexes are formed. Returning to the cross-correlation results of strands 1 and 2, the observed cross-correlation amplitude is smaller than would be expected due to the presence of FRET. Even though fluorophores are at opposite ends of the duplex, bulk fluorescence measurements suggest that FRET occurs with an efficiency of ∼25% as shown in Figure 3.12.

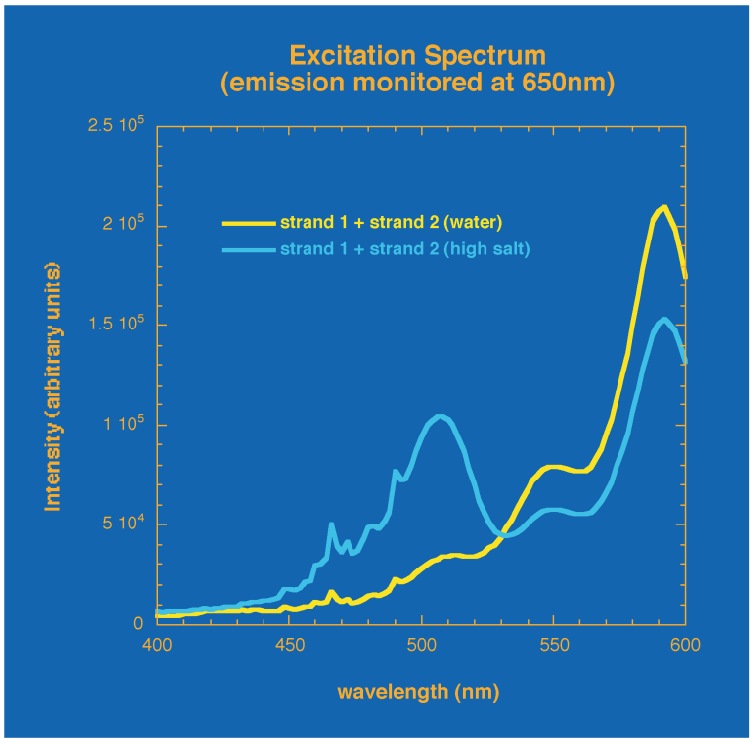

Figure 3.12: **Fluorescence spectra of labeled DNA strands in zero vs. high ionic strength solutions, demonstrating FRET in the complex**. Excitation spectra were taken by monitoring emission at 650 nm and sweeping over excitation wavelengths. Spectra of equimolar strand 1 (5'-RG-d(ACTCATAGATC)) and strand 2 (5'-TR-d(GATCTATGAGT)) in water (zero ionic strength) or in high salt (1.5 NaCl, 0.3 M $MgCl_2$) are shown in yellow or cyan, respectively.

3.3.3 Outlook

The development of a high-precision TCFFM instrument and the pilot qualitative experiments described on non-self-complementary oligonucleotides set the stage for quantitative studies of two-component interacting systems. The effects of FRET, fluorophore bleed-through, and background fluorescence on correlation function data need to be quantified and validated with respect to the theory established in Chapter 2. This is necessary in order to determine particle numbers and thus the K_d for the two interacting components. Below, I outline an approach to determine these particle numbers and the required calibration protocols.

Using Eqs. 2.5 and 2.6, we may express the general TCFFM correlation function as follows:

$$G_{xy}(\tau) = \sum_{i}^{m}\sum_{j}^{m} \frac{\eta_i^x \eta_j^y \sqrt{\overline{N}_i \overline{N}_j}}{\left(\sum_i^m \eta_i^x \overline{N}_i + \overline{b^x}\right)\left(\sum_j^m \eta_j^y \overline{N}_j + \overline{b^y}\right)} \cdot h_{ij}(\tau) \tag{3.2}$$

where i indexes a component of an m-component system, η_i^x is the specific brightness (counts per sec / molecule) in channel x or component i, $\overline{N}_i$ is the average number of particles of component i, $\overline{b^x}$ is the background fluorescence registered in channel x, and $h_{ij}(\tau)$ is the component correlation function (see Eq. 2.6 and Section 2.7). Although it is ideally more robust to fit over a range of time-lags, τ, $h_{ij}(\tau)$ typically is not easily separable from the double summation term unless the diffusion coefficient for all components in the system are identical (cf. Eq. 2.20 and Section 2.7).

For the bimolecular reaction, $A + B \underset{k_b}{\overset{k_a}{\rightleftharpoons}} C$, with 3 components of comparable

diffusion coefficients, Eq. 3.2 may be expressed more specifically as:

$$G_{xy}(\tau) = \sum_{i}^{3}\sum_{j}^{3} \frac{\eta_i^x \eta_j^y \left[\delta_{ij}\overline{N}_i + \gamma\left(\sum_k^3 \overline{N}_k^{-1}\right)^{-1}\left(e^{\tau/\tau_{reac}} - 1\right)\right]}{\left(\sum_i^3 \eta_i^x \overline{N}_i + \overline{b^x}\right)\left(\sum_j^3 \eta_j^y \overline{N}_j + \overline{b^y}\right)} \times \left(1 + \frac{\tau}{\tau_{diff}}\right)^{-1}\left(1 + \frac{\tau}{\kappa^2 \tau_{diff}}\right)^{-1/2} \tag{3.3}$$

where I have assumed a 3-dimensional Gaussian ellipsoidal focal volume, γ is +1 for reactants, A and B (component 1 and 2 respectively), and -1 for the complex, C (component 3), τ_{reac} is the characteristic time for reaction, τ_{diff} is the characteristic time for diffusion, and κ is the focal volume aspect ratio (see Eq. 2.20). I assume κ has been determined independently and previously, since it is specific to the TCFFM apparatus. Eq. 3.3 may be used to fit correlation function data to simultaneously to determine τ_{reac}, τ_{diff}, $\overline{N}_A$, $\overline{N}_B$, and $\overline{N}_C$ along with the set of calibration parameters η_A^x, η_A^y, η_B^x, η_B^y, η_C^x, η_C^y, $\overline{b^x}$, and $\overline{b^y}$. This amounts to 8 calibration unknowns for a given TCFFM setup (I assume background fluorescence in this case is not sample specific) and 5 experimental unknowns, or a total of 13 unknowns for simultaneous fitting. Each correlation function dataset can provide an equivalent of $4p$ equalities in which to satisfy (where p is the number of τ-lag time points acquired for the correlation function): two auto-correlation functions, $G_{xx}(\tau)$ and $G_{yy}(\tau)$, and two cross-correlation functions, $G_{xy}(\tau)$ and $G_{yx}(\tau)$. A direct global fit using Eq. 3.3 may be possible given the amount of data/equalities ($4p \cdot n$) per dataset (n) relative to unknowns ($8 + 5n$) However, given that the data points per correlation function, p, are derived from the same parent correlation function equation, they may be highly correlated and thus compromise a robust simultaneous fit over the high-dimensional space of unknown parameters, especially in the presence of statistical noise. A more thorough analysis of such

a global fitting strategy requires further consideration and experimental testing. Perhaps a more tractable solution would be to reduce the number of unknown parameters per dataset by measuring them independently. The simplified relation relating correlation function amplitudes to the parameters of particle number, bleed-through, and background fluorescence obtained in the $\tau = 0$ limit may also be used instead:

$$G_{xy}(0_+) = \sum_i^3 \frac{\eta_i^x \eta_i^y \overline{N}_i}{\left(\sum_i^3 \eta_i^x \overline{N}_i + \overline{b^x}\right)\left(\sum_i^3 \eta_i^y \overline{N}_i + \overline{b^y}\right)} \tag{3.4}$$

(Eq. 3.4 must be used instead of Eq. 3.3 in cases where $h_{ij}(\tau)$ is not separable from the double sum in Eq. 3.2.) In this case, the need to fit τ_{reac} and τ_{diff} has been circumvented, though at the cost of $p \to 1$ data points per correlation function dataset.

The number of unknowns for a given dataset (13 for Eq. 3.3 and 11 for Eq. 3.4) may be reduced immediately by 2 by simply measuring the steady-state background fluorescence, $\overline{b^x}$ and $\overline{b^y}$, under data-acquisition conditions without the presence of A, B, or C (e.g., using a buffer blank). The calibration variables, η_A^x, η_A^y, η_B^x and η_B^y, may then be determined by separate correlation function measurements of single-species-only samples over a concentration dilution series by globally fitting to the following set of equations:

$$\begin{aligned}
G_{xx}^{1-species,\,i}(\tau) &= \frac{\left(\eta_i^x\right)^2 \overline{N}_i}{\left(\eta_i^x \overline{N}_i + \underline{\overline{b^x}}\right)^2} \cdot H(\tau_{diff}, \tau_{reac}, \underline{\kappa}, \tau) \\
G_{yy}^{1-species,\,i}(\tau) &= \frac{\left(\eta_i^y\right)^2 \overline{N}_i}{\left(\eta_i^y \overline{N}_i + \underline{\overline{b^y}}\right)^2} \cdot H(\tau_{diff}, \tau_{reac}, \underline{\kappa}, \tau) \\
G_{xy,\,yx}^{1-species,\,i}(\tau) &= \frac{\eta_i^x \eta_i^y \overline{N}_i}{\left(\eta_i^x \overline{N}_i + \underline{\overline{b^x}}\right)\left(\eta_i^y \overline{N}_i + \underline{\overline{b^y}}\right)} \cdot H(\tau_{diff}, \tau_{reac}, \underline{\kappa}, \tau)
\end{aligned} \tag{3.5}$$

where the underscore, $\underline{\cdot}$, is use to denote that a variables is known or has been determined independently and $H(\tau_{diff}, \tau_{reac}, \kappa, \tau) \triangleq \left(1 + \frac{\tau}{\tau_{diff}}\right)^{-1} \left(1 + \frac{\tau}{\kappa^2 \tau_{diff}}\right)^{-1/2}$. For a dilution series with q samples and p τ-lag time points, 3 parameters remain constant over the con-

centration range (τ_{diff}, η_i^x, and η_i^y), $2q$ parameters are variable (τ_{reac} and $\overline{N}_i$), and $4p \cdot q$ correlation function data points are to be used for parameter fitting (2 auto-correlation and 2 cross-correlation functions). Considering a worst-case scenario for the moment, with $p = 1$ (e.g., treating only correlation function amplitudes) and access to only one cross-correlation function, there are $3 + 2q$ unknowns and $3q$ equality relations. This sets a conservative minimum of $q_{min} = 3$ number of dilution datasets that would be necessary for estimating the bleed-through parameters, η_A^x, η_A^y, η_B^x and η_B^y. If both forward and reverse cross-correlation data are available, this minimum would drop to $q_{min} \sim 2$. Of course, this aforementioned assessment assumes statistically noise-free data. As discussed in Chapter 2, each correlation function time point has an associated error dependent upon acquisition time, visibility, lagtime, etc. (cf. 2.19 and Saffarian and Elson (2003)[219]). A more thorough analysis of the effects of statistical noise on parameter estimation ability would be beneficial. Nonetheless, using p τ-lag time points should help leverage the statistical uncertainty associated with each data point with an over-determined number of correlation function equalities.

The estimation of bleed-through parameters, η_A^x, η_A^y, η_B^x and η_B^y may be further constrained if the dilution factors for the series of samples is known. Substituting $\overline{N}_i \rightarrow \underline{\upsilon_q}\overline{N}_i$, where υ_q is the experimental dilution factor for sample dilution q:

$$
\begin{aligned}
G_{xx}^{1-species,\,i}(\tau) &= \frac{\left(\eta_i^x\right)^2 \left(\underline{\upsilon_q}\overline{N}_i\right)}{\left(\eta_i^x \left(\underline{\upsilon_q}\overline{N}_i\right) + \overline{\underline{b^x}}\right)^2} \cdot H(\tau_{diff}, \tau_{reac}, \underline{\kappa}\,\tau) \\
G_{yy}^{1-species,\,i}(\tau) &= \frac{\left(\eta_i^y\right)^2 \left(\underline{\upsilon_q}\overline{N}_i\right)}{\left(\eta_i^y \left(\underline{\upsilon_q}\overline{N}_i\right) + \overline{\underline{b^y}}\right)^2} \cdot H(\tau_{diff}, \tau_{reac}, \underline{\kappa}, \tau) \\
G_{xy,\,yx}^{1-species,\,i}(\tau) &= \frac{\eta_i^x \eta_i^y \left(\underline{\upsilon_q}\overline{N}_i\right)}{\left(\eta_i^x \left(\underline{\upsilon_q}\overline{N}_i\right) + \overline{\underline{b^x}}\right)\left(\eta_i^y \left(\underline{\upsilon_q}\overline{N}_i\right) + \overline{\underline{b^y}}\right)} \cdot H(\tau_{diff}, \tau_{reac}, \underline{\kappa}, \tau) \qquad (3.6)
\end{aligned}
$$

In this case, 4 parameters remain constant over the concentration range (τ_{diff}, η_i^x, η_i^y, and $\overline{N}_i$) and only q parameters are variable (τ_{reac}), reducing the number of unknowns by $q-1$ compared to Eq. 3.5.

Unfortunately, for the DNA oligonucleotide experiments I describe above, I have found estimating bleed-through parameters using Eq. 3.6 to be difficult due to experimentally uncertainties in υ_q. The polystyrene walls of the Nunc chambered-coverslips used led to significant and unpredictable adherance problems with the labeled DNA oligonucleotides at concentrations below 1 μM. Future quantitative studies may attempt an estimation of bleed-through parameters using the more general Eq. 3.5. Alternatively, studies may use sample chambers with proven low-retention properties such as those I have subsequently identified (e.g., AssayChip, MicroCarrier microplates) by Evotec Technologies Inc. (Woburn, MA).

After determining the bleed-through parameters for each single species, 2 remaining calibration parameters remain: η_C^x and η_C^y, for the complex. These may be computed using Eq. 2.29, and if FRET is present, the energy transfer efficiency, E, may be determined by standard means.[109,145] Alternatively, these may be measured as detailed above, if doubly labeled complex can be exclusively formed and studied (e.g., labeled half-length oligos with excess unlabeled, complementary full length oligo).

Having determined all the necessary calibration parameters, the absolute particle numbers for A, B, and complex C may be deduced given an set of correlation function amplitudes by fitting with Eq. 3.4; in this case, we have essentially the same number of unknowns as correlation function equalities. The precision of such a fit is limited by the quality of estimating the intercept correlation function amplitude, though this can be

Acidic "RR" chain
—ITI RAAFLEK ENTALRT **R**VAEL**R**K **R**VGRC**R**NI—

Basic "EE" chain
—ITI RAAFLEK ENTALRT **E**VAEL**E**K **E**VGRC**E**NI—

Figure 3.13: **Proposed heterodimeric leucine zipper for *in vitro* and *in vivo* TCFFM studies**. Derived from the chicken vitellogenin binding protein (VBP), this leucine zipper preferentially heterodimerizes with a $K_d \sim 7$ nM while homodimerization is weak ($K_d \sim 10 - 100$ mM).[135,143,144] GFP fusions to these zippers have been expressed successfully in mammalian cells and appear to interact minimally to cytoplasmic components. Fluorescent proteins may be fused to either side of the zipper motifs.

improved by averaging multiple measurements for the same sample. The classic dissociation constant for the bimolecular reaction is then given by:

$$K_d = \frac{\overline{N}_A \overline{N}_B}{\overline{N}_C} (n_{avo} V)^{-1} \tag{3.7}$$

where n_{avo} is Avogadro's number and V is the focal volume. Importantly, the K_d can be determined from a *single* sample, without the need for a titration series.[138,173,199,208,226,234,249] In this way, TCFFM offers a unique methodological approach for measuring equilibrium constants.

Ultimately, this methodology should be developed and applied to quantify bimolecular interactions of proteins in live cells. Two model interacting systems that I believe may be worth pursuing towards this end are: (1) FKBP (FK506 binding protein) and FRB (FKBP-rapamycin binding domain) and (2) heterodimeric leucine zippers. FKBP and FRB bind over a range of nanomolar affinities depending on the concentration of the bifunctional ligand rapamycin.[7] The heterodimeric leucine zipper studied extensively by Charles Vinson's lab at the NIH and shown in Figure 3.13 also has affinities in the nanomolar range that can be tuned by ionic strength.[135,143,144] Both systems can be expressed as fusion

proteins to fluorescent proteins and I have been successful in cloning and expressing fluorescent chimeras (CFP:YFP or S65T-GFP:mRFP fluorescent protein pairs) for both these systems in bacterial, yeast, and mammalian tissue culture cells. This sets the stage for both *in vitro* biochemical validation experiments and *in vivo* measurements using TCFFM. A comparison of *in vitro* conditions and the milieu of a living cell on the thermodynamics of such interacting systems would greatly enhance our understanding of the physico-chemical basis for cellular metabolism and intracellular signaling.

Chapter 4

Simulations

A version of this chapter has been accepted for publication in the *Journal of Physical Chemistry-B* by James A. Dix, Erik F. Y. Hom and Alan S. Verkman as:

"Fluorescence Correlation Spectroscopy Simulations for Analysis of Photophysical Phenomena and Molecular Interactions: A Molecular Dynamics/Monte-Carlo Approach."

4.1 Abstract

We developed a general approach to simulate fluorescence fluctuation microscopy (FFM) experimental data. In FFM, fluctuations in detected fluorescence, $\delta F(t)$, are expressed as time-correlation functions, $G(\tau)$, and photon-count histograms, $P(k;\Delta T)$. We computed $G(\tau)$ and $P(k;\Delta T)$ for binary component diffusing systems with arbitrary geometry, photophysics, diffusion, and macromolecular interactions. These $G(\tau)$ and $P(k;\Delta T)$ were derived from $\delta F(t)$ traces generated by Brownian dynamics simulation of single molecule trajectories followed by Monte-Carlo simulation of fluorophore excitation and detection statistics. Simulations were validated by comparing analytical and simulated $G(\tau)$ and $P(k;\Delta T)$ of non-interacting diffusing fluorophores in a three-dimensional Gaussian excitation and detection volume. Inclusion of photobleaching and triplet-state relaxation produced significant changes in $G(\tau)$ and $P(k;\Delta T)$. The method was applied to study macromolecular interactions, including fluorophore binding to an immobile matrix, fluorophore diffusion in crowded media, cross-correlation analysis of interacting fluorophores, and anomalous sub- and super-diffusion. The computational method developed here is generally applicable for simulating FFM measurements on systems complicated by fluorophore interactions, macromolecular crowding, and experimental protocols for which $G(\tau)$ and $P(k;\Delta T)$ cannot be computed analytically.

4.2 Introduction

Fluorescence fluctuation microscopy (FFM) is being applied increasingly to study diffusive phenomena and macromolecular interactions in complex systems, including aqueous

and membranous compartments in living cells.[5,257,266] Typically, fluorescence intensity in a detection volume, $F(t)$, is monitored over time. Fluctuations in $F(t)$ are produced by kinetic processes that alter the number and/or intrinsic fluorescence of molecules in the detection volume. The fluorescence time course thus contains information about molecular diffusion and/or photophysical and chemical dynamics. The FFM approach has been used most widely to measure fluorophore diffusion coefficients and concentrations,[66,161] though many other biologically-relevant phenomena are in principal measurable including fluorophore rotation,[3,133] surface adsorption dynamics,[243] and fluorophore binding interactions.[20,107,116]

Although all information in an FFM measurement is contained in $F(t)$, derived functions are computed to extract useful information from $F(t)$. The commonly used derived functions are the time-correlation function $G(\tau)$,[65,161] and the photon-count histogram, $P(k;\Delta T)$.[32,132] where k represents the number of photons in a time interval ΔT. $G(\tau)$ characterizes the temporal memory of the fluorescence signal, while $P(k;\Delta T)$ characterizes the static distribution of fluorescence intensities over a specified time interval. Analytical expressions for $G(\tau)$ have been obtained for a few simple situations involving simple Brownian diffusion of fluorophores with a Gaussian detection volume with and without triplet-state photophysics[264] and fluorophore binding to a relatively immobile substrate.[208] Deviations from these analytical $G(\tau)$ cases have been noted or are anticipated for anomalous diffusion,[56,100,231] confined diffusion,[82] non-Gaussian detection volumes,[13,104] large diffusing particles compared to detection volume,[241] fluorophore photobleaching,[6,60,265] and Förster resonance energy transfer.[107,267] Expressions for $P(k;\Delta T)$ have been obtained for Brownian fluorophore diffusion.[32,131] The influence of triplet-state photophysics and other non-ideal

conditions mentioned above on $P(k;\Delta T)$, however, has not been investigated.

Measurements in cellular systems are complicated by geometric and phase heterogeneities that produce confined diffusion within organelles and/or macromolecular crowding. Molecular crowding by fixed and mobile obstacles can dramatically alter particle diffusion and interactions through excluded volume effects and spatial organization.[1,95,175,273] We have used photobleaching methods extensively to characterize the diffusion of macromolecules in cellular compartments,[256] and have developed analytical and computational methods to deal with complex diffusive behavior[192] and organellar geometry.[49,185] In principle, FFM measurements contain greater information content about diffusive and reaction dynamics than fluorescence recovery after photobleaching, in part because single molecule events are recorded over many orders of magnitude of time.

We establish a general approach to simulate FFM data for complex systems. The motivation for this work was the need to extract quantitative information on diffusion and binding from FFM measurements on living cells. The computational method involves Brownian dynamics simulation of particle trajectories followed by Monte-Carlo simulation of fluorescence statistics. The $G(\tau)$ and $P(k;\Delta T)$ derived functions are computed from the simulated $F(t)$. The simulation approach was validated and applied to examine the effect of photophysical phenomena and intermolecular interactions on $G(\tau)$ and $P(k;\Delta T)$.

4.3 Methods

4.3.1 Overview

The simulation of an FFM measurement was conducted in 3 stages: (a) generation of molecular trajectories; (b) generation of detected fluorescence time course, $F(t)$, based on the molecular trajectories; and (c) computation of $G(\tau)$ and $P(k;\Delta T)$ from $F(t)$ (Figure 4.1 A and B). Computations for each stage were handled independently of the other stages. Molecular trajectories were generated by Brownian dynamics simulations using the GROMACS molecular dynamics package.[157] The trajectories were filtered through a fluorescence statistics module to generate $F(t)$, which was stored efficiently as a list of photon arrival times. $F(t)$ was processed to generate $G(\tau)$and $P(k;\Delta T)$ using an algorithm based on the photon arrival times. As discussed below, the simulations utilized different timescale intervals: dt, for the Brownian dynamics time step; δt, for the time interval over which fluorescence is calculated from the molecular trajectories to generate $F(t)$; and Δt, for the minimum bin time used for the generation of $G(\tau)$. In general, $dt \leq \delta t \leq \Delta t$, where δt and Δt are integer multiples of dt.

4.3.2 Brownian dynamics simulations

A system of molecules evolving by Brownian dynamics in an isotropic highly-damping hydrodynamic fluid is described by the modified Langevin equation: $d\mathbf{r}_i/dt = \mathbf{F}_i/\gamma_i + \delta_i$ where $\mathbf{r}_i$ is the position of molecule i, $\mathbf{F}_i$ is the force acting on the molecule, γ_i is the friction coefficient of the molecule in the hydrodynamic fluid, and δ_i is a randomly varying force.[30] This equation was integrated using the GROMACS package[157] to obtain: $d\mathbf{r}_i =$

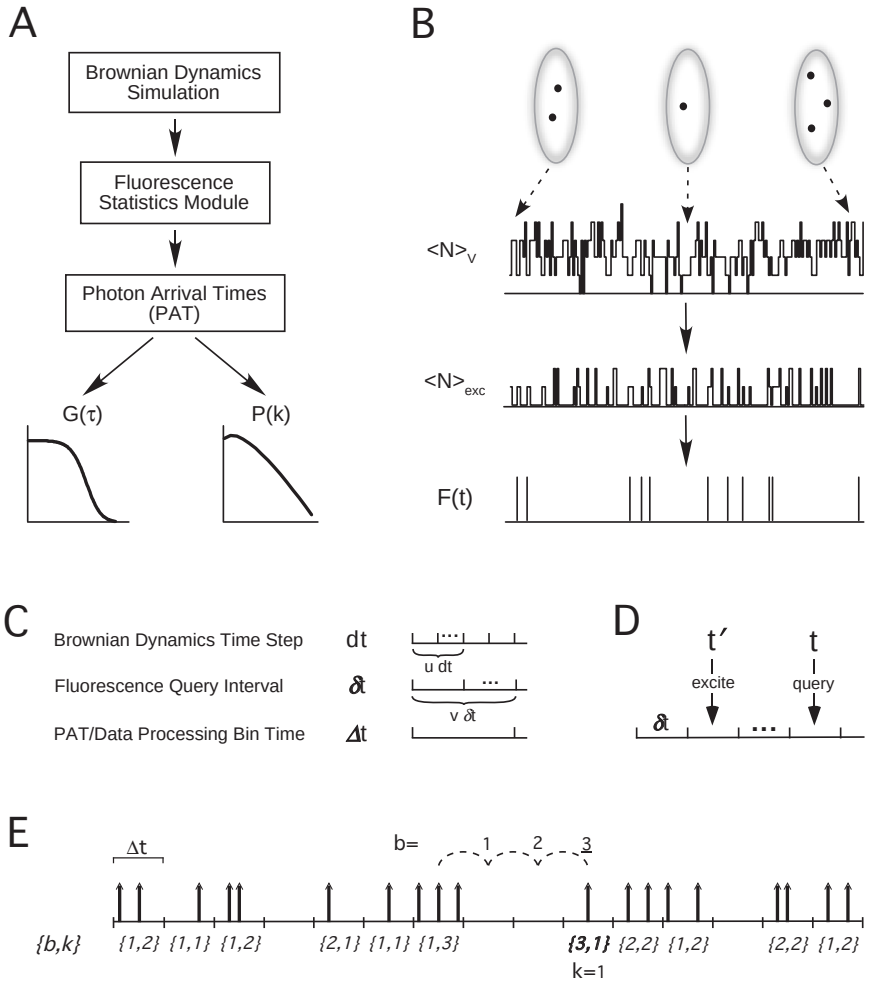

Figure 4.1: **Simulation method**. *(A)* Simulations were done in three steps: computation of Brownian dynamics trajectories using GROMACS software; computation of fluorescence time courses using custom software; and computation of correlation functions and photon count histograms from photon arrival times. *(B)* Brownian dynamics trajectories were generated to give coordinates of a collection of molecules in a periodic box. The number of molecules within a sub-volume of the box at each time, N_V, was computed. A fraction of these molecules, N_{ex}, were excited, and a fraction of the excited molecules emitted photons, generating a fluorescence time course, *F(t)* and photon count histogram, *P(k)*. *(C)* key diagramming the different time step intervals used in the simulation and data analysis. *(D)* key diagraming the relationship between the excitation time t' and query time, in units of the fluorescence query time interval, δt. *(E)* Photon arrival time (PAT) format. Given a user defined time bin, Δt, fluorescence photon counts are stored as a data pair: the first element is the number of empty bins, b, separating bins containing photons, and the second element is the number of photons, k, within the latter bin. Shown in the figure is the entry *(3,1)*. The dashed lines demonstrate that $b = 3$ and the single photon at the end of the dashed lines indicates $k = 1$, forming the entry *(3,1)*.

$(\mathbf{F}_i/\gamma_i)\,dt+\sqrt{2k_BT\,(dt)\,/\gamma_i\delta_0}$, where k_B is Boltzmann's constant, T is absolute temperature, dt is the simulation time step, and δ_0 is a Gaussian-distributed random number with average zero and standard deviation 1. The uniform random number generator in GROMACS was replaced by the program *ran2* of Press *et al.* (1996)[203] (with a random number generation period of $\sim 10^{18}$), and the Gaussian transformation was replaced by the program *gasdev* of Press *et al.* (1992a).[202] The GROMACS-parameterized friction coefficient, γ, was calibrated by simulating a system of identical spherical particles of known mass and radius a, and comparing the diffusion coefficient from the simulation, $D_{sim} \triangleq \langle r^2 \rangle /6t$, with the diffusion coefficient calculated from the Stokes-Einstein equation, $D_{SE} \triangleq k_BT/6\pi\eta a$. The friction coefficient varied with mass of the particle.

Intermolecular forces between the atoms i and j, $\mathbf{F}_{ij}$, were estimated by Lennard-Jones potentials: $\mathbf{F}_{ij}(r_{ij}) \triangleq A_{ij}/r_{ij}^{12} - C_{ij}/r_{ij}^{6}$, where r_{ij} is the distance between atoms i and j, and A_{ij} and C_{ij} are particle-specific coefficients governing the strength of the interaction. Electrostatic interactions were ignored. For most simulations reported here, $C_{ij} = 0$, yielding a collection of Lennard-Jones repulsive spheres. For crowding simulations, the repulsion was made softer by adding terms with $C_{ij} < 0$. For specified A_{ii} and C_{ii}, the effective length of the potential (and thus the effective radius of the particle) was operationally defined as the distance at which the potential reached k_BT. To simulate binding of a fluorophore to a large immobile object, the spatial coordinates of the fluorophore were frozen for a specified length of time. Whether binding occurs and the length of time remaining bound were specified in a Monte Carlo fashion with constant probability characterized by two time constants, τ_{on} and τ_{off}; these correspond to the reciprocal pseudo-first-order forward and reverse rate constant

for binding, respectively.

In a typical simulation, the trajectory of 1000 molecules, whose initial positions were chosen at random, was computed in a $10 \times 10 \times 10$ μm box with periodic boundary conditions and no pressure coupling (equivalent concentration 1.7 nM). All simulations were run at 300 °K. The system was typically equilibrated by a run of 3 s, followed by a production run of 1 s. The time step was set to 1-200 ns and chose to be the smallest value yielding a steady potential energy throughout the simulation, without large energy spikes. The GROMACS software was compiled and run on 2.8 MHz Pentium 4 computer running Linux emulation software on Windows XP. Dynamics for low particle concentrations were generated at a rate of $\sim 2 \times 10^6$ steps/hr for a 2.8 MHz Pentium 4 machine. Simulations at high particle concentrations were run on the Xeon cluster at the National Center for Supercomputer Applications at the University of Illinois, Urbana-Champaign.

4.3.3 Fluorescence statistics

$F(t)$was calculated from the Brownian dynamics trajectories according to:

$$F(t) = \sum_{i=1}^{N} \left[\int_{t'}^{t} p_{ex}(\mathbf{r}_i^{'}, \omega_i^{'}; t^{'}) \cdot p_{ph}(\mathbf{r}_i, \omega_i; t | \mathbf{r}_i^{'}, \omega_i^{'}; t^{'}) \cdot p_{em}(\mathbf{r}_i, \omega_i; t) \cdot Q_{det}(\omega_i)\, \delta t^{'} \right] \qquad (4.1)$$

where N is the number of molecules; $p_{ex}(\mathbf{r}_i^{'}, \omega_i^{'}; t^{'})$ is the probability that molecule i at position $\mathbf{r}_i^{'}$ with orientation $\omega_i^{'}$ is excited at time, $t^{'}$; $p_{ph}(\mathbf{r}_i, \omega_i; t | \mathbf{r}_i^{'}, \omega_i^{'}; t^{'})$ is the conditional probability that a molecule excited at time $t^{'}$ undergoes a photophysical conversion by a later time t; $p_{em}(\mathbf{r}_i, \omega_i; t)$ is the probability that a molecule subsequently emits a photon; and $Q_{det}(\omega_i)$ is the quantum yield of detecting emitted photons from a molecule in orientation ω_i (assuming negligible time to detection). For the simulations described here, the quantum

yield of photon detection will be assumed to be independent of the polarization of emitted photons and thus molecular orientation: $Q_{det}(\omega_i) \sim Q_{det}$. The bracketed integral in Eq. 4.1 is computed in units of δt, the fundamental fluorescence query interval. Each of the conditional probability terms as used in the simulations is defined explicitly below. Generation of the fluorescence trace, $F(t)$, and calculations of $G(\tau)$ and $P(k;\Delta T)$ were implemented in Compaq Visual FORTRAN 90 (source code available from J. Dix).

4.3.3.1 Molecular excitation

The probability molecule i is excited at a time $t^{'}$ can be expressed as:

$$p_{ex}(\mathbf{r}_i^{'}, \omega_i^{'}; t^{'}) = p_{S_0}(i) \cdot \epsilon(\omega_i^{'}) \cdot I_{app}(\mathbf{r}_i^{'}) \tag{4.2}$$

where $p_{S_0}(i)$ is the probability (0 or 1) that molecule i is in the ground state (S_0) (available for excitation), $\epsilon(\omega)$ is the orientation-dependent absorption probability per unit time, and $I_{app}(\mathbf{r})$ is the normalized apparent excitation profile. Here, we follow the convention of Rigler *et al.* (1993),[212] in using for the convolution of the excitation intensity profile and the detection efficiency profile (cf. Hong and Elson (1991)[108] and Schwille *et al.*, (1999a)[232]). For the simulations presented here, rotational correlation times were assumed to be much faster than the Brownian dynamics time step, permitting replacement of $\epsilon(\omega)$ by an orientationally-averaged $\overline{\epsilon}$. For a 3-dimensional Gaussian, $I_{app}(\mathbf{r})$, the excitation probability of molecule i at position $r_i = (x_i, y_i, z_i)$, is then:

$$p_{ex}(\mathbf{r}_i^{'}, \omega_i^{'}; t^{'}) = p_{S_0}(i) \cdot \overline{\epsilon} \cdot \exp\left[-\left(\frac{(x_i - x_0)^2 + (y_i - y_0)^2 + ((z_i - z_0)/\kappa)^2}{2w_{xy}^2}\right)\right] \tag{4.3}$$

where w_{xy} is the standard deviation of the Gaussian profile in the radial direction centered at (x_0, y_0, z_0), $\kappa = w_z/w_{xy}$, and w_z is the standard deviation of the Gaussian profile in

the axial direction. For each fluorescence query interval, δt, Eq. 4.3 was evaluated for each molecule and compared to a uniformly distributed random number between 0 and 1 to determine whether excitation occurred (see below for long-lived photodynamics). Typically, $\overline{\epsilon}$ was adjusted to yield $10^4 - 10^5$ detection events per second. For some computations, the functional form of $I_{app}(\mathbf{r})$ was adjusted to accommodate other excitation profiles.

4.3.3.2 Photophysical conversions

Molecules in the excited state were allowed to relax via fluorescence, intersystem crossing, or photobleaching mechanisms as described below.

Fluorescence. The fluorescence lifetime of the excited state, τ_F, was assumed to be much faster than the step time of the Brownian dynamics simulation so that excitation and de-excitation occurred during the same time step ($\tau_F \ll \delta t$). Fluorescence photons were emitted with a constant quantum yield probability, Q_F, simulated by comparing a specified Q_F with a uniformly distributed random number in the range 0-1:

$$\begin{aligned} p_{ph}(\mathbf{r}_i, \omega_i; t | \mathbf{r}_i^{'}, \omega_i^{'}; t^{'}) &= \delta(t - t^{'}) \\ p_{em}(\mathbf{r}_i, \omega_i; t) &= Q_F \end{aligned} \tag{4.4}$$

Since molecules are regenerated immediately after excitation-emission, $p_{S_0}(i) = 1$ for all i in Eq. 4.2.

Intersystem crossing. Excited molecules were allowed to cross over into a triplet state with a constant probability, Q_T. Once in the triplet state, molecules were allowed to decay non-radiatively to the ground state with a constant probability defined by a charac-

teristic exponential time constant, $\tau_T > \delta t$:

$$\begin{aligned} p_{ph}(\mathbf{r}_i, \omega_i; t|\mathbf{r}_i^{'}, \omega_i^{'}; t^{'}) &= Q_T/\tau_T \\ p_{em}(\mathbf{r}_i, \omega_i; t) &= 0 \end{aligned} \tag{4.5}$$

Molecules in the triplet state were excitable again only after relaxing to the ground state; while in the triplet state, $p_{S_0}(i)$ was set to 0 in Eq. 4.2. Molecules in the triplet state molecules that crossed a periodic boundary of the simulation box were assumed to have "escaped" and so were returned to the ground state.

Photobleaching. Excited molecules were forced to become unexcitable permanently with constant probability, Q_B:

$$\begin{aligned} p_{ph}(\mathbf{r}_i, \omega_i; t|\mathbf{r}_i^{'}, \omega_i^{'}; t^{'}) &= Q_B/\tau_B \\ p_{em}(\mathbf{r}_i, \omega_i; t) &= 0 \end{aligned} \tag{4.6}$$

with $p_{S_0}(i) = 0$. Photobleached molecules were regenerated ($p_{S_0}(i)$ set to 1) once they crossed the periodic boundary of the simulation box to prevent continuous depletion and non-steady-state effects.

4.3.3.3 Correlation function and histogram computations

$F(t)$, calculated from Eq. 4.1, was stored as a paired list of times between consecutive photons and number of photons (photon arrival times, PAT) (Figure 4.1C). To maximize computational efficiency where the simulation time step was much smaller than the characteristic time of photon arrival, a binned PAT format was used in which the number of bins, b, between consecutive *bins with photons* (bins i and $i+b$) was recorded along with the number

of photons counts, k, registered in bin $(i+b)$. For a list of PAT pairs, $p(j) = \{b(j),\, k(j)\}$, the time autocorrelation function of fluorescence fluctuations was computed as:

$$G\left(\tau = b(j)\Delta\tau\right) = \left[\left(\left(B - b(j)\right)^{-1} \sum_{i=1}^{M-1} \sum_{j=i+1}^{M} k(i)k(j-1)\right) / \left(K/B\right)^2\right] - 1 \qquad (4.7)$$

where M is the length of the PAT list, K is the total number of photons counted $\left(= \sum_{j=1}^{M} k(j)\right)$, and B is the total number of bins between the first and last detected photons $\left(= \sum_{j=2}^{M} b(j)\right)$.

For calculation of cross-correlation functions using paired $F_x(t)$ and $F_y(t)$, an absolute PAT format (absPAT) was used instead, in which $b(j)$ entries are replaced by the *absolute* time in which photons arrive (in units of Δt): $p^{abs}(j) = \{b^{abs}(j),\, k(j)\}$. For two absPAT records, $p_x^{abs}(j) = \{b_x^{abs}(j),\, k_x(j)\}$ and $p_y^{abs}(j) = \{b_y^{abs}(j),\, k_y(j)\}$, the cross-correlation function was computed as:

$$G_{cross}\left(\tau = \left[b_x(i) - b_y(j)\right]\Delta\tau\right) = \frac{\left[\left(\left(\frac{1}{B_{min} - \left[b_x(i) - b_y(j)\right]}\right) \sum_{i=1}^{M_x} \sum_{j=1}^{M_y} k_x(i) \cdot k_y(j-1)\right)\right]}{\left(K_x/B_x\right)\left(K_y/B_y\right)} - 1 \qquad (4.8)$$

where $B_{min} = \min\left[B_x, B_y\right]$. Eq. 4.7 can be used to compute simultaneously, forward ($\tau > 0$) and reverse ($\tau < 0$) cross-correlation functions, $G_{xy}(\tau)$ and $G_{yx}(\tau)$, respectively.

Computation of the correlation function using photon arrival times as described above is more efficient than the standard direct approach using the fluorescence trace, scaling approximately as M^2 (M = number of PAT pairs) instead of as B^2 (B = total number of simulation time bins). For a 2 s simulation with a 200 ns time step, a high photon count rate of 100 kHz/molecule, and an average of 1 molecule in the observation volume, $M \leq 2 \times 10^5$ whereas $B = 10^7$. In this case, computing the correlation function using the direct approach took seven hours on a 2.8 MHz Pentium 4 whereas the PAT method took 30 min.

The calculation of $G(\tau)$ was described by Eqs. 7 and 8 is similar to that of Davis *et al.*

(2003)[47] that mimics the computation of hardware correlator cards. In our approach, $G(\tau)$ is computed at each τ by multiplication of PAT counts corresponding to that photon arrival time, whereas $G(\tau)$ is computed by Davis *et al.* by addition. The computation of $G(\tau)$ by multiplication becomes efficient for large photon count rates where the number of bins containing more than one count is significant; multiple additions would then be necessary as opposed to a single multiplication. In practice, we found an insignificant difference (<1 s) in computation time between the two methods for the simulation described here.

To mimic the temporal resolution and time-binning structure of hardware correlators used in FFM experiments, $G(\tau)$ were averaged in a quasi-logarithmic manner.[222,223,269] Briefly, $G(\tau)$ values within each of the first 8 successive time blocks $\Delta\tau$ were averaged for a total of 8 initial averaged values of $G(\tau)$; here, $\Delta\tau$=32 or 200 ns, corresponding to the resolution of commercially available hardware cards. Each subsequent group of 8 $G(\tau)$ values were averaged using a width that was twice that of the preceding group. For example, averaged $G(\tau)$ values 9-16 were obtained with width $2\Delta\tau$; $G(\tau)$ values 17-24 had width $4\Delta\tau$; and so on. The averaging procedure was continued until all simulated $G(\tau)$ values were averaged.

Functions were fit to averaged and binned $G(\tau)$ by nonlinear least-squares fitting procedures. The fits were weighted by the standard deviation of $G(\tau)$, determined from multiple simulations with the same set of parameters but with different starting configurations and random number seeds.[205,219] Data analysis was conducted in either Microsoft Excel[98] or Igor Pro 4 (WaveMetrics, Inc., Lake Oswego, OR). Identical values of fitted Excel parameters were obtained using Mathematica 4.0 (Wolfram Research, Inc., Champaign, IL).

The photon count histogram (PCH), $P(k;\Delta T)$, was computed by re-binning the PAT using a specified time bin, ΔT, followed by tabulating the number of counts, k, in the re-binned PAT list (see Section 4.6). PCH data were fit by numerically integrating the equations of Chen *et al.* (1999)[32] and using a Levenberg-Marquardt routine[201] implemented in Mathematica 4.0 (see Section 4.7). The two fitting parameters were $\overline{N}$, the average number of molecules in the excitation volume, and $\overline{\epsilon}$, the average specific brightness, in units of counts·(time bin)$^{-1}$·molecule^{-1}.

4.3.3.4 FFM measurements

FFM measurements on 1-5 nM aqueous calcein solutions (Molecular Probes Inc., Eugene, OR) were done on by directing a 488 nm beam from a diode laser (Coherent Inc., Santa Clara, CA) through a 100x oil objective lens using a Nikon TE-300 inverted epifluorescence microscope. The excitation light was focused on thin fluid layers sandwiched between coverglasses. Emitted fluorescence passed through a 510 nm dichroic mirror and 525 ± 25 nm bandpass filter (Chroma Technologies Corp., Rockingham, VT), and was focused onto a 100 μm diameter fiberoptic cable (Fico Inc., Tyngsboro, MA). Photon counts were detected using an avalanche photodiode (Perkin Elmer Optoelectronics, Ltd.) and correlated with an ALV-5000 correlator card (ALV-Laser Vertriebsgesellschaft mbH, Langen, Germany).

4.4 Results

4.4.1 Validation: Brownian diffusion

To validate our computational approach, FFM simulations of Brownian diffusion in a Gaussian excitation volume were carried out where analytical expressions exist for $G(\tau)$ and $P(k;\Delta T)$. Figure 4.2A shows a linear plot of mean square displacement vs. time (r=0.99), confirming a lack of correlation in the 10^{10} random numbers generated for the Brownian dynamics simulation. The diffusion coefficient computed from the slope was 298 μm^2/s, in agreement with 300 μm^2/s used in the simulation.

A 1×1×3 μm observation box was set up at the center of the 10×10×10 μm simulation box, and the number of particles within the observation volume tracked throughout a 1 s simulation time. The average number of particles in the observation volume was 3.02, as expected from the observation volume of 3 μm^3 and the specified concentration of 1 particle/μm^3. The number of particles in the observation volume varied from 0 to 13 during the simulation. Figure 4.2B shows representative fluctuations in the number of particles in the observation volume over a representative 100 μs time interval. Figure 4.2C shows the number of fluorescence detection events (binned in 200 ns time intervals) during the same time after processing through the fluorescence filtering module.

Figure 4.2D shows $G(\tau)$ computed from $F(t)$, together with a fit of the analytical equation for Stokes-Einstein diffusion in a volume defined by a Gaussian excitation beam profile:[212]

$$G(\tau) = G(0_+)\left(1+\tau/\tau_D\right)^{-1}\left(1+\tau/\kappa^2\tau_D\right)^{-1/2} \tag{4.9}$$

where τ_D is the characteristic diffusion time through the excitation volume, and κ is the ratio

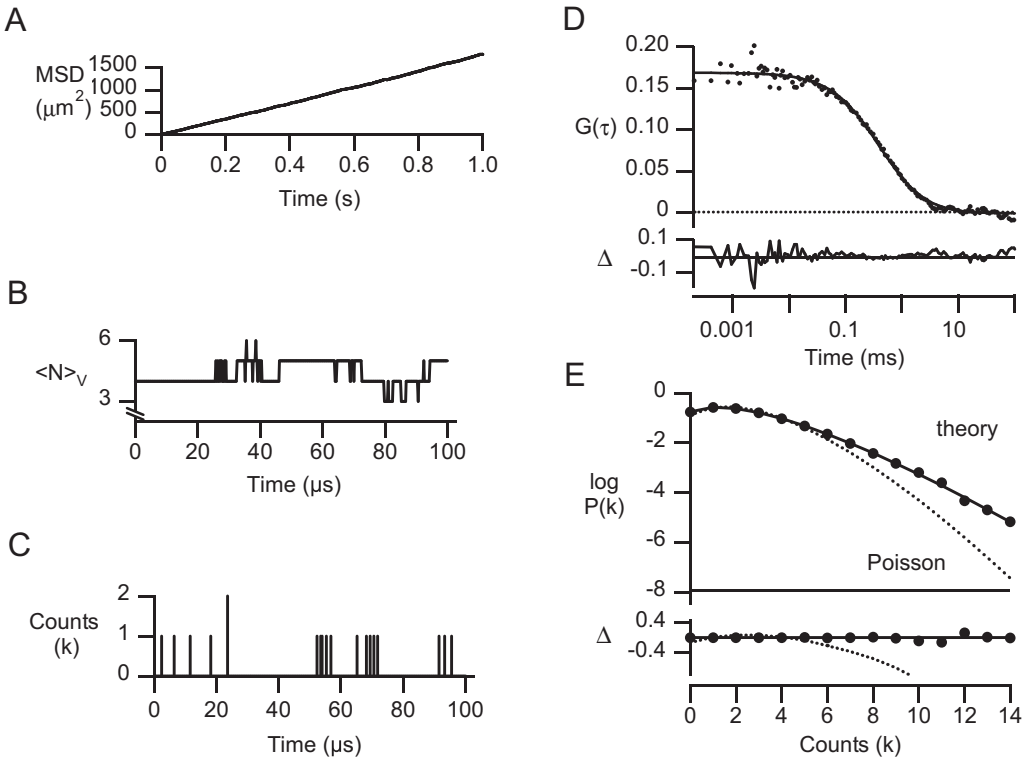

Figure 4.2: **Validation of simulation method**. The Brownian dynamics simulation of particle diffusion was run for 1 s using a 200 ns time step for 1000 molecules with diffusion coefficient 300 μm^2/s in a $10 \times 10 \times 10$ μm box (average concentration 1 particle/μm^3; 1.7 nM). *(A)* Mean squared displacement (MSD) plot of particle positions. The fitted slope gives a diffusion coefficient of 298 μm2/s. *(B)* Representative plot of the number of particles, N_V, in a $1 \times 1 \times 3$ μm cubic observation volume. *(C)* Corresponding plot for detected photons. Molecules were excited with a Gaussian excitation profile of $w_{xy} = 0.354$ μm, $w_z = 1.061$ μm ($\kappa = 3$), and specific brightness 17 kHz/molecule. *(D)* Autocorrelation function, $G(\tau)$, computed from *F(t)* from four separate simulations. The solid line is fitted $G(\tau)$ for a simple diffusion (Eq. 4.9) (see text for fitted parameters), with fractional deviation (Δ) shown in the lower panel. *(E)* Photon count histogram $P(k;\Delta T)$, generated from the fluorescence trace with $\Delta T = 20$ μs. Data were fitted with the $P(k;\Delta T)$ for Poisson distribution (dotted curve) and super-Poissonian model (theory; solid curve).[32] *(F)* Effect of excitation profile on $G(\tau)$. Trajectories were generated as above. The fluorescence module was modified to produce cubic, spherical, and symmetric Gaussian ($w_x = w_y = w_z$) excitation profiles. Simulated data were fitted to Eq. 4.9, and the fractional deviation between fit and simulation (Δ) plotted.

w_{xy}/w_z. The simulated data were fitted well, with τ_D of 405 ± 15 μs (SD) from an average of four separate 1 s simulations, in agreement with 419 μs calculated using the diffusion coefficient derived from Figure 4.2A and the specified Gaussian illumination volume $\tau_D = (2w_{xy})^2/4D$. The fitted $G(0_+)$ was 0.169 ± 0.003, in agreement of 0.169 calculated from the particle concentration, C_N, and Gaussian illumination volume $G(0_+) = \left(8\pi^{3/2} C_N \kappa w_{xy}^3\right)^{-1}$. Figure 4.2E shows $P(k;\Delta T)$ computed from $F(t)$, together with a fit to the theory given by Chen *et al.* (1999).[32] The simulated $P(k;\Delta T)$ was in excellent agreement with the theory predicting a "super-Poissonian" function, but quite different from a single Poisson distribution shown for comparison.

Additional computations were done to validate the model, including demonstrating predicted effects on τ_D and $G(0_+)$ upon changing particle concentrations and diffusion coefficients: τ_D was not affected by concentration and was inversely proportional to the friction coefficient, while $G(0_+)$ was not affected by the friction coefficient and was inversely proportional to concentration (data not shown). simulations done with non-Gaussian excitation and emission profiles (spherical, cubic, and symmetric Gaussian) at constant volume revealed small though significant changes in the $G(\tau)$ curve shape (Figure 4.2F) that could be misinterpreted as anomalous or other types of complex diffusion.

4.4.2 Effects of intersystem crossing on $G(\tau)$ and $P(k;\Delta T)$

The effect of triplet state intersystem crossing on $G(\tau)$ was simulated by allowing an excited molecule in state S_1 to enter the triplet state (T_1) as a first-order kinetic process characterized by time constant τ_{is} (Figure 4.3A). Decay from the triplet state to the ground state was also simulated as a first-order kinetic process characterized by triplet lifetime τ_{trip}.

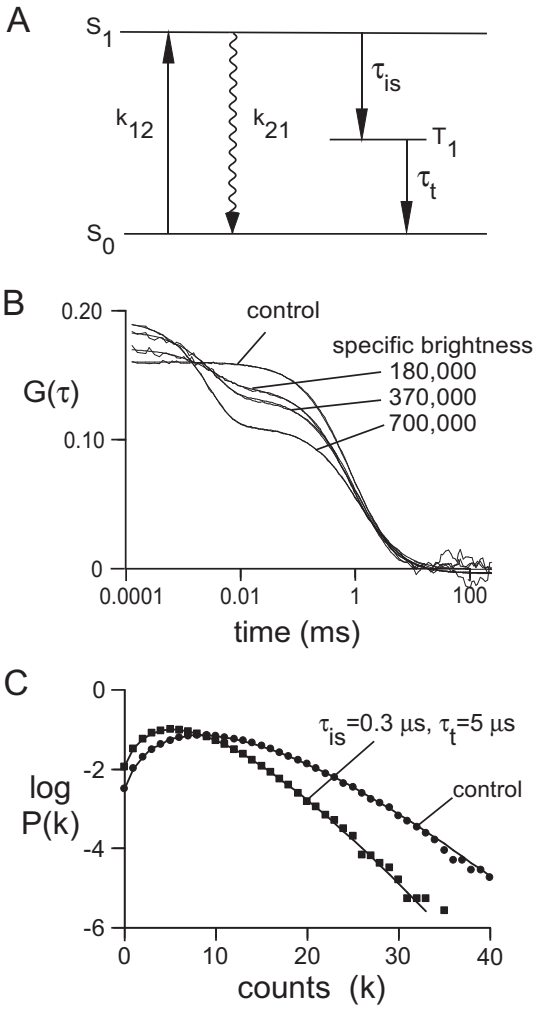

Figure 4.3: **Simulations of intersystem crossing**. *(A)* Kinetic scheme for intersystem crossing. *(B)* Simulated $G(\tau)$. Brownian dynamics trajectories (1 s) generated for 192 spherical molecules of diffusion coefficient 10^7 μm^2/s in a $4\times4\times12$ μm box (1 molecule/μm^3; 1.7 nM) with step time 50 ns (total of 10^7 steps), with $k_{12} = k_{21} = 2.0 \times 10^7$ s^{-1}, $\tau_{is} = 0.3$ μs^{-1}, and $\overline{\tau}_t = 5$ μs. *F(t)* generated using a Gaussian excitation beam ($w_{xy} = 0.354$ μm and $w_z = 1.061$ μm) with indicated specific brightness (in kHz/molecule). The smooth curves (which follow the simulated data very closely) are fits of Eq. 4.10 (see text for fitted parameters). *(C)* Effect of intersystem crossing on $P(k;\Delta T)$ with ΔT = 20 μs. Data were simulated as in (B) with specific brightness 370 kHz/molecule (in the absence of intersystem crossing). Solid lines are fits of the super-Poissonian model with parameters: control (observed simulation values in parentheses): $\overline{N} = 2.06$ (2.16), $\overline{\epsilon} = 5.07$ (4.86); triplet state: $\overline{N} = 2.01$ (2.62), $\overline{\epsilon} = 3.41$ (2.62).

Molecules in the triplet state were not subject to excitation, and decay from the triplet state occurs without photon emission.

Figure 4.3B shows $G(\tau)$ for a simulations with intersystem crossing at constant τ_{is} = 0.3 μs and τ_{trip}=5 μs as a function of excitation intensity. The excitation intensity in Figure 4.3B is expressed in terms of the specific brightness (detector counts per molecule per second) obtained from runs in the absence of triplet state kinetics. For this combination of τ_{is} and τ_{trip}, which are typical of values obtained experimentally,[264] high specific brightness is required to populate appreciably the triplet state.

For the case of isotropic diffusion in a hydrodynamic medium in which the time scale of triplet state kinetics is much faster than that of diffusion kinetics (the conditions under which Figure 4.3B was simulated), $G(\tau)$ is given by:[264]

$$G(\tau) = G(0_+)\left(1+\tau/\tau_D\right)^{-1}\left(1+\tau/\kappa^2\tau_D\right)^{-1/2}\left(\frac{1+\overline{T}\left(e^{-\tau/\overline{\tau}_T}-1\right)}{1-\overline{T}}\right) \tag{4.10}$$

where $\overline{T}$ is the steady-state fraction of molecules in the triplet state, and $\overline{\tau}_T$ is the characteristic time for triplet state decay. The smooth curves in Figure 4.3B are fits of simulated $G(\tau)$ to Eq. 4.9. The triplet state parameters obtained from the fit ($\overline{T}$=0.17, 0.28, 0.43 and $\overline{\tau}_T$= 3.6, 3.3, 2.8 μs, for specific brightness 1.8×10^5, 3.7×10^5 and 7.0×10^5, respectively) were in good agreement with those calculated from the parameters used to generate the simulation ($\overline{T}$= 0.16, 0.27, 0.40 and $\overline{\tau}_T$=3.5, 3.4, 2.9 μs, respectively). $\overline{T}$ and $\overline{\tau}_T$ are spatial averages weighted by the square of the fluorescence intensity across the excitation profile.[264] $\overline{T}$ was calculated numerically by dividing the simulation cell into sub-cells of 0.1 μm^3, tabulating the square of the fluorescence intensity (i^2) and the fraction of molecules in the triplet state (T) for each sub-cell, and then summing the product over the simulation

box and over all time steps: $\overline{T} = \sum i^2 F / \sum F$, where $F = T/(1-T)$. $\overline{\tau}_T$ was calculated for each sub-cell by determining the triplet state lifetime (τ_T) of molecules entering the triplet state in that sub-cell, then summing the product: $\overline{T} = \left(\sum \tau_T i^2 F/c\right) / \left(\sum i^2 F/c\right)$, where c is the concentration of molecules in the sub-cell. The time constant $\overline{\tau}_T$ is related to the triplet lifetime, $\overline{\tau}_T$, by $1/\tau_{trip} = 1/\tau_T - k_{12}/\left(\tau_{is}\left(k_{12}+k_{21}\right)\right)$.

Figure 4.3C shows the effect of triplet state kinetics on the PCH. As expected, triplet state kinetics lowered the most probable count rate. Interestingly, $P(k;\Delta T)$ for triplet state kinetics were fitted well by the "super-Poissonian" theory applicable in the absence of triplet state kinetics, albeit with altered specific brightness and concentration, indicating the inability to detect triplet state phenomena by PCH analysis alone.

4.4.3 Effects of photobleaching on $G(\tau)$ and $P(k;\Delta T)$

Photobleaching was simulated by including a first-order kinetic process that converts an excited molecule into a permanently dark state (Figure 4.4A). $G(\tau)$ and $P(k;\Delta T)$ were compared in the absence of photobleaching and for different photobleaching rates as given in Figs. 4.4B and C. In the absence of photobleaching, $G(\tau)$ was described by Eq. 4.9 with fitted $G(0_+)$ and τ_D (0.168, 0.422 ms) in agreement with parameters used in the simulation (0.169, 0.419 ms). As the photobleaching rate increased, simulated $G(\tau)$ were still described reasonably well by Eq. 4.9, with some deviation apparent at the highest rate. Photobleaching produced an increase in apparent $G(0_+)$ (0.296 and 0.428 for $\tau_{bleach} = 3$ μs and 1 μs, respectively) and decrease in τ_D (0.244 ms and 0.130 ms). Qualitatively, the increase in $G(0_+)$ with photobleaching arises from reduced steady-state fluorophore concentration in the illuminated volume, and the decrease in τ_D arises from enhanced apparent mobility as

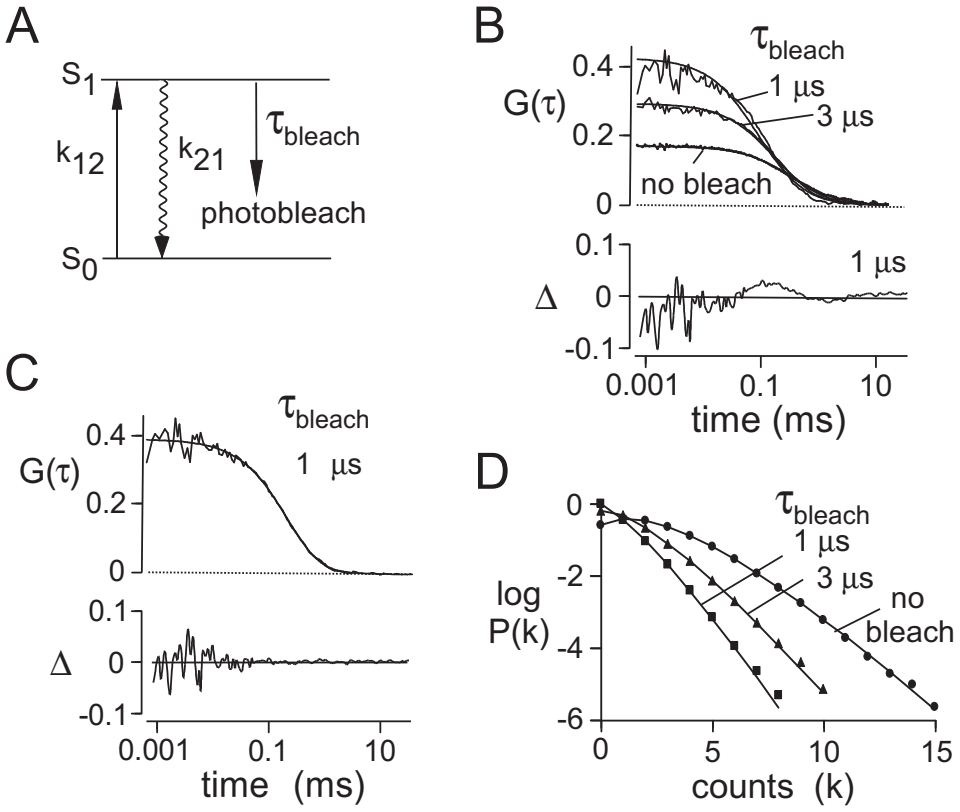

Figure 4.4: **Simulations of photobleaching**. *(A)* Kinetic scheme for photobleaching. *(B)* Effect of photobleaching on $G(\tau)$ Brownian dynamics trajectories generated as in Figure 2. *F(t)* was generated using a Gaussian excitation beam ($w_{xy} = 0.354$ μm, $w_z = 1.061$ μm) with indicated photobleach time constants. Specific brightness was 17 kHz/molecule (in the absence of photobleaching). Data were simulated at constant excitation light intensity. The solid lines are fits of Eq. 4.9 (see text for values of fitted parameters) with fractional deviation (Δ) at $\tau_{bl} = 1$ μs shown in the lower panel. *(C)* Fit of Eq. 4.11 with parameters: $G(0_+) = 0.40$, $\tau_D = 0.34$ ms, B=0.86, and $\tau_{bl} = 0.53$ ms with fractional deviation (Δ). (D) Effect of photobleaching on $P(k;\Delta T)$ Data were binned with $\Delta T = 20$ μs. The solid lines are fits to the super-Poissonian model (with observed simulation values in parentheses): control: $\overline{N} = 2.16$ (2.0862), $\overline{\epsilon} = 0.9463$ (0.98); 3 μs bleach: $\overline{N} = 1.30$ (1.19), $\overline{\epsilon} = 0.70$ (0.76); 1 μs bleach: $\overline{N} = 0.99$ (0.88), $\overline{\epsilon} = 0.45$ (0.51).

bleached fluorescent molecules disappeared from the excitation volume.

Photobleaching can be taken into account approximately by the inclusion of an additional exponential term in the correlation function:[56,60]

$$G(\tau) = G_D(\tau)\left(1 + B\left(e^{-\tau/\tau_{bleach}} - 1\right)\right) \tag{4.11}$$

where $G_D(\tau)$ is the autocorrelation function with no photobleaching (Eq. 4.9), B is the average fraction of excited molecules that photobleach, and τ_{bleach} is the average photobleach time constant. Figure 4.4C shows that this modified correlation function describes $G(\tau)$ well for $\tau_{bleach} = 1$ μs. Figure 4.4D shows the effect of photobleaching on $P(k;\Delta T)$. As expected, the count rate decreased with photobleaching, from 104 kHz (no photobleach) to 51.2 kHz ($\tau_{bleach} = 3$ μs) to 25.4 kHz ($\tau_{bleach} = 1$ μs). As was the case for triplet-state kinetics (Figure 4.3C), the $P(k;\Delta T)$ for photobleaching were fit well by the super-Poissonian theory applicable in the absence of photobleaching, indicating the inability to identify photobleaching by PCH analysis alone.

The predictions from the simulations of the effects of photobleaching on were tested experimentally by FFM measurements on aqueous calcein solutions. Representative $G(\tau)$ shown in Figure 4.5 indicate an increase in $G(0_+)$ and reduction in τ_D with increased excitation light intensity. The experimental data are qualitatively consistent with the predictions of Figure 4.4B, although the experimental data also show evidence for increased triplet state population with increased excitation intensity.

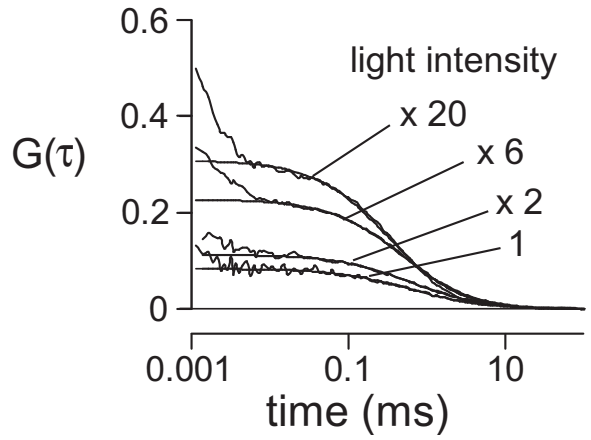

Figure 4.5: **Effect of excitation light intensity on $G(\tau)$ for calcein**. The solid lines are fits of Eq. 4.9 to the data (starting at 10 μs). Fitted parameters: $G(0_+)$= 0.082, 0.11, 0.23, 0.31 and τ_D = 0.60, 0.63, 0.43, 0.22 ms for relative light intensities of 1, $\times$2, $\times$6, and $\times$20, respectively.

4.4.4 Two-color cross-correlation validation and effects of beam mis-alignment

The effects of dimer formation on auto- and cross-correlation $G(\tau)$ in two-color FFM was simulated by configuring a system consisting of equal numbers of two kinds of particles, A and B, each of which could be excited and detected separately. A specified fraction of A and B were bound permanently as A-B rigid rod dimers of 50 nm bond length. Figure 4.6A shows the cross-correlation function, $G_{AB}(\tau)$, of A and B as a function of the fraction held bound. As expected, $G_{AB}(0_+)$, increased with fraction bound. Figure 4.6B shows that $G_{AB}(0_+)$ increased linearly with fraction bound, while the autocorrelated $G_{AB}(0_+)$ was not sensitive to binding, as expected.

The simulated effect of beam misalignment on FFM measurements on a collection of rigid A-B dimers is shown in Figure 4.6C. For these simulations, identical Gaussian excitation/detection profiles were used, and the centers of the two profiles were offset. The offset

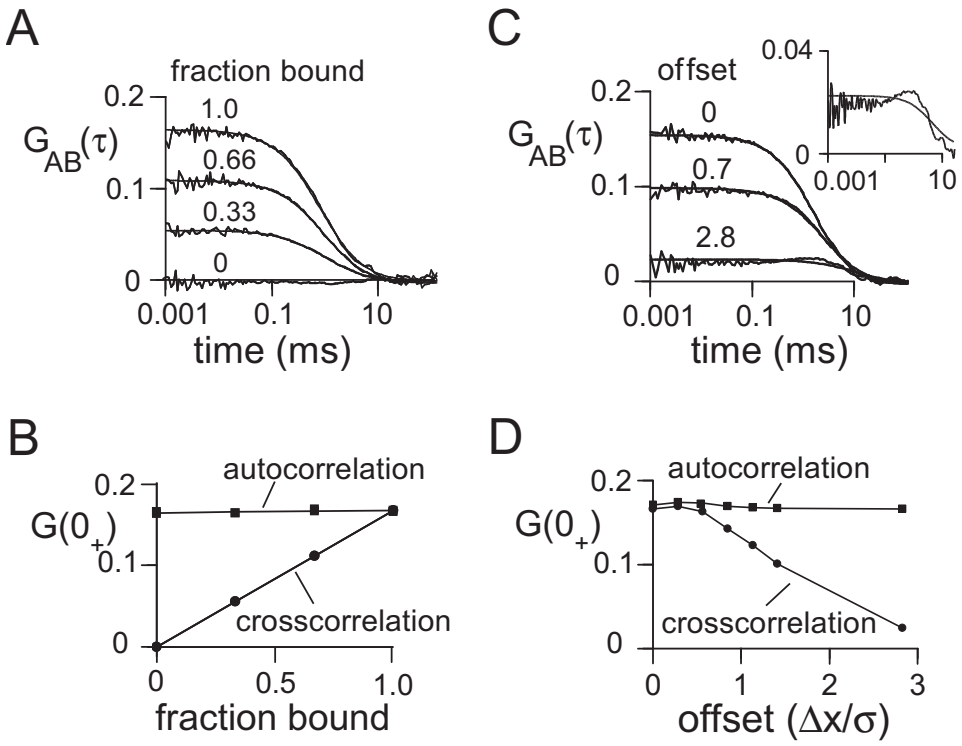

Figure 4.6: **Simulations of two-color FCS**. Brownian dynamics trajectories (1 s) generated for 192 spherical particles of type A and 192 spherical particles of type B (each with diffusion coefficient 273 μm^2/s) in a $4 \times 4 \times 12$ μm box using a step time of 100 ns for 107 steps. *F(t)* generated using a Gaussian excitation beam ($w_{xy} = 0.354$ μm, $w_z = 1.061$ μm) and specific brightness 17 kHz/molecule. *(A)* Effect of dimer formation on the cross-correlation function. Indicated fractions of A and B were constrained as 50 nm rigid-rod *A:B* dimers. Solid lines are a fit of Eq. 4.9. Fitted parameters: $G(0_+)$= 0.055, 0.112, 0.165 and τ_D = 0.97, 0.97, 0.83 ms for fraction bound 0.33, 0.66, 1.00, respectively. For unbound A and B, $G(0_+) = 0.163$ and $\tau_D = 0.42$ ms (data not shown). *(B)* Dependence of $G(0_+)$ on fraction bound. The autocorrelation of the A molecules, $G_{AA}(0_+)$, is shown. $G_{BB}(0_+)$ (not shown) was identical to $G_{AA}(0_+)$). *(C)* Effect of beam misalignment on cross-correlation function. A and B were constrained as 50 nm rigid-rod *A:B* dimers. Illumination and detection profiles for A and B were displaced in the x-direction by indicated distances. The solid lines represent a fit of Eq. 4.9 to the data. Fitted parameters: $G(0_+) = 0.158$, 0.102, 0.026 and τ_D = 1.63, 1.38, 5.96 μs for offset $\Delta x/\sigma = 0.0$, 0.7, and 2.8, respectively. Δx is the offset of the centers of the Gaussian excitation profiles and σ is the standard deviation in the x-direction. Inset shows lower curve on expanded y-scale. *(D)* Effect of misalignment of beams on auto and cross-correlation amplitudes.

in the x-direction was expressed as a fraction of the standard deviation of the Gaussian profile. As expected, $G_{AB}(0_+)$ decreased with increasing offset. The inset to Figure 4.6C shows an expansion of the lower curve, revealing a peak in cross-correlation at 1 μs when the beams are separated by 2.8 times the standard deviation. This peak in cross-correlation occurs near the characteristic diffusion time of 1.6 μs, and corresponds to the cross-correlation arising from diffusion of the *A*-*B* dimer from one detection volume to another. Figure 4.6D shows that the $G_{AB}(0_+)$ is relatively unaffected until the centers of the excitation profiles are separated by more than 0.2 times the standard deviation.

4.4.5 Effects of binding on $G(\tau)$

Simulations of binding were done for an ensemble of molecules in which there was a constant probability that a molecule would stop in its trajectory (characterized by a time constant τ_{on}), and once stopped, a constant probability that the molecule would resume its trajectory (characterized by time constant τ_{off}). This system corresponds to binding of a fluorophore to an immobile object with on and off rate constants $1/\tau_{on}$ and $1/\tau_{off}$, respectively. Simulations for $\tau_{on}/\tau_{off} = 1$ are shown in Figure 4.7A. For $\tau_{on} = \tau_{off} = 50$ μs, $G(0_+)$ is relatively unaffected though the apparent τ_D increases. As the on-off times increase to 5000 μs, $G(0_+)$ decreases and τ_D increases. The increase in apparent τ_D is related to slowed fluorophore diffusion in the excitation volume because of binding; the reduced $G(0_+)$ with slow on-off rates is related to fluorophores that do not escape the excitation beam over the course of the simulation, acting as background fluorescence. In the limit of very slow binding, bound fluorophores do not move whereas the free fluorophores diffuse without binding. Since $\tau_{on}/\tau_{off} = 1$ and half the fluorophores are bound for the simulations in

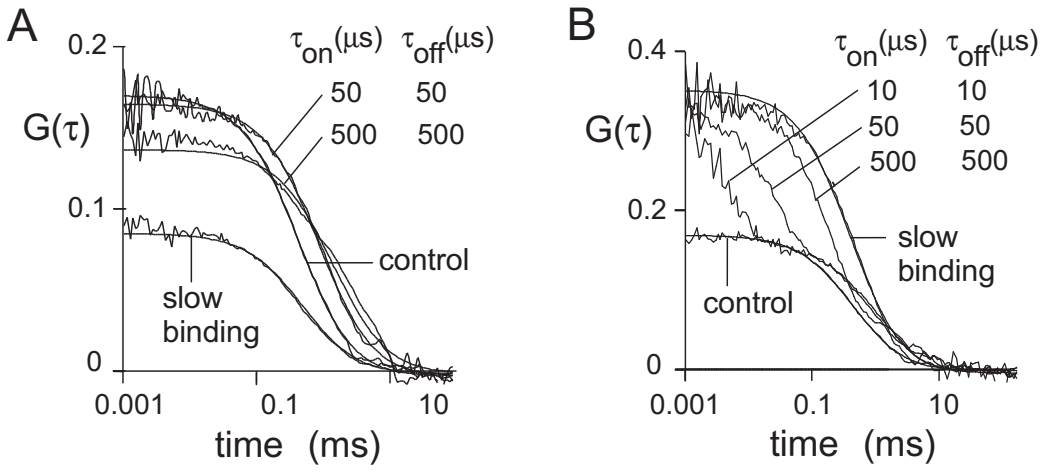

Figure 4.7: **Simulations of binding effects on FFM**. Brownian dynamics trajectories (1 s) generated for 192 spherical particles in a $4 \times 4 \times 12$ μm box using a step time of 100 ns for 107 steps. *F(t)* were generated using a Gaussian excitation beam ($w_{xy} = 0.354$ μm, $w_z = 1.061$ μm) and specific brightness of 17 kHz/molecule. Trajectories were modified by fixing the positions of particles for a given time, as described in the text, characterized by association time, τ_{on}, and dissociation time, τ_{off}. To simulate slow binding, particles selected at random were held fixed throughout the course of the simulation, and no additional particles were allowed to bind. The fraction of particles held fixed at $\tau_{off}/(\tau_{on}+\tau_{off}) = 0.5$. *(A)* Effect of binding on $G(\tau)$ with equally fluorescent bound and free particles. Solid lines are a fit of Eq. 4.5, with fitted parameters: $G(0_+)$= 0.170, 0.166, 0.136, 0.085 and $\tau_D = 0.45$, 0.93, 1.52, 0.52 ms for control, $\tau_{on} = 50$ μs, $\tau_{on} = 5000$ μs, and slow binding, respectively. *(B)* Same as in (A), except that bound particles were non-fluorescent. The solid curves are a fit of Eq. 4.9 with: $G(0_+) = 0.170$, 0.356 and $\tau_D = 0.45$, 0.41 ms for control and slow binding, respectively.

Figure 4.7A, $G(0_+)$ is reduced to half of its original value with no change in τ_D.

Simulations were also done for the case where the bound complex is non-fluorescent (Figure 4.7B). A second component is seen in autocorrelation functions, corresponding to a flickering of the fluorescence signal produced by binding-unbinding (cf. Elson and Magde (1974)[65]). As the binding rate slows, the second component becomes more prominent until, in the limit of infinitely slow binding, the system behaves as a collection of fluorophores at half the concentration of control. The fitted $G(0_+)$ values (0.170 and 0.356) and τ_D-values (0.45 ms and 0.41 ms) for control and slow binding support this interpretation. For slow binding data in Figure 4.7B, 50% of fluorophores are dark at any one time, producing a two-fold increase in $G(0_+)$ but no change in τ_D.

4.4.6 Effects of anomalous diffusion on $G(\tau)$

Anomalous super-diffusion was modeled by inclusion of drift in the Brownian dynamics simulation. Increasing drift (velocity from 0-3 mm/s) produced greater upward curvature in the MSD plot (Figure 4.8A) signifying super-diffusion. The corresponding $G(\tau)$ curve shape differed significantly from that for simple diffusion (Figure 4.8B), but reasonably well to the semi-empirical equation often used for FCS measurements of anomalous diffusion:[261]

$$G(\tau) = G(0_+)\left(1 + (\tau/\tau_D)^{\alpha}\right)^{-1}\left(1 + \left(\tau/\kappa^2\tau_D\right)^{\alpha}\right)^{-1/2} \tag{4.12}$$

Fitted α values were 1.5 and 2.5 for drifts of 1 and 3 mm/s, respectively. Fit results are shown in 4.1.

Anomalous sub-diffusion was modeled by confining diffusion to a box with reflecting boundaries. At box sizes comparable to the size of the Gaussian excitation beam (width

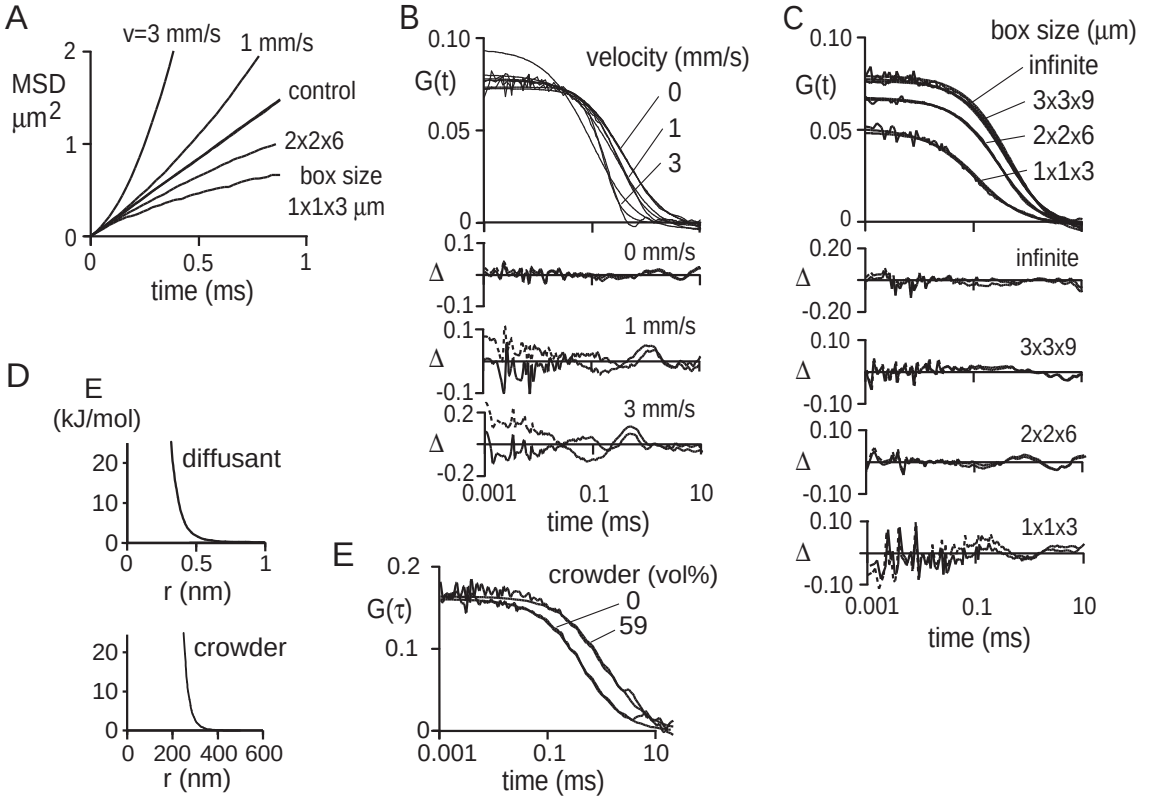

Figure 4.8: **Simulations of anomalous diffusion and molecular crowding**. *(A)* MSD plots for simulated super- and sub-diffusion. Brownian dynamics trajectories were generated for 0.73 μm particles at a concentration of 2 particles/μm^3 for 100 ms using a 200 ns time step (average of 50 trajectories). Super-diffusion was simulated by a constant velocity (v) in the x-direction. Sub-diffusion was simulated by confining the particle to a rectangular box of indicated dimensions. *(B)* Super-diffusion. *F(t)* were generated with a Gaussian excitation profile of $w_{xy} = 0.354$ μm, $w_z = 1.061$ μm ($\kappa = 3$) and specific brightness of 17 kHz/molecule. $G(\tau)$ as a function of velocity shown along with deviations (Δ) between fit of Eq. 4.9 (dashed line) or 11 (solid line) and simulation. Fitted parameters are given in 4.1 below. *(C)* Sub-diffusion. *F(t)* and fits generated as in (B). Infinite box size refers to a $3 \times 3 \times 9$ μm box with periodic boundary conditions. *(D)* Non-bonding potentials used in crowding simulations. The radius of the particles was defined operationally as the distance from the center of the particle at which the potential dropped to kT. *(E)* Effect of crowding on $G(\tau)$ Brownian dynamics trajectories (100 ms) were generated for 81 spherical diffusing particles (diffusion coefficient 95 μm^2/s, effective radius 0.45 nm) and 420 large crowder particles (diffusion coefficient 0.67 μm^2/s, effective radius 300 nm) in a $3 \times 3 \times 9$ μm box for a volume exclusion of 59%. The solid lines represent a fit of Eq. 4.9 to the data. Fitted parameters: $G(0_+) = 0.161$, 0.164 and τ_D= 0.80, 2.01 ms for volume fraction 0 and 59%, respectively.

	simple diffusion		anomalous diffusion		
Simulation	$G(0_+)$	τ_D (ms)	$G(0_+)$	τ_D (ms)	α
Super-diffusion, control	0.081	0.41	0.079	0.409	1.07
Super-diffusion, v=1 mm/s	0.085	0.28	0.074	0.31	1.5
Super-diffusion, v=3 mm/s	0.098	0.11	0.074	0.17	2.5
Sub-diffusion, control	0.080	0.39	0.077	0.39	1.08
Sub-diffusion, $3 \times 3 \times 9$ μm	0.086	0.47	0.085	0.48	1.03
Sub-diffusion, $2 \times 2 \times 6$ μm	0.070	0.30	0.068	0.30	1.07
Sub-diffusion, $1 \times 1 \times 3$ μm	0.049	0.13	0.051	0.12	0.89

Table 4.1: **Fitted parameters for simulations of anomalous diffusion and crowding of Figure 4.8**.

$0.7 \times 0.7 \times 2.1$ μm), MSD plots were downward curved (Figure 4.8A) signifying sub-diffusion. MSD plots leveled out at long times (data not shown). Corresponding $G(\tau)$ (Figure 4.8C) were fitted using Eq. 4.11 with α of 1.0 and 0.9 for box sizes of $2 \times 2 \times 6$ and $1 \times 1 \times 3$ μm, respectively.

As another possible cause of anomalous sub-diffusion, molecular crowding, was modeled by simulating the diffusion of small fluorophores (radius 0.73 nm) in a crowded environment containing large non-fluorescent mobile spheres (radius 150 nm). Intermolecular interactions were specified by the nonbonding potentials shown in Figure 4.8D. (The crowder volume fractionw as calculated by taking the effective crowder radius as the distance at which the intermolecular potential increased to kT.) At a crowder volume fraction of 59%, there was an increase in apparent τ_D by 2.5-fold without change in $G(0_+)$ (Figure 4.8E) and MSD plots linear with a 2.5-fold decrease in slope (data not shown). MSD plots of large crowder particles were also linear over the simulation time course (data not shown). The $G(\tau)$ shape was described adequately by a model without anomalous diffusion (Eq. 4.9). Because of computation time constraints it was not practical to carry out crowding

simulations at higher crowded volume fractions or using smaller crowder sphere diameters where greater slowing of diffusion is predicted.

4.5 Discussion

The purpose of this study was to develop a generalized computational approach for simulation of correlation functions and intensity histograms to investigate phenomena that can complicate the interpretation of FFM measurements on biological systems. Such simulations enable analysis of systems for which analytical expressions for $G(\tau)$ or $P(k;\Delta T)$ do not exist, such as non-Gaussian detection volumes, complex photophysical phenomena, diffusion through complex, inhomogenous or anisotropic media, or when the system is subject to a perturbing non-equilibrium process. The simulations described here were applied to analyze the impact of these non-idealities on FFM data: photobleaching, mis-aligned focal volume elements in two-color FFM (TCFFM) experiments, transient fluorophore binding to an immobile substrate, and diffusion through crowded media.

4.5.1 Simulation method

Our simulation approach used three distinct modules for the computation of particle trajectories, simulation of photon statistics to generate *F(t)*, and computation of correlation functions and histograms from *F(t)*. Trajectories were computed as Brownian molecular dynamics trajectories to enable the time and spatial resolution needed to simulate rapid photophysical effects and interparticle interactions. In contrast, in most FCS simulation methods trajectories are generated by random jumps between lattice points on a grid.[47,188]

While lattice methods are computationally efficient, intra- and inter-molecular interactions are difficult to simulate in a lattice framework. Here, we generated trajectories using the Langevin equation appropriate for a highly damped system of independent particles. This approximation is valid for low concentrations of small particles over time scales much greater than the characteristic relaxation time for particle motion.[30] The relaxation time is given by the ratio of particle mass to solvent friction coefficient For small molecules in aqueous solutions, the relaxation time is on the order of a few fs, and thus much smaller than the millisecond diffusion times simulated. The close agreement between the simulated data and that predicted theoretically (Figure 3.2) supports approach used here to compute trajectories for FFM simulation.

The modular nature of our simulation approach demonstrates how FFM simulations could be performed without the need for a specialized or proprietary software packages. Brownian dynamics trajectories were computed using the molecular dynamics package GROMACS because it is freely available and well supported, and because it would be straightforward to model the effect of conformation and mobility coupling of polymers on FFM experiments in future studies. Fluorescence statistics, correlation functions, and histograms were computed using custom software, which allowed us to simulate effects of photophysical phenomena and instrumental changes on FFM experiments.

Decoupling the molecular dynamics and fluorescence statistics components enabled us to examine photophysical phenomena and different illumination profiles easily without recomputing trajectories. Moreover, such an approach allows us to study separately the influence of fluorescence statistics and particle statistics on FFM measurements. Other

simulation approaches in which dynamics and fluorescence generation have been directly coupled[112, 269] do not have these advantages.

Diffusion through structures having complex geometry, such as cellular organelles, can produce significant deviations from $G(\tau)$ compared to isotropic diffusion. For example, significant deviations from Eq. 4.3 are found for diffusion of small molecules through dendritic tubules with diameters much smaller than the focal volume,[82] anomalous sub-diffusion through cell cytoplasm,[261] and non-Gaussian excitation profiles.[104] The simulation approach described here is readily adapted to include these phenomena. The effects of restricted diffusion can be studied computing Brownian dynamics trajectories under appropriate conditions, and of non-Gaussian excitation profiles by modifying the fluorescence statistics module.

The raw fluorescence trace data were stored in a photon arrival time (PAT) format. The PAT is the most efficient way of encoding photon count data in the regime where number of photon counts is much smaller than the number of available time bins in the data acquisition hardware.[62, 150] We developed an efficient approach to compute intensity auto- and cross-correlation functions and photon count histograms using PAT information directly. Storing F(t) and calculating $G(\tau)$ and $P(k;\Delta T)$ using the PAT format obviated the need to store and carry out computations of time bins that have zero counts.

4.5.2 Effects of photophysics on $G(\tau)$ and $P(k;\Delta T)$

FFM experiments at high excitation light intensity with photolabile fluorophores can be complicated by triplet state kinetics as well as by photobleaching (Figure 4.4D). These two phenomena are often found concurrently: excitation to higher energy levels increases both the probability of intersystem crossing and photobleaching. The effects are readily

controlled in our simulation method.

Analytical forms for $G(\tau)$[264]and $P(k;\Delta T)$[188] have been developed for molecules that undergo intersystem crossing into a triplet state. Simulations with triplet state photophysics (Figure 4.3B) show excellent agreement with $G(\tau)$ predicted from theory. The histogram analysis in Figure 4.3C showed that $P(k;\Delta T)$ computed with triplet state kinetics can be fit well by the super-Poissonian theory neglecting photophysical effects. Palo *et al.* (2000)[188] propose that the effects of triplet state trapping on $P(k;\Delta T)$ may be accounted for by using apparent specific brightness and concentration values according to:

$$\begin{aligned} N_{app} \propto c_{app}(\Delta T) &= \frac{c}{\Gamma_{trip}(\Delta T)\Gamma_{diff}(\Delta T)(1+\kappa\tau)} \\ \varepsilon_{app} = q_{app}(\Delta T) &= q\Gamma_{trip}(\Delta T)\Gamma_{diff}(\Delta T) \end{aligned} \tag{4.13}$$

where ΔT is the histogram bin time, κ is the singlet-triplet transition rate, τ is the triplet lifetime, and $\Gamma_{trip}(\Delta T)$ and $\Gamma_{diff}(\Delta T)$ are correction factors for triplet events and diffusive mixing, respectively, occuring within the time ΔT. Specifically for triplet state dynamics:

$$\Gamma_{trip}(\Delta T) = \frac{\left\{2\lambda f\left[1+f-\lambda\left(1-e^{-(1+f)/\lambda}\right)\right]\right\}}{(1+f)^3} \tag{4.14}$$

where $\lambda = \tau/\Delta T$ and $f = \kappa\tau$. Using Eq. 4.14, however, leads to a significant underestimation of the specific brightness and particle concentration compared to the values from the simulation and those obtained through $P(k;\Delta T)$-fitting (Figure 4.3C). Significantly, this implies that the current theory described by Palo *et al.* (2000)[188] is insufficient for use in determining triplet state parameters from $P(k;\Delta T)$.

Photobleaching effects become apparent on $G(0_+)$ and τ_D (with little change in the shape of $G(\tau)$) when the characteristic time constant for photobleaching is as low as 1%

of the diffusion time (Figure 4.4B). The simulations of photobleaching (Figs. 4.4 and 4.5) are qualitatively consistent with what is expected from removal of fluorophores from the excitation volumes. Ignoring the effects of photobleaching on $G(\tau)$ can produce significant underestimation of particle concentrations and overestimation of particle mobility. An important finding from our simulations is that the $P(k;\Delta T)$ shape profile is quite insensitive to photobleaching dynamics, as was also found for triplet state dynamics. The main determinants of $P(k;\Delta T)$ are the steady-state fluorescence properties of the molecules under study, even if the time scales for $P(k;\Delta T)$ binning are comparable to the timescale of the kinetics.

There is no analytical expression for the fluorescence autocorrelation as a function of photobleach time because the probability of photobleaching depends in an unknown way on the non-uniform excitation across the excitation volume. Eggeling *et al.* (1998)[60] and Dittrich and Schwille (2001)[56] have developed an approximate expression for $G(\tau)$ (Eq. 4.11) assuming the excitation probability is uniform across the excitation volume. Eq. 4.11 describes the data well (Figure 4.4C) indicating that photobleaching in FCS experiments can be thought of as a unimolecular kinetic process independent of the diffusional motion of the fluorophore through the excitation beam. According to this view, effects of photobleaching on FCS experiments become apparent when the effective photobleach time (τ_{bleach} of Eq. 4.11) becomes comparable to the characteristic time for diffusion through the excitation beam (e.g., $\tau_{bleach} = 0.53$ and $\tau_D = 0.34$ ms for the conditions in Figure 4.4C).

4.5.3 Molecular interactions

Two-color FFM (TCFFM) has been used to measure the concentration of bound fluorophores,[138] which relies on the fact that $G(0_+)$ and τ_D of the cross-correlation function contain information only about bound fluorophores. As predicted, our simulations showed that at constant fluorophore concentration $G(0_+)$ parallels the fraction of bound fluorophores (Figs. 4.6A and B). The fitted diffusion time for the cross-correlation function (0.83-0.97 ms) was greater than that of the monomer (0.42 ms), as expected for slower dimer diffusion. $G(0_+)$ for the cross-correlation function at 100% bound (0.165) was similar to that for the autocorrelation function (0.163), indicating that all fluorophores are detected. These simulations validate the use of cross-correlation methods to measure concentrations of bound fluorophores.

In a common implementation of two-color FFM, two laser beams are used, with each laser beam exciting a single class of fluorophores. It is generally advocated that the two laser beams must be of equal intensity and superimposed if $G(\tau)$ is to be analyzed by simple diffusional models (Schwille et al., 1997). Imperfect beam alignment was modeled as an application of the TCFCM simulation. Our results (Figure 4.6D) indicate that the beams may be displaced as much as 20% of the width of the excitation beam without significant effects on $G(\tau)$. However, an offset of several times the width can lead to a peak in the cross-correlation (Figure 4.6C, inset). Such a peak in $G_{AB}(\tau)$ is also seen for transient association of A and B,[107] so that mis-registration of the two excitation beams in two-color FFM could be wrongly interpreted in terms of kinetic phenomena.

Fluorophore binding can also change $G(\tau)$ curve shape.[233] Dynamic effects were

simulated by stopping a fluorophore in its trajectory for a randomly chosen time so as to produce first order unbinding kinetics. When binding occurs without a change in quantum yield and on the time scale of diffusion through the illumination volume (Figure 4.7A), significant effects on $G(0_+)$ and D were found even though the $G(\tau)$ curve shape was well described by simple diffusion (Eq. 4.9). The $G(\tau)$ curve shape differed from that predicted by simple diffusion when the diffusion time was increased by 10-fold. When binding occurs with a change in quantum yield (Figure 4.7B), there are significant changes in the shape of $G(\tau)$ for all rates of diffusion. Thus, fluorophore binding to a slowly diffusing or immobile object on a time scale of the diffusion time or faster may not be detected from a curve-shape analysis of $G(\tau)$ unless there is a change in fluorescence quantum yield upon binding.[107] Furthermore, immobile fluorophores are not detected, producing an overestimate (Figure 4.7A) or underestimate (Figure 4.7B) in fluorophore concentration.

4.5.4 Anomalous diffusion and molecular crowding

Anomalous diffution can generally be defined as diffusion in which the mean-squared-displacement (msd) of a particle is not proportional to time. Another commonly used definition of anomalous diffusion is that $msd \propto t^{\alpha}$, where $\alpha \neq 1$. In analysis of FFM data, the parameter α is determined by fitting Eq. 4.12 to the data and used as a semi-empirical measure of anomalous diffusion. The approach used here was to investigate the effects of three "non-normal" diffusive models (normal diffusion plus drift, reflecting boundary conditions, and crowding) on FFM data..

Anomalous diffusion has been reported for molecular diffusion in crowded biological environments such as membranes and cytoplasm.[229, 261] Anomalous super-diffusion, charac-

terized by upward-curved MSD plots, can be produced by directed movement by convective or motor-driven processes. Anomalous sub-diffusion, seen as downward-curved MSD plots, can be produced by confined or restricted diffusion. Anomalous diffusion in FFM analysis has been analyzed semi-empirically using Eq. 4.12, in which a parameter α is included. The parameter α describes the power-law behavior of the MSD: $r^2 \sim t^\alpha$. An α of unity signifies simple diffusion, with $\alpha < 1$ indicating sub-diffusion and $\alpha > 1$ super-diffusion.

Simulations of super-diffusion and sub-diffusion in Figure 4.8 produced non-linear MSD plots and altered $G(\tau)$ curve shape. Super-diffusion, modeled by convection, produced an upwardly curved MSD relation (Figure 4.8A) as expected. Significant deviations in $G(\tau)$ from simple diffusion were found (Figure 4.8B). $G(0_+)$ was unaffected by drift velocity, indicating the average number of particles in the excitation beam was unaffected by drift velocity. However, the apparent diffusion time τ_D increased with drift velocity as a consequence of the reduced time a particle remains in the excitation volume. Notably, $G(\tau)$ were fitted reasonably well such Eq. 4.12 with $\alpha > 1$, providing the first direct validation for use of Eq. 4.12 in FCS analysis of anomalous diffusion.

Sub-diffusion, modeled by confining particles to a rectangular box with reflecting boundary conditions, produced downwardly curved MSD plots (Figure 4.8A). When the dimensions of the box became comparable to those of the excitation volume both $G(0_+)$ and τ_D decreased, with a small change in α. $G(0_+)$ decreases because of the apparent increase in particle concentration as particles are unable to diffuse out of the beam. τ_D decreases because collisions with the box walls de-correlate particle motion, reducing apparent particle transit time across the excitation volume. An important implication of these simulations is

that FCS analysis of solute diffusion in a small confined compartments (such as an intracellular organelle) could produce overestimations of solute diffusion and concentration without significant change in $G(\tau)$ shape.

Molecular crowding, defined as the volume exclusion of solvent by a crowder, can strongly slow solute diffusion and potentially produce anomalous sub-diffusion.[45,93,273] Calculation of solute diffusion in crowded solutions using statistical mechanical theories, and comparison with experimental data, suggest that the solute and crowder can be modeled effectively as hard spheres with the solvent modeled as a continuum. Extensions to this model include attractive potentials[93] and Lennard-Jones and Coulomb interactions.[63] Here, crowding was simulated using Brownian dynamics with repulsive interactions between crowder and solute (Figure 4.8D). With large spheres at 59% by volume as crowder, solute diffusion was slowed 2.5-fold with $G(\tau)$ fitting well to a simple diffusion model ($\alpha = 1$) (Figure 4.8E). These results are in agreement with experimental data showing non-anomalous diffusion of the small solute Rhodamine G with Ficoll-70 crowder concentrations of up to 60 wt% producing a 140-fold slowing of diffusion.[45]

Measurement of the diffusion of larger solutes with Ficoll-70 as a crowding agent also show non-anomalous diffusion.[45,46] However, Weiss *et al.* (2004)[261] found anomalous diffusion of large dextrans (10-2000 kDa) and IgG when cell cytoplasm was used as a crowding agent. This apparent discrepancy has not been resolved. Because of computational time constraints, it was not possible here to carry out the computationally intensive simulations of crowding by large diffusing particles.

In conclusion, we have reported a general method for simulation of FCS data. The

method was used to investigate effects of beam geometry, photophysical processes, binding, anomalous diffusion, and crowding. Our approach should prove useful in the design and analysis of FCS studies on biological systems with complex diffusive phenomena. Moreover, our approach can be used to carefully study the consequences of measurement non-idealities such as FRET, background fluorescence, and detector cross-talk, on TCFFM data analysis, a subject for future development.

4.6 Appendix 4A: Procedure to construct a photon arrival time (PAT) list

A PAT list, $p^{\Delta t}(i) \triangleq \left\{b^{\Delta t}(i),\ k^{\Delta t}(i)\right\}$, of length M and bin time, Δt, can be re-binnd with time, $m\Delta t$, to generate the binned PST, $p^{m\Delta t}(i)$, using the following procedure:

$$
\begin{aligned}
&\texttt{For}\ \ (i = 1,\ i \leq M,\ i++)\ \ \{\\
&\qquad \texttt{If}\ \ (i == 1)\ \ \texttt{then}\ \ (remainder\,(i) \leftarrow 0)\\
&\qquad\qquad \texttt{else}\ \ \left(remainder\,(i) \leftarrow Mod\left[b^{\Delta t}(i-1) - carry(i-1),\ m\right]\right)\\
&\qquad \texttt{If}\ \ (remainder\,(i) == 0)\ \ \texttt{then}\ \ (carry\,(i) \leftarrow 0)\\
&\qquad\qquad \texttt{else}\ \ (carry\,(i) \leftarrow (m - remainder(i)))\\
&\qquad b^{temp}(i) \leftarrow RoundUp\left[\left(b^{\Delta t}(i) - remainder(i)\right)/m\right]\\
&\}\\
&\texttt{For}\ \ (i = M,\ i > 1,\ i--)\ \ \{\\
&\qquad \texttt{If}\ \ \left(b^{temp}(i) == 0\right)\ \ \texttt{then}\ \ \left(k^{temp}(i-1) \leftarrow k^{\Delta t}(i-1) + k^{\Delta t}(i)\right)\\
&\qquad\qquad \texttt{else}\ \ \left(k^{temp}(i-1) \leftarrow k^{\Delta t}(i)\right)\\
&\qquad p^{temp}(i) \leftarrow \left\{b^{temp}(i),\ k^{temp}(i)\right\}\\
&\}\\
&p^{m\Delta t}(i) = Select\left[p^{temp}(i),\ b^{temp}(i) > 0\right]
\end{aligned}
$$

where $Mod\,[x, y] = x - y \cdot RoundDown\,[x/y]$ and $Select\,[x, y]$ selects all elements of x for which y is true.

4.7 Appendix 4B: Levenberg-Marquardt fitting routines used to fit photon count histograms within Mathematica

■ Levenberg-Marquardt fitting of PCH data

```
<<Statistics‘DiscreteDistributions‘;
<<LinearAlgebra‘MatrixManipulation‘;

LMpch[Ptable_,M_,toler_,mult_,paramlist_List,PSF_:1]:=

  Module[{weitable,covar,oneda,da,Πtable,△table,DΠtable,atry,limits,oldchisq,
   chisq,oldatry,change,λ,condition,temp},

    Print["PSF = ", PSF]; Print["Ptable = ",Ptable];
    limits=Qlim[Ptable]; Print["limits = ",limits];
    weitable=Weipch[Ptable,limits,M]; Print["weitable = ",weitable];

    (*BEGIN LOOP TO CONVERGE CHISQ*)
    λ=-1;chisq=0; change=1000; Print["Begin LM loop"];Print["begin"];
    condition=True; iter=0; fail=0;

    While[condition && iter≤77,
        {Print["Iteration: ", iter++];
            (*INITIALISATION*)
            If[λ﹅-1,{{atry=paramlist,oldatry=atry},λ=mult,firsttime=0}];

            (*ASSIGNMENT OF THE MATRIX*)
            If[firsttime﹅0,{firsttime++;
                Print["atry = ",atry];
                Πtable=Pch[atry,limits,PSF]; Print["Πtable = ",Πtable];
                △table=Diffpch[Ptable,Πtable,limits];
                oldchisq=Chisquare[△table,weitable,limits];
                Print["oldchisq = ",oldchisq]; Print[first];}
              ];

            ptable=Pcharray[atry,limits,PSF];
            DΠtable=Derpch[ptable,limits,atry,PSF];
            covar=Alphapch[weitable,DΠtable,limits];
            covar[[1,1]]=covar[[1,1]]*(1+λ);
            covar[[2,2]]=covar[[2,2]]*(1+λ);
            oneda=Betapch[△table,weitable,DΠtable,limits];

            (*SOLUTION OF LINEAR EQNS AND SOLVE FOR A NEW CHISQ*)
            da=LinearSolve[covar,oneda];
            atry=atry+da;
            Πtable=Pch[atry,limits,PSF];
            △table=Diffpch[Ptable,Πtable,limits];
            chisq=Chisquare[△table,weitable,limits];

            (*DID THE TRIAL SUCCEED?*)
            If[oldchisq﹅0,change=0,
              If[chisq≤oldchisq,
                {(*SUCCESS,ACCEPT THE NEW SOLUTION*)
                  (change=(oldchisq-chisq)/oldchisq )≤toler;
                  λ=λ*mult;
                  Print["Iteration: ", iter++,"\t\tSUCCESS!","\t\tλ = ",λ];
                  oldchisq=chisq; oldatry=atry;
                  },
                {(*FAILURE,INCREASE λ AND RETURN*)
                  λ=λ/mult;
                  chisq=oldchisq; atry=oldatry;
                  Print["Iteration: ", iter++,"\t\tFAILED!","\t\tλ = ",λ];
                  fail++;
                  }]];
```

```
        If[((change<toler) && (Abs[λ]<toler)),condition=False];
        If [(chisq<1/(2M)),condition=False] ;
        Print[chisq,":",change,"::",atry];
        };
    ]

  Print["Failure rate = ", N[ fail/iter]];

(*NOW SET λ=0 AND SOLVE FOR covar^-1 TO GET ERRORS*)
λ=0;
ptable=Pcharray[atry,limits,PSF];
Dπtable=Derpch[ptable,limits,atry,PSF];
covar=Alphapch[weitable,Dπtable,limits];
covar[[1,1]]=covar[[1,1]]*(1+λ);
covar[[2,2]]=covar[[2,2]]*(1+λ);
oneda=Betapch[Δtable,weitable,Dπtable,limits];
da=LinearSolve[covar,oneda]; Print["LinearSolve = ",da];
atry=atry+da;Print["oldatry = ", oldatry]; Print["atry = ",atry];
πtable=Pch[atry,limits,PSF];
Δtable=Diffpch[Ptable,πtable,limits];
chisq=Chisquare[Δtable,weitable,limits];
Print["Chisquare = ", chisq];
Print["Errors in Parameters = ", Inverse[covar]];

Return[atry];
]
```

■ Levenberg-Marquardt fitting of log-scaled PCH data

```
LMlogpch[Ptable_,M_,toler_,mult_,paramlist_List,PSF_:1]:=

  Module[{weitable,covar,oneda,da,πtable,Δtable,Dπtable,atry,limits,
   oldchisq,chisq,oldatry,change,λ,condition,temp},

    limits=Qlim[Ptable]; Print["limits = ",limits];
    weitable=Weilogpch[Ptable,limits,M]; Print["weitable = ",weitable];

    (*BEGIN LOOP TO CONVERGE CHISQ*)
    λ=-1;chisq=0; change=1000; Print["Begin LM loop"]; Print["begin"];
    condition=True; iter=0; fail=0;

    While[condition && iter≤50,
        {Print["Iteration: ", iter++];
            (*INITIALISATION*)
            If[λ、-1,{{atry=paramlist,oldatry=atry},λ=mult,firsttime=0}];

            (*ASSIGNMENT OF THE MATRIX*)
            If[firsttime、0,{firsttime++; Print["atry = ",atry];
                temp=Pch[atry,limits,PSF];
                πtable=Transpose[{temp[[All,1]],Log[temp[[All,2]]]}];
                Δtable=Diffpch[Ptable,πtable,limits];
                oldchisq=Chisquare[Δtable,weitable,limits];
                Print["oldchisq = ",oldchisq]; Print[first];}
              ];

            ptable=Pcharray[atry,limits,PSF];
            Dπtable=Derlogpch[ptable,limits,atry,PSF];
            covar=Alphapch[weitable,Dπtable,limits];
            covar[[1,1]]=covar[[1,1]]*(1+λ);
            covar[[2,2]]=covar[[2,2]]*(1+λ);
            oneda=Betapch[Δtable,weitable,Dπtable,limits];

            (*SOLUTION OF LINEAR EQNS AND SOLVE FOR A NEW CHISQ*)
            da=LinearSolve[covar,oneda];
            atry=atry+da;
            temp=Pch[atry,limits,PSF];
```

```
          Πtable=Transpose[{temp[[All,1]],Log[temp[[All,2]]]}];
          Δtable=Diffpch[Ptable,Πtable,limits];
          chisq=Chisquare[Δtable,weitable,limits];

          (*DID THE TRIAL SUCCEED?*)
          If[oldchisq≠0, change=0,
            If[chisq≤oldchisq,
              {(*SUCCESS,ACCEPT THE NEW SOLN.*)
                (change=(oldchisq-chisq)/oldchisq )≤toler;
                Print["SUCCESS!"];
                λ=λ*mult; Print["λ = ",λ];
                oldchisq=chisq; oldatry=atry;
                },
              {(*FAILURE,INCREASE λ AND RETURN*)
                λ=λ/mult; chisq=oldchisq;
                atry=oldatry; Print["FAILED!"]; Print["λ = ",λ];
                fail++;
                }]];

          Print["change = ",change,"\ttoler = ",toler,"\tAbs[λ] = ",Abs[λ]];
          If[((change<toler) && (Abs[λ]<toler)),condition=False];
          If [(chisq<0.0001), condition=False] ;
          Print[chisq,":",change,"::",atry];
          };
      ]
    Print["Failure rate = ", N[ fail/iter]];

  (*NOW SET λ=0 AND SOLVE FOR covar^-1 TO GET ERRORS*)
  λ=0;
  ptable=Pcharray[atry,limits,PSF];
  DΠtable=Derlogpch[ptable,limits,atry,PSF];
  covar=Alphapch[weitable,DΠtable,limits];
  covar[[1,1]]=covar[[1,1]]*(1+λ);
  covar[[2,2]]=covar[[2,2]]*(1+λ);
  oneda=Betapch[Δtable,weitable,DΠtable,limits];
  da=LinearSolve[covar,oneda]; Print["LinearSolve = ",da];
  atry=atry+da; Print["oldatry = ", oldatry]; Print["atry = ",atry];
  Πtable=Pch[atry,limits,PSF];
  Δtable=Diffpch[Ptable,Πtable,limits];
  chisq=Chisquare[Δtable,weitable,limits];
  Print["Chisquare = ", chisq];
  Print["Errors in Parameters = ", Inverse[covar]];

  Return[atry];
  ]
```

■ Determine the k-range limit for a PCH

```
Qlim[Ptable_List]:=

  Module[{kmin,kmax,limits},
    kmin=Min[Ptable[[All,1]]];kmax=Max[Ptable[[All,1]]];

    (* go up k until one encounters a zero probability *)
    For[k=kmin, k≤kmax, k++,
      If[Ptable[[k-kmin+1, 2]]≠0,
        {kmax=k,kmax--,Break[]}]
      ];
    limits={kmin,kmax};

    Return[limits];
    ]
```

■ Calculate weights for fitting to a PCH

```
Weipch[Ptable_List,limits_List,M_]:=

  Module[{weitable,w,kmin,kmax,nelements,kcounts,p},

    kmin=limits[[1]]; kmax=limits[[2]]; nelements=(kmax-kmin+1);
    weitable=Array[w, {nelements,2}];
    For[j=1, j≤nelements, j++,
      {kcounts=kmin+j-1; w[j,1]=kcounts; p=Ptable[[j,2]];
        If[Ptable[[j,2]]、0, Print["WARNING! weights are off!"],
          w[j,2]=(M/(p(1-p)))];
        }
      ];

    Return[weitable];
    ]
```

■ Calculate the weights for fitting to a log-scaled PCH

```
Weilogpch[Plogtable_List,limits_List, M_]:=

  Module[{weitable,w,kmin,kmax,nelements,kcounts,p},

    kmin=limits[[1]]; kmax=limits[[2]]; nelements=(kmax-kmin+1);
    weitable=Array[w, {nelements,2}];
    For[j=1, j≤nelements, j++,
      {kcounts=kmin+j-1; w[j,1]=kcounts; p=Exp[Plogtable[[j,2]]];
        If[Ptable[[j,2]]、0, Print["WARNING! weights are off!"],
          w[j,2]=Log[Sqrt[M/(p(1-p))]]];
        }
      ];

    Return[weitable];
    ]
```

■ Calculate the difference between PCH data and en estimated PCH

```
Diffpch[Ptable_List,Πtable_List,limits_List]:=

  Module[{kmin,kmax,△,△table,nelements},

    kmin=limits[[1]]; kmax=limits[[2]]; nelements=(kmax-kmin+1);
    △table=Array[△,{nelements,2}];
    For[j=1, j≤nelements,j++,
      {△[j,1]=Ptable[[j,1]];
        △[j,2]=Ptable[[j,2]]-Πtable[[Ptable[[j,1]]+1,2]];
        }
      ];

    Return[△table];
    ]
```

■ Calculate the Chi squared for fitting a PCH

```
Chisquare[Δtable_List,weitable_List,limits_List]:=

  Module[{χ2,kmin,kmax,nelements},

    kmin=limits[[1]]; kmax=limits[[2]]; nelements=(kmax-kmin+1);
    χ2=Sum[weitable[[j,2]]*(Δtable[[j, 2]])^2, {j,1,nelements}];

    Return[χ2];
    ]
```

■ Calculate alpha factor for Levenberg-Marquardt fitting of PCH

```
Alphapch[weitable_List,DΠtable_List,limits_List]:=

  Module[{α,a,kmin,kmax,nelements},

    kmin=limits[[1]]; kmax=limits[[2]]; nelements=(kmax-kmin+1);

    α=Array[a,{2,2}];
    a[1,1]=Sum[weitable[[j,2]]*(DΠtable[[j, 2]])^2, {j,1,nelements}];
    a[2,2]=Sum[weitable[[j,2]]*(DΠtable[[j, 2]])^2, {j,1, nelements}];
    a[1,2]=a[2,1]=Sum[weitable[[j,2]]*(DΠtable[[j,2]]*DΠtable[[j,3]]),
     {j,1,nelements}];

    Return[α];
    ]
```

■ Calculate beta factor for Levenberg-Marquardt fitting of PCH

```
Betapch[Δtable_List,weitable_List,DΠtable_List,limits_List]:=

  Module[{β,b,kmin,kmax,nelements},

    kmin=limits[[1]]; kmax=limits[[2]]; nelements=kmax-kmin+1;
    β=Array[b,2];

    b[1]=Sum[weitable[[j,2]]*Δtable[[j,2]]*DΠtable[[j,2]],
     {j,1, nelements}];
    b[2]=Sum[weitable[[j,2]]*Δtable[[j,2]]*DΠtable[[j,3]],
     {j,1,nelements}];
    (* limits (+1) corrected to account for indexing *)

    Return[β];
    ]
```

■ Calculate the analytical derivatives for fitting a PCH

```
Derpch[ptable_List, limits_List, paramlist_List, PSF_: 1] :=

 Module[{ntotal, kmin, kmax, DΠtable, dΠ, dpϵ, s, nmean, ϵ, nelements, kcounts},

  kmin = limits[[1]]; kmax = limits[[2]];
  (* we use kmin and kmax here instead of 0->kmax to eliminate unnecessary
     calculations that could slow down the LM routine.  Note that as a
     result the indexing used here is different than than in the similarly
     structured Pch routine *)

  nmean = Abs[paramlist[[1]]]; ϵ = Abs[paramlist[[2]]];
  nelements = (kmax - kmin + 1);
  ntotal = Quantile[PoissonDistribution[nmean], 0.999999999];

  (* For k>0!! *)
  dp3DG[k_] := ((2 √(2/π)) / (ϵ k!)) NIntegrate[Exp[-ϵ Exp[-2 x^2]] (ϵ Exp[-2 x^2])^k,
     {x, 0, ∞}];
  dp2GL[k_] :=
   (((π/2)^(1-2 k)) / (ϵ k!)) NIntegrate[Exp[-4 ϵ/π^2 (1 + x^2)^2] (1 + x^2) (ϵ/(1 + x^2)^2)^k,
     {x, 0, ∞}];

  (* need to create an array of theoretical dp(n)/dϵ's as function of k *)
  dpϵtable = Array[dpϵ, {ntotal + 1, nelements}, 0];
  dpϵ[0, 0] = 0; (* dpϵ[0, k]=0 for all k=0->kmax.  See below *)
  For[n = 1, n / ntotal, n++, {
    s = 0;
    For[k = 1, k / kmax, k++, {
      If[n == 1,
       {dpϵ[0, k] = 0, (* dpϵ[0, k]=0 for all k=0->kmax *)
        If[PSF == 0, dpϵ[1, k] = dp3DG[k], dpϵ[1, k] = dp2GL[k]]
       },
       {dpϵ[n, k] = Sum[dpϵ[1, k - r] * ptable[[n - 1 + 1, r + 1]] +
           ptable[[1 + 1, k - r + 1]] * dpϵ[n - 1, r], {r, 0, k}]
       }
      ];
      s = s + dpϵ[n, k];}
    ];
    dpϵ[n, 0] = -s;}
  ];

  (* create array dΠ(k) corresponding to experimental values *)
  DΠtable = Array[dΠ, {nelements, 3}];
  For[j = 1, j / nelements, j++,
   {kcounts = kmin + j - 1,
    dΠ[j, 1] = kcounts,
    dΠ[j, 2] = (*nmean=*)
     Sum[ptable[[n + 1, kcounts + 1]] (i^-nmean (n - nmean) nmean^(-1+n) / n!),
      {n, 0, ntotal}],
    dΠ[j, 3] = (*ϵ=*) Sum[dpϵ[n, kcounts] (i^-nmean nmean^n / n!), {n, 1, ntotal}],
   }];

  Return[DΠtable];
 ]
```

■ Calculate the analytical derivatives for fitting a log-scaled PCH

```
Derlogpch[ptable_List, limits_List, paramlist_List, PSF_:1] :=

 Module[{ntotal, kmin, kmax, DΠtable, dΠ, dpϵ, s, nmean, ϵ, nelements, kcounts},

  kmin = limits[[1]]; kmax = limits[[2]];
  (* we use kmin and kmax here instead of 0↓kmax to eliminate unnecessary
     calculations that could slow down the LM routine.  Note that as a
     result the indexing used here is different than than in the similarly
     structured Pch routine *)

  nmean = Abs[paramlist[[1]]]; ϵ = Abs[paramlist[[2]]];
  nelements = (kmax - kmin + 1);
  ntotal = Quantile[PoissonDistribution[nmean], 0.999999999];

  (* For k>0 !! *)
  dp3DG[k_] := NIntegrate[Exp[-ϵ Exp[-2 x^2]] (ϵ Exp[-2 x^2])^k, {x, 0, ∞}] /
    (ϵ NIntegrate[Gamma[k, 0, ϵ Exp[-2 x^2], {x, 0, ∞}]]);
  dp2GL[k_] :=
   (2/π)^(2 k) NIntegrate[(1 + x^2) (ϵ/(1 + x^2)^2)^k Exp[-4 ϵ/(π^2 (1 + x^2)^2)],
      {x, 0, ∞}] / (ϵ NIntegrate[(1 + x^2) Gamma[k, 0, 4 ϵ/(π^2 (1 + x^2)^2)],
        {x, 0, ∞}]);

  (* need to create an array of theoretical dp(n)/dϵ's as function of k *)
  dpϵtable = Array[dpϵ, {ntotal + 1, nelements}, 0];
  dpϵ[0, 0] = 0; (* dpϵ[0, k]=0 for all k=0->kmax.  See below *)
  For[n = 1, n/ntotal, n++, {
    s = 0;
    For[k = 1, k/kmax, k++, {
      If[n == 1,
       {dpϵ[0, k] = 0, (* dpϵ[0, k]=0 for all k=0->kmax *)
        If[PSF == 0, dpϵ[1, k] = dp3DG[k], dpϵ[1, k] = dp2GL[k]]
       },
       {dpϵ[n, k] = Sum[dpϵ[1, k - r] * ptable[[n - 1 + 1, r + 1]] +
           ptable[[1 + 1, k - r + 1]] * dpϵ[n - 1, r], {r, 0, k}]
       }
      ];
      s = s + dpϵ[n, k];}
    ];
    dpϵ[n, 0] = -s;}
  ];

  (* create array dΠ(k) corresponding to experimental values *)
  DΠtable = Array[dΠ, {nelements, 3}];
  For[j = 1, j/nelements, j++,
   {kcounts = kmin + j - 1,
    dΠ[j, 1] = kcounts,
    dΠ[j, 2] = (*nmean=*) Sum[ptable[[n + 1, kcounts + 1]] + (-1 + n/nmean),
      {n, 0, ntotal}],
    dΠ[j, 3] = (*ϵ=*) Sum[dpϵ[n, kcounts] + Log[(nmean^n Exp[-nmean]/n!)],
      {n, 1, ntotal}],
   }];

  Return[DΠtable];
 ]
```

■ PCH array generator for use in Pch[] and DerΠ[]

```
Pcharray[paramlist_List, limits_List,  PSF_: 1] :=

 (* paramlist_List is {nmean, ∈} *)
 (* limits_List is {kmin, kmax} *)
 (* If PSF=0, use 3-d Gaussian form for p(1);
  otherwise, use Gaussian Lorentzian *)

 Module[{nmean, ∈, kmax, ntot, p, s, ptable},

  nmean = Abs[paramlist[[1]]];
  ∈ = Abs[paramlist[[2]]];
  kmax = limits[[2]];
  (* calculate  all k:0↓kmax entries.
      Need for the recursion relationships *)

  ntot = Quantile[PoissonDistribution[nmean], 0.999999999];

  p2GL[k_] := (π / (2 k!)) * NIntegrate[(1 + x^2) Gamma[k, 0, 4 ∈ / (π^2 (1 + x^2)^2)],
      {x, 0, ∞}];

  p3DG[k_] := Sqrt[2 / π] (2 / k!) NIntegrate[Gamma[k, 0, ∈ Exp[-2 x^2]],
      {x, 0, ∞}];

  ptable = Array[p, {ntot + 1, kmax + 1}, 0];
  p[0, 0] = 1;
  For[n = 1, n ⩽ ntot, n++, {
    s = 0,
    For[k = 1, k ⩽ kmax, k++, {
      If[n == 1,
       {p[0, k] = 0, {If[PSF ≠ 0, p[1, k] = p3DG[k], p[1, k] = p2GL[k]]}},
       p[n, k] = Sum[p[1, k - r] p[n - 1, r], {r, 0, k}]
      ],
      s = s + p[n, k]}
    ],
    p[n, 0] = 1 - s}
  ];

  Return[ptable];
  (* ptable is indexed from '0' while it is returned indexed at '1' *)
 ]
```

- **PCH generator. Returns a table of k counts vs. Π(k)**

```
Pch[paramlist_List,limits_List,PSF_:1]:=

 Module[{nmean,ϵ,kmax,ntot,ptotal,Π,Πtable,loggtable,logg,summation,
  kave,k,ptable},

  nmean=Abs[paramlist[[1]]];
  ϵ=Abs[paramlist[[2]]];
  kmax=limits[[2]];

  ntot=Quantile[PoissonDistribution[nmean],0.999999999];
  ptable=Pcharray[paramlist,limits,PSF];
  Πtable=Array[Π,{kmax+1,2},0];
  loggtable=Array[logg,{kmax+1,2},0]; summation=0;

  For[k=0,k≤kmax,k++,{
    Π[k,0]=logg[k,0]=k;
    Π[k,1]=Sum[ptable[[i+1,k+1]]((nmean^i)/i!) Exp[-nmean],{i,0,ntot}];
    logg[k,1]=Log[Π[k,1]]; summation=summation+Π[k,1];
    If[summation≥0.5&&(summation-Π[k,1])≤0.5,kave=k];
    }
   ];

  Return[Πtable];
 ]
```

- **Generates a random sequence of counts/sec according to statistics of atheoretical PCH specified. N.B.Genraw[] calls PCH[]. M is the number of data points.**

```
Genraw[paramlist_List,M_,PSF_:1]:=

  Module[{Π,kmax,rawdata, seq, t, s, randk, randΠ},

    nmean=paramlist[[1]]; ϵ=paramlist[[2]];
    Πtable=Pch[ paramlist,PSF];
    kmax=Max[Πtable[[All,1]]];
    Π=Πtable[[All,2]];

    t=1; s=0;
    OpenAppend["raw.dat"];
    While[t≤M,
      {randk=Random[Integer,{0,kmax}],
        randΠ=Random[Real,{0,1}],
        If[randΠ≤Π[[randk+1]],(* +1 for indexing...*)
          (*I believe the following criteria is more correct but it
            takes much longer to compute:
               randΠ≤Random[BinomialDistribution[M,Π[[randk+1]]]]/M
            This builds in the k-dependent variations in σ(k) for Π(k)
            *)
          {Write["raw.dat",randk], t++}]
        }];

    Close["raw.dat"];
    ]
```

■ Generates a simulated PCH

```
Simpch[paramlist_List, M_, PSF_: 1] :=

 Module[{nmean, ∈, kmax, ntotal, p, s, Π, Πtable, S, Stable, logS, logStable},

  nmean = paramlist[[1]];
  ∈ = paramlist[[2]];

  Print[ntotal = ,
   ntotal = Quantile[PoissonDistribution[nmean], 0.999999999]];
  Print[kmax = , kmax = Quantile[PoissonDistribution[∈ * nmean], 0.99999999]];

  p2GL[k_] := (π / (2 k !)) NIntegrate[(1 + x^2) Gamma[k, 0, 4 ∈ / (π^2 (1 + x^2)^2)]],
      {x, 0, :→}];
  p3DG[k_] :=
   Sqrt[2 / π] (2 / k !) NIntegrate[Gamma[k, 0, ∈ Exp[-2 x^2]], {x, 0, :→}];

  Array[p, {ntotal + 1, kmax + 1}, 0];
  p[0, 0] = 1;
  For[n = 1, n / ntotal, n++,
   {s = 0;
    For[k = 1, k / kmax, k++, {
      If[n == 1,
       {p[0, k] = 0, If[PSF ≠ 0, p[1, k] = p3DG[k], p[1, k] = p2GL[k]]},
       {p[n, k] = Sum[p[1, k - r] p[n - 1, r], {r, 0, k}]}
      ];
      s = s + p[n, k]}
    ];
    p[n, 0] = 1 - s}
  ];

  Πtable = Array[Π, kmax + 1, 0];
  Stable = Array[S, {kmax + 1, 2}, 0];
  logStable = Array[logS, {kmax + 1, 2}, 0];
  For[k = 0, k / kmax, k++,
   {Π[k] = Sum[p[i, k] ((nmean^i) / i !) Exp[-nmean], {i, 0, ntotal}],
    S[k, 0] = logS[k, 0] = k,
    S[k, 1] = Π[k] (* Use this if you want pure data *)
   }
  ];

  Return[Stable];
 ]
```

■ Simulate an "experimental" PCH from a sequence of counts/sec

```
Genpch[filename_]:=

  Module[{Ptable,P,kmax,kmin,kdatum,nelements,j,rawfile,s},

    (*Loop to determine kmax for initializing array size.
      Ideally,in C one can dynamically allocate memory to do this
     *)

    kmin=1000; kmax=0; kdatum=0;
    rawfile=OpenRead[filename];
    While[kdatum≠"EndOfFile",
      {kdatum=Read[rawfile],
        If[kdatum<kmin, kmin=kdatum];
        If[kdatum>kmax,{kmax=kdatum,Print[kmax]}]}];
    Close[rawfile]; kdatum=0;

    nelements=(kmax-kmin+1);
    Ptable=Array[P,{nelements,2}];
    Ptable[[All,All]]=0;

    (*This is the loop to read in the data into an array whose
      size was defined above*)
    rawfile=OpenRead[filename];
    While[kdatum≠"EndOfFile",{kdatum=Read[rawfile],
        If[kdatum≠"EndOfFile",{j=(kdatum-kmin+1),
        If[Ptable[[j,1]]、0,Ptable[[j,1]]=kdatum],Ptable[[j,2]]++}]}];
    Close[rawfile];

    kmin=Min[Ptable[[All,1]]];

    (* normalization to get (fractional) frequency/probablility *)
    s=Sum[Ptable[[j,2]],{j,1,nelements}];
    Ptable[[All,2]]/=s;

    Return[Ptable];
    ]
```

Chapter 5

Outlook

Since starting this work in 2000, there have been numerous and rapid advances in the development and application of FCS-based methods; a number of excellent reviews now exist documenting these advances.[26, 48, 64] Below, I highlight some of these advances along with new directions I feel merit further work.

One of the most promising and exciting uses of TCFFM for studying the dynamics and interactions of cellular components within living cells. The environments within cellular compartments can be drastically different from those often used in *in vitro* biochemical studies, with protein concentrations *in vivo* often being at least 100 times higher ($\geq$100 mg/mL) than those normally employed in biochemical assays. While a single protein component in a cell may be present at less than 1% of the total protein, the collectively high concentration of macromolecules has been predicted to result in significant chemical non-idealities that dramatically alter both the strength and dynamics of macromolecular associations. This principle of "macromolecular crowding" has been suggested to play an

important role in cell volume regulation, osmotic stress responses, macromolecular drug efficacy, protein-nucleic acid interactions, cellular homeostasis and metabolism, and signal transduction.[24,209,210,216,273] However, there is yet no direct evidence to indicate that macromolecular interactions *in vivo* are significantly different than they are *in vitro*, and that crowding effects can explain these differences. Recent FCS diffusional studies have shown, however, that macromolecular crowding can dramatically affect the diffusability of protein components within the cell.[8,261,262] While genetic approaches are often used to validate the *in vivo* relevance of biochemical measurements, this validation is only qualitative. Absent thus far from arsenal of experimental methods are reliable techniques by which biochemical parameters can be quantified in a living cell as is traditionally done in a test tube. TCFFM offers for the first time, a practical and intrinsic means to measure absolute particle numbers of fluorescent species from the amplitude of fluctuations correlation functions and photon count histogram analysis.

The feasibility of TCFFM in qualitatively monitoring the interactions of GFP-Fos and mRFP-Jun chimeras in living cells was demonstrated recently by Baudendistel *et al.* (2005).[9] Quantifying the affinity of such interacting proteins via TCFFM remains an important and groundbreaking goal. In Chapter 3.2.1, I outlined an experimental strategy for doing this for a bimolecular reactive system, taking into account background fluorescence, bleed-through, and FRET calibration corrections. Other strategies have been proposed recently.[59,72] Baudendistel *et al.*'s study was done using HeLa mammalian cells, which have endogenous pools of Fos and Jun that would confound a quantitative analysis at this point. Currently, no theory exists to account for the presence of "dark" pools among fluorescently

labeled interacting components. A recent exception is the theory developed by Lieto and Thompson (2004),[156] although their work is limited to 2-dimensional geometries and total internal reflection-based FFM. In the absence of a general theory, *in vivo* TCFFM experiments would need to be performed in cells for which such endogenous pools can be genetically removed (e.g., in the yeast *S. cerevisiae*), in order to get any quantitatively meaningful results. The simulation tools described in Chapter 4 may help in studying the consequences of dark reactant pools and effects of other third-party interacting components on the bimolecular reactive system of interest. Both scenarios are highly relevant to the types of reactions that occur within cells. For example, the MAP kinase pathway[230] would be a prime system for *in vivo* biochemical characterization using fluorescence-based studies as recently demonstrated by van Drogen *et al.* (2001).[254] The presence of tertiary interactions, however, would make interpretation of TCFFM data with the current theory difficult.

Both thermodynamic and chemical kinetics of interaction may be studied using TCFFM and the approach is fundamentally applicable to studies of protein-protein interactions in living cells.[64] The potential for TCFFM measurements in cells is exciting because of the prospects of testing macromolecular crowding predictions and studying questions of specificity[1] and the kinetics of interactions involved in cell signaling events.[119,153,197,224]

[1] "Specificity" in cell signalling is usually discussed within the framework of thermodynamics; the preference of a receptor for a ligand "A" over another ligand "B" is quantified using a ratio of dissociation constants, or the *specificity ratio*:

$$S(A,B) \triangleq \frac{K_d^B}{K_d^A}$$

These dissociation constants describe the interplay between forward and reverse binding constants: $K_d = k_{off}/k_{on}$. It is therefore possible to introduce two *kinetic specificity factors*, σ and ζ, defined as follows:

$$\sigma(A,B) \triangleq \frac{k_{on}^A}{k_{on}^B} \quad \text{and} \quad \zeta(A,B) \triangleq \frac{k_{off}^A}{k_{off}^B}$$

$$\ni \quad S(A,B) = \frac{\sigma(A,B)}{\zeta(A,B)}$$

Macromolecular crowding theory predicts that the association of interacting components is enhanced as a function of the following: (1) increasing concentration of background crowder macromolecules, and (2) increasing size of interacting components relative to background macromolecules.[273] Crowding theory also predicts that the specificity of a receptor for a ligand over another ligand is strongly dependent on the relative sizes of the competing ligands: in an increasingly crowded media, binding preference shifts to the larger of two ligands.[174] These predictions could be readily tested using polyethylene glycol (PEG) or dextrans of various molecular weights as crowder agents and concatenating inert β-galactosidase or bovine serum albumin units (∼65 kD each) to components of the model systems described at the end of Section 3.3.3. Extensions of the simulations described in Chapter 4, Section 4.5.4 would also be useful in testing these predictions; however, these simulations are very computationally costly, underscoring the need for improved computational approaches for simulating systems with high particle densities.

The ability of TCFFM to directly report on the chemical "activities" of biomolecules inside cells can be far more profound than simply deducing the difference between the ratio of reactant and product particle numbers measured under ideal conditions and under crowded conditions (see Section 3.3.3). The fluctuation theory of mixtures developed by Kirkwood and Buff over 50 years ago may be the important, though yet unexploited, bridge.[139,169] Kirkwood-Buff solution theory provides a basis for relating particle number fluctuations and

Recasting $S(A,B)$ in terms of σ and ζ can help illumine the kinetic basis for specificity. If $\sigma(A,B) > \zeta(A,B)$, then k_{on} is the major specificity determinant in the binding of ligands A and B. If $\sigma(A,B) < \zeta(A,B)$, however, then k_{off} is the major determinant of specificity. The latter case holds in instances where receptor and ligand are rigid before and after complex formation, as in antibody-hapten systems.[191] For reactions in which there is a disorder-to-order transition upon binding, k_{on} could play an influential role in binding specificity.[58]

non-ideality through the following relations:

$$k_B T \left[\frac{\partial \overline{N}_i}{\partial \mu_j}\right]_{V,T,\mu_{i\neq j}} = \frac{\overline{N}_i \overline{N}_j G_{ij}^{KB}}{V} + \delta_{ij}\overline{N}_i \tag{5.1}$$

where k_B is Boltzmann's constant, T is temperature, N_i is the particle number of species i in the volume V (of a grand canonical ensemble), μ_j is the chemical potential of species j, δ_{ij} is the Kronecker delta function, and $G_{ij}^{KB}$is known as the Kirkwood-Buff integral defined as:

$$G_{ij}^{KB} = 4\pi \int_0^\infty \left[\rho_{ij}(r_{ij}) - 1\right] r_{ij}^2 \, dr_{ij} = V\left[\frac{\langle \delta N_i \delta N_j \rangle}{\langle \delta N_i \rangle \langle \delta N_j \rangle} - \frac{\delta_{ij}}{\langle \delta N_i \rangle}\right] \tag{5.2}$$

where δN is the particle number fluctuation and ρ_{ij} is the pair or radial distribution function commonly used in statistical mechanics. From Eqs. 5.1 and 5.2, it is straightforward to derive a well established thermodynamic-fluctuations relation:[89]

$$\langle \delta N_i \delta N_j \rangle = k_B T \left[\frac{\partial \mu_j}{\partial \overline{N}_i}\right]^{-1}_{V,T,\mu_{l\neq j}} \tag{5.3}$$

where we have used the the fact that $\delta N = N - \overline{N}$. Since experiments are typically conducted under constant pressure and fixed average particle number conditions, (P, $\overline{N}_l$), rather than at constant volume and chemical potential, (V, μ_l),, working with Eq. 5.3 requires a Jacobian transformation:

$$\begin{aligned}
\left.\frac{\partial \mu_j}{\partial \overline{N}_i}\right]_{V,T,\mu_{l\neq j}} &= \left.\frac{\partial\left(\mu_j,\ V, \mu_1 \ldots \mu_{j-1}, \mu_{j+1} \ldots\right)}{\partial\left(\overline{N}_i,\ V, \mu_1 \ldots \mu_{j-1}, \mu_{j+1} \ldots\right)}\right]_T \\
&= \frac{\left.\frac{\partial(\mu_j,\, V, \mu_1 \ldots \mu_{j-1}, \mu_{j+1} \ldots)}{\partial\left(\overline{N}_i,\, P, \overline{N}_1, \ldots \overline{N}_{i-1}, \overline{N}_{i+1} \ldots\right)}\right]_T}{\left.\frac{\partial(V,\, \mu_1 \ldots \mu_{j-1}, \mu_{j+1} \ldots)}{\partial\left(P,\, \overline{N}_i, \ldots \overline{N}_{i-1}, \overline{N}_{i+1} \ldots\right)}\right]_{T,\overline{N}_i}}
\end{aligned} \tag{5.4}$$

where

$$\frac{\partial\left(n_1,\, n_2,\, n_3,\, \ldots\,,\, n_x\right)}{\partial\left(d_1,\, d_2,\, d_3,\, \ldots\,,\, d_x\right)} = \begin{vmatrix} \partial n_1/\partial d_1 & \partial n_1/\partial d_2 & \partial n_1/\partial d_3 & \partial n_1/\partial d_x \\ \partial n_2/\partial d_1 & & & \\ \partial n_3/\partial d_1 & & \ddots & \vdots \\ \vdots & & & \\ \partial n_x/\partial d_1 & & \cdots & \partial n_x/\partial d_x \end{vmatrix}$$

From the definition of the chemical potential:

$$\mu_j = \mu_j^{\circ}(P,T) + n_{Av}k_BT\ln\left(\gamma_j\overline{N}_i/\overline{N}_{tot}\right) \tag{5.5}$$

where μ_j° is the standard chemical potential, n_{Av} is Avogadro's number, and γ is the activity coefficient, the partial derivatives involved in Eq. 5.4 are as follows:

$$\left.\frac{\partial\mu_j}{\partial\overline{N}_i}\right\rfloor_{P,T,N_{l\neq i}} = n_{Av}k_BT\left(\frac{\delta_{ij}}{\overline{N}_j} - \frac{1}{\overline{N}_{tot}} + \frac{\partial\ln\gamma_j}{\partial\overline{N}_i}\right) \tag{5.6}$$

$$\left.\frac{\partial\mu_j}{\partial P}\right\rfloor_{T,N_{l\neq j}} = \left.\frac{\partial V}{\partial\overline{N}_j}\right\rfloor_{P,T,N_{l\neq i}} = v_j^{\dagger} \tag{5.7}$$

$$\left.\frac{\partial V}{\partial\overline{N}_i}\right\rfloor_{P,T,N_{l\neq i}} = v_i^{\dagger} \tag{5.8}$$

$$\left.\frac{\partial V}{\partial P}\right\rfloor_{T,N_l} = -V\kappa_T \tag{5.9}$$

where $v^{\dagger}$ is the partial specific volume, a Maxwell relation was used to evaluate $\left.\partial\mu_j/\partial P\right\rfloor_{T,N_{l\neq j}}$, and $\kappa_T \triangleq -\left.\partial\ln V/\partial P\right\rfloor_{T,N_l}$ is the isothermal compressibility. Eqs. 5.1-5.9 provide the basis for relating particle number fluctuations to statistical mechanical and thermodynamic quantities for non-ideal solutions. From Eqs. 2.5-2.7, we can express the measured TCFFM correlation functions as:

$$G_{xy}(\tau) \;=\; \aleph_x\aleph_y\cdot\sum_i^m\sum_j^m d_{ij}^{xy}\cdot\int Z_{ij}(\mathbf{q},\tau)\cdot\Omega(\mathbf{q})\,d\mathbf{q} \tag{5.10}$$

The precise relationship between $\langle \delta N_i \delta N_j \rangle$ in Eq. 5.3 and the spatio-temporal dissipation function $Z(\mathbf{q}, \tau)$ of Eq. 5.10 requires further work.

The derivation of explict expressions for $Z(\mathbf{q}, \tau)$ for a reactive system is not trivial, even for the simple bimolecular reaction, $A + B \underset{k_b}{\overset{k_a}{\rightleftharpoons}} C$, considered in this thesis (see Section 2.7). One main difficulty comes from the eigenvalue-eigenfunction calculation approach used to solve the differential equation governing the relaxation of concentration fluctuations (Eq. 2.4). For more complicated reactions, analytical expressions may not be possible via this approach, which would limit the utility of TCFFM in studying chemical systems. This analytical intractibility – at least with regards to measuring *kinetic rate constants* – may be circumvented by a matrix algebra method proposed 30 years ago by Yi-der Chen at the NIH.[35] In this approach, the noise power spectrum (real part of the Fourier transform of the time correlation function) is analyzed. Chen showed that the noise power spectrum matrix at zero frequency can be directly related to a reduced form of the kinetic relaxation matrix $\mathbf{M}$ (Eq. 2.21). Little has been done to follow up Chen's work, especially as it relates to TCFFM. As more complex reactive systems are studied by fluorescence fluctuation methods, the Chen matrix method may become necessary.

New methods of analysis may also be necessary for studying fluctuating systems in which the equilibrium approximation of TCFFM no longer holds. In this regard, the Chen matrix method may also be applicable in analyzing non-equilibrium systems.[36] Qian and Elson (2004) recently demonstrated how TCFFM could be used diagnostically to show the existence of a non-equilibrium steady-state system of cycling biochemical reactions. A living cell is strictly not in equilibrium. While some cellular reactions/events may be considered

in quasi-equilibrium (within a given experimental measurement time), they are principally part of a non-equilibrium steady-state network. It is also now clear that many cellular components exist in relatively "low copy numbers" and that fluctuations have a fundamental impact on the cell's biochemical circuitry.[190] While requiring further development, TCFFM is poised to become an important tool in studies of biological noise. Fundamental to TCFFM and fluctuation studies are new approaches in processing the information of noisy traces.[189] In addition to correlation function analysis, higher correlation moments analysis, and photon counting histograms, I believe methods based on photon arrival times will be equally important and merit further study.[150,168]

Experimentally, at least three technical innovations in FFM methodology merit further development. The first is the use of time-gated pulsed excitation along with synchronized gated-detection. Lamb *et al.* (2000)[147] have shown how such a strategy can be used to alter fluorophore contributions to correlation function data based on fluorescence lifetime. This approach can be useful for rejecting background fluorescence while improving the sensitivity for a particular fluorescent species. Second, by using pulsed-interleaved-excitation in TCFFM, whereby one fluorophore is excited and detected before another is excited, spectral cross-talk/bleed-through can essentially removed.[146,179,250] This greatly simplifies TCFFM data analysis, although as noted in Section 3.2.1, using two different laser lines may lead to spurious chromatic differences in focal volume. Nonetheless, published results obtained thus far through time gating and pulsed excitation demonstrate the promise of incorporating temporal filtering/sorting strategies into TCFFM.[146] Finally, expanding TCFFM from a single focal volume method to a multi-focal-point or *imaging* approach could be extremely useful for

studying biochemistry within the inhomogenous cell cytoplasm.[186] Spatio-temporal image correlation methods, first proposed by Nils Petersen a decade ago[194] and more thoroughly developed by Paul Wiseman and co-workers recently,[43,55,101,140] have proven to be useful in understanding the dynamics of membrane-associated proteins involved in cell signaling. Current image FFM approaches, however, are limited to studies of slow diffusion/reactions due to the point scanning confocal/two-photon implementations that cap temporal resolution to a few hundreds of ms. This makes studying most chemical and transport dynamics *within* the cell practically impossible via FFM. Wide-field microscopic approaches are attractive in being able to "see all at once" though FFM with these approaches have not yet been tried. There is currently a trade-off between the number of simultaneous parallel volumes that can be probed by image FFM approaches and the sensitivity available through single point FFM implementations. This is because current imaging CCD detectors fall short of the sensitivity and low-noise characteristics of the conventionally used avalanche photodiode detectors (APD). Focusing instead on a small array of points simultaneously may be an alternative solution to gaining spatial information while retaining detection and temporal sensitivity. Multi-focal TCFFM was demonstrated recently using 2 single excitation lasers, multiple APDs and a small 2×2 array of diffractive elements.[88] Multi-focal TCFFM would also be possible using two-photon excitation[61] and over a three-dimensional spatial array using the innovative method of Eric Betzig.[17] With continuing developments in APD detector array technologies (e.g., those by Sensors Unlimited, Inc., Princeton, NJ) it may soon be practical to use image/multi-focal TCFFM for studying both temporal and spatial dynamics of fast intracellular processes.

Part II

AIDA: A New Adaptive Image Deconvolution Algorithm for Microscopy

Synopsis

In Part II, I describe an Adaptive Image Deconvolution Algorithm (AIDA) for myopic deconvolution of multi-frame and three-dimensional data acquired through astronomical and microscopic imaging. AIDA is an extension of the MISTRAL method developed by Mugnier and co-workers and shown to yield object reconstructions with excellent edge preservation and photometric precision (*J. Opt. Soc. Am. A.* **21**, 1841 (2004)). Written in Numerical Python with calls to a robust constrained conjugate gradient method, AIDA has significantly improved runtimes over the original MISTRAL implementation. Included in AIDA is a scheme to automatically balance maximum-likelihood estimation and object regularization, which significantly decreases the amount of time and effort needed to generate satisfactory reconstructions. I validated AIDA using synthetic data spanning a broad range of signal-to-noise ratios and image types, and demonstrated the algorithm to be effective for experimental data from adaptive optics-equipped telescope systems and wide-field microscopy.

Portions of chapters in this part are reprinted from a manuscript to be submitted for publication in the *Journal of the Optical Society of America-A* by Erik F. Y. Hom, Franck Marchis, Timothy Lee, Sebastian Haase, David Agard, and John Sedat as:

"AIDA: An Adaptive Image Deconvolution algorithm with Application to Multi-Frame and Three-Dimensional Data".

Chapter 6

Theoretical Foundations

6.1 Introduction

Images acquired using any optical system are fundamentally limited in resolution by diffraction and corrupted by measurement noise. Aberrations intrinsic to the optical system and imaging medium result in further degradation and distortions of the observed images. In ground-based astronomical imaging, atmospheric turbulence is the primary source of aberrations. In microscopic/biological imaging, significant aberrations arise as a result of index of refraction inhomogenieties within the sample under study.

Aberration artifacts can be largely corrected using adaptive optics (AO) methods.[215] Limited by the spatial and/or temporal response of AO hardware, however, such corrections remain imperfect. AO-corrected images are often contaminated by residual blurring that can significantly reduce the contrast of fine image details. Significant de-noising and improved image contrast can be obtained using post-acquisition deconvolution techniques,[38] implying that both hardware and software correction strategies are needed for optimal image recovery.

Deconvolution is an explicit attempt to model and computationally compensate for measurement non-idealities. Classic approaches presume that the imaging point spread function (PSF) of the optical system is exactly known. In practice, however, the PSF is estimated either theoretically[84,255] or by imaging a sub-resolution point-like object (e.g., guide star/fluorescent bead).[105,151] Such estimates may deviate significantly from the true PSF, yet no margin is given in classical methods for the PSF to adjust to a more appropriate estimate. Using a fixed, imperfect PSF thus inherently limits one's ability to generate the most accurate and highest resolution object reconstructions.

Myopic or blind deconvolution approaches allow an imprecise or unknown PSF estimate to adapt to a more correct form and thereby offer the possibility of improved object reconstructions over classical methods. The success of these myopic/blind methods, however, is dependent upon *a priori* constraints that compensate for the lack of information associated with having the PSF be variable.[4,15,106,227,244]

In this chapter, I describe an Adaptive Image Deconvolution Algorithm, AIDA, for myopic deconvolution of two- and three-dimensional image data within a maximum *a posteriori* (MAP) framework. AIDA is a *de novo* implementation and extension of the proprietary MISTRAL (Myopic Iterative STep-preserving Restoration ALgorithm) method, originally developed by Mugnier and co-workers[177] to effectively deconvolve a broad range of astronomical targets with superior photometric restoration and sharp-edge feature preservation. I have significantly improved AIDA's runtime performance over the original MISTRAL code and have developed a simple yet effective scheme to balance maximum-likelihood estimation with object regularization in the deconvolution process. Moreover, AIDA has capabilities to

process multiple image frames simultaneously, thereby leveraging the information available through multiple observations.[38, 227]

6.2 Adaptive Deconvolution Approach

6.2.1 Imaging Model

Consider an image, $i(\mathbf{r})$, of an object, $o(\mathbf{r})$, observed through a telescope or microscope system and measured using a CCD detector array. This image may be viewed as a probabilistic mapping of the object's brightness distribution to an intensity count distribution sampled over the discrete pixel/voxel position, $\mathbf{r}$: $o(\mathbf{r}) \mapsto i(\mathbf{r})$. Assuming that: (i) image formation is linear and space invariant (isoplanatic approximation), (ii) the response of each CCD pixel element is equivalent and independent of all others, and (iii) signal-independent Gaussian and signal-dependent Poisson noise sources are present,[110] the image formed can be described by the following equation:

$$i(\mathbf{r}) = \underbrace{o(\mathbf{r}) \otimes h(\mathbf{r})}_{g(\mathbf{r})} \circ \check{n}_P(\mathbf{r}) + \check{n}_G \tag{6.1}$$

where $h(\mathbf{r})$ is the PSF, $g(\mathbf{r})$ denotes the noise-free image, $\check{n}_G(\mathbf{r})$ is a Gaussian random variable characterized by variance σ_G^2, and $\check{n}_P(\mathbf{r})$ represents a stochastic Poisson process with variance $\sigma_P^2 \sim g(\mathbf{r})$. The operator, $\otimes$, denotes a convolution and $\circ$ denotes a pixel-by-pixel operation. While the response of CCD pixel elements is rarely uniform in practice, I will assume that any non-uniformity can be accounted for through image flat-fielding with neglible effect on the validity of Eq. (6.1). Moreover, I assume that if any constant image background is present, it can be subtracted from $i(\mathbf{r})$ so that $\check{n}_G(\mathbf{r})$ is zero-centered.

When both Gaussian and Poisson noise sources are present and images are not photon-limited, a non-stationary but additive weighted-Gaussian noise model with variance:

$$w(\mathbf{r}) \triangleq \sigma^2_{\check{n}(\mathbf{r})}(\mathbf{r}) = \sigma^2_G + \sigma^2_P(\mathbf{r}) \tag{6.2}$$

is a very good approximation.[152,177] With this noise model, the operator, $\circ$, in Eq. (6.1) may be replaced by simple addition and Eq. (6.1) also expressed as:

$$I(\mathbf{k}) = O(\mathbf{k})H(\mathbf{k}) + \check{N}(\mathbf{k}) \tag{6.3}$$

where capitalization denotes the Fourier Transform of the variable, $H(\mathbf{k})$ is the optical transfer function (OTF), and $\mathbf{k}$ is the conjugate spatial frequency. For brevity, the dependence on $\mathbf{r}$ and $\mathbf{k}$ will often be implicit hereafter.

6.2.2 Bayesian Deconvolution Framework

The goal of deconvolution is to invert Eq. (6.1). Classical deconvolution approaches aim to find the best estimate, $\hat{o}$, of the true object given a single image frame, i, and an exactly known PSF convolution kernel, h. Such approaches are ill-posed (lacking a unique solution due to insufficient information) and ill-conditioned (numerically sensitive to small errors and thus unstable) for two reasons: (1) h is intrinsically bandlimited by the resolution limit of the optical system, and (2) noise is present at frequencies beyond the bandlimit.[15,52] This situation is further complicated in the case of myopic or blind deconvolution where the characteristics of the PSF kernel are poorly known, if at all. Because of ill-posedness, the quality of the deconvolution depends critically on how much *a priori* information is incorporated into the inversion process.[15,176] This *a priori* information can be divided into three classes related to $\check{n}$, o, and h.

Owing to the presence of noise, deconvolution may be viewed as a problem of stochastic inversion. It is helpful to state the goal of deconvolution in Bayesian terms, namely to maximize the *a posteriori* probability of observing the object, o, and point spread function, h, given an image, i, and a set of model assumptions, a:

$$p(o,h|i,a) = \frac{p(i|o,h,a)p(o|a)p(h|a)}{p(i|a)} \tag{6.4}$$

$p(i|o,h,a)$ is the posterior probability density of observing an image, i, as expressed by the forward imaging equation, Eq. (6.1). This term is the focus of maximum-likelihood methods, which aim to optimize the fidelity of the observed data to a set of parameters and subject to a particular noise model. $p(o|a)$, $p(h|a)$, and $p(i|a)$ are the *a priori* probability distributions for the object, PSF, and image, respectively. These *a priori* distributions must be inferred based on the assumptions, a. In classical deconvolution methods for which the PSF is known, for example, $p(h|a)$ is assumed to be a constant. In maximum entropy deconvolution methods, $p(o|a)$ is set implictly by the definition of the entropy measure used.[242] When the positivity of the variables o, h, and i can be assumed (e.g., under incoherent imaging conditions), the *a priori* probabilities for negative values can be set to zero.

Each probability term in Eq. (6.4) may be interpreted as a Gibbs distribution with energy cost function, $J(x)$, and partition function, $Z(x) \triangleq \int_x exp[-J(x)]dx$:[16,81]

$$p(x) = \exp\left[-J(x)\right]/Z(x) \tag{6.5}$$

so that:

$$\begin{aligned} p(o,h|i,a) &= exp[-J(o,h|i,a)]/Z \\ &= (Z_i/Z_nZ_oZ_hZ)\, exp[-J_n(i|o,h,a) - J_o(o|a) - J_h(h|a) + J_i(i|a)] \end{aligned} \tag{6.6}$$

where I have used the subscripts "n" to denote noise model-related data fidelity terms, "o" to denote the terms arising from the *a priori* object distribution, "h" to denote the terms arising from the *a priori* assumptions for the PSF, and "i" to denote the terms arising from the *a priori* distribution of images. The mode or best estimate for *both* o and h can then be found by maximizing Eq. (6.2.2) with respect to these variables or equivalently, by minimizing the corresponding negative log-likelihood, $J(o, h|i, a)$:

$$\begin{aligned} \left[\hat{o}, \hat{h}\right] &= \arg\min_{[o,h]} \{J(o, h|i, a)\} \\ &= \arg\min_{[o,h]} \{J_n(i|o, h, a) + J_o(o|a) + J_h(h|a)\} \end{aligned} \tag{6.7}$$

Since $J_i(i|a)$ is formally independent of variables o and h given the set of assumptions a, I have dropped this term in Eq. (6.7), along with a constant term involving the ratio of partition functions.

6.2.3 Myopic Deconvolution with Edge-Preservation

Our goal is to minimize Eq. (6.7) subject to a specific set of model assumptions for $J_n(i|o, h, a)$, $J_o(o|a)$, and $J_h(h|a)$. I follow the recommendations of Mugnier *et al.*[177] in assigning functional forms to each of these component terms as detailed below.

6.2.3.1 Data Fidelity Term: $J_n(i|o, h, a)$

Assuming the mixed-Gaussian noise model of Eq. (6.2), the fidelity of the reconstructed object $\hat{o}$ and PSF $\hat{h}$ with respect to the observed image i can be described by the following weighted maximum-likelihood term:

$$J_n(i|o,h,a) = \frac{1}{2}\sum_{\mathbf{r}} \frac{\left(i(\mathbf{r}) - \hat{o}(\mathbf{r}) \otimes \hat{h}(\mathbf{r})\right)^2}{w(\mathbf{r})} \tag{6.8}$$

Deconvolution approaches which are based solely on this term often lead to noise amplification and severe ringing artifacts. The Landweber method and Richardson-Lucy/expectation-maximization algorithm are examples of such approaches, which assume a stationary-Gaussian and Poisson noise model for $w(\mathbf{r})$, respectively.[15,242] To minimize noise amplification artifacts and find a unique and stable solution in practice, Eq. (6.8) must be "regularized." In the aforementioned methods, regularization is accomplished empirically by limiting the number of deconvolution iterations.

6.2.3.2 Edge-preserving Object Term: $J_o(o|a)$

Eq. (6.8) may also be regularized through a quadratic penalty term based on an object's spatial gradient.[52,176] Quadratic regularization, however, often yields results that are oversmoothed and have compromised image contrast when applied uniformly to all object features. Using a roughness penalty that is instead sub-quadratic for regions of high contrast has been very successful in preserving "edges" and other sharp object features.[22,31,52,247] The underlying assumption here is that large gradient discontinuities in the image arise from genuine object features and should be penalized comparatively less than small gradients due to noisy background features. The edge-preserving prior originally proposed by Brette and Idier[25] is used here:

$$J_o(o|a) = \lambda_o \sum_{\mathbf{r}} \Phi\left(\gamma\left(\hat{o}, \theta_{\mathbf{r}}\right)\right) \tag{6.9}$$

$$\Phi(\gamma) \triangleq \gamma - \ln(1+\gamma) \tag{6.10}$$

$$\gamma(\hat{o}, \theta_{\mathbf{r}}) \triangleq \left(\frac{\|\nabla \hat{o}(\mathbf{r})\|}{\theta_{\mathbf{r}}} \right) \tag{6.11}$$

where $\|\nabla \hat{o}(\mathbf{r})\| \triangleq \left[(\nabla_x \hat{o}(\mathbf{r}))^2 + (\nabla_y \hat{o}(\mathbf{r}))^2 + (\nabla_z \hat{o}(\mathbf{r}))^2 \right]^{1/2}$ is the norm of the spatial gradient of the object, $\theta_{\mathbf{r}}$ and λ_o are auxillary parameters or "hyperparameters" of the object prior distribution, γ is a "reduced" gradient modulus, and $\Phi(\gamma)$ is called the "clique" potential.

$\Phi(\gamma)$ is a function that characterizes the local object texture at a position $\mathbf{r}$ based on a subset or "clique" of neighboring pixels. This clique is defined in practice through the calculation of the gradient norm in Eq. (6.11). For large values of γ, $\Phi(\gamma) \approx \gamma$ whereas for small values of γ, $\Phi(\gamma) = \gamma - (\gamma - \gamma^2/2 + ...) \approx \gamma^2/2$, resulting in so-called L1-L2 (linear-quadratic) behavior. Numerous L1-L2 regularization functionals have been suggested in the literature (e.g., see Teboul *et al.*[247]). The advantage of Eq. (6.10) over other forms is that it is convex and its derivative with respect to $\hat{o}$ does not involve any transcendental or exponential functions, making cost function optimization easier and less expensive (see Section 3.3).

The scaling parameter λ_o plays an important role in balancing maximum-likelihood fidelity to the data with the preservation of high contrast features in the object estimate. The hyperparameter, $\theta_{\mathbf{r}}$, sets the width and shape of the Gibbs distribution in Eq. (6.5). It governs the point at which regularization transitions from being quadratic to being linear. In Mugnier *et al.*'s treatment,[177] the same scalar pair of values (λ_o, θ) is applied to each pixel element of the object. I have found, however, that using an inhomogenous hyperparameter model as advocated by others,[120,122,123,221] in which $\theta_{\mathbf{r}}$ is pixel-/voxel-dependent (as indicated by the subscript) and adapted to the local object texture, results in better

deconvolution results.

6.2.3.3 Harmonic Optical Transfer Function Constraint: $J_h(h|a)$

To myopically reconstruct the PSF, the following Fourier domain constraint is used:

$$J_h(h|a) = \frac{\lambda_H}{2} \sum_{\mathbf{k}} \frac{\left| \hat{H}(\mathbf{k}) - \bar{\mathcal{H}}(\mathbf{k}) \right|^2}{v(\mathbf{k})} \tag{6.12}$$

where λ_H controls the degree of the OTF regularization/constraint relative to the data fidelity term (Eq. (6.8)), $\hat{H}(\mathbf{k})$ is the estimate of the OTF, $\mathcal{H}(\mathbf{k})$ is a measured OTF, and the overbar denotes an average. $v(\mathbf{k})$ is the OTF sampling variance or power spectral density defined over the sampled OTFs as:

$$v(\mathbf{k}) = \left\langle \left| \mathcal{H}_i(\mathbf{k}) - \bar{\mathcal{H}}(\mathbf{k}) \right|^2 \right\rangle = \left\langle \left| \mathcal{H}_i(\mathbf{k}) \right|^2 \right\rangle - \left| \bar{\mathcal{H}}(\mathbf{k}) \right|^2 \tag{6.13}$$

$v(\mathbf{k})$ serves as a spring constant to harmonically constrain each OTF k-component to a mean value, consistent with a set of measured OTFs. Eq. (6.12) intrinsically handles bandlimitedness of the OTF; frequencies beyond the optical system's resolution are essentially ignored since they are not represented in the measured samples. Conan and co-workers[42,76] have shown that this harmonic OTF constraint performs noticeably better towards recovering the true OTF than a simple bandlimited constraint typically used in blind deconvolution methods.[106,126] Mugnier *et al.*[177] advocate using an harmonic constraint for each spatial *frequency*, $|\mathbf{k}|$, which is functionally equivalent to using a radially-averaged $v(\mathbf{k})$. I have found, however, that using Eq. (6.12) is sometimes more robust.

6.2.4 Extension to Multiple Frame Data

The focus thus far has been on a single image frame. One of our goals in developing AIDA was to combine the demonstrated strengths of MISTRAL with the multiple frame synthesis capabilities available in a method such as IDAC, the Iterative Deconvolution Algorithm in C.[38,40,126] Christou *et al.*[40] have argued that the use of multiple observations can serve as an additional deconvolution constraint: the ratio of unknown variables to measured quantities being reduced from 2:1 for a single image frame to $M+1 : M$ for M image frame observations. The simultaneous analysis of multiple observations implicitly accounts for correlations that may exist among variables as well as between variables and the data.[245] Consequently, multiple frame deconvolution should result in sytematically lower error bounds with more reliable results than when individual image frames are deconvolved separately or when multiple frames are merged into an averaged "shift-and-added" image (*i.e.*, an image generated by averaging the image frames after appropriate pixel shifts are made to maximize image correlation) and then deconvolved.[37–39,118,227,228]

The extension to "multi-frame" deconvolution is straightforward. For multiple image observations, Eq. (6.1) may be expressed generally in vector form:

$$\left\{ \begin{array}{c} i_1 = o_1 \otimes h_1 + \check{n}_1 \\ i_2 = o_2 \otimes h_2 + \check{n}_2 \\ \vdots \\ i_M = o_M \otimes h_M + \check{n}_M \end{array} \right\} \equiv \mathbf{i}(\mathbf{r}) = \underbrace{\mathbf{o}(\mathbf{r}) \ddot{\otimes} \mathbf{h}(\mathbf{r})}_{\mathbf{g}(\mathbf{r})} + \check{\mathbf{n}}(\mathbf{r}) \tag{6.14}$$

where $\ddot{\otimes}$ specifies a convolution performed over appropriate $o_j : h_j$ pairs and I have assumed the noise model of Eq. (6.2). In general, for M_i measured images, there may be M_o unique

objects and M_h unique PSFs: $M_i \geq M_o \geq M_h$. In addition to "mono-frame" datasets where $M_i = M_o = M_h = 1$, I consider two multi-frame dataset types: (i) "multi-PSF" datasets where $M_i = M_h$ and $M_o = 1$, and (ii) "multi-object" datasets where $M_i = M_o$ and $M_h = 1$. Multi-PSF deconvolution may be used to process adaptive optics images for which there is a common target object but a variable PSF per image observation. Multi-object deconvolution may be used to process time-lapsed microscopy images for which a single common PSF does not change between frames.

The cost function to be minimized for multi-PSF deconvolution is given by:

$$J_{M\_PSF}(o, \mathbf{h}|\mathbf{i}, a) = \left\{ \frac{1}{2} \sum_{\beta}^{M_h} \left[\sum_{\mathbf{r}} \frac{\left(i_\beta - \hat{o} \otimes \hat{h}_\beta \right)^2}{w_\beta} + \lambda_{h_\beta} \sum_{\mathbf{k}} \frac{\left| \hat{H}_\beta - \bar{\mathcal{H}} \right|^2}{v} \right] \right\} + \lambda_o \sum_{\mathbf{r}} \Phi\left(\gamma\left(\hat{o}, \theta_{\mathbf{r}}\right)\right) \tag{6.15}$$

and for multi-object deconvolution by:

$$J_{M\_object}(\mathbf{o}, h|\mathbf{i}, a) = \left\{ \sum_{\alpha}^{M_o} \left[\sum_{\mathbf{r}} \left(\frac{\left(i_\alpha - \hat{o}_\alpha \otimes \hat{h} \right)^2}{2w_\alpha} + \lambda_{o_\alpha} \Phi\left(\gamma\left(\hat{o}_\alpha, \theta_{\mathbf{r},\alpha}\right)\right) \right) \right] \right\} + \frac{\lambda_h}{2} \sum_{\mathbf{k}} \frac{\left| \hat{H} - \bar{\mathcal{H}} \right|^2}{v} \tag{6.16}$$

where α and β are used to index multiple objects and PSFs, respectively.

Chapter 7

Implemention Strategy

7.1 Algorithmic Overview

I implemented AIDA using Numerical Python/Numarray,[90] with calls to a specialized C++ conjugate gradient optimizer (see Section 3.2), which were handled by code generated using the Simplified Wrapper and Interface Generator (SWIG).[11,12] Fast Fourier Transforms were computed using the FFTW(v. 2.1.5) subroutine library[75] in lieu of the standard Numarray FFTPACK library, resulting in about a factor of 2 improvement in the overall speed of the algorithm. A schematic of the algorithm is shown in Figure 7.1.

AIDA begins with a pre-processing stage to estimate data fidelity weights, w (see below, Sec. 7.3), and to calculate the mean OTF, $\overline{\mathcal{H}}$, and OTF variance, v. It is assumed that all the images supplied have been properly flat-fielded and optionally background-subtracted. In cases where the image does not have negative pixels following background subtraction (as is the case for an image without true "dark" areas), the user must either supply a value for σ_G or a dark image from which it can be estimated.

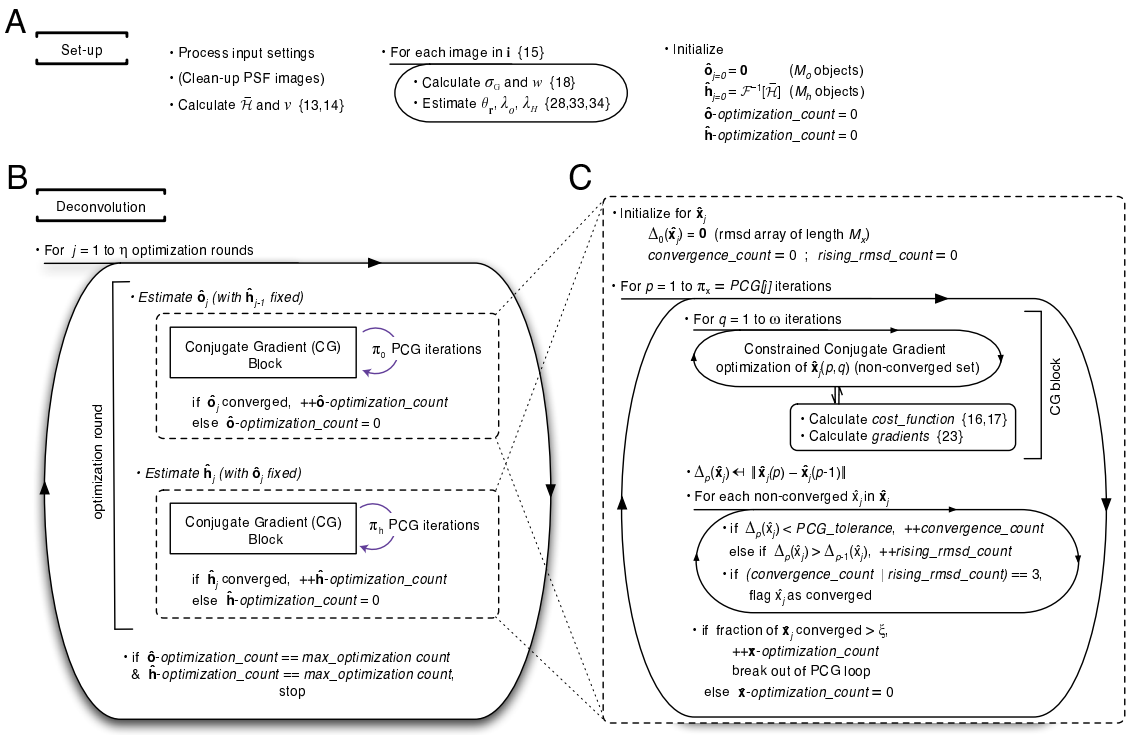

Figure 7.1: **AIDA optimization protocol**. *(A)* Set-up and variable initialization stage. Equation numbers for variables are shown in curly brackets. M_o and M_h are the number of objects and PSFs to be estimated, respectively. *(B)* Deconvolution scheme. The subscript j indexes the "optimization round," which consists of two partial conjugate gradient (PCG) estimation loops (each indicated by a dashed-box): one for the object(s), $\hat{\mathbf{o}}$, followed by one for the PSF(s), $\hat{\mathbf{h}}$. The deconvolution is stopped after a *max_optimization_count* number of sequential PCG estimation loops have converged (see below). *(C)* Schematic of the PCG estimation loop used to estimate the object(s) or PSF(s) (indicated generically by the variable ($\hat{\mathbf{x}}_j$)) for the j^{th} optimization round. Δ_p is an M_o- or M_h-length array of root-mean-square-deviations between sequential PCG iterations used to monitor convergence progress. Minimization of each $\hat{x}_j$ in $\hat{\mathbf{x}}_j$ is continued until Δ_p falls below some *PCG_tolerance* for a total of *convergence_count* times or until a *rising_rmsd_count* number of "uphill" moves is registered (default = 3 for both). Each "PCG iteration" entails a steepest descent minimization step followed by up to $\omega - 1$ conjugate gradient (CG) steps for the set of unconverged object or PSF estimates. When the fraction of object(s) or PSF(s) that have converged is $> \zeta$, the PCG estimation is stopped and convergence for that PCG estimation loop is noted.

The present version of AIDA expects *images* of reference PSFs (e.g., of a guide star or sub-diffraction sized bead), which are normalized to 1 and used to compute $\overline{\mathcal{H}}$ and v. If only one PSF image is supplied, v is calculated based on the noise statistics of the image as for w. AIDA is equipped with an optional clean-up module to remove hot/dark pixels from these PSF images and remove noise according to some user-defined threshold. An option to use a radially-averaged OTF variance is provided to enable the harmonic constraint of spatial frequencies as implemented in MISTRAL[177] (see Section 6.2.3.3).

The default mode for AIDA uses automatic hyperparameter settings as described below in Section 7.4. The option to directly specify hyperparameter values or a scale factor by which to multiply the automatic estimates is available for fine-tuning purposes. For mono-frame deconvolutions, AIDA is also capable of performing unsupervised deconvolutions over a grid of λ_o and $\theta_{\mathbf{r}}$ hyperparameter values centered about automatical estimates or user-defined centers.

Although it is possible to simultaneously estimate both sets of objects, $\hat{\mathbf{o}}$, and PSFs, $\hat{\mathbf{h}}$, by stacking them into a single variable to be optimized (see Eq. (6.7)), doing so could result in slower convergence since significant differences in magnitude between $\hat{\mathbf{o}}$ and $\hat{\mathbf{h}}$ can result in a skewed optimization landscape and ill-conditioning.[10] Although variable renormalization could solve this issue, I have chosen instead to alternate between the minimization of $\hat{\mathbf{o}}$ and $\hat{\mathbf{h}}$ in the current version of AIDA as advocated by Mugnier *et al.*[177]

For non-quadratic cost functions, solution convergence can often be improved by periodically restarting the conjugate gradient (CG) minimization after a defined number of steps to interlace steepest descent steps with CG steps. I have found this "partial" conjugate

gradient (PCG) approach[10] to be more effective than a simple CG approach in minimizing the quasi-quadratic cost functions Eqs. (6.16) and (6.15), consistent with the findings of Mugnier *et al.*[177]

Starting with each PSF in $\hat{\mathbf{h}}$ set to the the mean of the sampled PSFs ($\mathcal{F}^{-1}[\overline{\mathcal{H}}]$), each object in $\hat{\mathbf{o}}$ is optimized via a PCG approach. CG optimization is capped by a set number of iterations, ω (typically 25), constituting a "CG block" and repeated for π_o "PCG iterations." The resulting estimate for $\hat{\mathbf{o}}$ is then fixed and each PSF in $\hat{\mathbf{h}}$ optimized via π_h PCG iterations. The multi-frame estimates $\hat{\mathbf{o}}$ and $\hat{\mathbf{h}}$ are alternatively optimized, with each pair of estimations constituting one AIDA "optimization round." The number of PCG iterations per optimization round for $\hat{\mathbf{o}}$ and $\hat{\mathbf{h}}$ is typically increased progressively, with the possibility of separate PCG iteration plans for $\hat{\mathbf{o}}$ and $\hat{\mathbf{h}}$. By default, the number of PCG iterations executed per optimization round is given by: $PCG[j] = 2(j-1)+1$, where j is the round number from 1 to η, the maximum default number of optimization rounds (typically 8). Progressively increasing the number PCG iterations in this manner ensures that the optimization of the current variable (e.g., $\hat{\mathbf{o}}$) does not get fixed too quickly relative to the other variable (e.g., $\hat{\mathbf{h}}$), which may yet be suboptimal. Multi-frame optimization of $\hat{\mathbf{o}}$ and $\hat{\mathbf{h}}$ is continued until the fraction of individual $\hat{o}_j$ and $\hat{h}_j$ frame estimates that have converged is greater than some tolerance, ζ (typically 0.9), or until a specified maximum number of optimization rounds is reached. The convergence of each $\hat{o}_j$ or $\hat{h}_j$ frame optimization is achieved when the root-mean-square deviation between two consecutive PCG iteration estimates falls below a specified tolerance for at least three times within one optimization round.

7.2 Constrained Conjugate Gradient Minimization

AIDA's quasi-quadratic cost function was minimized using a Constrained Conjugate Gradient (CCG) algorithm developed by Goodman and co-workers[87] and freely available as part of the EDEN Holographic Method package.[239,246] This algorithm incorporates three significant advances over the conventional conjugate gradient method.[201] First, to ensure that solutions are positive (or within a user specified-bound) a projected gradient or active sets approach is used.[10] Johnston *et al.*[128] have shown that such an approach is superior to maintaining solution positivity via reparametrization since reparametrization often leads to the creation of spurious minima that can complicate the optimization process. Second, to prevent "zig-zagging" behavior that can arise when using an active sets approach or minimizing non-quadratic functions, an adaptive "bending" line search is used to set the most effective conjugate direction step size (typically called α). Third, to better preserve conjugacy between successive directions, the conjugate gradient deflection parameter (typically called β) is computed using the Hestenes-Stiefel formula instead of the standard Fletcher-Reeves or Polak-Ribiere formulas.[10]

7.3 Cost Function and Derivative Calculations

To facilitate modification and future developments of AIDA, the calculation of the cost function was written in an extensible manner in which cost function terms may be turned on or off. For computational efficiency, only terms which are dependent upon the variable being estimated are computed (e.g., for $\hat{o}_j$, data-fidelity and object regularization terms but not the OTF constraint are computed).

The data fidelity weights for each image frame, $w(\mathbf{r})$, (see Eq. 6.8) can be computed as a sum of Gaussian and Poissonian contributions according to Eq. 6.2 as suggested by Mugnier *et al.*:[177]

$$w(\mathbf{r}) = \underbrace{\frac{\pi}{2}\left(\langle i(\mathbf{r})\rangle_{\leq 0}\right)^2}_{\sigma_G^2} + \underbrace{\max\left[i(\mathbf{r}), 0\right]}_{\sigma_P^2} \tag{7.1}$$

The first term accounts for Gaussian detection/electronic readout noise, σ_G^2, which can be estimated using the average over all negative pixels in the image. For images of extended objects that do not have any negative-pixel areas (common in microscopy), a separate "dark" image is required from which σ_G^2 can be computed directly. The second term in Eq. 7.1 accounts for Poisson photonic noise, σ_P^2; this term is derived from the fact that the variance equals the mean and the mode for a Poisson distribution. Although this term should technically be determined using a noise-free image estimate, $\sigma_P^2 = \max\left[\hat{g}(\mathbf{r}), 0\right]$, I did not observe a significant improvement in deconvolution quality to merit using this more accurate though algorithmically complicated approach. In fact, I found that using $\hat{g}$ to recursively estimate w can sometimes lead to an unstable algorithm and sub-optimal reconstructions, especially in conjunction with the automatic hyperparameter estimation scheme described below in Section 3.4.

The estimates for the variances in Eq. 7.1 implicitly assume that i has been properly background subtracted so as to lead to a properly centered and sampled Gaussian distribution for readout noise. Only noise arising from the image formation is accounted for here. "Scientific noise" (e.g., cellular autofluorescence in microscopy imaging), which may be irrelevant to image features of scientific interest, are not accounted for here explicitly but treated as an optically genuine component of the object under observation.

The clique potential used for edge-preserving object regularization requires that effective spatial gradients of the object estimate be computed. This can be done efficiently by convolving the object estimate with a gradient mask:

$$\nabla_r \hat{o}(\mathbf{r}) = \hat{o}(\mathbf{r}) \otimes \chi \mathbf{G}_r \tag{7.2}$$

where $\mathbf{G}_r$ is a 3×3 matrix operator corresponding to the gradient of interest in the direction r, and χ is a scaling normalization factor. Many different gradient masks that have been developed for image segmentation may be used.[200,242] I prefer masks based on the work of Frei and Chen[73] since it is equally effective on horizontal, vertical, and diagonal edges, and I have found these operators to be more effective in recovering subtle object features than traditional nearest neighbor finite difference approximations (see e.g., Press *et al.* (1992), Section 5.7[201]). In 2 dimensions, this is given by:

$$\mathbf{G}_x \triangleq \begin{bmatrix} 1 & 0 & -1 \\ \sqrt{2} & 0 & -\sqrt{2} \\ 1 & 0 & -1 \end{bmatrix}; \quad \mathbf{G}_y \triangleq \begin{bmatrix} -1 & -\sqrt{2} & -1 \\ 0 & 0 & 0 \\ 1 & \sqrt{2} & 1 \end{bmatrix} \tag{7.3}$$

and in 3 dimensions:

$$\begin{aligned} \mathbf{G}_x &\triangleq \begin{bmatrix} (\mathbf{0}), \begin{pmatrix} 1 & 0 & -1 \\ \sqrt{2} & 0 & -\sqrt{2} \\ 1 & 0 & -1 \end{pmatrix}, (\mathbf{0}) \end{bmatrix}; \quad \mathbf{G}_y \triangleq \begin{bmatrix} (\mathbf{0}), \begin{pmatrix} -1 & -\sqrt{2} & -1 \\ 0 & 0 & 0 \\ 1 & \sqrt{2} & 1 \end{pmatrix}, (\mathbf{0}) \end{bmatrix}; \\ \mathbf{G}_z &\triangleq \zeta \cdot \begin{bmatrix} \begin{pmatrix} 0 & -1 & 0 \\ 0 & -\sqrt{2} & 0 \\ 0 & -1 & 0 \end{pmatrix}, (\mathbf{0}), \begin{pmatrix} 0 & 1 & 0 \\ 0 & \sqrt{2} & 0 \\ 0 & 1 & 0 \end{pmatrix} \end{bmatrix} \end{aligned} \tag{7.4}$$

where $\chi = \left(2+\sqrt{2}\right)^{-1}$ and ζ is a z-resolution compensation factor. In three-dimensional microscopic imaging, the OTF support in the axial direction is significantly smaller than in the radial direction. This leads to a greater loss of information and thus increased blurring in the z-direction relative to x- or y-directions; ζ is used to compensate for a more diffuse gradient observed in the z-direction of the image stack. Given the lateral and axial resolutions of a microscope, r_{xy} and r_z, ζ can be estimated as $\zeta \sim r_{xy}/r_z$. If we define optical resolution as the distance between the central maximum and first minimum of the lateral or axial component of a PSF Airy disk, the lateral and axial resolutions of a microscope are given by $r_{xy} = 0.6\lambda_{em}/\mathrm{NA}$ and $r_z = 2\lambda_{em}n/\mathrm{NA}^2$, where λ_{em} is the wavelength of light, n is the index of refraction of the sample, and NA is the numerical aperture of the microscope objective lens.[129] Thus,

$$\zeta \sim 3.33n/\mathrm{NA} \tag{7.5}$$

and using values typical in microscopic imaging, $n \approx 1.33$ and NA≈ 1.4, $\zeta \approx 3$.

Minimizing the AIDA cost function (Eq. 6.16 or 6.15) with the conjugate gradient method requires analytical derivatives with respect to both object and PSF estimates. These estimated can be determined through functional differentiation[218] and are given by:

$$\frac{\partial J}{\partial o_\alpha} = \left\{ \sum_{\beta}^{N_{PSFs}} \hat{h}_\beta \star \left(\frac{\hat{o}_\alpha \otimes \hat{h}_\beta - i_\beta}{w_\beta} \right) \right\} + \frac{\lambda_{o_\alpha}}{\theta_{\mathbf{r}}^2} \left(\frac{\nabla_{\mathbf{r}}^2 \hat{o}_\alpha}{1+\gamma\left(\hat{o}_\alpha, \theta_{\mathbf{r}}\right)} \right) \tag{7.6}$$

$$\frac{\partial J}{\partial h_\beta} = \left\{ \sum_{\alpha}^{N_{objects}} \hat{o}_\alpha \star \left(\frac{\hat{o}_\alpha \otimes \hat{h}_\beta - i_a}{w_a} \right) \right\} + \lambda_{h_\beta} \frac{(N_d+1)}{2} \mathcal{F}^{-1} \left[\frac{\left(\hat{H}_\beta - \bar{\mathcal{H}}\right)}{v} \right] \tag{7.7}$$

where $\star$ denotes a correlation. In practice, the terms in curly brackets are computed in the Fourier domain, in accordance with the convolution- and correlation-Fourier theorems.[23,201] I assume that the arrays (or region-of-interest sub-arrays) used in Fourier calculations are

sufficiently padded so that boundary aliasing problems can be ignored. In computing the derivative of the OTF constraint with respect to h (right most term in Eq. 7.7), I have used the property of the Discrete Fourier Transform, $\mathcal{F}[x^*] = N_d\mathcal{F}^{-1}[x]$, where x^* is the conjugate of x.

The spatial Laplacian of the object in Eq. 7.6 may be computed by convolving the spatial object gradient with a gradient mask (Eq. 7.2) as proposed by Mugnier *et al.*[178] Alternatively, the object may be convolved directly with the following Laplacian operator mask, which I find to be faster and yield finer results:

$$\nabla^2_{\mathbf{r}}\hat{o} = \hat{o}(\mathbf{r}) \otimes \chi\mathbf{L} \tag{7.8}$$

where in 2 dimensions:

$$\chi \triangleq \frac{1}{12}; \quad L \triangleq \begin{bmatrix} -1 & -2 & -1 \\ -2 & -12 & -2 \\ -1 & -2 & -1 \end{bmatrix} \tag{7.9}$$

and in 3 dimensions:

$$\chi \triangleq \frac{1}{16(1+\zeta)};$$

$$L \triangleq \left[\begin{bmatrix} -1 & -1 & -1 \\ -1 & -2\zeta & -1 \\ -1 & -1 & -1 \end{bmatrix}, \begin{bmatrix} -\zeta & -2\zeta & -\zeta \\ -2\zeta & 16(1+\zeta) & -2\zeta \\ -\zeta & -2\zeta & -\zeta \end{bmatrix}, \begin{bmatrix} -1 & -1 & -1 \\ -1 & -2\zeta & -1 \\ -1 & -1 & -1 \end{bmatrix} \right] \tag{7.10}$$

where ζ once again compensates for the relative loss in resolution in the z- vs. xy-directions (typically ~ 3).

7.4 Automatic Hyperparameter Estimation

Methods to estimate the hyperparameters that tune object regularization terms like Eq. 6.9 have been a subject of considerable attention.[41,78,86,114,120–123,198,221,272] A number of approaches have been advocated including L-curve analysis and generalized cross-validation.[78,86] These heuristic methods are computationally expensive, essentially requiring that multiple deconvolutions be performed over a grid of λ_o values for each image to be processed. Other more advanced and theoretically rigorous approaches attempt to optimize hyperparameters jointly with object reconstruction.[78,198,272] These methods aim to maximize the marginal likelihood (ML) of observing the measured image given an incomplete data set over the space of hyperparameters: $(\hat{\theta}_r, \hat{\lambda}_o) = \arg\max_{\theta_r,\lambda_o} p(i|\theta_r, \lambda_o)$; this is functionally equivalent to maximizing the ratio of partition functions, Z/Z_oZ_n (cf. Eq. 6.2.2), with respect to the hyperparameter variables.[123,272] In practice, these methods require non-trivial Monte Carlo expectation-maximization sampling steps prior to object reconstruction, which increases the computational expense of a deconvolution considerably.[121,221] In contrast to all of these methods, our AIDA approach directly calculates hyperparameter estimates using a semi-empirically based scheme, forgoing any stochasic sampling steps or comprehensive grid searching.

My initial efforts to derive an automatic scheme were founded upon a large collection of deconvolution results generated over a grid of θ_r and λ_o values spanning several orders of magnitude. I used a variety of different two-dimensional (2D) object types and natural scenes to build a reference set of images covering a broad range of signal-to-noise ratios. A subset of these reference objects is shown in Figure 7.2. These reference images were

Figure 7.2: **Subset of reference objects used to test AIDA and establish its automatic hyperparameter estimation scheme**. Each object (with max intensity set to 100, 1000, or 10000) was blurred with a Gaussian PSF (FWHM=4 pixels), had intensity-based Poisson noise and Gaussian detector noise added according to Eq. (8.1) to yield a series of images with SNR=-10, -3, 0, 7, 10, 17, 20, or 27 dB.

used to assess deconvolution quality as a function of hyperparameter pairs. From a grid search over hyperparameters, a "plane" of acceptable (θ_r, λ_o) solutions (determined by visual inspection) were found to exist, in agreement with observations by Jalobeanu *et al.*[122] This finding implies that one hyperparameter may be defined while the other hyperparameter is optimally adjusted to balance data-fidelity with object regularization. Within the AIDA cost function framework, I found a balance can be achieved by setting $\theta_{\mathbf{r}}$ according to:

$$\theta_{\mathbf{r}} \triangleq \sqrt{w(\mathbf{r})/\sigma_G} \tag{7.11}$$

and computing λ_o directly via the approach detailed below .

From Eqs. (6.8) and (6.9), the following partition function-like integrals may be defined over the distribution of possible data-model variations, $\delta \equiv i - o \otimes h$, and the distribution of possible gradient norm values for each pixel element:

$$\zeta_n(\mathbf{r})\rfloor_\delta \triangleq \int_\delta \exp\left[-\left(\delta_{\mathbf{r}}\right)^2 / 2w(\mathbf{r})\right] d\delta \tag{7.12}$$

$$\zeta_o(\mathbf{r})\rfloor_{\|\nabla o\|} \triangleq \int_{\|\nabla o(\mathbf{r})\|} \exp\left[-\lambda_o\left(\frac{\|\nabla o(\mathbf{r})\|}{\theta(\mathbf{r})} - \ln\left(1+\frac{\|\nabla o(\mathbf{r})\|}{\theta(\mathbf{r})}\right)\right)\right] d\,\|\nabla o(\mathbf{r})\| \tag{7.13}$$

A convenient relation linking $\theta_{\mathbf{r}}$ and λ_o can be obtained by equating these integrals:

$$\begin{aligned} \zeta_n(\mathbf{r})\rfloor_{\delta} &\doteq \zeta_o(\mathbf{r})\rfloor_{\|\nabla o\|} \\ \sqrt{2\pi w(\mathbf{r})} &= \theta_{\mathbf{r}} e^{\lambda} \int_1^{\infty} e^{-\lambda t}/t^{-\lambda} dt \\ &\approx \theta_{\mathbf{r}}\left(\frac{1}{\lambda_o}+1\right) \end{aligned} \tag{7.14}$$

where the approximation holds for $\lambda_o \lesssim 10$. An element-by-element equivalence of these integrals essentially assumes that the Gibbs distribution (and thus partition function Z) of Eq.(6.5) can be represented as a product of separable functions (*i.e.*, a mean-field approximation).[272] Solving for λ_o in Eq. 7.14:

$$\lambda_o = \left(\sqrt{2\pi w(\mathbf{r})}/\theta_{\mathbf{r}} - 1\right)^{-1} \tag{7.15}$$

This definition along with the vector definition of $\theta_{\mathbf{r}}$, Eq. 7.11, leads to a simple, pixel-independent *scalar* expression for λ_o:

$$\lambda_o \triangleq \left(\sqrt{2\pi\sigma_G} - 1\right)^{-1} \tag{7.16}$$

From Eq. 7.1 and given the quantized nature of real, noisy data, σ_G is guaranteed to be $\geq \sqrt{\pi/2}$ such that $\theta_{\mathbf{r}}$ and λ_o are well-defined by Eqs. 7.11 and 7.16. Using $w(\mathbf{r})$ as defined in Eq. 7.1 and object gradients and Laplacians calculated according to Eqs. 7.2-7.10, this estimation scheme is quite robust. In rare cases where this scheme over-regularizes results (likely due to noise model mismatch), I have found that simply scaling the λ_o hyperparameter estimate down, typically by no more than by a factor of 10, gives optimal reconstructions. It is important to note that careful estimates of σ_G and $w(\mathbf{r})$ in accordance with Eq. 7.1 are important for the success of this approach.

For the OTF constraint, a quadratic term in real space Eq. 6.8 must be balanced with a quadratic term in Fourier space Eq. 6.12. I have found that this balance can be roughly achieved by setting:

$$\lambda_H \triangleq 1/N_d \tag{7.17}$$

where N_d is the number of pixel/voxel elements. The heuristic motivation for this comes from the power conservation relation of Parseval's Theorem, in which $\sum_{r=0}^{N-1} |x(r)|^2 = (1/N_d) \sum_{k=0}^{N-1} |\widetilde{x}(k)|^2$.

Chapter 8

Application

8.1 Validation and Application to Mono-Frame Data

In Figure 8.1, I present deconvolution results for one of our synthesized datasets to demonstrate the effectiveness of the automatic estimation scheme. The "brain" object (256×256 pixels) shown in Figure 8.1A is from a magnetic resonance imaging scan available from the Computer Vision Group at the University of Granada.[184] This object was convolved with a Gaussian PSF of full-width-half-maximum (FWHM) of 4 pixels and normalized to a maximum intensity of 1000. This "noise-free" image, $g(\mathbf{r})$, was subjected to a Poisson noise transformation with varying amounts of Gaussian noise subsequently added (mimicking CCD detector read-out noise) according to a pre-determined image signal-to-noise ratio (SNR), which I define as:

$$SNR \triangleq 10 \log_{10} \frac{var[g(\mathbf{r})]}{\langle w(\mathbf{r}) \rangle_{\mathbf{r}}} \tag{8.1}$$

where $var[g(\mathbf{r})]$ is the variance of the noise-free image.[15]

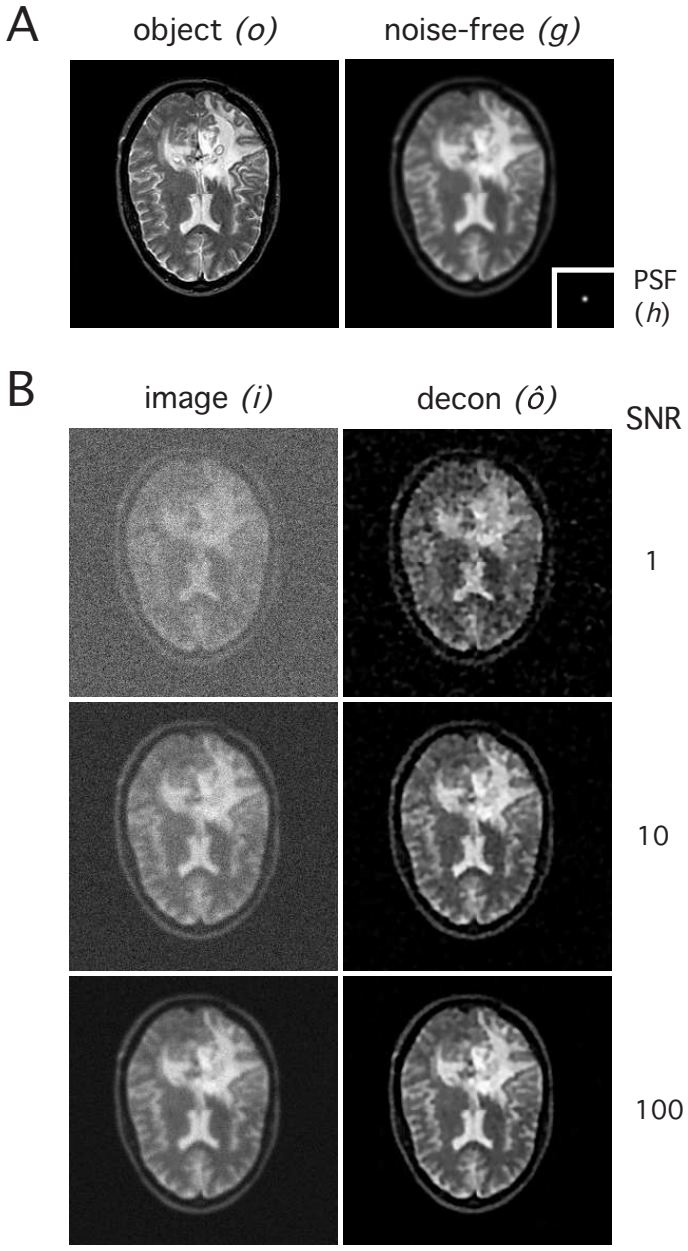

Figure 8.1: **Deconvolution test results using automatic hyperparameter estimation**. *(A) Left*, original 256 × 256 pixel "brain" object with intensities from 0-1000 (o); *right*, convolved noise-free image (g) with Gaussian PSF *(h)* inset (FWHM=4 pixels). *(B)* Deconvolution series for image SNR of -10, 10, and 20 dB; *left*, convolved image with Poisson and Gaussian noise (i); *right*, corresponding deconvolution result ($\hat{o}$).

Significant denoising can be observed after deconvolution (Figure 8.1B) with a contrast enhancement of about 50%. Average contrast improvement was computed by multiple ($N \geq 6$) comparisons of average intensities over an area of 3×3 pixels within a region of interest (I_{ROI}) versues over an adjacent background region ($I_{background}$) (separated by at least 4 pixels, the FWHM of the PSF):

$$\Delta Contrast \triangleq \left\langle \frac{\langle I_{ROI} \rangle_{area} - \langle I_{background} \rangle_{area}}{\langle I_{background} \rangle_{area}} \right\rangle_{N\ samples} \tag{8.2}$$

Using the definition:

$$\Delta SNR \triangleq 10 \log_{10} \frac{\|i - o\|}{\|\hat{o} - o\|} \tag{8.3}$$

I see signal-to-noise improvements of 10, 4.8, and 3 dB for the deconvolution results of SNR=1, 10, and 20 dB images, respectively.

Figure 8.2 shows the deconvolution results for the SNR=100 image of Figure 8.1 over a grid of λ_o or $\theta_{\mathbf{r}}$ values that are 20 times larger or smaller than those automatically estimated. Using the estimated hyperparameters (Figure 8.2, center) gave the best visual results and balance between data-fidelity and regularization. Using the estimated $\hat{\lambda}_o$ and a value of $\theta_{\mathbf{r}} = \hat{\theta}_{\mathbf{r}}/20$ also gave acceptable results (though contrast was slightly compromised). In general, the deconvolution results were generally less sensitive to changes in $\theta_{\mathbf{r}}$ than λ_o over the range of values examined. Although not shown, note that AIDA's hyperparameter estimation scheme works equally well for a range of maximum intensity scalings (*i.e.*, images for which the maximum intensity of the noise-free image is 100 or 10,000). Deconvolution results were typically be generated within $30 - 90$ sec per (256×256) image pixels on a 2.8 GHz Intel Xeon Linux machine.

Below, I demonstrate the effectiveness of AIDA in myopically deconvolving real imag-

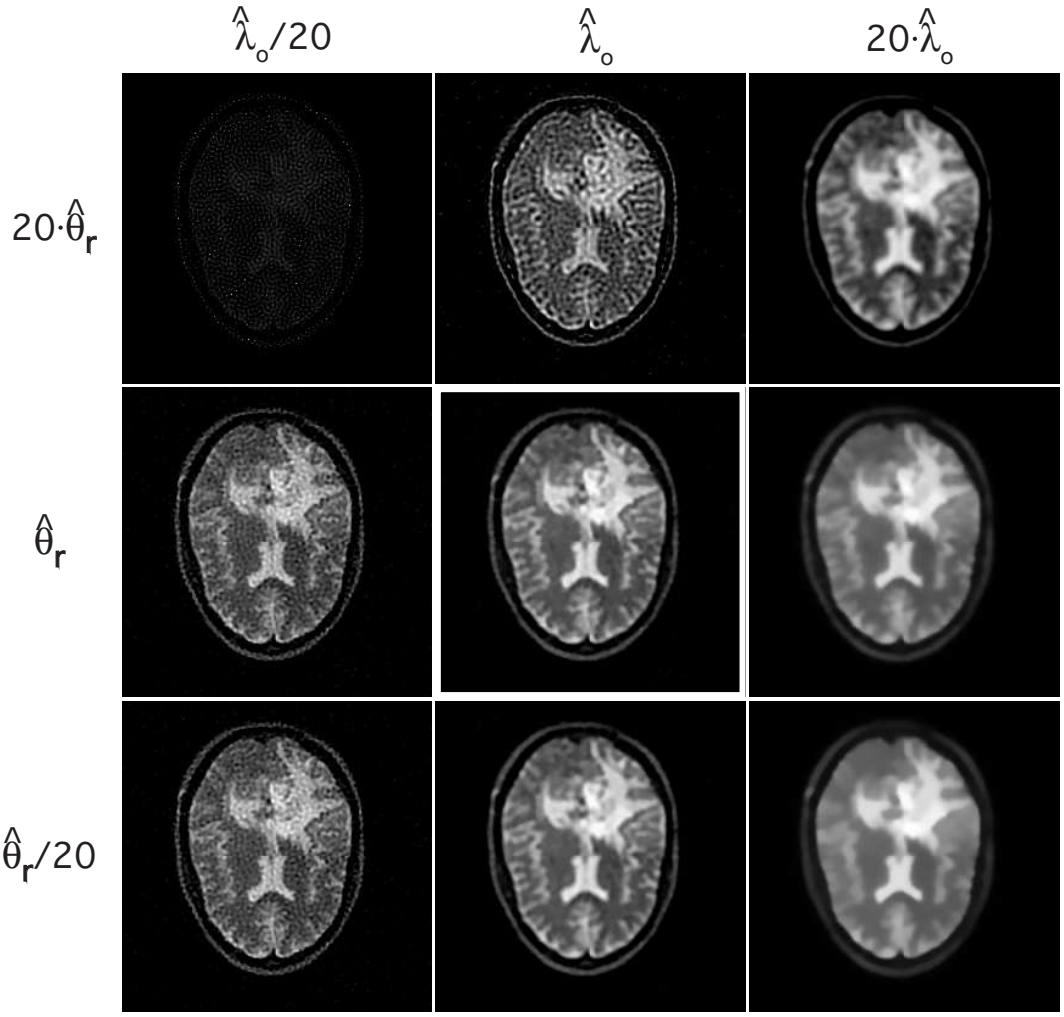

Figure 8.2: **Automatic hyperparameter estimation is nearly optimal**. Deconvolution results for the SNR=100 brain image from Figure 8.1, over a grid of λ_o and $\theta_\mathbf{r}$ values that are 20× larger or smaller than those estimated automatically. *Center*: deconvolution result using the automatically estimated hyperparameters.

ing data for two astronomical targets, Io and Titan.

8.1.1 Io

Io is the innermost Galilean satellite of Jupiter with a diameter similar to Earth's moon (∼3600 km) and is known to be volcanically active. To understand the origin of Io's volcanism, its time evolution, and relationship to tidal heating, the volcanic activity of Io needs to be monitored over a large time baseline. With the demise of the Galileo spacecraft, which was in orbit around the Jovian system from 1995-2003, the monitoring of Io volcanism now lies in the hands of ground-based observers.

When Io is closest to earth, its angular size is ∼1.2 arcsec, which is very close to the natural angular resolution ("seeing") provided by ground-based telescopes. Because of its brightness (apparent visual magnitude, m_v∼5), Io is ideally suited for observation by AO systems. Volcanism on Io has been monitored regularly in the near infrared (NIR) between 1 and 5 μm by one of us (F. Marchis) using the Keck-10 m telescope AO system.[165–167] The angular resolution provided by AO varies with the wavelength range of observations from 55 milli-arcsec (mas) in the Kc band (centered at 2.2 μm) to 100 mas in the Ms band (4.7 μm), corresponding respectively to ∼170 km and ∼305 km on the surface of the satellite. Such spatial resolution is comparable to those of the Galileo observations of Io in the same wavelength range.[57]

Marchis and co-workers[166,167] used MISTRAL to process the first high-resolution AO images of Io volcanic activity. Franck Marchis (UC Berkeley) and I compared the performance of AIDA (with automatic hyperparameter estimation) to that of MISTRAL with a set of Io images acquired in 2003. The deconvolution results for three different

broadband filter observations are shown in Figure 8.3. Each basic-processed filtered image was a shift-and-added synthesis of five observations ($<$ 5 min each; background subtracted and flat-fielded). The improvement in image constrast after deconvolution is obvious. In the Kc band, the surface reflectance or "albedo" markings including dark paterae and bright frost areas are visible on the surface of Io. The general features of Io are in excellent agreement with those of Galileo/Voyager maps shown in Figure 8.4. AIDA and MISTRAL deconvolution results are extremely similar, with a correlation coefficient of 99.4% when calculated over the area of the satellite.

For a single 512×512 image, our AIDA implementation was $15-20$ times faster than the original MISTRAL method (e.g., $\sim$25 min vs. $\sim$7 hr on a 1.8 GHz iMac G5 computer running Mac OS X 10.3). In practice, multiple MISTRAL deconvolutions must typically be performed to hone in on hyperparameter values that yield the "best" results. This is often a time-consuming and laborious process: between 10 to 20 MISTRAL deconvolution runs are usually necessary to locate an optimal (θ_r, λ_o) pair. Thus, the practical gain in processing time of AIDA compared with MISTRAL is $\gtrsim$200.

The image of Io in the Ms band is radically different than for the Kc band, being dominated by the localized thermal emission of the volcanoes. In the Lp band (intermediate wavelength, $\sim$ 3.8 μm), large scale albedo features on the surface are visible as are the thermal emissions of the active centers. After deconvolution several additional hot spots were revealed on the hemisphere of Io. Most of them can be found in the basic-processed image upon more careful scrutiny.

The accurate recovery of image intensities from which the temperature and emission

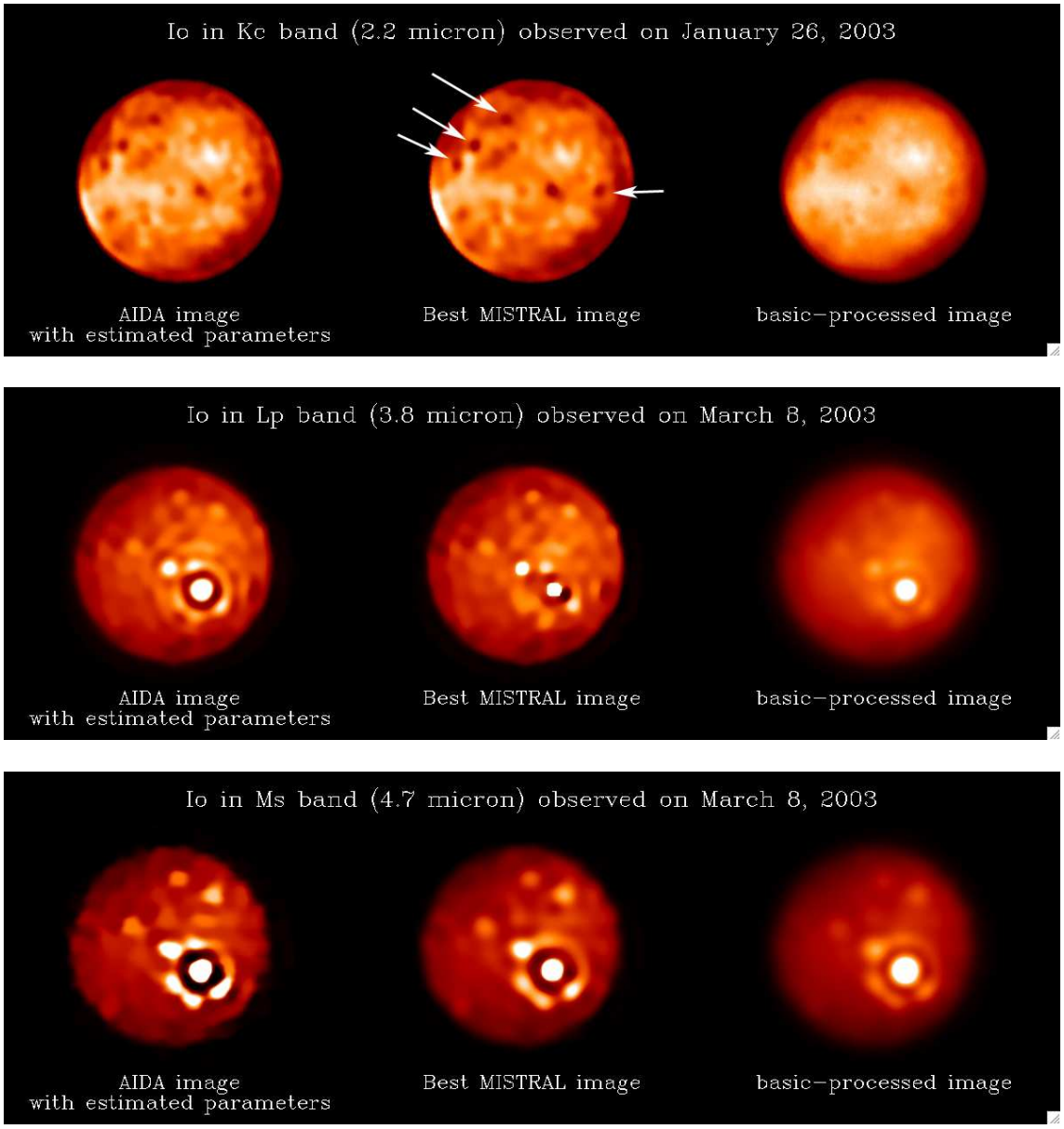

Figure 8.3: **Myopic deconvolution results for AO-corrected images of Io, a volcanically active moon of Jupiter**. The PSF of the system was estimated using images of a star located near the target with the same visible magnitude. PSF variability (characterized by v in Eq. (6.13)) depends mainly on the brightness of the target, the quality of the atmospheric turbulence, and the wavelength range of observations. We estimated that FWHM variability of the PSFs from 10 nights of observation to be $<6\%$ in the K band.[167]

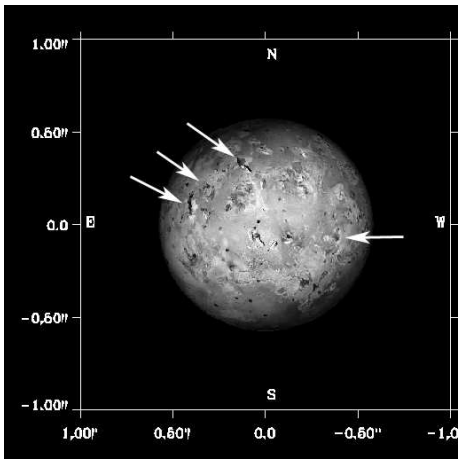

Figure 8.4: **Reconstructed appearance of Io on January 26, 2003 at 7:38 UT observed from Earth**. This image is based on Galileo/SSI and Voyager composite maps at a resolution of 20 km (courtesy of P. Descamps, Institute de Mécanique Céleste et des Calculs d'Éphémérides). Note that albedo features (e.g., calderas/craters) can also be seen on the deconvolve imaged (cf. Figure 8.3).

areas of these hot spots can be determined (e.g., assuming a black body emission law) are also of interest. Hot spot flux was measured using aperture photometry on the deconvolved image assuming that most of the flux is gathered in an area slightly larger than the angular resolution on the image.[164] This is a good approximation for hot spots with a peak contrast lower than 20%, since the intensity of the first Airy ring is negligible compared to the variation of brightness on the surface. For the extremely bright hot spot ("outburst") on the Ms band image, a prominent Airy ring remains after deconvolution. This residual artifact may be explained by the fact that the Keck PSF is hexagonal in shape[163] and that its orientation changes with the position of the telescope; optimizing the rotation of the sampled PSFs would likely minimize this artifact. Since this problem will not have a significant impact on the scientific analysis of the image, we have not pursued this matter further. The hot spot can be seen on the basic-processed image with a very good SNR, and

therefore its integrated intensity can be easily measured after comparison with the PSF. Overall, the deconvolution of Io images with AIDA provides excellent reconstructions which can be used to analyze surface changes on Io and to detect the faintest active centers and quantify their intensities.

8.1.2 Titan

Titan, Saturn's largest moon, was largely a mystery until very recently. Observations collected by the Voyager spacecraft in 1981[238] showed that Titan is obscured by a dense and opaque atmosphere consisting mainly of nitrogen. The surface of this 0.9" angular sized satellite, however, can be probed in the NIR through methane "windows" using such high resolution techniques as speckle imaging[83] and adaptive optics (AO).[44] Recent AO observations of its atmosphere revealed the presence of clouds and a complex structure with seasonal variability. The NASA-ESA Cassini-Huygens probe in orbit within the Saturnian system and an intensive campaign of observations using AO systems available on the Keck-10m telescope (Mauna Kea, Hawaii) and the ESO-8m Very Large Telescope (Cerro Paranal, Chile) are in place to help understand this complex satellite.

In Figure 8.5A, I show a ground based observation of Titan taken on January 15, 2005, one day after the Huygens probe landed on its surface. Titan was observed with the Keck AO using the NIRC-2 camera with a pixel scale of 9.94 mas through a narrow band He filter (2.06±0.03 μm). At this wavelength, the atmosphere is nearly transparent and most of the structures visible on the image are larger than 330 km (corresponding to 55 mas). A remarkable gain in image contrast is obtained after AIDA deconvolution, as shown in Figure 8.5B. This imaged hemisphere contains the landing site of the Huygens probe and was

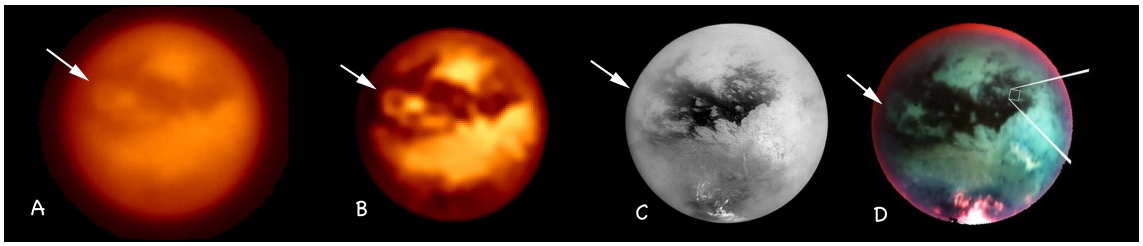

Figure 8.5: **Myopic deconvolution results for AO-corrected images of Titan, the largest moon of Saturn**. *(A)* Basic processed image of Titan taken on January 14, 2005 (1 day after the Cassini-Huygens probe landing) using the ground-based Keck AO system and a narrow band filter centered at 2.06 μm to probe surface albedo features.[50] *(B)* Keck AO image of Titan after myopic deconvolution with AIDA. *(C)* Mosaic image of Titan based on 1.3 km resolution data taken in the infrared with the Image Science Subsystem (ISS) instrument aboard the Cassini spacecraft (http://photojournal.jpl.nasa.gov/catalog/PIA06185). *(D)* False-color visible and infrared mosaic image of Titan taken by the ISS (http://photojournal.jpl.nasa.gov/catalog/PIA07965). Atmospheric features are shown in red and surface features in green and blue. Although the orientation of the Keck and ISS observations are slightly different, similar structures are seen on the deconvolved image as in the ISS image, validating the effectiveness of AIDA. Two ISS images were chosen to illustrate the variability of the satellite appearance due to the presence of haze and clouds. Arrows serve as reference markers to a common feature.

regularly observed by the Cassini spacecraft (Figs. 8.5C and D). The similarity between the Imaging Science Subsystem image (with a slight rotation of Titan) is striking. The smallest albedo structures detected after deconvolution have clear equivalents in the higher resolution image[50] (see arrow markings). This comparison validates the efficiency of our algorithm and demonstrates the absence of significant artifacts on the deconvolved image. A full scientific analysis of this and numerous other Titan observations and deconvolution results is presented elsewhere.[50]

8.2 Application to Multi-Frame Datasets

When multiple AO images of a common object are acquired, they are often simply combined into a single shift-and-added image which is then deconvolved. This practice has been demonstrated by others to be a sub-optimal; a more effective approach data-reduction strategy would be to deconvolve the set of images in a global fashion, linking common variables while maintaining the distinctiveness of each observation. Extending the MISTRAL approach to simultaneously deconvolve multiple image frames is a key feature of AIDA. Below, I present deconvolution results for 3 different multi-frame datasets. The first two datasets, one of synthetic AO retinal images and the other of real AO images of Uranus' atmosphere, are used to demonstrate AIDA's "multi-PSF" deconvolution capabilities, in which there is a common object but a variable PSF. The third dataset of time-lapsed fluorescence microscopy images of yeast microtubule dynamics is used to demonstrate AIDA's "multi-object" mode, in which there is a common PSF but different objects between frames.

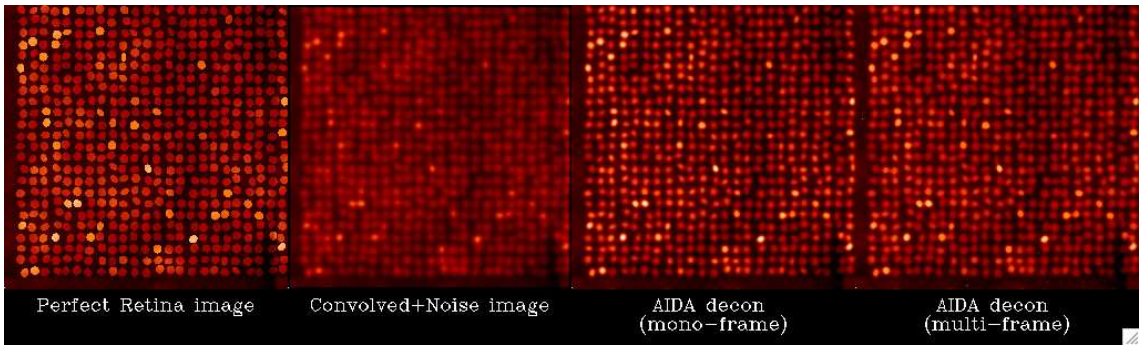

Figure 8.6: **Mono-frame and multi-frame deconvolution of simulated retinal images**. *(A)* An artificial 256×256 pixel retina object was created mimicking the characteristics of the data presented in Roorda *et al.*[217] (see text). *(B)* A representative degraded image (1 of 6) obtained by convolving with a Gaussian PSF (randomly generated with $FWHM_{avg}$=5 pixels and a FWHM variance of 20%) and adding Poisson and Gaussian noise. *(C)* Mono-frame deconvolution of the shift-and-added combination of 6 image frames. Contrast on the cones is improved by a factor of ~ 3. *D*: multi-PSF image deconvolution yields the best photometric results (see 8.1).

8.2.1 Synthetic Retinal Images (Multi-PSF)

Fine retinal features, such as individual photoreceptors, can be observed through the intact optics of a human eye using adaptive optics technology.[154] The correction provided by these systems is not perfect, and their PSFs display the same characteristics as those obtained with astronomical instruments (a coherent peak surrounding by an halo which blurs the image). The effect of blurring could be removed by deconvolution to sharpen the image and restore its photometry. To test the ability of AIDA on deconvolving such data, Franck Marchis and I generated a synthetic human retina image mimicking the characteristics of the data presented in Roorda *et al.*[217]

This synthetic 256 × 256 pixel image (Figure 8.6A) contains 576 ellipsoidal cones (aspect ratio = 0.8 ± 2) with an average radius of 5.6 ± 1 pixels and a mean centroid separation of 12 ± 2 pixels. Two types of uniform brightness cones were included in the

image. 90% of them were "dim" cones with photometric intensities of $\sim 22 \pm 2$ analog-to-digital units (ADU), roughly twice the background; 10% of the remaining cells were "bright" cones with an intensities of $\sim 35 \pm 5$ ADU. To the synthetic image, we added a background with 10% flux variation from the center to the edge of the image and shadows of blood vessels.

The positions, shape, and intensity of each cell were generated using a Monte-Carlo method with a > 4 pixel separation between each cell boundary. This simulated object frame was convolved with one of 6 Gaussian PSFs with a FWHM generated randomly from a distribution with mean FWHM of 5 pixels and variance of 20%. A second simulation with an average FWHM of 6 pixels and a variance of 25% was also considered. We exaggerated the instability of AO system in this simulation since for most AO retinal systems the PSF and stability are poorly characterized. Poisson and Gaussian noise were subsequently added to generate the noisy observed image, $i(\mathbf{r})$, with a SNR of ~ 25. After convolution and the addition of noise, cone contrast (see Eq. 8.2) was decreased by a factor of ~ 6 (Figure 8.6B).

We used AIDA in multi-PSF mode to deconvolve these images. A sampling of PSFs with the same characteristics as those used to generated the images were used to compute the average OTF and OTF variance, v. To estimate the gain in quality of the multi-frame deconvolution, we also deconvolved a shift-and-added mono-frame image synthesized from all 6 image frames. Figs. 8.6C and D show the result of these deconvolutions. In both cases, the sharpness of the image was restored and the contrast was improved by a factor of 3-4 compared to the raw image. The mono-frame result was more pixelated, however, and the photometric restoration was not as good compared to the multi-frame result. 8.1

Simulation	% intensity of true object, o		
	i	$\hat{o}_{mono}$	$\hat{o}_{M\_PSF}$
$\text{FWHM}_{\text{avg}} = 5$	85 ± 5	105 ± 6	98 ± 6
$\text{FWHM}_{\text{avg}} = 6$	82 ± 5	117 ± 77	90 ± 5

Table 8.1: **Photometric accuracy of cone intensities after mono- and multi-frame deconvolution**.

summarizes the photometric accuracy for the deconvolution results and demonstrates the superiority of multi-frame deconvolution over the mono-frame deconvolution of shift-and-added data, notably for the case with less precise PSFs ($\text{FWHM}_{\text{avg}}= 6$).

8.2.2 Atmosphere of Uranus (Multi-PSF)

Since the Voyager spacecraft encounter of the planet Uranus in 1986, interest in this planet has been revitalized with the discovery of that its atmosphere is considerably active.[240] High angular resolution imaging, however, is necessary to detect cloud motions,[94] faint rings, and small satellite systems.[51,54] The extended disk (diameter $\sim$ 3.6) of the planet (integrated apparent visual magnitude, $m_v \sim 6$) is bright enough to be used as a reference for wavefront sensor analysis on most AO systems. However, since the position of the centroid on the wavefront is not well-determined in the case of a quad-cell aperture for such an extended object, the atmospheric correction is degraded in the final image and artifacts may appear in several frames.[51] Franck Marchis and I tested AIDA on observations of Uranus taken on October 3, 2003 with the Keck AO system and its NIRC-2 camera using a broadband filter centered at 1.6 μm (H band). Five 30 s frames recorded in less than 8 min were processed using standard near-infrared data reduction techniques (flat-field, sky substraction and bad pixel removal). To estimate the PSF for myopic deconvolution, we imaged

Puck, a bright satellite of Uranus located 2.4" away from the center of the planet and whose motion was negligible during the exposure time. Given the large imaged size of Uranus and size of the image frames (1024×1024 pixels), using MISTRAL for deconvolution would not have been practical due to the long processing time needed ($\sim$ 23 h/deconvolution on a Sun Ultra 10 computer), especially since we would have needed to run multiple deconvolutions to determine a good choice for regularization parameters. Deconvolution using AIDA with automatic hyperparameter estimation was significantly faster (45 min for mono-frame deconvolution and 1.5 h for multi-PSF deconvolution on a 2.8 GHz Intel Xeon Linux machine) with the possibility of analyzing all AO data frames simultaneously.

Deconvolution results in significant image sharpening (Figure 8.7), with a gain in contrast of $\sim 2-3$ on the cloud features. A layered structure of the northern haze and some faint clouds at $\sim 40^{\circ}$ latitude are revealed and the structure of the large clouds on the southern hemisphere are clearer after deconvolution. A "ghost" outer ring artifact present in previous observations using the same Keck AO system,[51] is visible in several of the individual AO-corrected image frames (Figure 8.8A). This artifact remains in the mono-frame deconvolution of the shift-and-added combined image but is half as intense in the multi-frame deconvolution result (cf. Figs. 8.8B and C). The glare of Uranus (e.g., see area near the innermost ringlet) is also further reduced in the multi-frame deconvolution result than in the mono-frame deconvolution result. Overall, we find that simultaneous deconvolution of multiple frame data is better able to restore low SNR features and minimize artifacts than the deconvolution of a single shift-and-added representation of the multiple frame data.

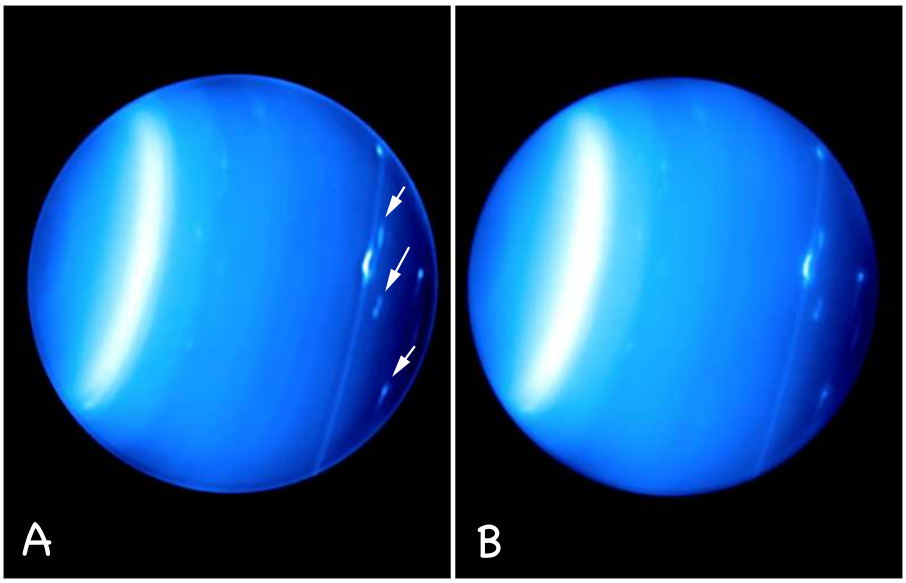

Figure 8.7: **Uranus observed with the Keck AO system and NIRC-2 camera on October 3, 2003**. *(A)* Multi-PSF deconvolution of 5 AO-corrected images of Uranus. *(B)* Combined "shift-and-added" image of 5 AO-corrected observations (30 s exposure for each). The gain in contrast after deconvolution is estimated to be $\sim$ 2, so that cloud features (arrows) can be more easily identified.

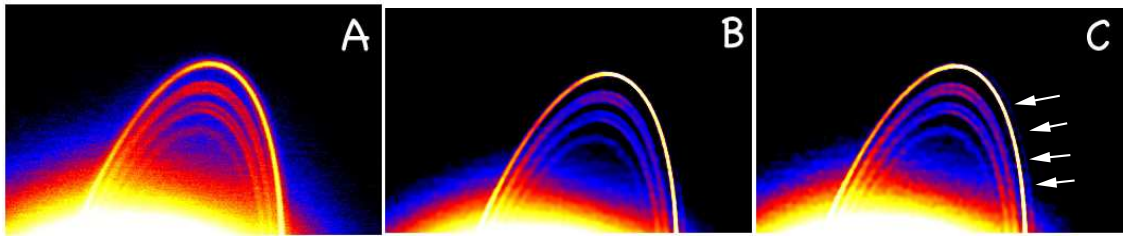

Figure 8.8: **Close-up of the ringlets of Uranus**. *(A)* Basic processed AO image. *(B)* Multi-PSF deconvolution using 6 image frames. *(C)* Mono-frame deconvolution of a shift-and-added image. This ring system is extremely faint and close to the disk of the planet; intensities of the ringlets are comparable to the intensity of the glare of Uranus as shown in the basic processed image (*A*). Deconvolution using AIDA significantly improves the contrast even on these faint features. The result is slightly better using multi-frame vs. mono-frame deconvolution. Arrows indicate a ghost artifact present in the mono-frame deconvolution result which is reduced in the multi-frame deconvolution result.

8.2.3 Yeast Microtubule Dynamics (Multi-Object)

Microtubules are hollow cylindrical polymers which radiate from near the nucleus of a cell and serve as "tracks" upon which cellular components are transported. Roughly 25 nm in diameter, these microtubules are formed from the stochastic polymerization and depolymerization of α- and β-tubulin proteins. The regulation of microtubule dynamics has been a topic of investigation for many years in cell biology, aided greatly by the direct observation of microtubules using time-lapsed video fluorescence microscopy.

I used AIDA in multi-object deconvolution mode to process time-series images of microtubule dynamics in the fission yeast, *Schizosaccharomyces pombe*. Using the OMX wide-field fluorescence microscope system developed recently in our lab at UCSF, a yeast cell whose microtubules were fluorescently labeled using the Green Fluorescence Protein fused to α-tubulin was imaged every second. Each image was formed by physically sweeping the microscope focus (by linearly moving the sample stage) through the entire z-depth of the cell ($\sim$ 4 μm in 50 ms) every second. Using estimates of the PSF based on a set of 3 images of a 100 μm fluorescent bead acquired under similar conditions, this time-series data was myopically deconvolved assuming a common (time-invariant) PSF for the whole dataset and assuming each image was simply a snapshot of a distinct "object."

In Figure 8.9A, I show the results of standard myopic deconvolution and multi-object deconvolution with automatic hyperparameter estimates for a single representative time slice. In Figure 8.9B, the corresponding "kymograph" plots − 1D maximum intensity projections of each image as a function of time − are shown for this data. The mono-frame deconvolution results are significantly denoised with improved microtubule contrast. The

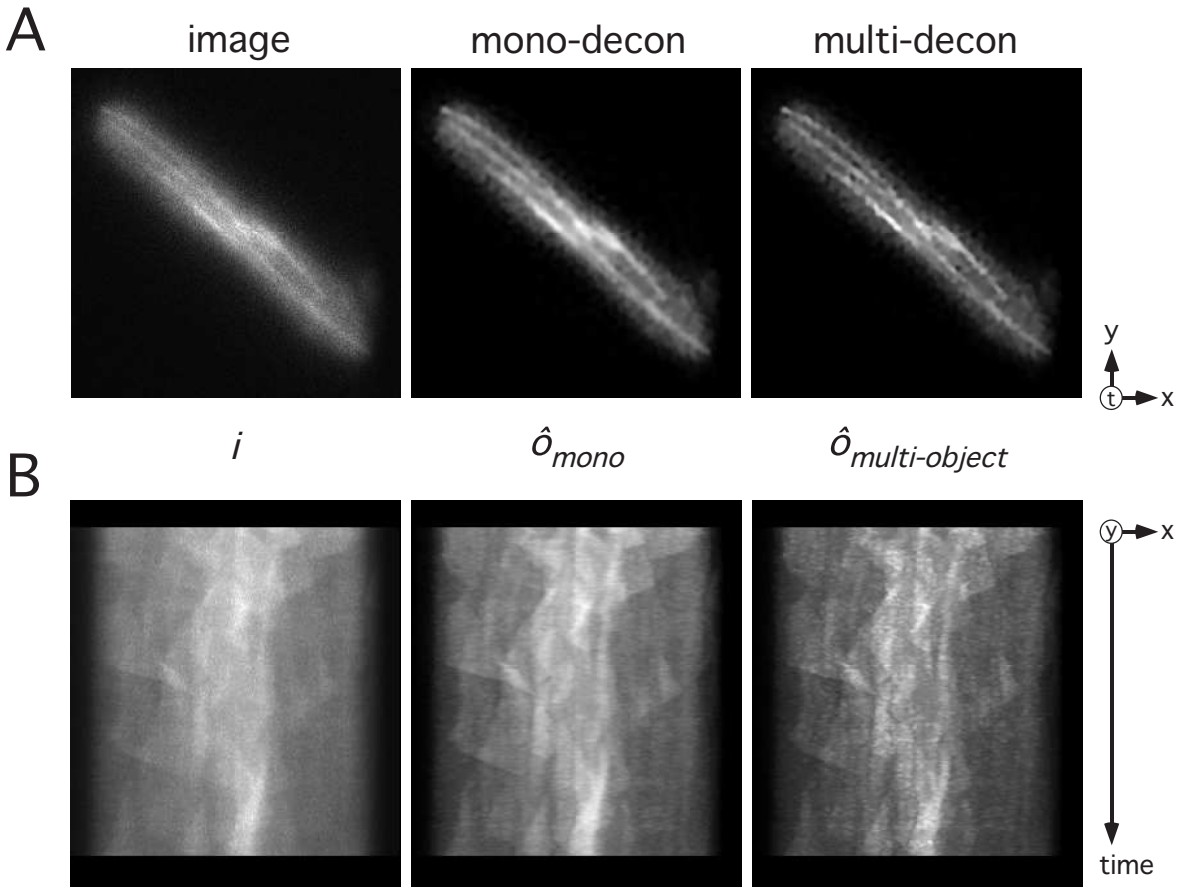

Figure 8.9: **Multi-object deconvolution of time-series images of a *S. pombe* (fission yeast) cell expressing α-tubulin-GFP**. Images were acquired using the OMX microscope system (data courtesy of Satoru Uzawa, Sedat Lab, UCSF). Each time-series slice was generated by axially sweeping the microscope focus over a 4 μm depth within 50 ms; an image slice was acquired every second for about 4 mins. *(A)* A single time-series slice of the original image data after basic processing (bad pixel removal and flat-fielding), mono-frame deconvolution, and multi-object deconvolution (image pixel size = 80 nm). *(B)* 2D maximum intensity projections (generated along the y-axis of the slice) plotted as a function of time (kymograph).

multi-object deconvolution results have even better contrast enhancement, exhibiting thinner microtubule fibers and a more textured "background" within the cell cytoplasm. It is unclear how much of this texturing may be artifactual. However, given that each image slice was deconvolved independently with respect to the time axis and that a number of cell background features are temporally persistent in the kymograph suggests that some of these grainy features are genuine.

8.3 Application to Three-Dimensional Datasets

One main advance of AIDA is the extention of the MISTRAL method to deconvolved three-dimensional data commonly encountered in biological imaging. Unlike the two-dimensional PSFs encountered in low numerical aperture astronomical imaging, the PSFs in optical microscopy are more diffuse, with significant axial blurring (z-dimension) on the order of 3 times the lateral blur. Deconvolution is expected to dramatically sharpen image data subject to such "out-of-focus" blur. Here, I show myopic deconvolution results for two three-dimensional (3D) datasets, one synthesized from magnetic resonance imaging (MRI) data of a frog and another of real, wide-field fluorescence microscopy data of chromosomes within cells undergoing cell division.

8.3.1 3D Frog MRI

I constructed synthetic 3D frog images ($128 \times 256 \times 256$ pixels) by convolving a MRI volume dataset from The Whole Frog Project (Lawrence Berkeley National Laboratory)[127] with a PSF derived from microscopic imaging of a sub-resolution (100 nm) fluorescent bead;

Poisson and Gaussian noise was added to the convolved image as described earlier. The PSF used had a FWHM in the lateral direction of ~ 3 pixels and an effective resolution-loss in the z-direction (ζ) of ~ 3 (see Eq. 7.5). Using an ensemble of similarly acquired experimental PSFs, these frog images were myopically deconvolved using automatic hyperparameter estimates (~ 6 hrs on a 2.8 GHz Intel Xeon Linux machine).

Additive 2D volume projections for the raw and deconvolved 3D image stacks for image SNRs of 0 and 20 dB are shown in Figs. 8.10A (*en face*) and B (side-view). The denoising and object reconstructions for this data are striking. The quality of the deconvolution results conveyed by these 2D projections are comparable to those seen from a comparison of individual 2D slices. Representative slices through the 3D volume stack of the original object, 20 dB SNR image, and deconvolution result are shown in Figure 8.11; also shown are intensity line profiles (denoted by an asterick) through the eye region of the 2D frog slices. Deconvolution with AIDA leads to subtantial photometric restoration of the original frog data, with a signal-to-noise improvement (ΔSNR) of 5.7 and 5.1 dB for image SNRs of 0 and 20 dB, respectively.

8.3.2 Mitotic Chromosomes in Drosophila Embryos

Nearly 50 years since the atomic structure of DNA was elucidated, the higher-order structural organization of DNA within chromosomes of cells remains poorly understood. With recent advances in high-resolution microscopic imaging and fluorescent labeling technology, however, discerning the mesoscopic arrangements of DNA within living cells is becoming more of a reality. A primary interest of our lab is to better understand the detailed structural changes of chromosomes as a cell divides in a process called mitosis. During mi-

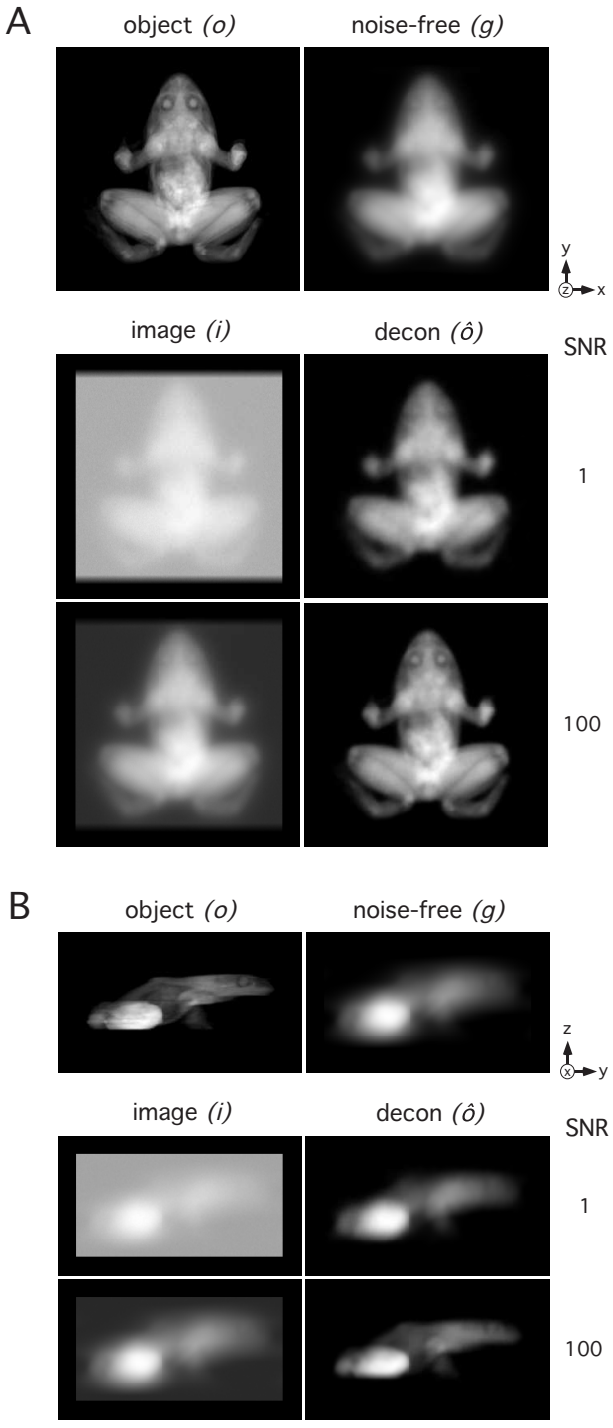

Figure 8.10: **2D volume projections for myopically deconvolved 3D frog image stacks with images SNRs of 1 and 100**. *(A) xy*-projection. *(B) yz*-projection. Automatic hyperparameter estimates were used along with an axial resolution gradient factor of $\zeta = 3$ (see Sec. 7.3).

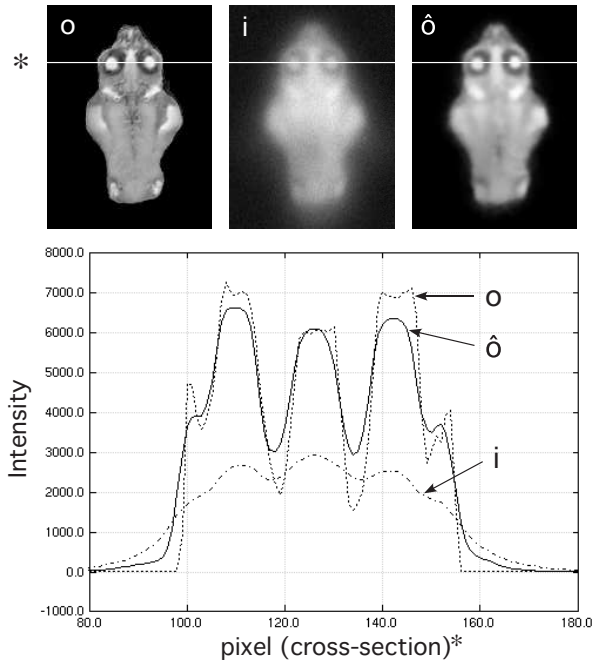

Figure 8.11: **Representative 2D slices and line profiles through the original 3D frog object** (o)**, 20 dB SNR image** (i)**, and deconvolution result** ($\hat{o}$).

tosis, a cell's chromosomes are unraveled, condensed, and separated; defects in chromosome structure during any of these mechanical steps could have devastating consequences on the fidelity of genetic transmission to daughter cells.

Drosophila melanogaster (fruit fly) embryos offer a unique opportunity to study chromosome structural changes during mitosis. Cells in early embryos (within 2-3 hrs) undergo multiple rounds of cell division in a synchronized and highly reproducible manner. Using the OMX microscope system mentioned earlier (Sec. 8.2.3), a 3D image stack ($32 \times 512 \times 512$ pixels) was acquired of a "cell cycle 10" *D. melanogaster* embryo fixed in 10% formaldehyde and mounted in glycerol. Cells in this embryo were stained with the a DNA-specific dye DAPI and captured undergoing anaphase, the stage of mitosis in which chromosomes separate. This image stack was deconvolved myopically using a PSF derived from an image of a

170 μm fluorescent bead under similar imaging settings. Image pixel spacing was 80 nm in xy and 150 nm in z, for a total image stack thickness of 4.8 μm. ζ was set to 3.2 based on the extent of the OTF in the lateral vs. axial directions.

Shown in Figure 8.12 are 2D maximum intensity projections of representative portions of the original 3D image stack and the result after myopic deconvolution. Although the original data shown is of especially good quality so that most chromosome arms can be distinguished in Figure 8.12A, chromosome boundaries are significantly more demarcated in the deconvolution result. The benefits of deconvolution are even more pronounced in Figure 8.12B in which there is greater blurring in the axial direction vs. lateral directions: finer structures and corrogated banding patterns of the chromosome arms become noticeable. Some residual "hour-glass" PSF blur remains after deconvolution, however, and appears to become more prominent with increasing z-depth (see e.g., lower left of deconvolution result, Figure 8.12B). This blur may be attributed to greater index of refraction abberations between the microscope objective lens and the sample as one focuses deeper into the embryo. The true PSF in this case is thus likely to be depth-dependent, although space-invariant PSFs are assumed in the current AIDA deconvolution framework.

To achieve the non-blurry, visually balanced deconvolution result of Figure 8.12, I found it necessary to scale the automatic hyperparameter estimate, $\hat{\lambda}_o$, down by a factor of 10. Inaccurate hyperparameter estimation is likely due to at least one of three possible causes. First, as alluded to above, depth-dependent variations of the true PSF are not accounted for in our imaging model and may lead to compromised object reconstructions. Second, there may be noise sources (e.g., out-of-focus, scattered background light) that

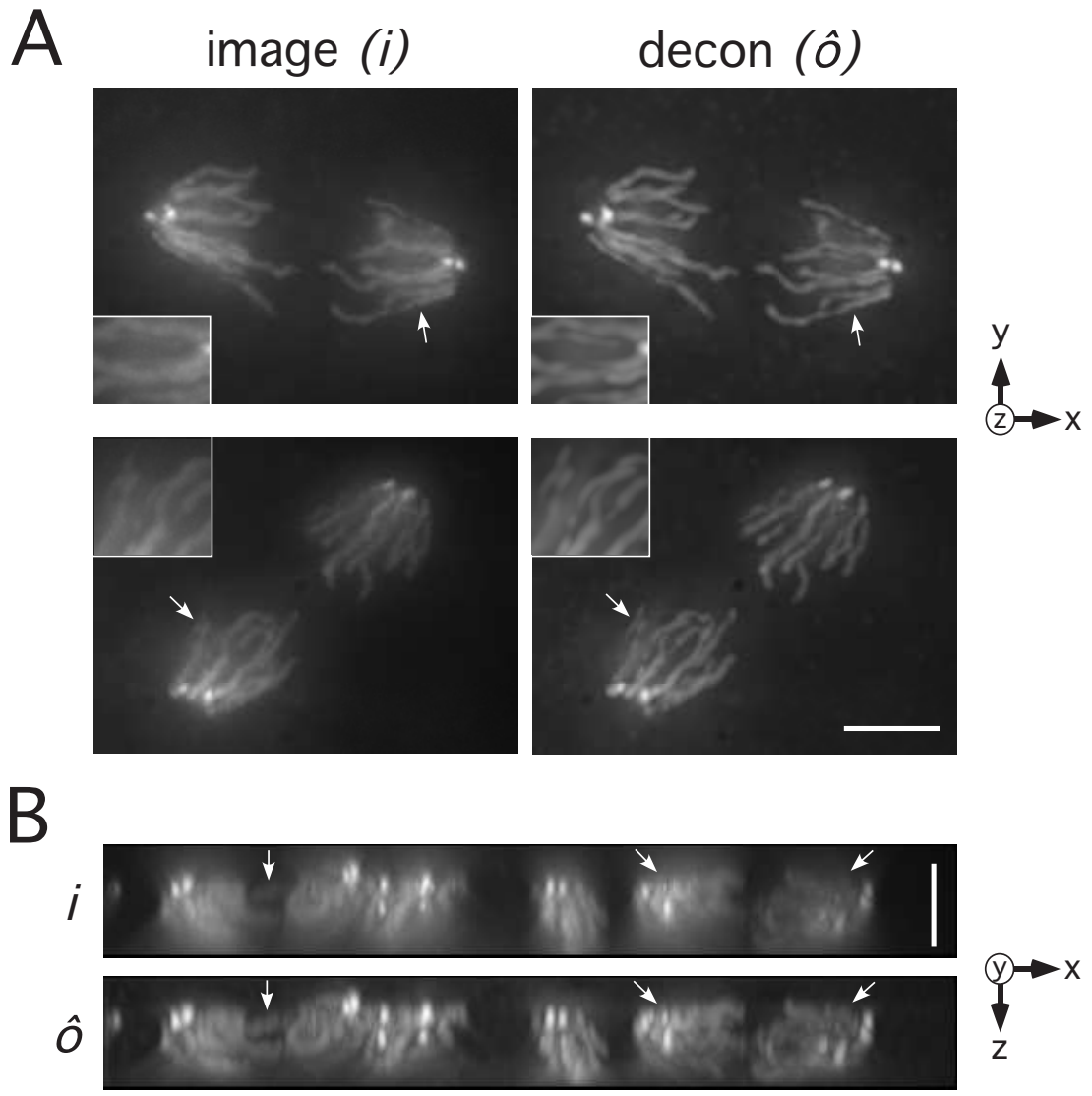

Figure 8.12: **Chromosomes of mitotically dividing cells (cell cycle 10, anaphase) within a *D. melanogaster* (fruit fly) embryo**. Chromosomes were stained with the fluorescent dye, DAPI, and embryos fixed in 10% formaldehyde fixation buffer, mounted in glycerol, and imaged using the OMX microscope system with a 100X oil-immersion objective (data courtesy of Yuri Strukov, Sedat Lab, UCSF). *(A)* Maximum intensity *xy*-projections of 2 subregions of an acquired 3D image stack after basic processing (removal of bad-pixels and flat-fielding) and myopic deconvolution result using $\zeta = 3.2$ and $\lambda_o = \hat{\lambda}_o/10$ (see text). Insets (see arrows) highlight corresponding areas of improved contrast after AIDA deconvolution. *(B)* *xz*-projections for the full data stack of (*A*). Areas of improved contrast are again highlighted by arrows. More dramatic restoration is observed in the axial (*z*-) direction, although some residual blurring remains, noticeably with increasing *z*. Image pixel size was 80 nm in the lateral (*xy*-) direction and 150 nm in the axial direction. Bar length = 4 μm

are not accounted for by the assumed noise model; the effectiveness of the hyperparameter estimation scheme is predicated upon good estimates for the Gaussian and Poisson noise statistics (as discussed in Sec. 7.4). Third, out-of-focus contributions to the image stack from areas of the embryo *outside* the image stack are not accounted for in the current imaging framework. The effects of these factors on deconvolution outcome and strategies to compensate for them are are currently being explored by our group.

Chapter 9

Outlook

I have extended the MISTRAL approach[177] to myopically deconvolve, for the first time, multiple image frame data and three dimensional image stacks. Our adaptive image deconvolution algorithm, AIDA, runs at least 15 times faster then the original MISTRAL algorithm and is intended for open-source development. Endowed with a simple yet robust scheme to estimate regularization hyperparameters, AIDA greatly simplifies the tedious and delicate though practically necessary task of balancing maximum likelihood estimation with object regularization/noise suppression. AIDA can generate high quality, edge-preserved, photometrically-precise object reconstructions without the need to sample (typically 10-20) different hyperparameter settings to identify an optimal set. This results in a practical efficiency gain of AIDA over MISTRAL of at least $\sim$ 200-fold.

Multiple image observations are commonly acquired in adaptive optics imaging, although they are often combined into a single averaged image before deconvolution. Deconvolving these images simultaneously, however, is a far more effective data reduction strat-

egy.[39,40,227,245] The multiframe deconvolution results of this paper show that by leveraging invariable aspects of the data while retaining the unique variations between distinct observations leads to object reconstructions with crisper details, higher photometric precision, and fewer artifacts than the corresponding mono-frame deconvolution results.

AIDA's multi-frame deconvolution capabilities are currently limited to data with a single object and multiple variable PSFs ($M_o = 1$; $M_h > 1$) or a single PSF and multiple variable objects ($M_h = 1$; $M_o > 1$). It would be straightforward to extend the algorithm to handle datasets in which multiple objects are imaged using different though known transformations of a fundamental PSF describing the optical system. This is relevant, for example, to multi-wavelength imaging in astronomy[118] and microscopy in which the PSF characteristics as a function of wavelength are well established and can be predicted. Such an approach could also be applied to process tomographic imaging data in which the dependence of the transfer function is known/parametrizable as a function of tilt angle. Using such a multi-object:multi-linked-PSF approach, our group is currently exploring the application of AIDA to deconvolve electron microscopy (EM) images, with the goal of improving 3D object reconstructions from EM tomographic data.

AIDA is equally effective in deconvolving 3D image data and 2D data, and deconvolution times scale linearly with the size of the image data. In the current AIDA framework, each image pixel element is treated as a variable to be optimized, leading to substantial computational demands as image/volume size increases. Work in our group is in progress to recast the optimization of the PSF in terms of Zernike polynomials and the more computationally compact "pupil function" that characterizes the optical wavefront at the exit

pupil of an imaging system arising from a point source.[96,97] In addition to greater computational efficiency for larger image datasets, myopic deconvolution using the pupil function and a Zernike expansion can provide explicit insight into the inherent or dynamic aberration modes of an optical system. The ease in which the pupil function can be modified to account for aberrations makes it particularly amenable to use in cases where the PSF is space-variant[96,97] (e.g., with depth-dependent index of refraction variations in microscopy or anisoplanatic imaging in astronomy). Moreover, use of the pupil function could help bridge the synthesis of wavefront sensing data from adaptive optics and imaging data in the deconvolution process.[178]

At least three issues merit futher development and exploration. First, the development of a multi-object deconvolution mode more specifically taylored for time-series data. In deconvolving the microtubule dynamics data in Sec. 8.2.3, the temporal independence of each object in the time-series was assumed. While this was helpful in highlighting common, persistent features between time frames, incorporating a cost function term or procedure within the deconvolution algorithm to maximize the temporal correlation between adjacent time slices may help reinforce object features that are self-similar and suppress temporally-uncorrelated noise artifacts. Second, as image datasets become larger and/or deviations from the assumed noise model become more pronounced, optimization convergence may become seriously compromised. Convergence might be improved by switching from a weighted least-squares (L2-norm) form for the data-fidelity term to a robust L1-norm form which is computationally simpler and less sensitive to noise model mismatch and data outliers.[67,111,136] Deconvolution efficiency might also be improved by a reparametrization of the object, for

example, using wavelets, and by incorporating aspects of multi-resolution/hierarchical scaling into the deconvolution algorithm.[71,204,242,258] Finally, it would be interesting see how the edge-preserving and noise suppression advantages of AIDA deconvolution could improve the processing of data from super-resolution imaging modalities such as multi-frame mosaicing[19,67] and structured illumination microscopy.[91,92]

Bibliography

[1] M. Adams and S. Fraden. Phase behavior of mixtures of rods (tobacco mosaic virus) and spheres (polyethylene oxide, bovine serum albumin). *Biophysical Journal*, 74(1):669–677, 1998.

[2] H. V. Andersen, A. Friderichsen, S. Clausen, and J. Bak. Comparison of noise sources in dual- and single-beam fourier-transform near-infrared spectrometry. *Applied Optics*, 44(29):6167–6175, 2005.

[3] S. R. Aragon and R. Pecora. Fluorescence correlation spectroscopy as a probe of molecular dynamics. *Journal of Chemical Physics*, 64(4):1791–1803, 1976.

[4] G. R. Ayers and J. C. Dainty. Iterative blind deconvolution method and its applications. *Optics Letters*, 13(7):547–549, 1988.

[5] K. Bacia and P. Schwille. A dynamic view of cellular processes by in vivo fluorescence auto- and cross-correlation spectroscopy. *Methods*, 29(1):74–85, 2003.

[6] J. Balaji, P. Sengupta, G. R. Kumar, and S. Maiti. Localized photo-excitation: Measuring diffusion, multiphoton cross-section, and photobleaching. *Biophysical Journal*, 80(1):168A–169A, 2001.

[7] L. A. Banaszynski, C. W. Liu, and T. J. Wandless. Characterization of the fkbp.rapamycin.frb ternary complex. *Journal of the American Chemical Society*, 127(13):4715–4721, 2005.

[8] D. S. Banks and C. Fradin. Anomalous diffusion of proteins due to molecular crowding. *Biophysical Journal*, 89(5):2960–2971, 2005.

[9] N. Baudendistel, G. Muller, W. Waldeck, P. Angel, and J. Langowski. Two-hybrid fluorescence cross-correlation spectroscopy detects protein-protein interactions in vivo. *ChemPhysChem*, 6(5):984–990, 2005.

[10] M. S. Bazaraa, H. D. Sherali, and C. M. Shetty. *Nonlinear Programming: Theory and Algorithms, 2nd Edition*. Wiley, New York, 1993.

[11] D. M. Beazley. Automated scientific software scripting with swig. *Future Generation Computer Systems*, 19(5):599–609, 2003.

[12] D. M. Beazley and co workers. A simplified wrapper and interface generator. http://www.swig.org.

[13] K. M. Berland, P. T. So, and E. Gratton. Two-photon fluorescence correlation spectroscopy: method and application to the intracellular environment. *Biophysical Journal*, 68(2):694–701, 1995.

[14] C. F. Bernasconi. *Relaxation Kinetics*. Academic Press, New York, 1976.

[15] M. Bertero and P. Boccacci. *Introduction to Inverse Problems in Imaging*. Institute of Physics Pub, Philadelphia, PA, 1998.

[16] J. Besag. On the statistical-analysis of dirty pictures. *Journal of the Royal Statistical Society Series, B - Methodological*, 48(3):259–302, 1986.

[17] E. Betzig. Excitation strategies for optical lattice microscopy. *Optics Express*, 13(8):3021–2036, 2005.

[18] P. R. Bevington and D. K. Robinson. *Data Reduction and Error Analysis for the Physical Sciences, 2nd Edition*. McGraw-Hill, New York, 1992.

[19] D. S. Biggs, C.-L. Wang, T. J. Holmes, and A. Khodjakov. Subpixel deconvolution of 3d optical microscope imagery. In Andrew G. Tescher, editor, *Proceedings of the SPIE: Applications of Digital Image Processing XXVII*, volume 5559, pages 369–380, 2004.

[20] E. Bismuto, E. Gratton, and D. C. Lamb. Dynamics of ans binding to tuna apomyoglobin measured with fluorescence correlation spectroscopy. *Biophysical Journal*, 81(6):3510–3521, 2001.

[21] G. Bonnet, O. Krichevsky, and A. Libchaber. Kinetics of conformational fluctuations in dna hairpin-loops. *Proceedings of the National Academy of Sciences, USA*, 95(15):8602–8606, 1998.

[22] C. Bouman and K. Sauer. A generalized gaussian image model for edge-preserving map estimation. *IEEE Transactions of Image Processing*, 2(3):296–310, 1993.

[23] R. N. Bracewell. *The Fourier Transform and Its Applications*. McGraw-Hill, New York, 1999.

[24] D. Bray. Signaling complexes: biophysical constraints on intracellular communication. *Annual Review of Biophysics and Biomolecular Structure*, 27(5):59–75, 1998.

[25] S. Brette and J. Idier. Optimized single site update algorithms for image deblurring. In *Proceedings of IEEE International Conference on Image Processing*, volume 3, pages 65–68, New York, 1996. Institute of Electrical and Electronics Engineers.

[26] D. A. Bulseco and D. E. Wolf. Fluorescence correlation spectroscopy: molecular complexing in solution and in living cells. *Methods in Cell Biology*, 72:465–498, 2003.

[27] R. E. Campbell, O. Tour, A. E. Palmer, P. A. Steinbach, G. S. Baird, D. A. Zacharias, and R. Y. Tsien. A monomeric red fluorescent protein. *Proceedings of the National Academy of Sciences, USA*, 99(12):7877–7882, 2002.

[28] C. R. Cantor and P. R. Schimmel. *Biophysical Chemistry. Part III: The Behavior of Biological Macromolecules.* W. H. Freeman, San Francisco, 1980.

[29] David Chandler. *Introduction to Modern Statistical Mechanics.* Oxford University Press, 1987.

[30] S. Chandrasekhar. Stochastic problems in physics and astronomy. *Reviews of Modern Physics*, 15:1–89, 1943.

[31] P. Charbonnier, L. Blanc-Feraud, G. Aubert, and M. Barlaud. Deterministic edge-preserving regularization in computed imaging. *IEEE Transactions of Image Processing*, 6(2):298–311, 1997.

[32] Y. Chen, J. D. Müller, P. T. So, and E. Gratton. The photon counting histogram in fluorescence fluctuation spectroscopy. *Biophysical Journal*, 77(1):553–567, 1999.

[33] Y. Chen, J. D. Müller, S. Y. Tetin, J. D. Tyner, and E. Gratton. Probing ligand protein binding equilibria with fluorescence fluctuation spectroscopy. *Biophysical Journal*, 79(2):1074–1084, 2000.

[34] Y. Chen, M. Tekmen, L. Hillesheim, J. Skinner, B. Wu, and J. D. Müller. Dual-color photon-counting histogram. *Biophysical Journal*, 88(3):2177–2192, 2005.

[35] Y. D. Chen. Matrix method for fluctuations and noise in kinetic systems. *Proceedings of the National Academy of Sciences, USA*, 72(10):3807–3811, 1975.

[36] Y. D. Chen. Differentiation between equilibrium and nonequilibrium kinetic systems by noise analysis. *Biophysical Journal*, 21(3):279–285, 1978.

[37] C. Christou, J., E. K. Hege, M. Jefferies, S., and C. U. Keller. Application of multiframe iterative blind deconvolution for diverse astronomical imaging. In James B. Breckinridge, editor, *Proceedings of the SPIE: Amplitude and Intensity Spatial Interferometry II*, volume 2200, pages 433–444, 1994.

[38] J. C. Christou, D. Bonnacini, N. Ageorges, and F. Marchis. Myopic deconvolution of adaptive optics images. *The Messenger*, 97:14–22, 1999.

[39] J. C. Christou, E. K. Hege, and S. M. Jefferies. Speckle deconvolution imaging using an iterative algorithm. In Natalie Clark and John D. Gonglewski, editors, *Proceedings of the SPIE: Advanced Imaging Technologies and Commercial Applications*, volume 2566, pages 134–143, 1995.

[40] J. C. Christou, A. Roorda, and D. R. Williams. Deconvolution of adaptive optics retinal images. *Journal of the Optical Society of America, A*, 21(8):1393–1401, 2004.

[41] C. K. Chu, I. K. Glad, F. Godtliebsen, and J. S. Marron. Edge-preserving smoothers for image processing. *Journal of the American Statistical Association*, 93(442):526–541, 1998.

[42] J.-M. Conan, L. M. Mugnier, T. Fusco, V. Michau, and G. Rousset. Myopic deconvolution of adaptive optics images by use of object and point-spread function power spectra. *Applied Optics*, 37:4614–4622, 1998.

[43] S. Costantino, J. W. Comeau, D. L. Kolin, and P. W. Wiseman. Accuracy and dynamic range of spatial image correlation and cross-correlation spectroscopy. *Biophysical Journal*, 89(2):1251–1260, 2005.

[44] A. Coustenis, E. Gendron, O. Lai, J.-P. Véran, J. Woillez, M. Combes, L. Vapillon, T. Fusco, L. Mugnier, and P. Rannou. Images of titan at 1.3 and 1.6 μm with adaptive optics at the cfht. *Icarus*, 154:501–515, 2001.

[45] E. Dauty and A. S. Verkman. Molecular crowding reduces to a similar extent the diffusion of small solutes and macromolecules: measurement by fluorescence correlation spectroscopy. *Journal of Molecular Recognition*, 17(5):441–447, 2004.

[46] E. Dauty and A. S. Verkman. Actin cytoskeleton as the principal determinant of size-dependent dna mobility in cytoplasm: a new barrier for non-viral gene delivery. *Journal of Biological Chemistry*, 280(9):7823–7828, 2005.

[47] L. M. Davis, D. A. Ball, P. E. Williams, K. M. Swift, and E. D. Matayoshi. Dealing with reduced data acquisition times in fluorescence correlation spectroscopy (fcs) for high-throughput screening (hts) applications. In V. Nicolau Dan and Raghavachari Ramesh, editors, *Proceedings of the SPIE: Microarrays and Combinatorial Technologies for Biomedical Applications: Design, Fabrication, and Analysis*, volume 4966(1), pages 117–128, San Jose, CA, USA, 2003. SPIE.

[48] R. N. Day and F. Schaufele. Imaging molecular interactions in living cells. *Molecular Endocrinology*, 19(7):1675–1686, 2005.

[49] M. J. Dayel, E. F. Hom, and Alan S. Verkman. Diffusion of green fluorescent protein in the aqueous-phase lumen of endoplasmic reticulum. *Biophysical Journal*, 76(5):2843–2851, 1999.

[50] I. de Pater, M. Ádámkovics, A. H. Bouchez, M. E. Brown, S. G. Gibbard, F. Marchis, H. G. Roe, E. Schaller, and E. Young. Titan imagery with keck ao during and after probe entry. *Journal of Geophysical Research*, submitted, 2005.

[51] I. de Pater, S. G. Gibbard, B. A. Macintosh, H.G. Roe, D. T. Gavel, and C. E. Max. Keck adaptive optics images of uranus and its rings. *Icarus*, 160(2):359–374, 2002.

[52] G. Demoment. Image reconstruction and restoration: overview of common estimation structures and problems. *IEEE Transactions on Acoustics, Speech, and Signal Processing*, 37(12):2024–2036, 1989.

[53] W. Denk, J. H. Strickler, and W. W. Webb. Two-photon laser scanning fluorescence microscopy. *Science*, 248(4951):73–76, 1990.

[54] P. Descamps, F. Marchis, J. Berthier, R. Prangé, T. Fusco, and C. Le Guyader. First ground-based astrometric observations of puck. *Comptes rendus de l'Académie des sciences, Physique*, 3:121–128, 2002.

[55] M. A. Digman, P. Sengupta, P. W. Wiseman, C. M. Brown, A. R. Horwitz, and E. Gratton. Fluctuation correlation spectroscopy with a laser-scanning microscope: exploiting the hidden time structure. *Biophysical Journal*, 88(5):L33–6, 2005.

[56] P. Dittrich, F. Malvezzi-Campeggi, M. Jahnz, and P. Schwille. Accessing molecular dynamics in cells by fluorescence correlation spectroscopy. *Biological Chemistry*, 382(3):491–494, 2001.

[57] S. Douté, B. Schmitt, R. Lopes-Gautier, R. Carlson, L. Soderblom, J. Shirley, and The Galileo NIMS Team (T. G. N. T). Mapping so_2 frost on io by the modeling of nims hyperspectral images. *Icarus*, 149:107–132, 2001.

[58] A. K. Dunker, E. Garner, S. Guilliot, P. Romero, K. Albrecht, J. Hart, Z. Obradovic, C. Kissinger, and J. E. Villafranca. Protein disorder and the evolution of molecular recognition: theory, predictions and observations. *Pacific Symposium on Biocomputing*, 115(2):473–484, 1998.

[59] C. Eggeling, P. Kask, D. Winkler, and S. Jager. Rapid analysis of forster resonance energy transfer by two-color global fluorescence correlation spectroscopy: trypsin proteinase reaction. *Biophysical Journal*, 89(1):605–168, 2005.

[60] C. Eggeling, J. Widengren, R. Rigler, and C. A. M. Seidel. Photobleaching of fluores-

cent dyes under conditions used for single-molecule detection: Evidence of two-step photolysis. *Analytical Chemistry*, 70(13):2651–2659, 1998.

[61] A. Egner and S. W. Hell. Time multiplexing and parallelization in multifocal multiphoton microscopy. *Journal of the Optical Society of America, A*, 17(7):1192–1201, 2000.

[62] J. S. Eid, J. D. Muller, and E. Gratton. Data acquisition card for fluctuation correlation spectroscopy allowing full access to the detected photon sequence. *Review of Scientific Instruments*, 71(2):361–368, 2000.

[63] A. H . Elcock. Atomic-level observation of macromolecular crowding effects: escape of a protein from the groel cage. *Proceedings of the National Academy of Sciences, USA*, 100(5):2340–2344, 2003.

[64] E. L. Elson. Quick tour of fluorescence correlation spectroscopy from its inception. *Journal of Biomedical Optics*, 9(5):857–864, 2004.

[65] E. L. Elson and D. Magde. Fluorescence correlation spectroscopy. i. conceptual basis and theory. *Biopolymers*, 13(1):1–27, 1974.

[66] E. L. Elson and H. Qian. Interpretation of fluorescence correlation spectroscopy and photobleaching recovery in terms of molecular interactions. *Methods in Cell Biology*, 30(2):307–332, 1989.

[67] S. Farsiu, D. Robinson, M. Elad, and P. Milanfar. Advances and challenges in superresolution. *International Journal of Imaging Systems and Technology (Special Issue on High Resolution Image Reconstruction)*, 14(2):47–57, 2004.

[68] M. C. Faux and J. D. Scott. Molecular glue: kinase anchoring and scaffold proteins. *Cell*, 85(1):9–12, 1996.

[69] P. Fekkes, T. den Blaauwen, and A. J. Driessen. Diffusion-limited interaction between unfolded polypeptides and the escherichia coli chaperone secb. *Biochemistry*, 34(31):10078–10085, 1995.

[70] A. R. Fersht. *Structure and Mechanism in Protein Science : A Guide to Enzyme Catalysis and Protein Folding*. W. H. Freeman, 1998.

[71] M. A. T. Figueiredo and R. D. Nowak. An em algorithm for wavelet-based image restoration. *IEEE Transactions of Image Processing*, 12(8):906–916, 2003.

[72] Z. Foldes-Papp. How the molecule number is correctly quantified in two-color fluorescence cross-correlation spectroscopy: corrections for cross-talk and quenching in experiments. *Current Pharmaceutical Biotechnology*, 6(6):437–444, 2005.

[73] W. Frei and C. Chung-Ching. Fast boundary detection: a generalization and a new algorithm. *IEEE Transactions on Computers*, C26(10):988–998, 1977.

[74] David M. Freifelder. *Physical Biochemistry : Applications to Biochemistry and Molecular Biology*. W. H. Freeman, 1982.

[75] M. Frigo and S. G. Johnson. The design and implementation of fftw3. *Proceedings of the IEEE*, 93(2):216–231, 2005.

[76] T. Fusco, J.-P. Véran, J.-M. Conan, and L. M. Mugnier. Myopic deconvolution method

for adaptive optics images of stellar fields. *Astronomy and Astrophysics Supplement Series*, 134:193–200, 1999.

[77] R. R. Gabdoulline and R. C. Wade. Protein-protein association: investigation of factors influencing association rates by brownian dynamics simulations. *Journal of Molecular Biology*, 306(5):1139–1155, 2001.

[78] N. P. Galatsanos and A. K. Katsaggelos. Methods for choosing the regularization parameter and estimating the noise variance in image restoration and their relation. *IEEE Transactions of Image Processing*, 1(3):332–336, 1992.

[79] M. F. Garcia-Parajo, M. Koopman, E. M. van Dijk, V. Subramaniam, and N. F. van Hulst. The nature of fluorescence emission in the red fluorescent protein dsred, revealed by single-molecule detection. *Proceedings of the National Academy of Sciences, USA*, 98(25):14392–14397, 2001.

[80] H. Geerts. Experimental realization and optimalization of a fluorescence correlation spectroscopy apparatus. *Journal of Biochemical and Biophysical Methods*, 7(3):255–261, 1983.

[81] S. Geman and D. Geman. Stochastic relaxation, gibbs distributions, and bayesian restoration of images. *IEEE Transactions on Pattern Analysis and Machine Intelligence*, 6(6):721–741, 1984.

[82] A. Gennerich and D. Schild. Anisotropic diffusion in mitral cell dendrites revealed by fluorescence correlation spectroscopy. *Biophysical Journal*, 83(1):510–522, 2002.

[83] S. G. Gibbard, I. de Pater, B. A. Macintosh, H. G. Roe, C. E. Max, E. F. Young, and C. P. McKay. Titan's 2 μm surface albedo and haze optical depth in 1996-2004. *Geophysical Research Letters*, 31, 2004.

[84] S. F. Gibson and F. Lanni. Experimental test of an analytical model of aberration in an oil-immersion objective lens used in three-dimensional light microscopy. *Journal of the Optical Society of America, A*, 8(10):1601–1613, 1991.

[85] Jay A. Glasel and Murray P. Deutscher. *Introduction to Biophysical Methods for Protein and Nucleic Acid Research*. Academic Press, 1995.

[86] G. H. Golub, M. Heath, and G. Wahba. Generalized cross-validation as a method for choosing a good ridge parameter. *Technometrics*, 21(2):215–223, 1979.

[87] D. M. Goodman, E. M. Johansson, and T. W. Lawrence. On applying the conjugate gradient algorithm to image processing problems, chapter 11. In C. Radhakrishna Rao, editor, *Multivariate Analysis: Future Directions: North-Holland Series in Statistics and Probability; v. 5*, pages 209–232. North-Holland, Amsterdam, 1993.

[88] M. Gosch, H. Blom, S. Anderegg, K. Korn, P. Thyberg, M. Wells, T. Lasser, R. Rigler, A. Magnusson, and S. Hard. Parallel dual-color fluorescence cross-correlation spectroscopy using diffractive optical elements. *Journal of Biomedical Optics*, 10(5):54008, 2005.

[89] R. F. Greene and H. B. Callen. On the formalism of thermodynamic fluctuation theory. *Physical Review*, 83(6):1231–1235, 1951.

[90] P. Greenfield, T. Miller, W. Rick, J. C. Hsu, P. Barrett, J. Kupper, and P. J. Verveer. Numarray: An open source project. http://www.stsci.edu/resources/software_hardware/numarray.

[91] M. G. Gustafsson. Surpassing the lateral resolution limit by a factor of two using structured illumination microscopy. *Journal of Microscopy*, 198(2):82–87, 2000.

[92] M. G. Gustafsson. Nonlinear structured-illumination microscopy: wide-field fluorescence imaging with theoretically unlimited resolution. *Proceedings of the National Academy of Science, USA*, 102(37):13081–13086, 2005.

[93] D. Hall and A. P. Minton. Macromolecular crowding: qualitative and semiquantitative successes, quantitative challenges. *Biochimica Biophysica Acta*, 1649(2):127–139, 2003.

[94] H. B. Hammel, Imke de Pater, S. G. Gibbard, G. W. Lockwood, and K. Rages. New cloud activity on uranus in 2004: first detection of a southern feature at 2.2 μm. *Icarus*, 175(1), 2005.

[95] J. Han and J. Herzfeld. Macromolecular diffusion in crowded solutions. *Biophysical Journal*, 65(3):1155–1161, 1993.

[96] B. M. Hanser, M. G. L. Gustafsson, D. A. Agard, and J. W. Sedat. Phase retrieval for high-numerical-aperture optical systems. *Optics Letters*, 28(10):801–803, 2003.

[97] B. M. Hanser, M. G. L. Gustafsson, D. A. Agard, and J. W. Sedat. Phase-retrieved pupil functions in wide-field fluorescence microscopy. *Journal of Microscopy*, 216:32–48, 2004.

[98] D. C. Harris. Nonlinear least-squares curve fitting with microsoft excel solver. *Journal of Chemical Education*, 75(1):119–121, 1998.

[99] U. Haupts, S. Maiti, P. Schwille, and W. W. Webb. Dynamics of fluorescence fluctuations in green fluorescent protein observed by fluorescence correlation spectroscopy. *Proceedings of the National Academy of Sciences, USA*, 95(23):13573–13578, 1998.

[100] E. Haustein and P. Schwille. Ultrasensitive investigations of biological systems by fluorescence correlation spectroscopy. *Methods*, 29(2):153–166, 2003.

[101] B. Hebert, S. Costantino, and P. W. Wiseman. Spatiotemporal image correlation spectroscopy (stics) theory, verification, and application to protein velocity mapping in living cho cells. *Biophysical Journal*, 88(5):3601–3614, 2005.

[102] A. A. Heikal, S. T. Hess, G. S. Baird, R. Y. Tsien, and W. W. Webb. Molecular spectroscopy and dynamics of intrinsically fluorescent proteins: coral red (dsred) and yellow (citrine). *Proceedings of the National Academy of Sciences, USA*, 97(22):11996–12001, 2000.

[103] K. G. Heinze, A. Koltermann, and P. Schwille. Simultaneous two-photon excitation of distinct labels for dual-color fluorescence cross-correlation analysis. *Proceedings of the National Academy of Sciences, USA*, 97(19):10377–10382, 2000.

[104] S. T. Hess and W. W. Webb. Focal volume optics and experimental artifacts in confocal fluorescence correlation spectroscopy. *Biophysical Journal*, 83(4):2300–2317, 2002.

[105] Y. Hiraoka, J. W. Sedat, and D. A. Agard. The use of a charge-coupled device for quantitative optical microscopy of biological structures. *Science*, 238(4823):36–41, 1987.

[106] T. J. Holmes. Blind deconvolution of quantum-limited incoherent imagery: maximum-likelihood approach. *Journal of the Optical Society of America, A*, 9:1052–1061, 1992.

[107] E. F. Hom and A. S. Verkman. Analysis of coupled bimolecular reaction kinetics and diffusion by two-color fluorescence correlation spectroscopy: enhanced resolution of kinetics by resonance energy transfer. *Biophysical Journal*, 83(1):533–546, 2002.

[108] Q. Hong and E. L. Elson. Analysis of confocal laser-microscope optics for 3-d fluorescence correlation spectroscopy. *Applied Optics*, 30(10):1185–1195, 1991.

[109] A. Hoppe, K. Christensen, and J. A. Swanson. Fluorescence resonance energy transfer-based stoichiometry in living cells. *Biophysical Journal*, 83(6):3652–3664, 2002.

[110] S. B. Howell. *Handbook of CCD astronomy*. Cambridge University Press, New York, 2000.

[111] P. J. Huber. *Robust Statistics*. Wiley-Interscience, New York, 2003.

[112] M. Huertas de la Torre, R. Forni, and G. Chirico. Brownian dynamics simulations of fluorescence fluctuation spectroscopy. *European Biophysical Journal*, 30(2):129–139, 2001.

[113] J. H. Hurley and T. Meyer. Subcellular targeting by membrane lipids. *Current Opinion in Cell Biology*, 13(2):146–152, 2001.

[114] M. V. Ibáñez and A. Simó. Parameter estimation in markov random field image modeling with imperfect observations. a comparative study. *Pattern Recognition Letters*, 24(14):2377–2389, 2003.

[115] R. D. Icenogle. *Fluorescence correlation spectroscopy and fluorescence photobleaching recovery studies of the binding of ethidium to deoxyribonucleic acid*. PhD thesis, Cornell University, Ithaca, NY, 1981.

[116] R. D. Icenogle and E. L. Elson. Fluorescence correlation spectroscopy and photobleaching recovery of multiple binding reactions. i. theory and fcs measurements. *Biopolymers*, 22(8):1919–1948, 1983.

[117] R. D. Icenogle and E. L. Elson. Fluorescence correlation spectroscopy and photobleaching recovery of multiple binding reactions. ii. fpr and fcs measurements at low and high dna concentrations. *Biopolymers*, 22(8):1949–1966, 1983.

[118] H. R. Ingleby and D. R. McGaughey. Experimental results of parallel multiframe blind deconvolution using wavelength diversity. In John C. Armitage, Simon Fafard, Roger A. Lessard, and George A. Lampropoulos, editors, *Proceedings of the SPIE: Optical Components and Devices*, volume 5578, pages 8–14, 2004.

[119] M. Iwashima. Kinetic perspectives of t cell antigen receptor signaling. a two-tier model for t cell full activation. *Immunological Reviews*, 191:196–210, 2003.

[120] A. Jalobeanu, L. Blanc-Féraud, and J. Zerubia. Adaptive parameter estimation for satellite image deconvolution. *Rapport de Recherche de l'INRIA-Sophia Antipolis, Equipe:ARIANA*, RR-3956, 2000.

[121] A. Jalobeanu, L. Blanc-Féraud, and J. Zerubia. Estimation of adaptive parameters for satellite image deconvolution. In A. Sanfeliu, J. J. Villanueva, M. Vanrell, R. Alquezar, J. O. Eklundh, and Y. Aloimonos, editors, *Proceedings of the IEEE International Conference on Pattern Recognition*, volume 3, pages 318–321, New York, 2000. Institute of Electrical and Electronic Engineers.

[122] A. Jalobeanu, L. Blanc-Féraud, and J. Zerubia. Hyperparameter estimation for satellite image restoration using a mcmc maximum-likelihood method. *Pattern Recognition*, 35(2):341–352, 2002.

[123] A. Jalobeanu, L. Blanc-Féraud, and J. Zerubia. An adaptive gaussian model for satellite image deblurring. *IEEE Transactions of Image Processing*, 13(4):613–621, 2004.

[124] J. Janin. The kinetics of protein-protein recognition. *Proteins*, 28(2):153–161, 1997.

[125] Joël Janin. Kinetics and thermodynamics of protein-protein interactions. In Colin Kleanthous, editor, *Protein-Protein Recognition*, pages 1–32. Oxford University Press, New York, 2000.

[126] S. M. Jefferies and J. C. Christou. Restoration of astronomical images by iterative blind deconvolution. *Astrophysical Journal*, 415:862–874, 1993.

[127] W. Johnson, D. Robertson, and and others. The whole frog project. http://froggy.lbl.gov.

[128] R. A. Johnston, T. J. Connolly, and R. G. Lane. An improved method for deconvolving a positive image. *Optics Communications*, 181(4-6):267–278, 2000.

[129] J. E. N. Jonkman and E. H. K. Stelzer. Resolution and contrast in confocal and two-photon microscopy, chapter 5. In Alberto Diaspro, editor, *Confocal and Two-Photon Microscopy : Foundations, Applications and Advances*, pages 101–125. Wiley-Liss, New York, 2001.

[130] P. Kask, R. Gunther, and P. Axhausen. Statistical accuracy in fluorescence fluctuation experiments. *European Biophysics Journal*, 25(3):163–169, 1997.

[131] P. Kask, K. Palo, N. Fay, L. Brand, Ü. Mets, D. Ullmann, J. Jungmann, J. Pschorr, and K. Gall. Two-dimensional fluorescence intensity distribution analysis: theory and applications. *Biophysical Journal*, 78(4):1703–1713, 2000.

[132] P. Kask, K. Palo, D. Ullmann, and K. Gall. Fluorescence-intensity distribution analysis and its application in biomolecular detection technology. *Proceedings of the National Academy of Sciences, USA*, 96(24):13756–13761, 1999.

[133] P. Kask, P. Piksarv, Ü. Mets, M. Pooga, and E. Lippmaa. Fluorescence correlation spectroscopy in the nanosecond time range: rotational diffusion of bovine carbonic anhydrase b. *European Biophysics Journal*, 14(4):257–261, 1987.

[134] L. Kastrup, H. Blom, C. Eggeling, and S. W. Hell. Fluorescence fluctuation spectroscopy in subdiffraction focal volumes. *Physical Review Letters*, 94(17):178104, 2005.

[135] B. Z. Katz, D. Krylov, S. Aota, M. Olive, C. Vinson, and K. M. Yamada. Green fluorescent protein labeling of cytoskeletal structures–novel targeting approach based on leucine zippers. *Biotechniques*, 25(2):298–304, 1998.

[136] Q. Ke and T. Kanade. Robust subspace computation using l1 norm. http://reports-archive.adm.cs.cmu.edu/anon/2003/CMU-CS-03-172.pdf.

[137] J. Keizer. *Statistical Thermodynamics of Nonequilibrium Processes*. Springer, 1987.

[138] U. Kettling, A. Koltermann, P. Schwille, and M. Eigen. Real-time enzyme kinetics monitored by dual-color fluorescence cross-correlation spectroscopy. *Proceedings of the National Academy of Sciences, USA*, 95(4):1416–1420, 1998.

[139] J. G. Kirkwood and F. P. Buff. The statistical mechanical theory of solutions. i. *Journal of Chemcal Physics*, 19(6):774–777, 1951.

[140] D. L. Kolin, S. Costantino, and P. W. Wiseman. Sampling effects, noise, and photobleaching in temporal image correlation spectroscopy. *Biophysical Journal*, 90(2):628–639, 2006.

[141] D. E. Koppel. Statistical accuracy in fluorescence correlation spectroscopy. *Physical Review A*, 10(6):1938–1945, 1974.

[142] R. Koren and G. G. Hammes. A kinetic study of protein-protein interactions. *Biochemistry*, 15(5):1165–1171, 1976.

[143] D. Krylov, J. Barchi, and C. Vinson. Inter-helical interactions in the leucine zipper coiled coil dimer: ph and salt dependence of coupling energy between charged amino acids. *Journal of Molecular Biology*, 279(4):959–972, 1998.

[144] D. Krylov, I. Mikhailenko, and C. Vinson. A thermodynamic scale for leucine zipper

stability and dimerization specificity: e and g interhelical interactions. *EMBO Journal*, 13(12):2849–2861, 1994.

[145] J. R. Lakowicz. *Principles of Fluorescence Spectroscopy*. Springer, 1999.

[146] D. C. Lamb, B. K. Muller, and C. Brauchle. Enhancing the sensitivity of fluorescence correlation spectroscopy by using time-correlated single photon counting. *Current Pharmaceutical Biotechnology*, 6(5):405–414, 2005.

[147] D. C. Lamb, A. Schenk, C. Rocker, C. Scalfi-Happ, and G. U. Nienhaus. Sensitivity enhancement in fluorescence correlation spectroscopy of multiple species using time-gated detection. *Biophysical Journal*, 79(2):1129–1138, 2000.

[148] K. Lange. Convergence of em image-reconstruction algorithms with gibbs smoothing. *IEEE Transactions on Medical Imaging*, 9(4):439–446, 1990.

[149] J. Langowski and M. Tewes. Determination of dna-ligand interactions by fluorescence correlation spectroscopy. In A. A. Travers, Malcolm Buckle, and Andrew Travers, editors, *DNA-Protein Interactions: A Practical Approach*, pages 95–111. Oxford University Press, New York, 2000.

[150] T. A. Laurence, A. N. Kapanidis, X. X. Kong, D. S. Chemla, and S. Weiss. Photon arrival-time interval distribution (paid): a novel tool for analyzing molecular interactions. *Journal of Physical Chemistry, B*, 108(9):3051–3067, 2004.

[151] D. Le Mignant, F. Marchis, D. Bonaccini, P. Prado, E. Barrios, R. Tighe, V. Merino, A. Sanchez, The 3.60m Telescope Team, and ESO AO Team. The eso adonis system:

A 3 years experience in observing methods. In Domenico Bonaccini, editor, *ESO Conference and Workshop Proceedings*, volume 56, page 287, Sonthofen, Germany, 1999. Garching, Germany: European Southern Observatory.

[152] W.-Y. V. Leung and Richard G. Lane. Blind deconvolution of images blurred by atmospheric speckle. In Michael A. Fiddy and Rick P. Millane, editors, *Proceedings of the SPIE: Image Reconstruction from Incomplete Data*, volume 4123, pages 73–83, 2000.

[153] G. Li and H. Qian. Sensitivity and specificity amplification in signal transduction. *Cell Biochemistry and Biophysics*, 39(1):45–59, 2003.

[154] J. Liang, D. R. Williams, and D. T. Miller. Supernormal vision and high-resolution retinal imaging through adaptive optics. *Journal of the Optical Society of America, A*, 14(11):2884–2892, 1997.

[155] J. W. Lichtman and J. A. Conchello. Fluorescence microscopy. *Nature Methods*, 2(12):910–919, 2005.

[156] A. M. Lieto and N. L. Thompson. Total internal reflection with fluorescence correlation spectroscopy: nonfluorescent competitors. *Biophysical Journal*, 87(2):1268–1278, 2004.

[157] E. Lindahl, B. Hess, and D. van der Spoel. Gromacs 3.0: a package for molecular simulation and trajectory analysis. *Journal of Molecular Modeling*, 7(8):306–317, 2001.

[158] D. Magde. Concentration correlation analysis and chemical kinetics. In I. Pecht and R. Rigler, editors, *Chemical Relaxation in Molecular Biology*, pages 43–83. Springer-Verlag, Berlin, 1977.

[159] D. Magde, E. Elson, and W. W. Webb. Thermodynamic fluctuations in a reacting system: measurement by fluorescence correlation spectroscopy. *Physical Review Letters*, 29(11):705–708, 1972.

[160] D. Magde, E. L. Elson, and W. W. Webb. Fluorescence correlation spectroscopy. ii. an experimental realization. *Biopolymers*, 13(1):29–61, 1974.

[161] S. Maiti, U. Haupts, and W. W. Webb. Fluorescence correlation spectroscopy: diagnostics for sparse molecules. *Proceedings of the National Academy of Sciences, USA*, 94(22):11753–11757, 1997.

[162] J. S. Marchant, G. E. Stutzmann, M. A. Leissring, F. M. LaFerla, and I. Parker. Multiphoton-evoked color change of dsred as an optical highlighter for cellular and subcellular labeling. *Nature Biotechnology*, 19(7):645–649, 2001.

[163] F. Marchis. http://astron.berkeley.edu/∼fmarchis/science/keck/perfectpsf/.

[164] F. Marchis. *High resolution imaging of the solar system bodies by means of adaptive optics: A study of Io*. PhD thesis, European Southern Observatory, Chile and Institut d'Astrophysique Spatiale, France, 2000.

[165] F. Marchis, A. G. Davies, S. G. Gibbard, D. Le Mignant, R. M. Lopes, B. Macintosh, and I. de Pater. Volcanic activity of io monitored with keck-10m ao in 2003-2004. In *American Geophysical Union, Fall Meeting 2004 Abstracts*, page C1483, 2004.

[166] F. Marchis, I. de Pater, A. G. Davies, H. G. Roe, T. Fusco, D. Le Mignant, P. Descamps, B. A. Macintosh, and R. Prangé. High-resolution keck adaptive optics imaging of violent volcanic activity on io. *Icarus*, 160:124–131, 2002.

[167] F. Marchis, D. Le Mignant, F. H. Chaffee, A. G. Davies, S. H. Kwok, R. Prangé, I. de Pater, P. Amico, R. Campbell, T. Fusco, R. W. Goodrich, and A. Conrad. Keck ao survey of io global volcanic activity between 2 and 5 μm. *Icarus*, 176:96–122, 2005.

[168] M. Martynski, J. Zydlewicz, N. Boens, and A. Molski. Determination of photophysical parameters from photon arrival time trajectories in single molecule fluorescence spectroscopy. *Journal of Chemical Physics*, 122(13):134507, 2005.

[169] E. Matteoli and G. A. Nasoori. *Fluctuation Theory of Mixtures*. Taylor & Francis, New York, 1990.

[170] J. Mertz. Molecular photodynamics involved in multi-photon excitation fluorescence microscopy. *European Physical Journal D*, 3(1):53–66, 1998.

[171] U. Meseth. *Structural and functional investigations of channel forming peptides in lipid membranes*. PhD thesis, Ecole Polytechnique Fédéral de Lausanne, Lausanne, Switzerland, 1996.

[172] U. Meseth, T. Wohland, R. Rigler, and H. Vogel. Resolution of fluorescence correlation measurements. *Biophysical Journal*, 76(3):1619–1631, 1999.

[173] F. J. Meyer-Almes, K. Wyzgol, and M. J. Powell. Mechanism of the alpha-complementation reaction of e. coli beta-galactosidase deduced from fluorescence correlation spectroscopy measurements. *Biophysical Chemistry*, 75(2):151–160, 1998.

[174] A. P. Minton. Macromolecular crowding and molecular recognition. *Journal of Molecular Recognition*, 6(4):211–214, 1993.

[175] A. P. Minton. The influence of macromolecular crowding and macromolecular confinement on biochemical reactions in physiological media. *Journal of Biological Chemistry*, 276(14):10577–10580, 2001.

[176] R. Molina, J. Nunez, F. J. Cortijo, and J. Mateos. Image restoration in astronomy: a bayesian perspective. *IEEE Signal Processing Magazine*, 18(2):11–29, 2001.

[177] L. M. Mugnier, T. Fusco, and J.-M. Conan. Mistral: a myopic edge-preserving image restoration method, with application to astronomical adaptive-optics-corrected long-exposure images. *Journal of the Optical Society of America, A*, 21:1841–1854, 2004.

[178] L. M. Mugnier, C. Robert, J.-M. Conan, V. Michau, and S. Salem. Myopic deconvolution from wave-front sensing. *Journal of the Optical Society of America, A*, 18:862–872, 2001.

[179] B. K. Muller, E. Zaychikov, C. Brauchle, and D. C. Lamb. Pulsed interleaved excitation. *Biophysical Journal*, 89(5):3508–3522, 2005.

[180] J. D. Müller, Y. Chen, and E. Gratton. Resolving heterogeneity on the single molecular level with the photon-counting histogram. *Biophysical Journal*, 78(1):474–486, 2000.

[181] M. Müller, J. Squier, and G. J. Brakenhoff. Measurement of femtosecond pulses in the focal point of a high-numerical-aperture lens by two-photon absorption. *Optics Letters*, 20(9):1038–1040, 1995.

[182] K. C. Neuman, E. H. Chadd, G. F. Liou, K. Bergman, and S. M. Block. Characterization of photodamage to escherichia coli in optical traps. *Biophysical Journal*, 77(5):2856–2863, 1999.

[183] S. H. Northrup and H. P. Erickson. Kinetics of protein-protein association explained by brownian dynamics computer simulation. *Proceedings of the National Academy of Sciences, USA*, 89(8):3338–3342, 1992.

[184] University of Granada Computer Vision Group. Brain magnetic resonance dataset (mr030.pgm). http://decsai.ugr.es/cvg/dbimages/gbio256.php.

[185] B. P. Olveczky and A. S. Verkman. Monte carlo analysis of obstructed diffusion in three dimensions: application to molecular diffusion in organelles. *Biophysical Journal*, 74(5):2722–2730, 1998.

[186] J. Ovadi and V. Saks. On the origin of intracellular compartmentation and organized metabolic systems. *Molecular and Cellular Biochemistry*, 256-257(1-2):5–12, 2004.

[187] C. G. Pack, G. Nishimura, M. Tamura, K. Aoki, H. Taguchi, M. Yoshida, and M. Kinjo. Analysis of interaction between chaperonin groel and its substrate using fluorescence correlation spectroscopy. *Cytometry*, 36(3):247–253, 1999.

[188] K. Palo, Ü. Mets, S. Jager, P. Kask, and K. Gall. Fluorescence intensity multiple distributions analysis: concurrent determination of diffusion times and molecular brightness. *Biophysical Journal*, 79(6):2858–2866, 2000.

[189] K. Palo, U. Mets, V. Loorits, and P. Kask. Calculation of photon count number distributions via master equations. *Biophysical Journal*, page to be published, 2005.

[190] J. Paulsson. Summing up the noise in gene networks. *Nature*, 427(6973):415–418, 2004.

[191] I. Pecht and R. Rigler. Kinetics of antibody-hapten interactions. In I. Pecht and Rudolf Rigler, editors, *Chemical Relaxation in Molecular Biology*, pages 306–338. Springer-Verlag, Berlin, 1977.

[192] N. Periasamy and A. S. Verkman. Analysis of fluorophore diffusion by continuous distributions of diffusion coefficients: application to photobleaching measurements of multicomponent and anomalous diffusion. *Biophysical Journal*, 75(1):557–567, 1998.

[193] R. Peters, A. Brunger, and K. Schulten. Continuous fluorescence microphotolysis: a sensitive method for study of diffusion processes in single cells. *Proceedings of the National Academy of Sciences, USA*, 78(2):962–966, 1981.

[194] N. O. Petersen, P. L. H́oddelius, P. W. Wiseman, O. Seger, and K. E. Magnusson. Quantitation of membrane receptor distributions by image correlation spectroscopy: concept and application. *Biophysical Journal*, 65(3):1135–1146, 1993.

[195] N. Peyret and J. Jr. SantaLucia. Hyther version 1.0. http://ozone2.chem.wayne.edu.

[196] N. Peyret, P. A. Seneviratne, H. T. Allawi, and J. Jr. SantaLucia. Nearest-neighbor thermodynamics and nmr of dna sequences with internal a.a, c.c, g.g, and t.t mismatches. *Biochemistry*, 38(12):3468–3477, 1999.

[197] R. D. Phair and T. Misteli. Kinetic modelling approaches to in vivo imaging. *Nature Reviews in Molecular and Cell Biology*, 2(12):898–907, 2001.

[198] G. G. Potamianos and J. K. Goutsias. Partition function estimation of gibbs random-field images using monte carlo simulations. *IEEE Transactions on Information Theory*, 39(4):1322–1332, 1993.

[199] A. Pramanik. Ligand-receptor interactions in live cells by fluorescence correlation spectroscopy. *Current Pharmaceutical Biotechnology*, 5(2):205–212, 2004.

[200] W. K. Pratt. *Digital Image Processing: PIKS Inside, 3rd Edition*. Wiley-Interscience, New York, 2001.

[201] W. H. Press, B. P. Flannery, S. A. Teukolsky, and W. T. Vetterling. *Numerical Recipes in C : The Art of Scientific Computing*. Cambridge University Press, 1992.

[202] W. H. Press, B. P. Flannery, S. A. Teukolsky, and W. T. Vetterling. *Numerical Recipes in FORTRAN Example Book : The Art of Scientific Computing (The Art of Scientific Computing)*. Cambridge University Press, 1992.

[203] W. H. Press, S. A. Teukolsky, W. T. Vetterling, and B. P. Flannery. *Numerical Recipes in Fortran 90*. Cambridge University Press, 1996.

[204] R. C. Puetter. Pixon-based multiresolution image reconstruction and the quantification of picture information content. *International Journal of Imaging Systems and Technology*, 6:314–331, 1995.

[205] H. Qian. On the statistics of fluorescence correlation spectroscopy. *Biophysical Chemistry*, 38(1-2):49–57, 1990.

[206] H. Qian and E. L. Elson. Fluorescence correlation spectroscopy with high-order and dual-color correlation to probe nonequilibrium steady states. *Proceedings of the National Academy of Sciences, USA*, 101(9):2828–2833, 2004.

[207] S. G. Rabinovich and M. E. Alferieff. *Measurement Errors and Uncertainties: Theory and Practice, 2nd Edition.* American Institute of Physics, New York, 1999.

[208] B. Rauer, E. Neumann, J. Widengren, and R. Rigler. Fluorescence correlation spectrometry of the interaction kinetics of tetramethylrhodamin α-bungarotoxin with torpedo californica acetylcholine receptor. *Biophysical Chemistry*, 58(1-2):3–12, 1996.

[209] Jr. Record, M. T., E. S. Courtenay, D. S. Cayley, and H. J. Guttman. Responses of e. coli to osmotic stress: large changes in amounts of cytoplasmic solutes and water. *Trends in Biochemical Sciences*, 23(4):143–148, 1998.

[210] Jr. Record, M. T., E. S. Courtenay, S. Cayley, and H. J. Guttman. Biophysical compensation mechanisms buffering e. coli protein-nucleic acid interactions against changing environments. *Trends in Biochemical Sciences*, 23(5):190–194, 1998.

[211] R. Rigler, Z. Foldes-Papp, F. J. Meyer-Almes, C. Sammet, M. Volcker, and A. Schnetz. Fluorescence cross-correlation: a new concept for polymerase chain reaction. *Journal of Biotechnology*, 63(2):97–109, 1998.

[212] R. Rigler, Ü. Mets, J. Widengren, and P. Kask. Fluorescence correlation spectroscopy with high count rate and low background: analysis of translational diffusion. *European Biophysics Journal*, 22(3):169–175, 1993.

[213] R. Rigler, J. Widengren, and Ü. Mets. Interactions and kinetics of single molecules as observed by fluorescence correlation spectroscopy. In Otto S. Wolfbeis, editor, *Fluorescence Spectroscopy: New Methods and Applications*, pages 13–24. Springer-Verlag, New York, 1993.

[214] K. Rippe. Simultaneous binding of two dna duplexes to the ntrc-enhancer complex studied by two-color fluorescence cross-correlation spectroscopy. *Biochemistry*, 39(9):2131–2139, 2000.

[215] F. Roddier. *Adaptive Optics in Astronomy*. Cambridge University Press, Cambridge, UK, 2004.

[216] J. M. Rohwer, P. W. Postma, B. N. Kholodenko, and H. V. Westerhoff. Implications of macromolecular crowding for signal transduction and metabolite channeling. *Proceedings of the National Academy of Sciences, USA*, 95(18):10547–10552, 1998.

[217] A. Roorda and D. R. Williams. The arrangement of the three cone classes in the living human eye. *Nature*, 397(6719):520–522, 1999.

[218] L. H Ryder. *Quantum Field Theory*. Cambridge University Press, New York, 1985.

[219] S. Saffarian and E. L. Elson. Statistical analysis of fluorescence correlation spectroscopy: the standard deviation and bias. *Biophysical Journal*, 84(3):2030–2042, 2003.

[220] J. Jr. SantaLucia. A unified view of polymer, dumbbell, and oligonucleotide dna nearest-neighbor thermodynamics. *Proceedings of the Natonal Academy of Sciences, USA*, 95(4):1460–1465, 1998.

[221] S. S. Saquib, C. A. Bouman, and K. Sauer. Ml parameter estimation for markov random fields with applications to bayesian tomography. *IEEE Transactions on Image Processing*, 7(7):1029–1044, 1998.

[222] K. Schatzel. Correlation techniques in dynamic light scattering. *Applied Physics, B - Photophysics and Laser Chemistry*, 42(4):193–213, 1987.

[223] K. Schatzel, M. Drewel, and S. Stimac. Photon correlation measurements at large lag times: improving statistical accuracy. *Journal of Modern Optics*, 35(4):711–718, 1988.

[224] G. Schreiber. Kinetic studies of protein-protein interactions. *Current Opinion in Structural Biology*, 12(1):41–47, 2002.

[225] G. Schreiber and A. R. Fersht. Rapid, electrostatically assisted association of proteins. *Nature Structural Biology*, 3(5):427–431, 1996.

[226] J. Schüler, J. Frank, U. Trier, M. Schäfer-Korting, and W. Saenger. Interaction kinetics of tetramethylrhodamine transferrin with human transferrin receptor studied by fluorescence correlation spectroscopy. *Biochemistry*, 38(26):8402–8408, 1999.

[227] T. J. Schulz. Multiframe blind deconvolution of astronomical images. *Journal of the Optical Society of America, A*, 10(5):1064–1073, 1993.

[228] T. J. Schulz, B. E. Stribling, and J. J. Miller. Multiframe blind deconvolution with real data: imagery of the hubble space telescope. *Optics Express*, 1(11):355–362, 1997.

[229] G. J Schutz, H. Schindler, and T. Schmidt. Single-molecule microscopy on model membranes reveals anomalous diffusion. *Biophysical Journal*, 73(2):1073–1080, 1997.

[230] M. A. Schwartz and H. D. Madhani. Principles of map kinase signaling specificity in saccharomyces cerevisiae. *Annual Review of Genetics*, 38:725–748, 2004.

[231] P. Schwille, U. Haupts, S. Maiti, and W. W. Webb. Molecular dynamics in living cells observed by fluorescence correlation spectroscopy with one- and two-photon excitation. *Biophysical Journal*, 77(4):2251–2265, 1999.

[232] P. Schwille, J. Korlach, and W. W. Webb. Fluorescence correlation spectroscopy with single-molecule sensitivity on cell and model membranes. *Cytometry*, 36(3):176–182, 1999.

[233] P. Schwille, S. Kummer, A. A. Heikal, W. E. Moerner, and W. W. Webb. Fluorescence correlation spectroscopy reveals fast optical excitation-driven intramolecular dynamics of yellow fluorescent proteins. *Proceedings of the National Academy of Sciences, USA*, 97(1):151–156, 2000.

[234] P. Schwille, F. J. Meyer-Almes, and R. Rigler. Dual-color fluorescence cross-correlation spectroscopy for multicomponent diffusional analysis in solution. *Biophysical Journal*, 72(4):1878–1886, 1997.

[235] P. Schwille, F. J. Meyer-Almes, and R. Rigler. Kinetic investigations by fluorescence correlation spectroscopy: the analytical and diagnostic potential of diffusion studies. *Biophysical Chemistry*, 66(2-3):1878–1886, 1997.

[236] A. E. Siegman. *Lasers*. University Science Books, Sausalito, CA, 1986.

[237] H. A. Simon. The structure of complexity in an evolving world: the role of near decomposability. In Werner Callebaut and Diego Rasskin-Gutman, editors, *Modularity : Understanding the Development and Evolution of Natural Complex Systems (Vienna Series in Theoretical Biology)*, pages ix–xiii. The MIT Press, 2005.

[238] B. A. Smith, L. Soderblom, R. F. Beebe, J. M. Boyce, G. Briggs, A. Bunker, S. A. Collins, C. Hansen, T. V. Johnson, J. L. Mitchell, R. J. Terrile, M. H. Carr, A. F. Cook, J. N. Cuzzi, J. B. Pollack, G. E. Danielson, A. P. Ingersoll, M. E. Davies, G. E. Hunt, H. Masursky, E. M. Shoemaker, D. Morrison, T. Owen, C. Sagan, J. Veverka, R. Strom, and V. E. Suomi. Encounter with saturn - voyager 1 imaging science results. *Science*, 212:163–191, 1981.

[239] J. R. Somoza, H. Szoke, D. M. Goodman, P. Beran, D. Truckses, S. H. Kim, and A. Szoke. Holographic methods in x-ray crystallography .4. a fast algorithm and its application to macromolecular crystallography. *Acta Crystallographica, A*, 51:691–708, 1995.

[240] L. A. Sromovsky, J. R. Spencer, K. H. Baines, and P. M. Fry. Ground-based observations of cloud features on uranus. *Icarus*, 146(1):307–311, 2000.

[241] K. Starchev, J. W. Zhang, and J. Buffle. Applications of fluorescence correlation spectroscopy - particle size effect. *Journal of Colloid and Interface Science*, 203(1):189–196, 1998.

[242] J.-L Starck and F. Murtagh. *Astronomical Image and Data Analysis*. Springer, New York, 2002.

[243] T. E. Starr and N. L. Thompson. Total internal reflection with fluorescence correlation spectroscopy: combined surface reaction and solution diffusion. *Biophysical Journal*, 80(3):1575–1584, 2001.

[244] T. G. Stockham, T. M. Cannon, and R. B. Ingebretsen. Blind deconvolution through digital signal-processing. *Proceedings of the IEEE*, 63(4):678–692, 1975.

[245] M. Straume. Sequential versus simultaneous analysis of data: differences in reliability of derived quantitative conclusions. *Methods in Enzymology*, 240(1):89–121, 1994.

[246] H. Szoke, A. Szoke, J. Somoza, and F. Maia. The eden holographic method. http://www.edencrystallography.org/.

[247] S. Teboul, L. Blanc-Feraud, G. Aubert, and M. Barlaud. Variational approach for edge-preserving regularization using coupled pde's. *IEEE Transactions on Image Processing*, 7(3):387–397, 1998.

[248] A. V. Terskikh, A. F. Fradkov, A. G. Zaraisky, A. V. Kajava, and B. Angres. Analysis of dsred mutants. space around the fluorophore accelerates fluorescence development. *Journal of Biological Chemistry*, 277(10):7633–7636, 2002.

[249] S. Y. Tetin, K. M. Swift, and E. D. Matayoshi. Measuring antibody affinity and performing immunoassay at the single molecule level. *Analytical Biochemistry*, 307(1):84–91, 2002.

[250] E. Thews, M. Gerken, R. Eckert, J. Zapfel, C. Tietz, and J. Wrachtrup. Cross talk free fluorescence cross correlation spectroscopy in live cells. *Biophysical Journal*, 89(3):2069–2076, 2005.

[251] N. L. Thompson. Fluorescence correlation spectroscopy. In Joseph R. Lakowicz, editor, *Topics in Fluorescence Spectroscopy: Techniques (Volume 1)*, pages 337–378. Plenum Press, New York, 1991.

[252] L. O. Tjernberg, A. Pramanik, S. Björling, P. Thyberg, J. Thyberg, C. Nordstedt, K. D. Berndt, L. Terenius, and R. Rigler. Amyloid β-peptide polymerization studied using fluorescence correlation spectroscopy. *Chemistry and Biology*, 6(1):53–62, 1999.

[253] E. Van Craenenbroeck and Y. Engelborghs. Quantitative characterization of the binding of fluorescently labeled colchicine to tubulin in vitro using fluorescence correlation spectroscopy. *Biochemistry*, 38(16):5082–5088, 1999.

[254] F. van Drogen, V. M. Stucke, G. Jorritsma, and M. Peter. Map kinase dynamics in response to pheromones in budding yeast. *Nature Cell Biology*, 3(12):1051–1059, 2001.

[255] J.-P. Véran, F. Rigaut, H. Maître, and D. Rouan. Estimation of the adaptive optics long-exposure point-spread function using control loop data. *Journal of the Optical Society of America, A*, 14:3057–3069, 1997.

[256] A. S. Verkman. Solute and macromolecule diffusion in cellular aqueous compartments. *Trends in Biochemical Sciences*, 27(1):27–33, 2002.

[257] M. Wachsmuth, W. Waldeck, and J. Langowski. Anomalous diffusion of fluorescent probes inside living cell nuclei investigated by spatially-resolved fluorescence correlation spectroscopy. *Journal of Molecular Biology*, 298(4):677–689, 2000.

[258] B. P. Wakker and U. J. Schwarz. The multi-resolution clean and its application to the short-spacing problem in interferometry. *Astronomy and Astrophysics*, 200(1-2):312–322, 1988.

[259] N. Wax. *Selected Papers on Noise and Stochastic Processes (Dover Phoenix Editions)*. Dover Publications, New York, 2003.

[260] J. Wei and C. D. Prater. The structure and analysis of complex reaction systems. *Advances in Catalysis*, 13:203–392, 1962.

[261] M. Weiss, M. Elsner, F. Kartberg, and T. Nilsson. Anomalous subdiffusion is a measure for cytoplasmic crowding in living cells. *Biophysical Journal*, 87(5):3518–2354, 2004.

[262] M. Weiss, H. Hashimoto, and T. Nilsson. Anomalous protein diffusion in living cells as seen by fluorescence correlation spectroscopy. *Biophysical Journal*, 84(6):4043–4052, 2003.

[263] E. W. Weisstein. *CRC Concise Encyclopedia of Mathematics, Second Edition*. Chapman and Hall/CRC, 2002.

[264] J. Widengren, Ü. Mets, and R. Rigler. Fluorescence correlation spectroscopy of triplet states in solution - a theoretical and experimental study. *Journal of Physical Chemistry*, 99(36):13368–13379, 1995.

[265] J. Widengren and R. Rigler. Photobleaching investigations of dyes using fluorescence correlation spectroscopy (fcs). *Progress in Biophysics and Molecular Biology*, 65:PH109–PH109, 1996.

[266] J. Widengren and R. Rigler. Fluorescence correlation spectroscopy as a tool to investigate chemical reactions in solutions and on cell surfaces. *Cellular and Molecular Biology*, 44(5):857–879, 1998.

[267] J. Widengren, E. Schweinberger, S. Berger, and C. A. M. Seidel. Two new concepts to measure fluorescence resonance energy transfer via fluorescence correlation spec-

troscopy: Theory and experimental realizations. *Journal of Physical Chemistry, A*, 105(28):6851–6866, 2001.

[268] T. Wohland, K. Friedrich, R. Hovius, and H. Vogel. Study of ligand-receptor interactions by fluorescence correlation spectroscopy with different fluorophores: evidence that the homopentameric 5-hydroxytryptamine type 3as receptor binds only one ligand. *Biochemistry*, 38(27):8671–8681, 1999.

[269] T. Wohland, R. Rigler, and H. Vogel. The standard deviation in fluorescence correlation spectroscopy. *Biophysical Journal*, 80(6):2987–2999, 2001.

[270] C. Xu, W. Zipfel, J. B. Shear, R. M. Williams, and W. W. Webb. Multiphoton fluorescence excitation: new spectral windows for biological nonlinear microscopy. *Proceedings of the National Academy of Sciences, USA*, 93(20):10763–10768, 1996.

[271] R. Yuste. Fluorescence microscopy today. *Nature Methods*, 2(12):902–904, 2005.

[272] Z. Y. Zhou, R. M. Leahy, and J. Y. Qi. Approximate maximum likelihood hyperparameter estimation for gibbs priors. *IEEE Transactions on Image Processing*, 6(6):844–861, 1997.

[273] S. B. Zimmerman and A. P. Minton. Macromolecular crowding: biochemical, biophysical, and physiological consequences. *Annual Review of Biophysics and Biomolecular Structure*, 22(2):27–65, 1993.

Appendix A

Diffusion of Green Fluorescent Protein in the Aqueous-Phase Lumen of Endoplasmic Reticulum

This chapter was published by Mark Dayel, Erik F. Y. Hom, and Alan S. Verkman under the same title in the *Biophysical Journal* **76**(5):2843-2851 (1999).

Biophysical Journal Volume 76 May 1999 2843–2851

Diffusion of Green Fluorescent Protein in the Aqueous-Phase Lumen of Endoplasmic Reticulum

Mark J. Dayel,* Erik F. Y. Hom,# and A. S. Verkman*
*Departments of Medicine and Physiology, Cardiovascular Research Institute, and #The Graduate Group in Biophysics, University of California, San Francisco, California 94143-0521 USA

ABSTRACT The endoplasmic reticulum (ER) is the major compartment for the processing and quality control of newly synthesized proteins. Green fluorescent protein (GFP) was used as a noninvasive probe to determine the viscous properties of the aqueous lumen of the ER. GFP was targeted to the ER lumen of CHO cells by transient transfection with cDNA encoding GFP (S65T/F64L mutant) with a C-terminus KDEL retention sequence and upstream prolactin secretory sequence. Repeated laser illumination of a fixed 2-μm diameter spot resulted in complete bleaching of ER-associated GFP throughout the cell, indicating a continuous ER lumen. A residual amount ($<$1%) of GFP-KDEL was perinuclear and noncontiguous with the ER, presumably within a pre- or cis-Golgi compartment involved in KDEL-substrate retention. Quantitative spot photobleaching with a single brief bleach pulse indicated that GFP was fully mobile with a $t_{1/2}$ for fluorescence recovery of 88 $\pm$ 5 ms (SE; 60$\times$ lens) and 143 $\pm$ 8 ms (40$\times$). Fluorescence recovery was abolished by paraformaldehyde except for a small component of reversible photobleaching with $t_{1/2}$ of 3 ms. For comparison, the $t_{1/2}$ for photobleaching of GFP in cytoplasm was 14 $\pm$ 2 ms (60$\times$) and 24 $\pm$ 1 ms (40$\times$). Utilizing a mathematical model that accounted for ER reticular geometry, a GFP diffusion coefficient of 0.5–1 $\times$ 10^{-7} cm^2/s was computed, 9–18-fold less than that in water and 3–6-fold less than that in cytoplasm. By frequency-domain microfluorimetry, the GFP rotational correlation time was measured to be 39 $\pm$ 8 ns, $\sim$2-fold greater than that in water but comparable to that in the cytoplasm. Fluorescence recovery after photobleaching using a 40$\times$ lens was measured (at 23°C unless otherwise indicated) for several potential effectors of ER structure and/or lumen environment: $t_{1/2}$ values (in ms) were 143 $\pm$ 8 (control), 100 $\pm$ 13 (37°C), 53 $\pm$ 13 (brefeldin A), and 139 $\pm$ 6 (dithiothreitol). These results indicate moderately slowed GFP diffusion in a continuous ER lumen.

INTRODUCTION

The diffusion of solutes in intracellular aqueous compartments is essential for a number of cellular processes including enzyme-substrate reactions in the cytoplasm and mitochondria, and replication and nucleic acid transport in the nucleus. In the endoplasmic reticulum (ER), diffusion could be an important factor influencing protein folding and membrane protein translocation events (Simon et al., 1992). The ER lumen is densely filled with small solutes (e.g., calcium and glutathione) and proteins (e.g., lipid synthases and molecular chaperones) at very high concentrations (100–200 mg protein/ml) (Koch et al., 1987; Helenius et al., 1992; Hammond and Helenius, 1995). It is not known, however, whether molecular crowding in the ER lumen is an important determinant and potential regulator of protein transport and posttranslational processing.

The rheological properties of cellular aqueous compartments has been a subject of longstanding interest. Initial studies of cytoplasmic viscosity utilized exogenously added magnetic resonance and fluorescent probes. Fluorescence recovery after photobleaching (FRAP) measurements of microinjected fluorescein isothiocyanate-labeled (FITC)-dextrans and FITC-Ficolls of molecular size $<10^6$ Da showed translational mobilities only a fewfold slower in cytoplasm than in water, but substantially slower for much larger molecules (Luby-Phelps et al., 1987; Seksek et al., 1997). Spot photobleaching of the small chemical fluorophore BCECF indicated that compared to its translational diffusion in water, BCECF diffusion was slowed 3–4-fold in bulk cytoplasm (Kao et al., 1993) and membrane-adjacent cytoplasm (Swaminathan et al., 1996). Analysis of individual factors responsible for the slowed BCECF diffusion indicated that the primary barrier to BCECF translation is molecular crowding, with lesser effects of BCECF binding to cellular components and increased local microviscosity (the apparent local viscosity in the absence of binding or collisional interactions) (Kao et al., 1993). Measurements of cytoplasmic microviscosity by BCECF rotation (Fushimi and Verkman, 1991; Bicknese et al., 1993) and by the use of viscosity-sensitive fluorophores (Luby-Phelps et al., 1993) indicated a microviscosity at most 1.5-fold that of water.

The molecular cloning of green fluorescent protein (GFP) has permitted noninvasive measurements of probe mobility with excellent targeting specificity and suitable optical properties for photophysical studies (reviewed in Verkman, 1999). GFP has been targeted to multiple organelles (Rizzuto et al., 1995; Degiorgi et al., 1996; Gerdes and Kaether, 1996; Ellenberg et al., 1997; Presley et al., 1997; Kneen et al., 1998) and used to follow the slow diffusion of membrane proteins in plasma membranes and organelles (Cole et

Received for publication 26 August 1998 and in final form 2 February 1999.

Address reprint requests to Alan S. Verkman, M.D., Ph.D., 1246 Health Sciences East Tower, Cardiovascular Research Institute, University of California, San Francisco, San Francisco, CA 94143-0521. Tel.: 415-476-8530; Fax: 415-665-3847; E-mail: verkman@itsa.ucsf.edu; http://www.ucsf.edu/verklab.

0006-3495/99/05/2843/09 $2.00

al., 1996; Barak et al., 1997). An initial study evaluated GFP as a probe of translational and rotational dynamics in cytoplasm using photobleaching recovery and time-resolved anisotropy methods (Swaminathan et al., 1997). GFP was found to be a suitable probe of solute translation with the caveat that (diffusion-independent) reversible GFP recovery after photobleaching involving triplet state relaxation is sometimes detected. GFP translational diffusion in the cytoplasm was similar to that of a microinjected FITC-dextran of comparable size. As measured by time-resolved anisotropy, GFP rotation was found to provide an excellent index of local viscosity because of the absence of intramolecular depolarizing rotations of the GFP triamino acid chromophore. Recently, GFP was used as a probe to measure viscosity in the mitochondrial matrix (Partikian et al., 1998). Mathematical models were developed to deduce absolute diffusion coefficients from photobleaching studies of fluorophore diffusion in the aqueous lumen of cellular organelles having complex geometries (Ölveczky and Verkman, 1998).

A goal of this study was to determine whether the crowded ER lumen restricts the translational and rotational diffusion of a protein-size molecule. GFP was used as a probe of solute mobility in the ER lumen because of its excellent targeting specificity to the ER lumen, minimal binding interactions with cellular components, and suitable optical properties for quantitative photobleaching and time-resolved anisotropy measurements. It was found that GFP is freely diffusible throughout the ER lumen, but that its diffusion is 9–18-fold slower than in water and 3–6-fold slower that in the cytoplasm, with minimal binding to ER luminal contents. The quantitative methods developed here were subsequently used to evaluate the consequences of several conditions and effectors that have been proposed to modify ER structure and/or luminal environment.

METHODS

Cell culture and transfection

CHO-K1 cells (ATCC CRL9618) were grown on 18-mm diameter round glass coverslips in a 95% air, 5% CO_2 incubator at 37°C in Ham's F12 medium containing 10% fetal bovine serum, 100 units/ml penicillin, and 100 mg/ml streptomycin. Cells were transfected 1 day after plating just before confluence was reached. Cells in each well of a six-well plastic dish containing a coverglass were transfected with a mixture consisting of 1 μg plasmid DNA encoding an ER-targeted GFP-fusion construct within the vector pcDNA3.1(+) (Invitrogen Corp., Carlsbad, CA) and 12 μg lipofectamine (Life Technologies, Gaithersburg, MD) in a 0.2-ml volume of OPTI-MEM (Life Technologies). After 5 h the transfection mixture was replaced with 1 ml culture medium. Cell were used 2 days after transient transfection. As reported previously (Kneen et al., 1998), the ER-targeting construct consisted of the EGFP coding sequence (Clontech Laboratories, Inc., Palo Alto, CA) cloned downstream from the preprolactin signal sequence, in which a KDEL ER-retention/retrieval sequence was inserted just before the stop codon in the GFP cDNA. Immunofluorescence showed colocalization of GFP fluorescence with staining by an antibody against the ER resident protein GRP94 (Tamarappoo and Verkman, 1998).

Fluorescence recovery after photobleaching

FRAP measurements were carried out on an apparatus described previously (Kao and Verkman, 1996) with slight modifications. An argon ion laser beam (488 nm; Innova 70–4, Coherent Inc., Santa Clara, CA) was modulated by an acousto-optic modulator (Brimrose, Inc., Baltimore, MD; 1.5 μs response time) and directed through an objective onto the stage of an inverted epifluorescence microscope (Diaphot, Nikon Inc., Melville, NY). An electronic shutter was introduced in the excitation pathway to completely eliminate sample illumination as needed. The microscope was also equipped for full-field epiillumination to visualize all cells to target the focused laser beam. The full-field and laser beams were reflected by a dichroic mirror (510 nm) onto the sample by an objective lens (Nikon 100× oil Fluor, N.A. 1.4; 60× oil Fluor, N.A. 1.4; 40× oil Fluor, N.A. 1.3). For measurements performed at 37°C the objective was heated by a commercial thermoregulator (Bioptechs Inc., Butler, PA) and the sample chamber was heated by a home-built heating coil with thermocouple temperature feedback. For most experiments, the laser beam power was set to 200–500 mW (488 nm) and the attenuation ratio (the ratio of bleach to probe beam intensity) was set to 5000–15000. Sample fluorescence was filtered by serial barrier (Schott glass OG 515) and interference (530 $\pm$ 15 nm) filters and detected using a photomultiplier and 14-bit analog-to-digital converter. A gating circuit transiently decreased photomultiplier gain during photobleaching. Fluorescence was sampled every 0.2 s for 4 s before the bleach pulse; subsequently, sampling was performed over three different time intervals specified as follows: high-resolution data (1 MHz sampling rate) generally over 500 ms, low-resolution data (generally 10^4 points) over 0.5–5 s, and late-time data (0.2 s sampling time every 1–4 s). For FRAP measurements in the ER, 15–25 individual fluorescence recovery curves (each from a different cell) were averaged, and the data set was repeated 4–10 times using different transfections.

Cell preparations

Transfected cells grown on glass coverslips were placed in a home-built perfusion chamber and flushed with Ham's F12 phenol red-free medium. Photobleaching measurements were generally performed within 30–60 min. In some experiments, cells were preincubated with brefeldin A (5 mM, 5 h, 37°C), dithiothreitol (1 mM, 3 h, 37°C), or the calcium ionophore A23187 (5 mM, 10 min, 23°C). In other experiments, cells were incubated for 10 min at 23°C with hyperosmolar media (containing added sucrose) or hypoosmolar media (contained added water).

Analysis of FRAP data

As described in the Appendix and a previous paper (Ölveczky and Verkman, 1998), fluorophore diffusion coefficients (D, in cm^2/s) were determined from recovery half-times ($t_{1/2}$) (time at which fluorescence recovers by 50%) using a mathematical model of diffusion in an ER composed of plates or interconnected cylinders. The $t_{1/2}$ values were determined by nonlinear least-squares fit of recovery data $F(t)$ to a semiempirical equation reported previously (Feder et al., 1996): $F(t) = F_0 + [F_0 + R(F_{init} - F_0)](t/t_{1/2})^\alpha/[1 + (t/t_{1/2})^\alpha]$, where R is the fractional fluorescence recovery and α is an empirical exponent related to anomalous diffusion (Periasamy and Verkman, 1998). The $t_{1/2}$ values for the recovery data in this paper were found to be insensitive to the fitting method, with similar values (generally <5% difference) obtained by a different method described by Swaminathan et al. (1997).

Time-resolved anisotropy measurements

Fluorescence lifetime and anisotropy decay measurements were performed using a Fourier Transform Fluorimeter (48000 MHF, SLM Instruments Inc., Urbana, IL) in which epifluorescence microscopy optics replaced the cuvette compartment (Fushimi and Verkman, 1991). The impulse-modulated, vertically polarized light (488 nm) was reflected onto the sample by

a 510-nm dichroic mirror and objective lens; emitted fluorescence was filtered by a 515-nm cut-on filter and passed through a rotatable analyzing calcite polarizer. Analysis of lifetime and time-resolved anisotropy were conducted by a comparative approach as described previously (Verkman et al., 1991). Fluorescein in 0.1 N NaOH was used as a 4.0-ns lifetime standard. Anisotropy decay measured by microscopy required the inclusion of a geometric factor (generally ~1.3) to correct for the differential detection of parallel versus perpendicular emission polarization arising mainly from differential reflectivity of the dichroic mirror.

Photobleaching with widefield or confocal image detection

A Nipkow wheel confocal microscope (Leitz upright microscope with Technical Instruments K2-Bio coaxial-confocal attachment) and cooled CCD camera detector (Photometrics Inc., Tucson, AZ) were used to acquire cell images after bleaching. An electronically shuttered bleach beam from the argon laser was directed onto the cell sample from below using a Leitz 25× long-working-distance air objective. The beam diameter in the sample plane was controlled by adjusting the objective z-position. Cells were viewed from above by epifluorescence using a 100× oil immersion objective and GFP filter set. Software was written to coordinate the bleach pulse, excitation and camera shutters, and image acquisition.

RESULTS

Photobleaching imaging experiments were carried out on transfected CHO cells expressing GFP in the ER lumen. Fig. 1 *A* contains a series of micrographs showing the cellular distribution of GFP before and at different times after photobleaching. The distribution of GFP is clearly reticular and indicative of ER localization. A large bleach spot (*upper left panel*) was used to bleach a substantial fraction of cellular GFP. The darkened zone produced by the bleach pulse was progressively filled in with unbleached GFP diffusing into the bleach zone by diffusion through the ER lumen. By 50 s, GFP fluorescence appears uniformly distributed throughout the cell ER. As expected for irreversible bleaching of GFP, the final whole cell fluorescence of the bleached cell is clearly less than that of an adjacent unbleached cell (*arrow*). The apparently complete ER redistribution of GFP after photobleaching suggests that most, if not all, of the GFP is mobile.

Fig. 1 *B* shows the results of a similar experiment after cell fixation with paraformaldehyde, an amine-reactive agent that is predicted to immobilize all proteins. GFP was bleached with comparable efficiency after paraformaldehyde fixation; however, recovery of fluorescence in the bleached region was not observed. Thus the fluorescence recovery in Fig. 1 *A* can be attributed to GFP diffusion.

To test directly for ER lumen continuity, a small spot located on a single cell was bleached by repeated pulsed laser illumination. Fig. 2 shows that almost all fluorescence throughout the cell could be eliminated by point bleaching. The fluorescence of an adjacent cell (*arrow*) was not diminished, indicating that the reduction in fluorescence throughout the bleached cell resulted from GFP diffusion through a continuous ER lumen and not from a broad laser beam profile. At high camera gain, a small (<1%) amount of residual fluorescence after bleaching was seen with perinuclear locale and Golgi-like pattern (Fig. 2, *right panel*), consistent with models for the recycling of KDEL-tagged proteins (see Discussion). Nonetheless, in the steady state the vast majority of GFP was localized to the ER lumen.

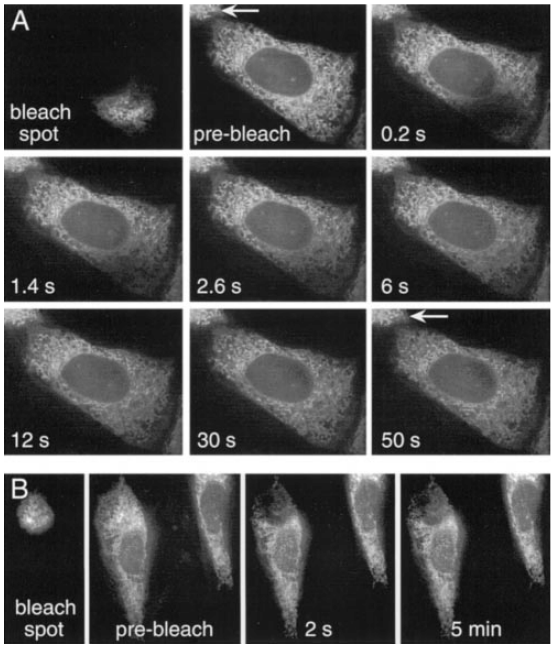

FIGURE 1 Photobleaching of GFP in the ER lumen. (*A*) Serial epifluorescence micrographs of a CHO cell expressing GFP in the ER lumen. The bleach beam profile is shown in the upper leftmost panel. Micrographs are shown before bleaching (pre-bleach) and at indicated times after bleaching (bleach time 200 ms). An adjacent unbleached cell is indicated by an arrow. (*B*) Same as in (*A*) except that cells were fixed by incubation in 4% paraformaldehyde for 60 min before photobleaching.

Spot photobleaching was performed for quantitative analysis of GFP diffusion. Fig. 3 *A* shows representative fluorescence recovery curves for the bleaching of GFP in the ER lumen with the indicated objective lenses producing different spot sizes. The bleach times for these studies were selected to be much less than the observed recovery times (see figure legend). GFP fluorescence recovered to well above 90% of the initial fluorescence, again suggesting that GFP diffuses within a continuous ER lumen. As expected, the fluorescence recovery rates depended strongly on beam spot size with $t_{1/2}$ values of 22 ± 3 ms, 88 ± 5 ms, and 143 ± 8 ms for 100×, 60×, and 40× lenses, respectively. For comparison, Fig. 3 *B* shows similar bleaching studies in cells containing GFP throughout their aqueous-phase cytoplasm and nucleus; $t_{1/2}$ values (in ms) were 6.0 ± 0.5 (100×), 14 ± 2 (60×), and 24 ± 1 (40×). For the 60× and 40× lenses, $t_{1/2}$ values for the ER were ~6-fold greater than for the cytoplasm, suggesting slowed diffusion of GFP in the ER (see below).

Fig. 3 *C* shows fluorescence recovery curves for fixed cells containing GFP in the ER lumen or cytoplasm (note

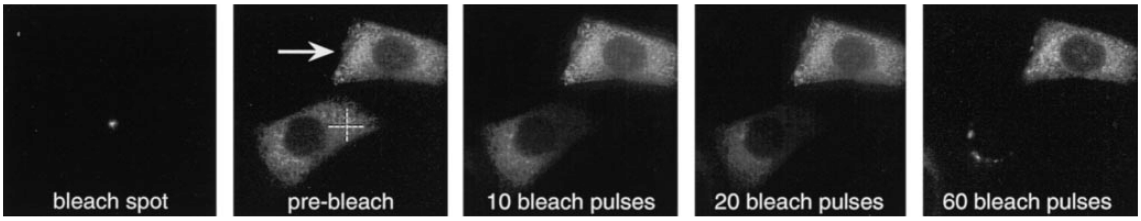

FIGURE 2 Evidence that the ER lumen is continuous. A single spot (at crosshairs) was repeatedly illuminated (200 ms illumination every 2 s) with an intense laser beam. Images were obtained after indicated number of illumination pulses. The arrow indicates an adjacent unbleached cell. Residual perinuclear, Golgi-like fluorescence is seen under high camera gain after 60 bleach pulses (*right panel*) (see text).

different time scale). Although the majority of fluorescence recovery was abolished over long times, there existed a transient ($t_{1/2}$, 3 ± 1 ms) fluorescence recovery whose rate did not depend on laser spot diameter. Further experiments showed that the transient recovery could be produced by relatively low bleach intensities for short bleach times (not shown). As described previously for fluorescein (Periasamy et al., 1996) and GFP (Swaminathan et al., 1997), the rapid fluorescence recovery probably arises from reversible GFP photobleaching due to triplet state relaxation. Because the recovery time for reversible GFP photobleaching is very short and independent of bleach spot size, subsequent experiments were conducted with a 40× objective ($t_{1/2}$ of 100–150 ms for irreversible photobleaching) to be able to neglect the reversible photobleaching process.

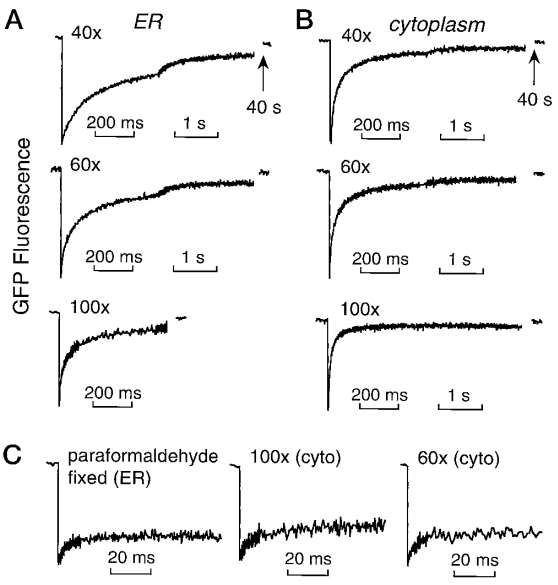

FIGURE 3 Spot photobleaching of GFP in the ER and cytoplasm. (*A*) Bleaching of cells expressing GFP in the ER lumen with indicated objective lenses. Bleach times were 2 ms (40×), 1 ms (60×), 0.3 ms (100×); bleach depth was 25–28%. (*B*) Same as in (*A*) but with cells expressing GFP uniformly in cytoplasm and nucleus (cells described in Swaminathan et al., 1997). (*C*) Same as in (*A*) but after paraformaldehyde fixation. See text for fitted $t_{1/2}$ values.

The diffusion of GFP through the ER lumen of defined geometry was modeled to estimate an absolute GFP translational diffusion coefficient (D) from photobleaching recovery data. Previously, the ER was modeled as a reticulum of orthogonally interconnected cylinders of specified diameter and density (Ölveczky and Verkman, 1998). The principal conclusion of those Monte Carlo computations was that the confinement of fluorophores to a tubular ER geometry had a small effect on their apparent diffusion. At constant D, the apparent recovery $t_{1/2}$ was slowed <1.5-fold for GFP confined to the ER lumen versus GFP uniformly distributed in a slab simulating cell geometry. To validate the robustness of this conclusion based on interconnected cylinders, additional computations were performed for a ribbonlike geometry in which GFP is confined within narrow planes.

The ribbonlike geometry was modeled as described in the Appendix. Fig. 4 *A* shows the geometry in which a bleach beam of diameter d intersects a thin slab containing GFP oriented at an angle θ with respect to the horizontal. The fluorescence recovery time course $F(\tau)$ ($\tau = Dt/d^2$ is a reduced dimensionless time) was computed by numerical integration of the point source solution to the diffusion equation over an ellipse (minor axis $d/2$, major axis $d/2 \cos \theta$) at each time point. Fig. 4 *B* gives $F(\tau)$ for different angles θ. As θ increases, the recovery slows due to the greater mean path a diffusing particle must travel to reach the center of the bleach spot. However, the effect is relatively small because the minor axis of the ellipse is independent of slab orientation. Fig. 4 *C* shows a minor influence of a random distribution of slab orientations. Fig. 4 *D* summarizes correction factors, $1 + (\Delta t_{1/2}/t_{1/2})$, which account for the confinement of GFP to the ER lumen. For example, a correction factor of 1.2 indicates that the apparent $t_{1/2}$ recovery time is increased 1.2-fold for GFP confined in the ER lumen versus uniformly distributed GFP. The range of correction factors for ribbonlike geometry, 1–1.4, is similar to that of 1–1.5 reported for the interconnected cylinder geometry. A more conservative range of the correction factors would be 1–2, presuming that recovery data were obtained from samples with ER sheets that were nonrandomly oriented with respect

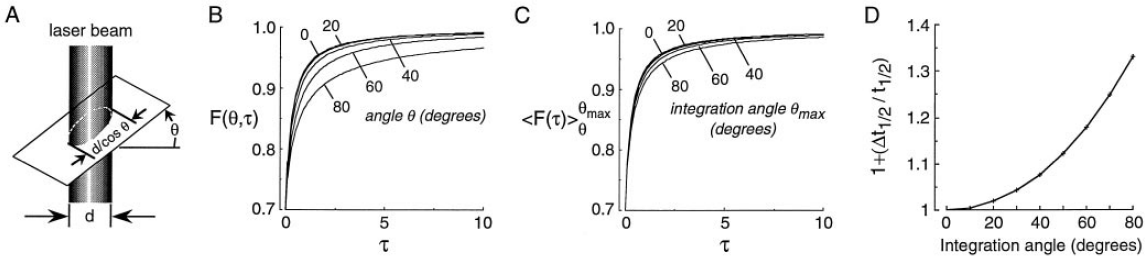

FIGURE 4 Quantitative determination of diffusion coefficients from photobleaching data. (*A*) Sheetlike ER geometry showing laser beam of diameter d intersecting a slab containing GFP oriented at angle θ with respect to the horizontal. (*B*) $F(\theta, \tau)$ computed from Eq. A4 at indicated angles θ. (*C*) $\langle F(\tau) \rangle$ computed from Eq. A5 for randomly oriented slabs from 0° to angle θ_{max}. (*D*) Correction factors $1 + (\Delta t_{1/2}/t_{1/2})$, where $\Delta t_{1/2} = |t_{1/2}(\theta = 0) - t_{1/2}(\theta)|$, for $\theta_{max} = 0-80°$. See Appendix for details.

to the beam axis (see Fig. 4 *B*). Because of uncertainties in the orientation of the ER, a range of D values will be reported corresponding to correction factors of 1–2.

Table 1 summarizes D values for GFP in different aqueous cellular compartments. The deduced D for GFP translational diffusion in the ER was 0.5–1 $\times$ 10^{-7} cm^2/s. This value of D is 3–6-fold less than that in cytoplasm, and 9–18-fold less than that for GFP diffusion in water.

The average rotational diffusion of GFP in the ER lumen was measured by time-resolved anisotropy. Fig. 5 shows a representative differential phase-modulation plot for GFP rotation in the ER lumen. The major rotational correlation time was 39 $\pm$ 5 ns (SE, four sets of measurements), ~2-fold greater than that of water (20 ns). The absence of a very slow component of GFP rotation suggests that GFP does not bind significantly to the ER wall or to slowly rotating proteins in the ER lumen. A similar measurement of GFP rotation in the ER lumen in paraformaldehyde-fixed cells gave a major rotational correlation time of >100 ns, indicating substantial GFP immobilization. Rotational mobilities of GFP in other cellular aqueous compartments are summarized in Table 1.

The translational diffusion of GFP in the ER lumen was measured in response to various maneuvers that might affect ER geometry and/or matrix environment. Representative fluorescence recovery curves are shown in Fig. 6 *A* and averaged data are summarized in Fig. 6 *C*. In an attempt to change solute concentration in the ER lumen, cells were incubated in anisomolar solutions. There was no significant effect of 150–450 mOsm extracellular solutions (Fig. 6 *C*), a 1.3-fold slowing of GFP diffusion by a 600 mOsm solution, and a more marked effect of a 900 mOsm solution. The lack of a significant change of GFP diffusion in the ER in the presence of 150–450 mOsm extracellular solutions is in contrast with the 4–6-fold change observed for cytoplasmic GFP diffusion (Swaminathan et al., 1997).

Photobleaching measurements performed at 37°C ($t_{1/2}$, 100 $\pm$ 13 ms) gave a 1.4-fold faster recovery rate compared to 23°C, as expected by the difference in solute diffusion at these temperatures (see Discussion). Incubation of cells with the calcium ionophore A23187, which produced ER vesiculation within 10 s (Fig. 6 *B, middle panel*), resulted in incomplete GFP fluorescence recovery because of the loss of ER continuity. DTT, a disulfide reducing agent that elicits the "unfolded protein response"-associated expansion of the ER compartment in CHO cells (Helenius et al., 1992), did not have a significant effect on GFP diffusion ($t_{1/2}$, 139 $\pm$ 6 ms). Brefeldin A, which blocks ER-to-Golgi anterograde vesicle traffic (Klausner et al., 1992; Sciaky et al., 1997), gave a significant 2.5-fold increased rate of GFP fluorescence recovery ($t_{1/2}$, 53 $\pm$ 13 ms). However, brefeldin A did not affect ER structure at the light microscopic level (Fig. 6 *B, right panel*).

TABLE 1 Diffusion of GFP in aqueous cellular compartments

	Translational Diffusion		Rotational Diffusion	
	$D(cm^2/s)$	D(water)/D	τ_c (ns)	τ_c/τ_c(water)
Water	8.7×10^{-7}	1	20 $\pm$ 1	1
Cytoplasm	2.5–3 $\times$ 10^{-7}	2.9–3.5	36 $\pm$ 2	1.8
Mitochondria	2–3 $\times$ 10^{-7}	3–4	23 $\pm$ 1	1.2
ER	0.5–1 $\times$ 10^{-7}	9–18	39 $\pm$ 5	1.9

Data taken from Swaminathan et al. (1997), Partikian et al. (1998), and this study.

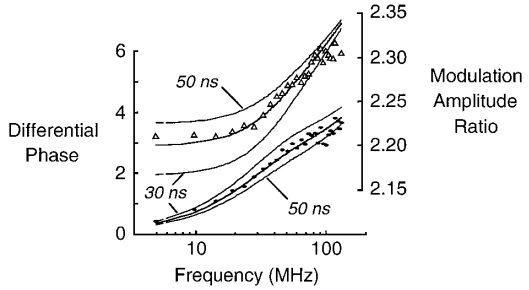

FIGURE 5 Rotational diffusion of GFP in the ER lumen. Differential phase angles (*filled circles*) and modulation amplitude ratios (*open triangles*) for GFP rotation. Fitted rotational correlation times (SE, $n = 4$) were 39 $\pm$ 5 ns (fractional amplitude 0.8) and 0.34 $\pm$ 0.04 ns. Curves corresponding to correlation times of 30 ns and 50 ns are shown for comparison.

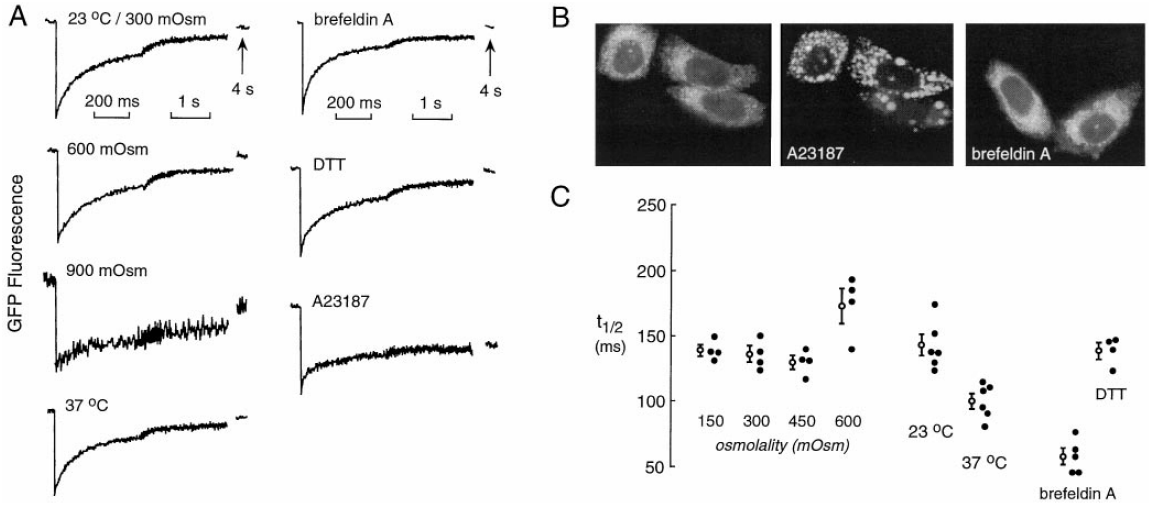

FIGURE 6 Effectors of ER environment of structure. (*A*) Spot photobleaching recovery for cells expressing GFP in the ER lumen for indicated conditions (see Methods for details). Bleach time was 2 ms and bleach depth was 25–28%. (*B*) Fluorescence micrographs before (*left*) and after 10 s incubation with A23187 (*middle*), and after incubation with brefeldin A (*right*). (*C*) Summary of recovery $t_{1/2}$ values. Each point is the average of data from 15–25 individual cells.

DISCUSSION

A principal finding of this study was that GFP, an ~30-kDa protein, diffuses freely throughout the ER lumen, but that its diffusion is slowed moderately ($D = 0.5–1 \times 10^{-7}$ cm^2/s). GFP rotational diffusion in the ER lumen was 2-fold slower than in water, whereas GFP translational diffusion was 9–18-fold slower in the ER versus water and 3–6-fold slower versus the cytoplasm. The rate of GFP translational diffusion formally represents a lower limit to ER diffusion because it assumes no GFP binding and incorporates a minor correction for ER geometry. The time-resolved anisotropy measurements supported the validity of the assumption about little GFP binding, and the mathematical modeling addressed the issue about ER geometry (see below). As discussed with respect to GFP diffusion in cytoplasm and mitochondria (Swaminathan et al., 1997; Partikian et al., 1998), the greater slowing of GFP translation versus rotation is probably related to collisional interactions that occur during translation.

In a study by Terasaki et al. (1996), photobleaching measurements of GFP diffusion were done to assess the effects of cellular calcium and fertilization on ER structure and continuity in starfish eggs. However, they did not quantify the diffusion coefficient of GFP for the purpose of relating it to the physicochemical environment in the ER lumen. In a photobleaching study by Subramanian and Meyer (1997), the diffusion coefficient of a 60-kDa ER-targeted elastase-GFP fusion protein was measured to be ~0.05×10^{-7} cm^2/s. However, the influence of binding interactions on the elastase-GFP diffusion coefficient was not considered. Their estimated elastase-GFP diffusion coefficient is 10–20 times smaller than that reported here for GFP alone (half the molecular weight of elastase-GFP). Assuming spherically distributed mass and free diffusion, one would expect a 1.26-fold slower diffusion of elastase-GFP versus GFP. Assuming a more realistic model of the proteins as prolate ellipsoids and that elastase-GFP is 2–3 times more prolate than GFP, Perrin's equations (Cantor and Schimmel, 1980) would predict an even smaller difference in the diffusion of elastase-GFP versus GFP. It is thus likely that elastase-GFP is extensively bound and/or significantly geometrically constrained in the ER lumen. We think it unlikely that the very different diffusion coefficients arise from cell type differences: Subramanian and Meyer conducted their studies using rat leukemia 2H3 and mouse fibroblast 3T3 cells, whereas the experiments here were done on Chinese Hamster Ovary cells. Nonetheless, we emphasize the importance of performing time-resolved fluorescence anisotropy measurements in conjunction with photobleaching experiments to clarify such issues.

A small component of reversible GFP photobleaching was detected in the spot photobleaching measurements. It was seen as a very fast fluorescence recovery ($t_{1/2}$ of ~3 ms), which was independent of bleach spot size and thus unrelated to GFP diffusion. Similar reversible GFP photobleaching was observed for photobleaching of expressed GFP in cytoplasm and purified GFP in viscous saline solutions (Swaminathan et al., 1997). Reversible recovery is thought to arise from population of the triplet state during the bleach pulse, followed by relaxation to the S_0 ground state during the recovery period producing increasing fluorescence. For fluorescein, the recovery due to triplet state relaxation can be made immeasurably fast by addition of triplet state quenchers such as O_2 and Mn^{2+} (Periasamy et

al., 1996); however, such maneuvers do not affect GFP photobleaching because of the inaccessibility of the buried triamino acid chromophore to small molecules (Yang et al., 1996; Ormø et al., 1996; Swaminathan et al., 1997). The reversible photobleaching was not seen in the imaging experiments of fixed cells because the images were acquired well after the reversible component was complete. For measurements conducted with a 40× objective, the time course of recovery from irreversible GFP photobleaching was well resolved (>25-fold slower) from that of the recovery from reversible photobleaching.

The determination of absolute diffusion coefficients from photobleaching recovery data required modeling of ER geometry and made the assumption of a single time-independent diffusion coefficient. The confinement of GFP to the ER lumen is predicted to result in mildly slowed fluorescence recovery compared to the situation in cytoplasm or aqueous solution layers in which GFP is distributed homogeneously over three dimensions. Computation of a "correction factor" for ER geometry requires knowledge of the ER geometry. Precise three-dimensional reconstructions of ER geometry are needed using electron microscopy tomography or other approaches. Current descriptions of ER geometry derived from conventional transmission electron microscopy depict the ER lumen as layers of planar ribbons or interconnected cylinders that vary with cell type and position within the cell (Alberts et al., 1994). The modeling described here and by Ölveczky and Verkman (1998) indicated that small (<1.5-fold) correction factors are needed even when very different assumptions are made about ER geometry. The robustness of the modeling suggests that the computed absolute D value ranges are reasonably accurate. The issue of heterogeneity in diffusion coefficients and anomalous diffusion in the ER lumen is difficult to address using the available data. We recently developed analysis procedures to deduce complex diffusive phenomena from photobleaching recovery data (Periasamy and Verkman, 1998); however, the complexity of ER geometry and the relatively poor signal-to-noise ratio in individual fluorescence recovery curves precluded the use of these procedures.

Repeated bleaching of a single spot (Fig. 2) demonstrated that the ER lumen was continuous and that almost all of the observed GFP fluorescence was associated with the ER reticular network. The <1% residual fluorescence most likely arises from a pre-Golgi or cis-Golgi compartment based on its pattern of perinuclear localization. This result supports and corroborates biochemical- and electron micrographic-based models of KDEL recycling in which proteins with a C-terminal KDEL amino acid sequence that escape from the ER are returned via an intermediate ER-Golgi compartment (Klausner et al., 1992; Griffiths et al., 1994; Stinchcombe et al., 1995; Sciaky et al., 1997).

Several potential effectors of ER geometry or lumen environment were studied. External solution osmolality was changed in an attempt to alter ER lumen volume, and thus luminal solute concentrations. This maneuver was previously shown to change cell volume effectively (Farinas et al., 1995). Similar experiments for GFP diffusion in the cytoplasm gave 2.9-fold slowing of GFP diffusion for 2-fold cell shrinking and 1.6-fold increased diffusion for 2-fold cell swelling (Swaminathan et al., 1997). The data here showed surprisingly little effect of solution osmolality on GFP diffusion in the ER. We believe that the most likely explanation is that geometric restrictions and/or volume homeostatic mechanisms maintain the constancy of ER luminal volume under the strains of external solution osmolality. Such volume homeostasis might be achieved through cytoskeletal reinforcements such as microtubules, which associate with the ER and are involved in ER reorganization (Terasaki et al., 1986; Lee and Chen, 1988). Experiments using isolated ER membrane vesicles containing expressed GFP will be needed to examine the effect of lumen solute concentration on GFP diffusion.

Increasing temperature from 23 to 37°C produced a small 1.4-fold increase in the rate of GFP diffusion in the ER lumen. The water solvent viscosities at 23°C (0.933 cp) and 37°C (0.692) (Weast, 1986) predict a 1.35 increase in solute diffusion over this temperature range. While it is possible that ER reticular structure is altered by an increase in temperature, it does not seem necessary to invoke this as an explanation for increased GFP diffusion based on the anticipated differences in viscosity.

Increasing cytosolic calcium concentration by the ionophore A23187 produced vesiculation of CHO cell ER and an expected decrease in the fraction of fluorescence recovery in photobleaching measurements. These results are in agreement with those determined using starfish eggs (Terasaki et al., 1996), rat basophilic leukemia 2H3 cells, and mouse fibroblast 3T3 cells (Subramanian and Meyer, 1997).

The reducing agent DTT disrupts disulfide bonding and leads to the unfolding of disulfide-containing proteins in the normally oxidative ER. Most cells treated with DTT mount a so-called unfolded protein response (UPR) characterized morphologically by a gross expansion of the ER compartment. Helenius et al. (1992) have shown by electron microscopy that DTT-treated CHO cells contain proliferated ER compartments. We found that DTT incubation did not significantly affect GFP diffusion in the ER. This suggests that DTT-induced ER expansion occurs in a manner in which the ER luminal density of solutes does not change. In an effort to counter the unfolding effects of DTT, cells up-regulate the synthesis of ER luminal molecular chaperones involved in protein quality control (McMillan et al., 1994). As the ER compartment proliferates, it would be expected that lipid membrane production is concomitantly up-regulated. Indeed, Cox et al. (1997) have demonstrated that the biosynthetic pathways for protein and lipid production in the ER are intimately coupled in yeast during UPR. Our biophysical characterization of solute diffusion in the ER lumen of DTT-treated CHO cells is consistent with these qualitative findings in yeast.

Whereas DTT-treatment resulted in little change in the apparent rate of GFP diffusion in the ER lumen, brefeldin A produced a 2.7-fold increase. The deduced GFP diffusion

coefficient after brefeldin A treatment was $1.4–2.8 \times 10^{-7}$ cm^2/s, slightly less than that for GFP diffusion in cytoplasm. Brefeldin A blocks vesicular traffic from the ER to the Golgi without any gross change in ER ultrastructure at the light microscopic level. We believe the most likely explanation for the increased GFP diffusion in brefeldin A-treated cells is that the inhibition of anterograde vesicle movement without effect on retrograde transport leads to an expansion of the ER compartment in a manner that decreases molecular crowding. In a study on the effects of brefeldin A on Golgi tubule traffic, Sciaky et al. (1997) demonstrated that brefeldin A treatment in CHO cells leads to the collapse of the Golgi compartment onto the ER within ~10 min. We propose that molecular crowding in the ER lumen is decreased by Golgi coalescence with the ER compartment; an increase in the ratio of total ER membrane lipid to total luminal protein results in the dilution of ER luminal contents.

Slowed diffusion of GFP can be viewed as arising from three factors: collisions with obstacles, increased intrinsic viscosity of the medium, and binding interactions (Kao et al., 1993). The greater slowing of translational diffusion as compared to rotational diffusion suggests that the major factor influencing the mobility of GFP in the ER lumen is collisional in nature. The decrease in both translational and rotational mobilities may indicate some component(s) of binding. While a more detailed study would be necessary to delineate the precise contributions of these three factors, the results here establish quantitative methods for determining the mobility of proteins in the ER and provide the groundwork for further studies of ER-related processes.

APPENDIX

Model of solute diffusion in the ER lumen

The ER was modeled as planar sheets, each sheet inclined at an angle θ to the horizontal (see Fig. 4 *A*). The vertically oriented bleach/probe beam was modeled as a uniform disk profile of diameter d. It was assumed that the planar sheets to which GFP is confined are very thin and that bleach time is very brief. The intersection of the bleach/probe beam with each planar sheet produces an ellipse of minor axis $d/2$ and major axis $(d/2)\cos\theta$.

The diffusion equation for *bleached* fluorophore moving *out of* an ellipse (formally identical to unbleached fluorophore moving into an ellipse) was solved numerically by superposition of point source diffusion profiles. The solution of the two-dimensional diffusion equation for a point source is given by Crank (1975)

$$C(\vec{r}, Dt) = (M/4\pi Dt)e^{(r^2/4Dt)} \tag{A1}$$

where M is the amount of bleached fluorophore and D is the diffusion coefficient. Equation A1 can be rewritten in terms of $\tau = Dt/d^2$, a dimensionless time variable:

$$C(\vec{r}, \tau) = (M'/4\pi\tau)e^{(r^2d^2/4\tau)} \tag{A2}$$

where $M' = (M/d^2)$ is the normalized concentration of bleached fluorophore at position $\vec{r}$. The concentration of bleached fluorophore contributed by point sources at a set of positions $\{\vec{r}_p\}$, distributed throughout an ellipse of area E, and observed at a position $\vec{r}_q$ within the ellipse, is given by

$$C(\vec{r}_q, \tau) = \sum_{p\in E} C(|\vec{r}_q - \vec{r}_p|, \tau) \tag{A3}$$

The total fluorescence intensity arising from the elliptical cross-section between a planar sheet of fluorophore at an angle θ and an illuminating beam is then given as the sum over all observation points within the ellipse,

$$F(\theta, \tau) = A \cdot \sum_{q\in E} C(\vec{r}_q, \tau) \tag{A4}$$

where A is a constant relating to bleached fluorophore concentration to fluorescence intensity. For planes of random orientations between angles θ and θ_{max} the total mean fluorescence intensity is given by

$$\langle F(\tau)\rangle_\theta^{\theta_{max}} = \sum_\theta^{\theta_{max}} F(\theta, \tau) \cdot \cos\theta \Big/ \sum_\theta^{\theta_{max}} \cos\theta \tag{A5}$$

Computations were performed in Cartesian coordinates with $\Delta x = \Delta y = d/40$ and $\theta = 2°$. For the case of a horizontal plane yielding a circular cross-sectional area, computed and analytical solutions were indistinguishable using this discretization scheme.

We thank Katherine Chen for cell culture and plasmid preparations, and Drs. Javier Farinas and N. Periasamy for helpful advice.

This work was supported by National Institutes of Health Grants DK43840, HL60288, DK16095, DK35124, and HL59198 and a grant from the National Cystic Fibrosis Foundation.

REFERENCES

Alberts, B., D. Dennis, J. Lewis, M. Raff, K. Roberts, and J. D. Watson. 1994. Molecular Biology of the Cell, 3rd ed. Garland Press, New York. 577–598.

Barak, L. S., S. S. Ferguson, J. Zhang, C. Matenson, T. Meyer, and M. G. Caron. 1997. Internal trafficking and surface mobility of a functionally intact β2-adrenergic receptor-green fluorescent protein conjugate. *Mol. Pharmacol.* 51:177–184.

Bicknese, S., N. Periasamy, S. B. Shohet, and A. S. Verkman. 1993. Cytoplasmic viscosity near the cell plasma membrane: measurement by evanescent field frequency-domain microfluorimetry. *Biophys. J.* 165: 1272–1282.

Cantor, C. R., and P. R. Schimmel. 1980. Biophysical Chemistry. Part II: Techniques for the study of Biological Structure and Function. W. H. Freeman, New York. 560–567.

Cole, N. B., C. L. Smith, N. Sciaky, M. Terasaki, M. Edidin, and J. Lippincott-Schwartz. 1996. Diffusional mobility of Golgi proteins in membranes of living cells. *Science*. 273:797–801.

Cox, J. S., R. E. Chapman, and P. Walter. 1997. The unfolded protein response coordinates the production of endoplasmic reticulum protein and endoplasmic reticulum membrane. *Mol. Biol. Cell*. 8:1805–1814.

Crank, J. 1975. The Mathematics of Diffusion, 2nd Ed. Oxford University Press, New York. 29.

DeGiorgi, F., M. Brini, C. Bastianutto, R. Marsault, M. Montero, P. Pizzo, R. Rozzi, and R. Rizzuto. 1996. Targeting aequorin and green fluorescent protein to intracellular organelles. *Gene*. 173:113–117.

Ellenberg, J., E. D. Siggia, J. E. Moreira, C. L. Smith, J. F. Presley, H. J. Worman, and J. Lippincott-Schwartz. 1997. Nuclear membrane dynamics and reassembly in living cells: targeting of an inner nuclear membrane protein in interphase and mitosis. *J. Cell. Biol.* 138:1193–1206.

Farinas, J., V. Simenak, and A. S. Verkman. 1995. Cell volume measured in adherent cells by total internal reflection microfluorimetry: application to permeability in cells transfected with water channel homologs. *Biophys. J.* 68:1613–1620.

Feder, T. J., I. Brust-Mascher, J. P. Slattery, B. Baird, and W. W. Webb. 1996. Constrained diffusion or immobile fraction on cell surfaces: a new interpretation. *Biophys. J.* 70:2367–2373.

Fushimi, K., and A. S. Verkman. 1991. Low viscosity in the aqueous domain of cytoplasm measured by picosecond polarization microscopy. *J. Cell Biol.* 112:719–725.

Gerdes, H.-H., and C. Kaether. 1996. Green fluorescent protein: applications to cell biology. *FEBS Lett.* 389:44–47.

Griffiths, G., M. Ericsson, J. Krijnse-Locker, T. Nilsson, B. Goud, H. D. Sàling, B. L. Tang, S. H. Wong, and W. Hong. 1994. Localization of the Lys, Asp, Glu, Leu tetrapeptide receptor to the Golgi complex and the intermediate compartment in mammalian cells. *J. Cell Biol.* 127: 1557–1574.

Hammond, C., and A. Helenius. 1995. Quality control in the secretory pathway. *Curr. Opin. Cell Biol.* 7:525–539.

Helenius, A., T. Marquardt, and I. Braakman. 1992. The endoplasmic reticulum as a protein-folding compartment. *Trends Cell Biol.* 2:227–231.

Kao, H. P., J. R. Abney, and A. S. Verkman. 1993. Determinants of the translational diffusion of a small solute in cytoplasm. *J. Cell Biol.* 120:175–184.

Kao, H. P., and A. S. Verkman. 1996. Construction and performance of a FRAP instrument with microsecond time resolution. *Biophys. Chem.* 59:203–210.

Klausner, R. D., J. G. Donaldson, and J. Lippincott-Schwartz. 1992. Brefeldin A: insights into the control of membrane traffic and organelle structure. *J. Cell Biol.* 116:1071–1080.

Kneen, M., J. Farinas, Y. Li, and A. S. Verkman. 1998. Green fluorescent protein as a noninvasive intracellular pH indicator. *Biophys. J.* 74: 1591–1600.

Koch, G. L. E., D. R. J. Macer, and M. J. Smith. 1987. Visualization of the intact endoplasmic reticulum by immunofluorescence with antibodies to the major ER glycoprotein, endoplasmin. *J. Cell. Sci.* 87:535–542.

Lee, C., and L. B. Chen. 1988. Dynamic behavior of endoplasmic reticulum in living cells. *Cell* 54:37–46.

Luby-Phelps, K., P. E. Castle, D. L. Taylor, and F. Lanni. 1987. Hindered diffusion of inert tracer particles in the cytoplasm of mouse 3T3 fibroblasts. *Proc. Natl. Acad. Sci. USA.* 84:4910–4913.

Luby-Phelps, K., S. Mujundar, R. Mujundar, L. Ernst, W. Galbraith, and A. Waggoner. 1993. A novel fluorescence ratiometric method confirms the low solvent viscosity of the cytoplasm. *Biophys. J.* 65:236–242.

McMillan, D. R., M. J. Gething, and J. Sambrook. 1994. The cellular response to unfolded proteins: intercompartmental signaling. *Curr. Opin. Biotechnol.* 5:540–545.

Ölveczky, B. P., and A. S. Verkman. 1998. Monte Carlo analysis of obstructed diffusion in three dimensions: application to molecular diffusion in organelles. *Biophys. J.* 74:2722–2730.

Ormø, M., A. B. Cubitt, K. Kallio, L. A. Gross, R. Y. Tsien, and S. J. Remington. 1996. Crystal structure of the *Aequorea victoria* green fluorescent protein. *Science*. 273:1392–1395.

Partikian, A., B. Ölveczky, R. Swaminathan, Y. Li, and A. S. Verkman. 1998. Rapid diffusion of green fluorescent protein in the mitochondrial matrix. *J. Cell Biol.* 140:821–829.

Periasamy, N., S. Bicknese, and A. S. Verkman. 1996. Reversible photobleaching of fluorescein conjugates in air-saturated viscous solutions: molecular tryptophan as a triplet state quencher. *Photochem. Photobiol.* 63:265–271.

Periasamy, N., and A. S. Verkman. 1998. Analysis of fluorophore diffusion by continuous distributions of diffusion coefficients: application to photobleaching measurements of simple and anomalous diffusion. *Biophys. J.* 75:557–567.

Presley, J. F., N. B. Cole., T. A. Schroer, K. Hirschberg, K. J. M. Zaal, and J. Lippincott-Schwartz. 1997. ER to Golgi transport visualized in living cells: microtubule dependent translocation of tubulovesiclar intermediates. *Nature*. 389:81–85.

Rizzuto, R., M. Brini, P. Pizzo, M. Murgia, and T. Pozzan. 1995. Chimeric green fluorescent protein as a tool for visualizing subcellular organelles in living cells. *Curr. Biol.* 5:636–642.

Sciaky, N., J. Presley, C. Smith, K. J. M. Zaal, N. Cole, J. E. Moreira, M. Terasaki, E. Siggia, and J. Lippincott-Schwartz. 1997. Golgi tubule traffic and the effects of brefeldin A visualized in living cells. *J. Cell Biol.* 139:1137–1155.

Seksek, O., J. Biwersi, and A. S. Verkman. 1997. Translational diffusion of macromolecule-size solutes in cytoplasm and nucleus. *J. Cell. Biol.* 138:131–142.

Simon, S., C. S. Peskin, and G. F. Oster. 1992. What drives the translocation of proteins? *Proc. Natl. Acad. Sci. U.S.A.* 89:3770–3774.

Stinchcombe, J. C., H. Nomoto, D. F. Cutler, and C. R. Hopkins. 1995. Anterograde and retrograde traffic between the rough endoplasmic reticulum and the Golgi complex. *J. Cell Biol.* 131:1387–1401.

Subramanian, K., and T. Meyer. 1997. Calcium-induced restructuring of nuclear envelope and endoplasmic reticulum calcium stores. *Cell.* 89: 963–71.

Swaminathan, R., S. Bicknese, N. Periasamy, and A. S. Verkman. 1996. Cytoplasmic viscosity near the cell plasma membrane: translation of BCECF measured by total internal reflection-fluorescence photobleaching recovery. *Biophys. J.* 71:1140–1151.

Swaminathan, R., C. P. Hoang, and A. S. Verkman. 1997. Photochemical properties of green fluorescent protein GFP-S65T in solution and transfected CHO cells: analysis of cytoplasmic viscosity by GFP translational and rotational diffusion. *Biophys. J.* 72:1900–1907.

Tamarappoo, B. K., and A. S. Verkman. 1998. Defective trafficking of AQP2 water channels in nephrogenic diabetes insipidus and correction by chemical chaperones. *J. Clin. Invest.* 101:2257–2267.

Terasaki, M., L. A. Jaffe, G. R. Hunnicutt, and J. A. Hammer. 1996. Structural change of the endoplasmic reticulum during fertilization: evidence for loss of membrane continuity using the green fluorescent protein. *Dev. Biol.* 179:320–328.

Verkman, A. S. 1999. Green fluorescent protein as a probe to study intracellular solute diffusion. *Meth. Enzymol* 302:250–265.

Verkman, A. S., M. Armijo, and K. Fushimi. 1991. Construction and evaluation of a frequency-domain epifluorescence microscope for lifetime and anisotropy decay measurements in subcellular domains. *Biophys. Chem.* 40:117–125.

Weast, R. C., editor. 1986. CRC Handbook of Chemistry and Physics, 67th Ed. CRC Press, Boca Raton.

Yang, F., L. G. Moss, and G. N. Phillips. 1996. The molecular structure of green fluorescent protein. *Nature Biotech.* 14:1264–1251.